



1 Global Carbon Budget 2022

2

3 Pierre Friedlingstein^{1,2}, Michael O’Sullivan¹, Matthew W. Jones³, Robbie M. Andrew⁴, Luke
4 Gregor⁵, Judith Hauck⁶, Corinne Le Quéré³, Ingrid T. Lujckx⁷, Are Olsen^{8,9}, Glen P. Peters⁴,
5 Wouter Peters^{7,10}, Julia Pongratz^{11,12}, Clemens Schwingshackl¹¹, Stephen Sitch¹, Josep G.
6 Canadell¹³, Philippe Ciais¹⁴, Robert B. Jackson¹⁵, Simone Alin¹⁶, Ramdane Alkama¹⁷, Almut
7 Arneeth¹⁸, Vivek K. Arora¹⁹, Nicholas R. Bates^{20,21}, Meike Becker^{8,9}, Nicolas Bellouin²², Henry
8 C. Bittig²³, Laurent Bopp², Frédéric Chevallier¹⁴, Louise P. Chini²⁴, Margot Cronin²⁵, Wiley
9 Evans²⁶, Stefanie Falk¹¹, Richard A. Feely¹⁶, Thomas Gasser²⁷, Marion Gehlen¹⁴, Thanos
10 Gkritzalis²⁸, Lucas Gloege^{29,30}, Giacomo Grassi¹⁷, Nicolas Gruber⁵, Özgür Gürses⁶, Ian
11 Harris³¹, Matthew Hefner^{32,33}, Richard A. Houghton³⁴, George C. Hurtt²⁴, Yosuke Iida³⁵,
12 Tatiana Ilyina¹², Atul K. Jain³⁶, Annika Jersild¹², Koji Kadono³⁵, Etsushi Kato³⁷, Daniel
13 Kennedy³⁸, Kees Klein Goldewijk³⁹, Jürgen Knauer^{40,41}, Jan Ivar Korsbakken⁴, Peter
14 Landschützer^{12,28}, Nathalie Lefèvre⁴², Keith Lindsay⁴³, Junjie Liu⁴⁴, Zhu Liu⁴⁵, Gregg
15 Marland^{32,33}, Nicolas Mayot³, Matthew J. McGrath¹⁴, Nicolas Metzler⁴², Natalie M. Monacci⁴⁶,
16 David R. Munro^{47,48}, Shin-Ichiro Nakaoka⁴⁹, Yosuke Niwa^{49,50}, Kevin O’Brien^{51,16}, Tsuneo
17 Ono⁵², Paul I. Palmer^{53,54}, Naiqing Pan^{55,56}, Denis Pierrot⁵⁷, Katie Pocock²⁶, Benjamin
18 Poulter⁵⁸, Laure Resplandy⁵⁹, Eddy Robertson⁶⁰, Christian Rödenbeck⁶¹, Carmen Rodriguez⁶²,
19 Thais M. Rosan¹, Jörg Schwinger^{63,9}, Roland Séférian⁶⁴, Jamie D. Shutler¹, Ingunn Skjelvan^{63,9},
20 Tobias Steinhoff⁶⁵, Qing Sun⁶⁶, Adrienne J. Sutton¹⁶, Colm Sweeney⁴⁸, Shintaro Takao⁴⁹, Toste
21 Tanhua⁶⁵, Pieter P. Tans⁶⁷, Xiangjun Tian⁶⁸, Hanqin Tian⁵⁶, Bronte Tilbrook^{69,70}, Hiroyuki
22 Tsujino⁵⁰, Francesco Tubiello⁷¹, Guido R. van der Werf⁷², Anthony P. Walker⁷³, Rik
23 Wanninkhof⁵⁷, Chris Whitehead⁷⁴, Anna Willstrand Wranne⁷⁵, Rebecca Wright³, Wenping
24 Yuan⁷⁶, Chao Yue⁷⁷, Xu Yue⁷⁸, Sönke Zaehle⁶¹, Jiye Zeng⁴⁹, Bo Zheng⁷⁹

25

26 ¹ Faculty of Environment, Science and Economy, University of Exeter, Exeter EX4 4QF, UK

27 ² Laboratoire de Météorologie Dynamique / Institut Pierre-Simon Laplace, CNRS, Ecole Normale
28 Supérieure / Université PSL, Sorbonne Université, Ecole Polytechnique, Paris, France

29 ³ Tyndall Centre for Climate Change Research, School of Environmental Sciences, University of
30 East Anglia, Norwich Research Park, Norwich NR4 7TJ, UK

31 ⁴ CICERO Center for International Climate Research, Oslo 0349, Norway

32 ⁵ Environmental Physics Group, ETH Zürich, Institute of Biogeochemistry and Pollutant Dynamics
33 and Center for Climate Systems Modeling (C2SM), Zurich, Switzerland

34 ⁶ Alfred-Wegener-Institut Helmholtz-Zentrum für Polar- und Meeresforschung, Postfach 120161,
35 27515 Bremerhaven, Germany

36 ⁷ Wageningen University, Environmental Sciences Group, P.O. Box 47, 6700AA, Wageningen, The
37 Netherlands

38 ⁸ Geophysical Institute, University of Bergen, Bergen, Norway

39 ⁹ Bjerknes Centre for Climate Research, Bergen, Norway

40 ¹⁰ University of Groningen, Centre for Isotope Research, Groningen, The Netherlands

41 ¹¹ Ludwig-Maximilians-Universität München, Luisenstr. 37, 80333 München, Germany

42 ¹² Max Planck Institute for Meteorology, Hamburg, Germany

43 ¹³ CSIRO Oceans and Atmosphere, Canberra, ACT 2101, Australia

44 ¹⁴ Laboratoire des Sciences du Climat et de l’Environnement, LSCE/IPSL, CEA-CNRS-UVSQ,
45 Université Paris-Saclay, F-91191 Gif-sur-Yvette, France

46 ¹⁵ Department of Earth System Science, Woods Institute for the Environment, and Precourt
47 Institute for Energy, Stanford University, Stanford, CA 94305–2210, United States of America

48 ¹⁶ National Oceanic & Atmospheric Administration, Pacific Marine Environmental Laboratory
49 (NOAA/PMEL), 7600 Sand Point Way NE, Seattle, WA 98115, USA

50 ¹⁷ Joint Research Centre, European Commission, Ispra, Italy

51 ¹⁸ Karlsruhe Institute of Technology, Institute of Meteorology and Climate Research/Atmospheric
52 Environmental Research, 82467 Garmisch-Partenkirchen, Germany

53



- 54 ¹⁹ Canadian Centre for Climate Modelling and Analysis, Climate Research Division, Environment
55 and Climate Change Canada, Victoria, BC, Canada
56 ²⁰ Bermuda Institute of Ocean Sciences (BIOS), 17 Biological Lane, St. Georges, GE01, Bermuda
57 ²¹ Department of Ocean and Earth Science, University of Southampton, European Way,
58 Southampton, SO14 3ZH, UK
59 ²² Department of Meteorology, University of Reading, Reading, UK
60 ²³ Leibniz Institute for Baltic Sea Research Warnemuende (IOW), Seestrasse 15; 18119 Rostock,
61 Germany
62 ²⁴ Department of Geographical Sciences, University of Maryland, College Park, Maryland 20742,
63 USA
64 ²⁵ Marine Institute, Galway, Ireland
65 ²⁶ Hakai Institute, Heriot Bay, BC, Canada
66 ²⁷ International Institute for Applied Systems Analysis (IIASA), Schlossplatz 1
67 A-2361 Laxenburg, Austria
68 ²⁸ Flanders Marine Institute (VLIZ), InnovOceanSite, Wandelaarkaai 7, 8400 Ostend, Belgium
69 ²⁹ Lamont-Doherty Earth Observatory and Department of Earth and Environmental Sciences,
70 Columbia University, New York, NY, USA
71 ³⁰ Open Earth Foundation, Marina del Rey, CA, USA
72 ³¹ NCAS-Climate, Climatic Research Unit, School of Environmental Sciences, University of East
73 Anglia, Norwich Research Park, Norwich, NR4 7TJ, UK
74 ³² Research Institute for Environment, Energy, and Economics, Appalachian State University,
75 Boone, North Carolina, USA
76 ³³ Department of Geological and Environmental Sciences, Appalachian State University, Boone,
77 North Carolina, USA
78 ³⁴ Woodwell Climate Research Center, Falmouth, MA 02540, USA
79 ³⁵ Atmosphere and Ocean Department, Japan Meteorological Agency, Minato-Ku, Tokyo 105-
80 8431, Japan
81 ³⁶ Department of Atmospheric Sciences, University of Illinois, Urbana, IL 61821, USA
82 ³⁷ Institute of Applied Energy (IAE), Minato-ku, Tokyo 105-0003, Japan
83 ³⁸ National Center for Atmospheric Research, Climate and Global Dynamics, Terrestrial Sciences
84 Section, Boulder, CO 80305, USA
85 ³⁹ Utrecht University, Faculty of Geosciences, Department IMEW, Copernicus Institute of
86 Sustainable Development, Heidelberglaan 2, P.O. Box 80115, 3508 TC, Utrecht, the Netherlands
87 ⁴⁰ Hawkesbury Institute for the Environment, Western Sydney University, Penrith, New South
88 Wales, Australia
89 ⁴¹ Climate Science Centre, CSIRO Oceans and Atmosphere, Canberra, ACT, Australia
90 ⁴² LOCEAN/IPSL laboratory, Sorbonne Université, CNRS/IRD/MNHN, Paris, France
91 ⁴³ National Center for Atmospheric Research, Climate and Global Dynamics, Oceanography
92 Section, Boulder, CO 80305, USA
93 ⁴⁴ Jet Propulsion Laboratory, California Institute of Technology, Pasadena, CA, USA
94 ⁴⁵ Department of Earth System Science, Tsinghua University, Beijing, China
95 ⁴⁶ University of Alaska Fairbanks, College of Fisheries and Ocean Sciences, PO Box 757220,
96 Fairbanks, AK, USA
97 ⁴⁷ Cooperative Institute for Research in Environmental Sciences, University of Colorado, Boulder,
98 CO, 80305, USA
99 ⁴⁸ National Oceanic & Atmospheric Administration/Global Monitoring Laboratory (NOAA/GML),
100 Boulder, CO, 80305, USA
101 ⁴⁹ Earth System Division, National Institute for Environmental Studies (NIES), 16-2 Onogawa,
102 Tsukuba Ibaraki, 305-8506, Japan
103 ⁵⁰ Meteorological Research Institute, 1-1 Nagamine, Tsukuba, Ibaraki, 305-0052 Japan
104 ⁵¹ Cooperative Institute for Climate, Ocean and Ecosystem Studies (CICOES), University of
105 Washington, Seattle, WA, USA
106 ⁵² Japan Fisheries Research and Education Agency, 2-12-4 Fukuura, Kanazawa-Ku, Yokohama 236-
107 8648, Japan
108 ⁵³ National Centre for Earth Observation, University of Edinburgh, UK
109 ⁵⁴ School of GeoSciences, University of Edinburgh, UK
110 ⁵⁵ College of Forestry, Wildlife and Environment, Auburn University, Auburn, AL 36849, USA
111 ⁵⁶ Schiller Institute for Integrated Science and Society, Department of Earth and Environmental
112 Sciences, Boston College, Chestnut Hill, MA 02467, USA
113



- 114 ⁵⁷ National Oceanic & Atmospheric Administration/Atlantic Oceanographic & Meteorological
115 Laboratory (NOAA/AOML), Miami, FL 33149, USA
116 ⁵⁸ NASA Goddard Space Flight Center, Biospheric Sciences Laboratory, Greenbelt, Maryland
117 20771, USA
118 ⁵⁹ Princeton University, Department of Geosciences and Princeton Environmental Institute,
119 Princeton, NJ, USA
120 ⁶⁰ Met Office Hadley Centre, FitzRoy Road, Exeter EX1 3PB, UK
121 ⁶¹ Max Planck Institute for Biogeochemistry, P.O. Box 600164, Hans-Knöll-Str. 10, 07745 Jena,
122 Germany
123 ⁶² University of Miami, RSMAS, 4600 Rickenbacker Causeway, Miami, FL 33149, USA
124 ⁶³ NORCE Norwegian Research Centre, Jahnebakken 5, 5007 Bergen, Norway
125 ⁶⁴ CNRM, Université de Toulouse, Météo-France, CNRS, Toulouse, France
126 ⁶⁵ GEOMAR Helmholtz Centre for Ocean Research Kiel, Düsternbrooker Weg 20, 24105 Kiel,
127 Germany
128 ⁶⁶ Climate and Environmental Physics, Physics Institute and Oeschger Centre for Climate Change
129 Research, University of Bern, Bern, Switzerland
130 ⁶⁷ National Oceanic & Atmospheric Administration, Earth System Research Laboratory
131 (NOAA ESRL), Boulder, CO 80305, USA
132 ⁶⁸ Institute of Tibetan Plateau Research, Chinese Academy of Sciences, Beijing 100101, China
133 ⁶⁹ CSIRO Oceans and Atmosphere, PO Box 1538, Hobart, Tasmania 7001, Australia
134 ⁷⁰ Australian Antarctic Partnership Program, University of Tasmania, Hobart, Australia
135 ⁷¹ Statistics Division, Food and Agriculture Organization of the United Nations, Via Terme di
136 Caracalla, Rome 00153, Italy
137 ⁷² Department of Earth sciences, Faculty of Science, Vrije Universiteit, Amsterdam, the
138 Netherlands
139 ⁷³ Environmental Sciences Division and Climate Change Science Institute, Oak Ridge National
140 Laboratory, Oak Ridge, TN, 37831, USA
141 ⁷⁴ Sitka Tribe of Alaska, 456 Katlian Street, Sitka, Alaska 99835, USA
142 ⁷⁵ Swedish Meteorological and Hydrological Institute, Sven Källfeltsgata 15, 426 68 Västra
143 Frölunda, Sweden
144 ⁷⁶ School of Atmospheric Sciences, Sun Yat-sen University, Zhuhai, Guangdong 510245, China.
145 ⁷⁷ Institute of Soil and Water Conservation, Northwest A&F University, Yangling, Shaanxi 712100,
146 P.R. China
147 ⁷⁸ School of Environmental Science and Engineering, Nanjing University of Information Science
148 and Technology (NUIST), China
149 ⁷⁹ Institute of Environment and Ecology, Tsinghua Shenzhen International Graduate School,
150 Tsinghua University, Shenzhen 518055, China
151
152 *Correspondence to:* Pierre Friedlingstein (p.friedlingstein@exeter.ac.uk)



153

154

155 **Abstract**

156 Accurate assessment of anthropogenic carbon dioxide (CO₂) emissions and their redistribution among the
157 atmosphere, ocean, and terrestrial biosphere in a changing climate is critical to better understand the global
158 carbon cycle, support the development of climate policies, and project future climate change. Here we describe
159 and synthesise data sets and methodology to quantify the five major components of the global carbon budget
160 and their uncertainties. Fossil CO₂ emissions (EFOS) are based on energy statistics and cement production data,
161 while emissions from land-use change (ELUC), mainly deforestation, are based on land-use and land-use
162 change data and bookkeeping models. Atmospheric CO₂ concentration is measured directly, and its growth rate
163 (GATM) is computed from the annual changes in concentration. The ocean CO₂ sink (SOCEAN) is estimated
164 with global ocean biogeochemistry models and observation-based data-products. The terrestrial CO₂ sink
165 (SLAND) is estimated with dynamic global vegetation models. The resulting carbon budget imbalance (BIM),
166 the difference between the estimated total emissions and the estimated changes in the atmosphere, ocean, and
167 terrestrial biosphere, is a measure of imperfect data and understanding of the contemporary carbon cycle. All
168 uncertainties are reported as $\pm 1\sigma$.

169 For the year 2021, EFOS increased by 5.1% relative to 2020, with fossil emissions at 10.1 ± 0.5 GtC yr⁻¹ ($9.9 \pm$
170 0.5 GtC yr⁻¹ when the cement carbonation sink is included), ELUC was 1.1 ± 0.7 GtC yr⁻¹, for a total
171 anthropogenic CO₂ emission of 11.1 ± 0.8 GtC yr⁻¹ (40.8 ± 2.9 GtCO₂). Also, for 2021, GATM was 5.2 ± 0.2
172 GtC yr⁻¹ (2.5 ± 0.1 ppm yr⁻¹), SOCEAN was 2.9 ± 0.4 GtC yr⁻¹ and SLAND was 3.5 ± 0.9 GtC yr⁻¹, with a
173 BIM of -0.6 GtC yr⁻¹ (i.e. total estimated sources too low or sinks too high). The global atmospheric CO₂
174 concentration averaged over 2021 reached 414.71 ± 0.1 ppm. Preliminary data for 2022, suggest an increase in
175 EFOS relative to 2021 of +1.1% (0% to 1.7%) globally, and atmospheric CO₂ concentration reaching 417.3
176 ppm, more than 50% above pre-industrial level. Overall, the mean and trend in the components of the global
177 carbon budget are consistently estimated over the period 1959-2021, but discrepancies of up to 1 GtC yr⁻¹ persist
178 for the representation of annual to semi-decadal variability in CO₂ fluxes. Comparison of estimates from
179 multiple approaches and observations shows: (1) a persistent large uncertainty in the estimate of land-use
180 changes emissions, (2) a low agreement between the different methods on the magnitude of the land CO₂ flux in
181 the northern extra-tropics, and (3) a discrepancy between the different methods on the strength of the ocean sink
182 over the last decade. This living data update documents changes in the methods and data sets used in this new
183 global carbon budget and the progress in understanding of the global carbon cycle compared with previous
184 publications of this data set (Friedlingstein et al., 2022a; Friedlingstein et al., 2020; Friedlingstein et al., 2019;
185 Le Quéré et al., 2018b, 2018a, 2016, 2015b, 2015a, 2014, 2013). The data presented in this work are available at
186 <https://doi.org/10.18160/GCP-2022> (Friedlingstein et al., 2022b).

187

188



189 **Executive Summary**

190 **Global fossil CO₂ emissions (excluding cement carbonation) further increased in 2022, being now slightly**
191 **above their pre-COVID19 pandemic level.** The 2021 emission increase was 0.46 GtC yr⁻¹ (1.7 GtCO₂ yr⁻¹),
192 bringing 2021 emissions to 10.1 ± 0.5 GtC yr⁻¹ (36.9 ± 1.8 GtCO₂ yr⁻¹), slightly below the emissions level of
193 2019. Preliminary estimates based on data available suggest fossil CO₂ emissions continued to increase in 2022,
194 by 1.1% relative to 2021 (0% to 1.7%), bringing emissions at 10.2 GtC yr⁻¹ (37.3 GtCO₂ yr⁻¹), slightly above the
195 2019 level (10.1 ± 0.5 GtC yr⁻¹, 37.0 ± 1.8 GtCO₂ yr⁻¹). Emissions from coal, oil, and gas in 2022 are expected
196 to be above their 2021 levels (by 0.8%, 2.2% and 1.1% respectively). Regionally, emissions in 2022 are
197 expected to have been decreasing by 1.5% in China (3.0 GtC, 11.1 GtCO₂), and 1% in the European Union (0.8
198 GtC, 2.8 GtCO₂), but increasing by 1.6% in the United States (1.4 GtC, 5.1 GtCO₂), 5.6% in India (0.8 GtC, 2.9
199 GtCO₂) and 2.5% for the rest of the world (4.2 GtC, 15.5 GtCO₂).

200 **Fossil CO₂ emissions decreased in 24 countries during the decade 2010-2019.** Altogether, these 24 countries
201 contribute to about 2.4 GtC yr⁻¹ (8.8 GtCO₂) fossil fuel CO₂ emissions over the last decade, only about one
202 quarter of world CO₂ fossil emissions.

203 **Global CO₂ emissions from land-use, land-use change, and forestry (LUC) averaged at 1.2 ± 0.7 GtC yr⁻¹**
204 **(4.5 ± 2.6 GtCO₂ yr⁻¹) for the 2012-2021 period with a preliminary projection for 2022 of 1.0 ± 0.7 GtC yr⁻¹**
205 **(3.6 ± 2.6 GtCO₂ yr⁻¹).** A small decrease over the past two decades is not robust given the large model
206 **uncertainty.** Deforestation emissions remain high at 1.8 ± 0.4 GtC yr⁻¹ over the 2012-2021 period, highlighting
207 a substantial mitigation potential for emissions reductions. Sequestration of 0.9 ± 0.3 GtC yr⁻¹ through re-
208 /afforestation and forestry offsets one half of the deforestation emissions. Emissions from other transitions and
209 from peat drainage and peat fire add further, small contributions. The highest emitters during 1959-2021 in
210 descending order were Brazil, Indonesia, and the Democratic Republic of the Congo, with these 3 countries
211 contributing more than half of the global total land-use emissions.

212 **The remaining carbon budget for a 50% likelihood to limit global warming to 1.5°C, 1.7°C and 2°C has**
213 **respectively reduced to 105 GtC (380 GtCO₂), 200 GtC (730 GtCO₂) and 335 GtC (1230 GtCO₂) from the**
214 **beginning of 2023, equivalent to 9, 18 and 30 years, assuming 2022 emissions levels.** Total anthropogenic
215 emissions were 11.1 GtC yr⁻¹ (40.8 GtCO₂ yr⁻¹) in 2021, with a preliminary estimate of 11.1 GtC yr⁻¹ (40.9
216 GtCO₂ yr⁻¹) for 2022. The remaining carbon budget to keep global temperatures below these climate targets has
217 shrunk by 33 GtC (121 GtCO₂) since the release of the IPCC AR6 Working Group 1 assessment in 2019.
218 Reaching zero CO₂ emissions by 2050 entails cutting total anthropogenic CO₂ emissions by about 0.4 GtC (1.4
219 GtCO₂) each year on average, comparable to the decrease during 2020, highlighting the scale of the action
220 needed.

221 **The concentration of CO₂ in the atmosphere is set to reach 417.3 ppm in 2022, 51% above pre-industrial**
222 **levels.** The atmospheric CO₂ growth was 5.2 ± 0.02 GtC yr⁻¹ during the decade 2012-2021 (48% of total CO₂
223 emissions) with a preliminary 2022 growth rate estimate of around 5.5 GtC yr⁻¹ (2.6 ppm).

224 **The ocean CO₂ sink resumed a more rapid growth in the past decade after low or no growth during the**
225 **1991-2002 period.** However, the growth of the ocean CO₂ sink in the past decade has an uncertainty of a factor



226 of three, with estimates based on data products and estimates based on models showing an ocean sink trend of
227 $+0.7 \text{ GtC yr}^{-1} \text{ decade}^{-1}$ and $+0.2 \text{ GtC yr}^{-1} \text{ decade}^{-1}$ since 2010, respectively. The discrepancy in the trend
228 originates from all latitudes but is largest in the Southern Ocean. The ocean CO_2 sink was $2.9 \pm 0.4 \text{ GtC yr}^{-1}$
229 during the decade 2011-2020 (26% of total CO_2 emissions), with a similar preliminary estimate of 2.9 GtC yr^{-1}
230 for 2022.

231 **The land CO_2 sink continued to increase during the 2012-2021 period primarily in response to increased**
232 **atmospheric CO_2 , albeit with large interannual variability.** The land CO_2 sink was $3.1 \pm 0.6 \text{ GtC yr}^{-1}$
233 during the 2012-2021 decade (29% of total CO_2 emissions), 0.4 GtC yr^{-1} larger than during the previous decade
234 (2000-2009), with a preliminary 2022 estimate of around 3.4 GtC yr^{-1} . Year to year variability in the land sink is
235 about 1 GtC yr^{-1} , making small annual changes in anthropogenic emissions hard to detect in global atmospheric
236 CO_2 concentration.
237



238 1 Introduction

239 The concentration of carbon dioxide (CO₂) in the atmosphere has increased from approximately 277 parts per
240 million (ppm) in 1750 (Joos and Spahni, 2008), the beginning of the Industrial Era, to 414.7 ± 0.1 ppm in 2021
241 (Dlugokencky and Tans, 2022); Figure 1). The atmospheric CO₂ increase above pre-industrial levels was,
242 initially, primarily caused by the release of carbon to the atmosphere from deforestation and other land-use
243 change activities (Canadell et al., 2021). While emissions from fossil fuels started before the Industrial Era, they
244 became the dominant source of anthropogenic emissions to the atmosphere from around 1950 and their relative
245 share has continued to increase until present. Anthropogenic emissions occur on top of an active natural carbon
246 cycle that circulates carbon between the reservoirs of the atmosphere, ocean, and terrestrial biosphere on time
247 scales from sub-daily to millennia, while exchanges with geologic reservoirs occur at longer timescales (Archer
248 et al., 2009).

249 The global carbon budget (GCB) presented here refers to the mean, variations, and trends in the perturbation of
250 CO₂ in the environment, referenced to the beginning of the Industrial Era (defined here as 1750). This paper
251 describes the components of the global carbon cycle over the historical period with a stronger focus on the
252 recent period (since 1958, onset of atmospheric CO₂ measurements), the last decade (2012-2021), the last year
253 (2021) and the current year (2022). Finally, it provides cumulative emissions from fossil fuels and land-use
254 change since the year 1750, the pre-industrial period; and since the year 1850, the reference year for historical
255 simulations in IPCC AR6 (Eyring et al., 2016).

256 We quantify the input of CO₂ to the atmosphere by emissions from human activities, the growth rate of
257 atmospheric CO₂ concentration, and the resulting changes in the storage of carbon in the land and ocean
258 reservoirs in response to increasing atmospheric CO₂ levels, climate change and variability, and other
259 anthropogenic and natural changes (Figure 2). An understanding of this perturbation budget over time and the
260 underlying variability and trends of the natural carbon cycle is necessary to understand the response of natural
261 sinks to changes in climate, CO₂ and land-use change drivers, and to quantify emissions compatible with a given
262 climate stabilisation target.

263 The components of the CO₂ budget that are reported annually in this paper include separate and independent
264 estimates for the CO₂ emissions from (1) fossil fuel combustion and oxidation from all energy and industrial
265 processes; also including cement production and carbonation (E_{FOS} ; GtC yr⁻¹) and (2) the emissions resulting
266 from deliberate human activities on land, including those leading to land-use change (E_{LUC} ; GtC yr⁻¹); and their
267 partitioning among (3) the growth rate of atmospheric CO₂ concentration (G_{ATM} ; GtC yr⁻¹), and the uptake of
268 CO₂ (the ‘CO₂ sinks’) in (4) the ocean (S_{OCEAN} ; GtC yr⁻¹) and (5) on land (S_{LAND} ; GtC yr⁻¹). The CO₂ sinks as
269 defined here conceptually include the response of the land (including inland waters and estuaries) and ocean
270 (including coastal and marginal seas) to elevated CO₂ and changes in climate and other environmental
271 conditions, although in practice not all processes are fully accounted for (see Section 2.7). Global emissions and
272 their partitioning among the atmosphere, ocean and land are in balance in the real world. Due to the combination
273 of imperfect spatial and/or temporal data coverage, errors in each estimate, and smaller terms not included in our
274 budget estimate (discussed in Section 2.7), the independent estimates (1) to (5) above do not necessarily add up
275 to zero. We therefore (a) additionally assess a set of global atmospheric inversion system results that by design
276 close the global carbon balance (see Section 2.6), and (b) estimate a budget imbalance (B_{IM}), which is a measure



277 of the mismatch between the estimated emissions and the estimated changes in the atmosphere, land and ocean,
278 as follows:

$$279 \quad B_{IM} = E_{FOS} + E_{LUC} - (G_{ATM} + S_{OCEAN} + S_{LAND}) \quad (1)$$

280 G_{ATM} is usually reported in ppm yr^{-1} , which we convert to units of carbon mass per year, GtC yr^{-1} , using 1 ppm
281 $= 2.124 \text{ GtC}$ (Ballantyne et al., 2012; Table 1). All quantities are presented in units of gigatonnes of carbon
282 (GtC , 10^{15} gC), which is the same as petagrams of carbon (PgC ; Table 1). Units of gigatonnes of CO_2 (or billion
283 tonnes of CO_2) used in policy are equal to 3.664 multiplied by the value in units of GtC .

284 We also quantify E_{FOS} and E_{LUC} by country, including both territorial and consumption-based accounting for
285 E_{FOS} (see Section 2), and discuss missing terms from sources other than the combustion of fossil fuels (see
286 Section 2.7).

287 The global CO_2 budget has been assessed by the Intergovernmental Panel on Climate Change (IPCC) in all
288 assessment reports (Prentice et al., 2001; Schimel et al., 1995; Watson et al., 1990; Denman et al., 2007; Ciais et
289 al., 2013; Canadell et al., 2021), and by others (e.g. Ballantyne et al., 2012). The Global Carbon Project (GCP,
290 www.globalcarbonproject.org, last access: 25 September 2022) has coordinated this cooperative community
291 effort for the annual publication of global carbon budgets for the year 2005 (Raupach et al., 2007; including
292 fossil emissions only), year 2006 (Canadell et al., 2007), year 2007 (GCP, 2008), year 2008 (Le Quéré et al.,
293 2009), year 2009 (Friedlingstein et al., 2010), year 2010 (Peters et al., 2012b), year 2012 (Le Quéré et al., 2013;
294 Peters et al., 2013), year 2013 (Le Quéré et al., 2014), year 2014 (Le Quéré et al., 2015a; Friedlingstein et al.,
295 2014), year 2015 (Jackson et al., 2016; Le Quéré et al., 2015b), year 2016 (Le Quéré et al., 2016), year 2017 (Le
296 Quéré et al., 2018a; Peters et al., 2017), year 2018 (Le Quéré et al., 2018b; Jackson et al., 2018), year 2019
297 (Friedlingstein et al., 2019; Jackson et al., 2019; Peters et al., 2020), year 2020 (Friedlingstein et al., 2020; Le
298 Quéré et al., 2021) and more recently the year 2021 (Friedlingstein et al., 2022a; Jackson et al., 2022). Each of
299 these papers updated previous estimates with the latest available information for the entire time series.

300 We adopt a range of ± 1 standard deviation (σ) to report the uncertainties in our estimates, representing a
301 likelihood of 68% that the true value will be within the provided range if the errors have a Gaussian distribution,
302 and no bias is assumed. This choice reflects the difficulty of characterising the uncertainty in the CO_2 fluxes
303 between the atmosphere and the ocean and land reservoirs individually, particularly on an annual basis, as well
304 as the difficulty of updating the CO_2 emissions from land-use change. A likelihood of 68% provides an
305 indication of our current capability to quantify each term and its uncertainty given the available information.
306 The uncertainties reported here combine statistical analysis of the underlying data, assessments of uncertainties
307 in the generation of the data sets, and expert judgement of the likelihood of results lying outside this range. The
308 limitations of current information are discussed in the paper and have been examined in detail elsewhere
309 (Ballantyne et al., 2015; Zscheischler et al., 2017). We also use a qualitative assessment of confidence level to
310 characterise the annual estimates from each term based on the type, amount, quality, and consistency of the
311 evidence as defined by the IPCC (Stocker et al., 2013).

312 This paper provides a detailed description of the data sets and methodology used to compute the global carbon
313 budget estimates for the industrial period, from 1750 to 2022, and in more detail for the period since 1959. This
314 paper is updated every year using the format of ‘living data’ to keep a record of budget versions and the changes



315 in new data, revision of data, and changes in methodology that lead to changes in estimates of the carbon
316 budget. Additional materials associated with the release of each new version will be posted at the Global Carbon
317 Project (GCP) website (<http://www.globalcarbonproject.org/carbonbudget>, last access: 25 September 2022),
318 with fossil fuel emissions also available through the Global Carbon Atlas (<http://www.globalcarbonatlas.org>,
319 last access: 25 September 2022). All underlying data used to produce the budget can also be found at
320 <https://globalcarbonbudget.org/> (last access: 25 September 2022). With this approach, we aim to provide the
321 highest transparency and traceability in the reporting of CO₂, the key driver of climate change.

322 2 Methods

323 Multiple organisations and research groups around the world generated the original measurements and data used
324 to complete the global carbon budget. The effort presented here is thus mainly one of synthesis, where results
325 from individual groups are collated, analysed, and evaluated for consistency. We facilitate access to original
326 data with the understanding that primary data sets will be referenced in future work (see Table 2 for how to cite
327 the data sets). Descriptions of the measurements, models, and methodologies follow below, and detailed
328 descriptions of each component are provided elsewhere.

329 This is the 17th version of the global carbon budget and the 11th revised version in the format of a living data
330 update in Earth System Science Data. It builds on the latest published global carbon budget of Friedlingstein et
331 al. (2022a). The main changes are: the inclusion of (1) data to year 2021 and a projection for the global carbon
332 budget for year 2022; (2) the inclusion of country level estimates of E_{LUC}; (3) a process-based decomposition of
333 E_{LUC} into its main components (deforestation, carbon uptake on forests, emissions from organic soils, and net
334 flux from other transitions).

335 The main methodological differences between recent annual carbon budgets (2018-2022) are summarised in
336 Table 3 and previous changes since 2006 are provided in Table A7.

337 2.1 Fossil CO₂ emissions (E_{FOS})

338 2.1.1 Historical period 1850-2021

339 The estimates of global and national fossil CO₂ emissions (E_{FOS}) include the oxidation of fossil fuels through
340 both combustion (e.g., transport, heating) and chemical oxidation (e.g. carbon anode decomposition in
341 aluminium refining) activities, and the decomposition of carbonates in industrial processes (e.g. the production
342 of cement). We also include CO₂ uptake from the cement carbonation process. Several emissions sources are not
343 estimated or not fully covered: coverage of emissions from lime production are not global, and decomposition of
344 carbonates in glass and ceramic production are included only for the “Annex 1” countries of the United Nations
345 Framework Convention on Climate Change (UNFCCC) for lack of activity data. These omissions are
346 considered to be minor. Short-cycle carbon emissions - for example from combustion of biomass - are not
347 included here but are accounted for in the CO₂ emissions from land use (see section 2.2).

348 Our estimates of fossil CO₂ emissions are derived using the standard approach of activity data and emission
349 factors, relying on data collection by many other parties. Our goal is to produce the best estimate of this flux,
350 and we therefore use a prioritisation framework to combine data from different sources that have used different
351 methods, while being careful to avoid double counting and undercounting of emissions sources. The CDIAC-FF



352 emissions dataset, derived largely from UN energy data, forms the foundation, and we extend emissions to year
353 Y-1 using energy growth rates reported by BP. We then proceed to replace estimates using data from what we
354 consider to be superior sources, for example Annex 1 countries' official submissions to the UNFCCC. All data
355 points are potentially subject to revision, not just the latest year. For full details see Andrew and Peters (2021).
356 Other estimates of global fossil CO₂ emissions exist, and these are compared by Andrew (2020a). The most
357 common reason for differences in estimates of global fossil CO₂ emissions is a difference in which emissions
358 sources are included in the datasets. Datasets such as those published by the energy company BP, the US Energy
359 Information Administration, and the International Energy Agency's 'CO₂ emissions from fuel combustion' are
360 all generally limited to emissions from combustion of fossil fuels. In contrast, datasets such as PRIMAP-hist,
361 CEDS, EDGAR, and GCP's dataset aim to include all sources of fossil CO₂ emissions. See Andrew (2020a) for
362 detailed comparisons and discussion.

363 Cement absorbs CO₂ from the atmosphere over its lifetime, a process known as 'cement carbonation'. We
364 estimate this CO₂ sink as the average of two studies in the literature (Cao et al., 2020; Guo et al., 2021). Both
365 studies use the same model, developed by Xi et al. (2016), with different parameterisations and input data. The
366 Global Cement and Concrete Association reports a much lower carbonation rate, but this is based on the highly
367 conservative assumption of 0% mortar (GCCA, 2021). Since carbonation is a function of both current and
368 previous cement production, we extend these estimates by one year to 2021 by using the growth rate derived
369 from the smoothed cement emissions (10-year smoothing) fitted to the carbonation data.

370 We use the Kaya Identity for a simple decomposition of CO₂ emissions into the key drivers (Raupach et al.,
371 2007). While there are variations (Peters et al 2017), we focus here on a decomposition of CO₂ emissions into
372 population, GDP per person, energy use per GDP, and CO₂ emissions per energy. Multiplying these individual
373 components together returns the CO₂ emissions. Using the decomposition, it is possible to attribute the change
374 in CO₂ emissions to the change in each of the drivers. This method gives a first order understanding of what
375 causes CO₂ emissions to change each year.

376 **2.1.2 2022 projection**

377 We provide a projection of global CO₂ emissions in 2022 by combining separate projections for China, USA,
378 EU, India, and for all other countries combined. The methods are different for each of these. For China we
379 combine monthly fossil fuel production data from the National Bureau of Statistics, import/export data from the
380 Customs Administration, and monthly coal consumption estimates from SX Coal (2022), giving us partial data
381 for the growth rates to date of natural gas, petroleum, and cement, and of the consumption itself for raw coal.
382 We then use a regression model to project full-year emissions based on historical observations. For the USA our
383 projection is taken directly from the Energy Information Administration's (EIA) Short-Term Energy Outlook
384 (EIA, 2022), combined with the year-to-date growth rate of cement clinker production. For the EU we use
385 monthly energy data from Eurostat to derive estimates of monthly CO₂ emissions through July, with coal
386 emissions extended through August using a statistical relationship with reported electricity generation from coal
387 and other factors. Given the very high uncertainty in European energy markets in 2022, we forego our usual
388 history-based projection techniques and use instead the year-to-date growth rate as the full-year growth rate for
389 both coal and natural gas. EU emissions from oil are derived using the EIA's projection of oil consumption for
390 Europe. EU cement emissions are based on available year-to-date data from three of the largest producers,



391 Germany, Poland, and Spain. India's projected emissions are derived from estimates through July (August for
392 oil) using the methods of Andrew (2020b) and extrapolated assuming normal seasonal patterns. Emissions for
393 the rest of the world are derived using projected growth in economic production from the IMF (2022) combined
394 with extrapolated changes in emissions intensity of economic production. More details on the E_{FOS} methodology
395 and its 2022 projection can be found in Appendix C.1.

396 2.2 CO₂ emissions from land-use, land-use change and forestry (E_{LUC})

397 2.2.1 Historical Period

398 The net CO₂ flux from land-use, land-use change and forestry (E_{LUC} , called land-use change emissions in the
399 rest of the text) includes CO₂ fluxes from deforestation, afforestation, logging and forest degradation (including
400 harvest activity), shifting cultivation (cycle of cutting forest for agriculture, then abandoning), and regrowth of
401 forests following wood harvest or abandonment of agriculture. Emissions from peat burning and drainage are
402 added from external datasets. Compared to our earlier assessments, this year we include spatially explicit
403 information also for peat drainage and combine three independent datasets for peat drainage.
404 Three bookkeeping approaches (updated estimates each of BLUE (Hansis et al., 2015), OSCAR (Gasser et al.,
405 2020), and H&N2017 (Houghton and Nassikas, 2017)) were used to quantify gross sources and sinks and the
406 resulting net E_{LUC} . Uncertainty estimates were derived from the Dynamic Global vegetation Models (DGVMs)
407 ensemble for the time period prior to 1960, using for the recent decades an uncertainty range of ± 0.7 GtC yr⁻¹,
408 which is a semi-quantitative measure for annual and decadal emissions and reflects our best value judgement
409 that there is at least 68% chance ($\pm 1\sigma$) that the true land-use change emission lies within the given range, for the
410 range of processes considered here. This uncertainty range had been increased from 0.5 GtC yr⁻¹ after new
411 bookkeeping models were included that indicated a larger spread than assumed before (Le Quéré et al., 2018).
412 Projections for 2021 are based on fire activity from tropical deforestation and degradation as well as emissions
413 from peat fires and drainage.
414 Our E_{LUC} estimates follow the definition of global carbon cycle models of CO₂ fluxes related to land-use and
415 land management and differ from IPCC definitions adopted in National GHG Inventories (NGHGI) for
416 reporting under the UNFCCC, which additionally generally include, through adoption of the IPCC so-called
417 managed land proxy approach, the terrestrial fluxes occurring on land defined by countries as managed. This
418 partly includes fluxes due to environmental change (e.g. atmospheric CO₂ increase), which are part of S_{LAND} in
419 our definition. This causes the global emission estimates to be smaller for NGHGI than for the global carbon
420 budget definition (Grassi et al., 2018). The same is the case for the Food Agriculture Organization (FAO)
421 estimates of carbon fluxes on forest land, which include, compared to S_{LAND} , both anthropogenic and natural
422 sources on managed land (Tubiello et al., 2021). Using the approach outlined in Grassi et al. (2021), here we
423 map as additional information the two definitions to each other, to provide a comparison of the anthropogenic
424 carbon budget to the official country reporting to the climate convention.

425 2.2.2 2022 Projection

426 We project the 2022 land-use emissions for BLUE, the updated H&N2017 and OSCAR, starting from their
427 estimates for 2021 assuming unaltered peat drainage, which has low interannual variability, and the highly



428 variable emissions from peat fires, tropical deforestation and degradation as estimated using active fire data
429 (MCD14ML; Giglio et al., 2016). More details on the E_{LUC} methodology can be found in Appendix C.2

430 **2.3 Growth rate in atmospheric CO₂ concentration (G_{ATM})**

431 **2.3.1 Historical period**

432 The rate of growth of the atmospheric CO₂ concentration is provided for years 1959-2021 by the US National
433 Oceanic and Atmospheric Administration Earth System Research Laboratory (NOAA/ESRL; Dlugokencky and
434 Tans, 2022), which is updated from Ballantyne et al. (2012) and includes recent revisions to the calibration scale
435 of atmospheric CO₂ measurements (Hall et al., 2021). For the 1959-1979 period, the global growth rate is based
436 on measurements of atmospheric CO₂ concentration averaged from the Mauna Loa and South Pole stations, as
437 observed by the CO₂ Program at Scripps Institution of Oceanography (Keeling et al., 1976). For the 1980-2020
438 time period, the global growth rate is based on the average of multiple stations selected from the marine
439 boundary layer sites with well-mixed background air (Ballantyne et al., 2012), after fitting a smooth curve
440 through the data for each station as a function of time, and averaging by latitude band (Masarie and Tans, 1995).
441 The annual growth rate is estimated by Dlugokencky and Tans (2022) from atmospheric CO₂ concentration by
442 taking the average of the most recent December-January months corrected for the average seasonal cycle and
443 subtracting this same average one year earlier. The growth rate in units of ppm yr⁻¹ is converted to units of GtC
444 yr⁻¹ by multiplying by a factor of 2.124 GtC per ppm, assuming instantaneous mixing of CO₂ throughout the
445 atmosphere (Ballantyne et al., 2012; Table 1).

446 Since 2020, NOAA/ESRL provides estimates of atmospheric CO₂ concentrations with respect to a new
447 calibration scale, referred to as WMO-CO₂-X2019, in line with the recommendation of the World
448 Meteorological Organization (WMO) Global Atmosphere Watch (GAW) community (Hall et al., 2021). The
449 WMO-CO₂-X2019 scale improves upon the earlier WMO-CO₂-X2007 scale by including a broader set of
450 standards, which contain CO₂ in a wider range of concentrations that span the range 250-800 ppm (versus 250–
451 520 ppm for WMO-CO₂-X2007). In addition, NOAA/ESRL made two minor corrections to the analytical
452 procedure used to quantify CO₂ concentrations, fixing an error in the second virial coefficient of CO₂ and
453 accounting for loss of a small amount of CO₂ to materials in the manometer during the measurement process.
454 The difference in concentrations measured using WMO-CO₂-X2019 versus WMO-CO₂-X2007 is $\sim +0.18$ ppm
455 at 400 ppm and the observational record of atmospheric CO₂ concentrations have been revised accordingly. The
456 revisions have been applied retrospectively in all cases where the calibrations were performed by NOAA/ESRL,
457 thus affecting measurements made by members of the WMO-GAW programme and other regionally
458 coordinated programmes (e.g., Integrated Carbon Observing System, ICOS). Changes to the CO₂ concentrations
459 measured across these networks propagate to the global mean CO₂ concentrations. The re-calibrated data were
460 first used to estimate G_{ATM} in the 2021 edition of the global carbon budget (Friedlingstein et al., 2022a).
461 Friedlingstein et al. (2022a) verified that the change of scales from WMO-CO₂-X2007 to WMO-CO₂-X2019
462 made a negligible difference to the value of G_{ATM} (-0.06 GtC yr⁻¹ during 2010-2019 and -0.01 GtC yr⁻¹ during
463 1959-2019, well within the uncertainty range reported below).

464 The uncertainty around the atmospheric growth rate is due to four main factors. First, the long-term
465 reproducibility of reference gas standards (around 0.03 ppm for 1σ from the 1980s; Dlugokencky and Tans,



466 2022). Second, small unexplained systematic analytical errors that may have a duration of several months to two
467 years come and go. They have been simulated by randomising both the duration and the magnitude (determined
468 from the existing evidence) in a Monte Carlo procedure. Third, the network composition of the marine boundary
469 layer with some sites coming or going, gaps in the time series at each site, etc (Dlugokencky and Tans, 2022).
470 The latter uncertainty was estimated by NOAA/ESRL with a Monte Carlo method by constructing 100
471 "alternative" networks (Masarie and Tans, 1995; NOAA/ESRL, 2019). The second and third uncertainties,
472 summed in quadrature, add up to 0.085 ppm on average (Dlugokencky and Tans, 2022). Fourth, the uncertainty
473 associated with using the average CO₂ concentration from a surface network to approximate the true
474 atmospheric average CO₂ concentration (mass-weighted, in 3 dimensions) as needed to assess the total
475 atmospheric CO₂ burden. In reality, CO₂ variations measured at the stations will not exactly track changes in
476 total atmospheric burden, with offsets in magnitude and phasing due to vertical and horizontal mixing. This
477 effect must be very small on decadal and longer time scales, when the atmosphere can be considered well
478 mixed. Preliminary estimates suggest this effect would increase the annual uncertainty, but a full analysis is not
479 yet available. We therefore maintain an uncertainty around the annual growth rate based on the multiple stations
480 data set ranges between 0.11 and 0.72 GtC yr⁻¹, with a mean of 0.61 GtC yr⁻¹ for 1959-1979 and 0.17 GtC yr⁻¹
481 for 1980-2020, when a larger set of stations were available as provided by Dlugokencky and Tans (2022) but
482 recognise further exploration of this uncertainty is required. At this time, we estimate the uncertainty of the
483 decadal averaged growth rate after 1980 at 0.02 GtC yr⁻¹ based on the calibration and the annual growth rate
484 uncertainty but stretched over a 10-year interval. For years prior to 1980, we estimate the decadal averaged
485 uncertainty to be 0.07 GtC yr⁻¹ based on a factor proportional to the annual uncertainty prior and after 1980
486 (0.02 * [0.61/0.17] GtC yr⁻¹).

487 We assign a high confidence to the annual estimates of G_{ATM} because they are based on direct measurements
488 from multiple and consistent instruments and stations distributed around the world (Ballantyne et al., 2012; Hall
489 et al., 2021).

490 To estimate the total carbon accumulated in the atmosphere since 1750 or 1850, we use an atmospheric CO₂
491 concentration of 277 ± 3 ppm or 286 ± 3 ppm, respectively, based on a cubic spline fit to ice core data (Joos and
492 Spahni, 2008). For the construction of the cumulative budget shown in Figure 3, we use the fitted estimates of
493 CO₂ concentration from Joos and Spahni (2008) to estimate the annual atmospheric growth rate using the
494 conversion factors shown in Table 1. The uncertainty of ±3 ppm (converted to ±1σ) is taken directly from the
495 IPCC's AR5 assessment (Ciais et al., 2013). Typical uncertainties in the growth rate in atmospheric CO₂
496 concentration from ice core data are equivalent to ±0.1-0.15 GtC yr⁻¹ as evaluated from the Law Dome data
497 (Etheridge et al., 1996) for individual 20-year intervals over the period from 1850 to 1960 (Bruno and Joos,
498 1997).

499 **2.3.2 2022 projection**

500 We provide an assessment of G_{ATM} for 2022 based on the monthly calculated global atmospheric CO₂
501 concentration (GLO) through August (Dlugokencky and Tans, 2022), and bias-adjusted Holt–Winters
502 exponential smoothing with additive seasonality (Chatfield, 1978) to project to January 2023. Additional
503 analysis suggests that the first half of the year (the boreal winter-spring-summer transition) shows more
504 interannual variability than the second half of the year (the boreal summer-autumn-winter transition), so that the



505 exact projection method applied to the second half of the year has a relatively smaller impact on the projection
506 of the full year. Uncertainty is estimated from past variability using the standard deviation of the last 5 years'
507 monthly growth rates.

508 2.4 Ocean CO₂ sink

509 2.4.1 Historical Period

510 The reported estimate of the global ocean anthropogenic CO₂ sink S_{OCEAN} is derived as the average of two
511 estimates. The first estimate is derived as the mean over an ensemble of ten global ocean biogeochemistry
512 models (GOBMs, Table 4 and Table A2). The second estimate is obtained as the mean over an ensemble of
513 seven observation-based data-products (Table 4 and Table A3). An eighth product (Watson et al., 2020) is
514 shown, but is not included in the ensemble average as it differs from the other products by adjusting the flux to a
515 cool, salty ocean surface skin (see Appendix C.3.1 for a discussion of the Watson product). The GOBMs
516 simulate both the natural and anthropogenic CO₂ cycles in the ocean. They constrain the anthropogenic air-sea
517 CO₂ flux (the dominant component of S_{OCEAN}) by the transport of carbon into the ocean interior, which is also
518 the controlling factor of present-day ocean carbon uptake in the real world. They cover the full globe and all
519 seasons and were recently evaluated against surface ocean carbon observations, suggesting they are suitable to
520 estimate the annual ocean carbon sink (Hauck et al., 2020). The data-products are tightly linked to observations
521 of $f\text{CO}_2$ (fugacity of CO₂, which equals $p\text{CO}_2$ corrected for the non-ideal behaviour of the gas; Pfeil et al.,
522 2013), which carry imprints of temporal and spatial variability, but are also sensitive to uncertainties in gas-
523 exchange parameterizations and data-sparsity. Their asset is the assessment of interannual and spatial variability
524 (Hauck et al., 2020). We further use two diagnostic ocean models to estimate S_{OCEAN} over the industrial era
525 (1781-1958).

526 The global $f\text{CO}_2$ -based flux estimates were adjusted to remove the pre-industrial ocean source of CO₂ to the
527 atmosphere of 0.65 GtC yr⁻¹ from river input to the ocean (Regnier et al., 2022), to satisfy our definition of
528 S_{OCEAN} (Hauck et al., 2020). The river flux adjustment was distributed over the latitudinal bands using the
529 regional distribution of Aumont et al. (2001; North: 0.17 GtC yr⁻¹, Tropics: 0.16 GtC yr⁻¹, South: 0.32 GtC yr⁻¹),
530 acknowledging that the boundaries of Aumont et al (2001; namely 20°S and 20°N) are not consistent with the
531 boundaries otherwise used in the GCB (30°S and 30°N). A recent study based on one ocean biogeochemical
532 model (Lacroix et al., 2020) suggests that more of the riverine outgassing is located in the tropics than in the
533 Southern Ocean; and hence this regional distribution is associated with a major uncertainty. Anthropogenic
534 perturbations of river carbon and nutrient transport to the ocean are not considered (see section 2.7).

535 We derive S_{OCEAN} from GOBMs by using a simulation (sim A) with historical forcing of climate and
536 atmospheric CO₂, accounting for model biases and drift from a control simulation (sim B) with constant
537 atmospheric CO₂ and normal year climate forcing. A third simulation (sim C) with historical atmospheric CO₂
538 increase and normal year climate forcing is used to attribute the ocean sink to CO₂ (sim C minus sim B) and
539 climate (sim A minus sim C) effects. A fourth simulation (sim D; historical climate forcing and constant
540 atmospheric CO₂) is used to compare the change in anthropogenic carbon inventory in the interior ocean (sim A
541 minus sim D) to the observational estimate of Gruber et al. (2019) with the same flux components (steady state
542 and non-steady state anthropogenic carbon flux). Data-products are adjusted to represent the full ice-free ocean



543 area by a simple scaling approach when coverage is below 99%. GOBMs and data-products fall within the
544 observational constraints over the 1990s ($2.2 \pm 0.7 \text{ GtC yr}^{-1}$, Ciais et al., 2013) after applying adjustments.
545 S_{OCEAN} is calculated as the average of the GOBM ensemble mean and data-product ensemble mean from 1990
546 onwards. Prior to 1990, it is calculated as the GOBM ensemble mean plus half of the offset between GOBMs
547 and data-products ensemble means over 1990-2001.
548 We assign an uncertainty of $\pm 0.4 \text{ GtC yr}^{-1}$ to the ocean sink based on a combination of random (ensemble
549 standard deviation) and systematic uncertainties (GOBMs bias in anthropogenic carbon accumulation,
550 previously reported uncertainties in $f\text{CO}_2$ -based data-products; see section C.3.3). We assess a medium
551 confidence level to the annual ocean CO_2 sink and its uncertainty because it is based on multiple lines of
552 evidence, it is consistent with ocean interior carbon estimates (Gruber et al., 2019, see section 3.5.5) and the
553 interannual variability in the GOBMs and data-based estimates is largely consistent and can be explained by
554 climate variability. We refrain from assigning a high confidence because of the systematic deviation between
555 the GOBM and data-product trends since around 2002. More details on the S_{OCEAN} methodology can be found in
556 Appendix C.3.

557 **2.4.2 2022 Projection**

558 The ocean CO_2 sink forecast for the year 2022 is based on the annual historical and estimated 2022 atmospheric
559 CO_2 concentration (Dlugokencky and Tans 2021), the historical and estimated 2022 annual global fossil fuel
560 emissions from this year's carbon budget, and the spring (March, April, May) Oceanic Niño Index (ONI) index
561 (NCEP, 2022). Using a non-linear regression approach, i.e., a feed-forward neural network, atmospheric CO_2 ,
562 the ONI index and the fossil fuel emissions are used as training data to best match the annual ocean CO_2 sink
563 (i.e. combined S_{OCEAN} estimate from GOBMs and data products) from 1959 through 2021 from this year's
564 carbon budget. Using this relationship, the 2022 S_{OCEAN} can then be estimated from the projected 2021 input
565 data using the non-linear relationship established during the network training. To avoid overfitting, the neural
566 network was trained with a variable number of hidden neurons (varying between 2-5) and 20% of the randomly
567 selected training data were withheld for independent internal testing. Based on the best output performance
568 (tested using the 20% withheld input data), the best performing number of neurons was selected. In a second
569 step, we trained the network 10 times using the best number of neurons identified in step 1 and different sets of
570 randomly selected training data. The mean of the 10 trainings is considered our best forecast, whereas the
571 standard deviation of the 10 ensembles provides a first order estimate of the forecast uncertainty. This
572 uncertainty is then combined with the S_{OCEAN} uncertainty (0.4 GtC yr^{-1}) to estimate the overall uncertainty of the
573 2022 projection.

574 **2.5 Terrestrial CO_2 sink**

575 **2.5.1 Historical Period**

576 The terrestrial land sink (S_{LAND}) is thought to be due to the combined effects of fertilisation by rising
577 atmospheric CO_2 and N inputs on plant growth, as well as the effects of climate change such as the lengthening
578 of the growing season in northern temperate and boreal areas. S_{LAND} does not include land sinks directly
579 resulting from land-use and land-use change (e.g., regrowth of vegetation) as these are part of the land-use flux



580 (E_{LUC}), although system boundaries make it difficult to attribute exactly CO_2 fluxes on land between S_{LAND} and
581 E_{LUC} (Erb et al., 2013).
582 S_{LAND} is estimated from the multi-model mean of 16 DGVMs (Table A1). As described in Appendix C.4,
583 DGVMs simulations include all climate variability and CO_2 effects over land, with 11 DGVMs also including
584 the effect of N inputs. The DGVMs estimate of S_{LAND} does not include the export of carbon to aquatic systems
585 or its historical perturbation, which is discussed in Appendix D3. See Appendix C.4 for DGVMs evaluation and
586 uncertainty assessment for S_{LAND} , using the International Land Model Benchmarking system (ILAMB; Collier et
587 al., 2018). More details on the S_{LAND} methodology can be found in Appendix C.4.

588 2.5.2 2022 Projection

589 Like for the ocean forecast, the land CO_2 sink (S_{LAND}) forecast is based on the annual historical and estimated
590 2022 atmospheric CO_2 concentration (Dlugokencky and Tans 2021), historical and estimated 2022 annual
591 global fossil fuel emissions from this year's carbon budget, and the summer (June, July, August) ONI index
592 (NCEP, 2022). All training data are again used to best match S_{LAND} from 1959 through 2021 from this year's
593 carbon budget using a feed-forward neural network. To avoid overfitting, the neural network was trained with a
594 variable number of hidden neurons (varying between 2-15), larger than for S_{OCEAN} prediction due to the stronger
595 land carbon interannual variability. As done for S_{OCEAN} , a pre-training selects the optimal number of hidden
596 neurons based on 20% withheld input data, and in a second step, an ensemble of 10 forecasts is produced to
597 provide the mean forecast plus uncertainty. This uncertainty is then combined with the S_{LAND} uncertainty for
598 2021 (0.9 GtC yr^{-1}) to estimate the overall uncertainty of the 2022 projection.

599 2.6 The atmospheric perspective

600 The world-wide network of in-situ atmospheric measurements and satellite derived atmospheric CO_2 column
601 (xCO_2) observations put a strong constraint on changes in the atmospheric abundance of CO_2 . This is true
602 globally (hence our large confidence in G_{ATM}), but also regionally in regions with sufficient observational
603 density found mostly in the extra-tropics. This allows atmospheric inversion methods to constrain the magnitude
604 and location of the combined total surface CO_2 fluxes from all sources, including fossil and land-use change
605 emissions and land and ocean CO_2 fluxes. The inversions assume E_{FOS} to be well known, and they solve for the
606 spatial and temporal distribution of land and ocean fluxes from the residual gradients of CO_2 between stations
607 that are not explained by fossil fuel emissions. By design, such systems thus close the carbon balance ($B_{IM} = 0$)
608 and thus provide an additional perspective on the independent estimates of the ocean and land fluxes.
609 This year's release includes nine inversion systems that are described in Table A4. Each system is rooted in
610 Bayesian inversion principles but uses different methodologies. These differences concern the selection of
611 atmospheric CO_2 data or xCO_2 , and the choice of a-priori fluxes to refine. They also differ in spatial and
612 temporal resolution, assumed correlation structures, and mathematical approach of the models (see references in
613 Table A4 for details). Importantly, the systems use a variety of transport models, which was demonstrated to be
614 a driving factor behind differences in atmospheric inversion-based flux estimates, and specifically their
615 distribution across latitudinal bands (Gaubert et al., 2019; Schuh et al., 2019). Four inversion systems (CAM5-
616 FT21r2, CMS-flux, GONGGA, THU) used satellite xCO_2 retrievals from GOSAT and/or OCO-2, scaled to the



617 WMO 2019 calibration scale. One inversion this year (CMS-Flux) used these xCO₂ datasets in addition to the
618 in-situ observational CO₂ mole fraction records.

619 The original products delivered by the inverse modellers were modified to facilitate the comparison to the other
620 elements of the budget, specifically on two accounts: (1) global total fossil fuel emissions including cement
621 carbonation CO₂ uptake, and (2) riverine CO₂ transport. Details are given below. We note that with these
622 adjustments the inverse results no longer represent the net atmosphere-surface exchange over land/ocean areas
623 as sensed by atmospheric observations. Instead, for land, they become the net uptake of CO₂ by vegetation and
624 soils that is not exported by fluvial systems, similar to the DGVMs estimates. For oceans, they become the net
625 uptake of anthropogenic CO₂, similar to the GOBMs estimates.

626 The inversion systems prescribe global fossil fuel emissions based on the GCP's Gridded Fossil Emissions
627 Dataset versions 2022.1 or 2022.2 (GCP-GridFED; Jones et al., 2022), which are updates to GCP-
628 GridFEDv2021 presented by Jones et al. (2021). GCP-GridFEDv2022 scales gridded estimates of CO₂
629 emissions from EDGARv4.3.2 (Janssens-Maenhout et al., 2019) within national territories to match national
630 emissions estimates provided by the GCB for the years 1959-2021, which were compiled following the
631 methodology described in Section 2.1. Small differences between the systems due to for instance regridding to
632 the transport model resolution, or use of different GridFED versions with different cement carbonation sinks
633 (which were only present starting with GridFEDv2022.1), are adjusted in the latitudinal partitioning we present,
634 to ensure agreement with the estimate of E_{POS} in this budget. We also note that the ocean fluxes used as prior by
635 6 out of 9 inversions are part of the suite of the ocean process model or fCO₂ data products listed in Section 2.4.
636 Although these fluxes are further adjusted by the atmospheric inversions, it makes the inversion estimates of the
637 ocean fluxes not completely independent of S_{OCEAN} assessed here.

638 To facilitate comparisons to the independent S_{OCEAN} and S_{LAND}, we used the same corrections for transport and
639 outgassing of carbon transported from land to ocean, as done for the observation-based estimates of S_{OCEAN} (see
640 Appendix C.3).

641 The atmospheric inversions are evaluated using vertical profiles of atmospheric CO₂ concentrations (Figure B4).
642 More than 30 aircraft programs over the globe, either regular programs or repeated surveys over at least 9
643 months (except for SH programs), have been used to assess system performance (with space-time observational
644 coverage sparse in the SH and tropics, and denser in NH mid-latitudes; Table A6). The nine systems are
645 compared to the independent aircraft CO₂ measurements between 2 and 7 km above sea level between 2001 and
646 2021. Results are shown in Figure B4 and discussed in Section 3.7.

647 With a relatively small ensemble (N=9) of systems that moreover share some a-priori fluxes used with one
648 another, or with the process-based models, it is difficult to justify using their mean and standard deviation as a
649 metric for uncertainty across the ensemble. We therefore report their full range (min-max) without their mean.
650 More details on the atmospheric inversions methodology can be found in Appendix C.5.

651 **2.7 Processes not included in the global carbon budget**

652 The contribution of anthropogenic CO and CH₄ to the global carbon budget is not fully accounted for in Eq. (1)
653 and is described in Appendix D1. The contributions to CO₂ emissions of decomposition of carbonates not



654 accounted for is described in Appendix D2. The contribution of anthropogenic changes in river fluxes is
655 conceptually included in Eq. (1) in S_{OCEAN} and in S_{LAND} , but it is not represented in the process models used to
656 quantify these fluxes. This effect is discussed in Appendix D3. Similarly, the loss of additional sink capacity
657 from reduced forest cover is missing in the combination of approaches used here to estimate both land fluxes
658 (E_{LUC} and S_{LAND}) and its potential effect is discussed and quantified in Appendix D4.
659

660 3 Results

661 For each component of the global carbon budget, we present results for three different time periods: the full
662 historical period, from 1850 to 2021, the six decades in which we have atmospheric concentration records from
663 Mauna Loa (1960-2021), a specific focus on last year (2021), and the projection for the current year (2022).
664 Subsequently, we assess the combined constraints from the budget components (often referred to as a bottom-up
665 budget) against the top-down constraints from inverse modelling of atmospheric observations. We do this for
666 the global balance of the last decade, as well as for a regional breakdown of land and ocean sinks by broad
667 latitude bands.

668 3.1 Fossil CO₂ Emissions

669 3.1.1 Historical period 1850-2021

670 Cumulative fossil CO₂ emissions for 1850-2021 were 465 ± 25 GtC, including the cement carbonation sink
671 (Figure 3, Table 8, all cumulative numbers are rounded to the nearest 5GtC).
672 In this period, 46% of fossil CO₂ emissions came from coal, 35% from oil, 15% from natural gas, 3% from
673 decomposition of carbonates, and 1% from flaring.
674 In 1850, the UK stood for 62% of global fossil CO₂ emissions. In 1891 the combined cumulative emissions of
675 the current members of the European Union reached and subsequently surpassed the level of the UK. Since
676 1917 US cumulative emissions have been the largest. Over the entire period 1850-2021, US cumulative
677 emissions amounted to 115GtC (24% of world total), the EU's to 80 GtC (17%), and China's to 70 GtC (14%).
678 There are three additional global datasets with long time series that include all sources of fossil CO₂ emissions:
679 CDIAC-FF (Gilfillan and Marland, 2021), CEDS version v_2021_04_21 (Hoesly et al., 2018); O'Rourke et al.,
680 2021) and PRIMAP-hist version 2.3.1 (Gütschow et al., 2016, 2021), although these datasets are not entirely
681 independent from each other. CDIAC-FF has the lowest cumulative emissions over 1750-2018 at 437 GtC, GCP
682 has 443 GtC, CEDS 445 GtC, PRIMAP-hist TP 453 GtC, and PRIMAP-hist CR 455 GtC. CDIAC-FF excludes
683 emissions from lime production, while neither CDIAC-FF nor GCP explicitly include emissions from
684 international bunker fuels prior to 1950. CEDS has higher emissions from international shipping in recent years,
685 while PRIMAP-hist has higher fugitive emissions than the other datasets. However, in general these four
686 datasets are in relative agreement as to total historical global emissions of fossil CO₂.

687 3.1.2 Recent period 1960-2021

688 Global fossil CO₂ emissions, E_{FOS} (including the cement carbonation sink), have increased every decade from an
689 average of 3.0 ± 0.2 GtC yr⁻¹ for the decade of the 1960s to an average of 9.6 ± 0.5 GtC yr⁻¹ during 2012-2021
690 (Table 6, Figure 2 and Figure 5). The growth rate in these emissions decreased between the 1960s and the



1990s, from 4.3% yr⁻¹ in the 1960s (1960-1969), 3.2% yr⁻¹ in the 1970s (1970-1979), 1.6% yr⁻¹ in the 1980s (1980-1989), to 0.9% yr⁻¹ in the 1990s (1990-1999). After this period, the growth rate began increasing again in the 2000s at an average growth rate of 3.0% yr⁻¹, decreasing to 0.5% yr⁻¹ for the last decade (2012-2021). China's emissions increased by +1.5% yr⁻¹ on average over the last 10 years dominating the global trend, and India's emissions increased by +3.8% yr⁻¹, while emissions decreased in EU27 by -1.8% yr⁻¹, and in the USA by -1.1% yr⁻¹. Figure 6 illustrates the spatial distribution of fossil fuel emissions for the 2012-2021 period. E_{FOS} includes the uptake of CO₂ by cement via carbonation which has increased with increasing stocks of cement products, from an average of 20 MtC yr⁻¹ (0.02 GtC yr⁻¹) in the 1960s to an average of 200 MtC yr⁻¹ (0.2 GtC yr⁻¹) during 2012-2021 (Figure 5).

3.1.3 Final year 2021

Global fossil CO₂ emissions were 5.1% higher in 2021 than in 2020, because of the global rebound from the worst of the COVID-19 pandemic, with an increase of 0.5 GtC to reach 10.1 ± 0.5 GtC (9.9 ± 0.5 GtC when including the cement carbonation sink) in 2021 (Figure 5), distributed among coal (41%), oil (32%), natural gas (22%), cement (5%) and others (1%). Compared to the previous year, 2021 emissions from coal, oil and gas increased by 5.7%, 5.8% and 4.8% respectively, while emissions from cement increased by 2.1%. All growth rates presented are adjusted for the leap year, unless stated otherwise.

In 2021, the largest absolute contributions to global fossil CO₂ emissions were from China (31%), the USA (14%), the EU27 (8%), and India (7%). These four regions account for 59% of global CO₂ emissions, while the rest of the world contributed 41%, including international aviation and marine bunker fuels (2.8% of the total). Growth rates for these countries from 2020 to 2021 were 3.5% (China), 6.2% (USA), 6.8% (EU27), and 11.1% (India), with +4.5% for the rest of the world. The per-capita fossil CO₂ emissions in 2021 were 1.3 tC person⁻¹ yr⁻¹ for the globe, and were 4.0 (USA), 2.2 (China), 1.7 (EU27) and 0.5 (India) tC person⁻¹ yr⁻¹ for the four highest emitting countries (Figure 5).

The post-COVID-19 rebound in emissions of 5.1% in 2021 is close to the projected increase of 4.8% published in Friedlingstein et al. (2021) (Table 7). Of the regions, the projection for the 'rest of world' region was least accurate, largely because of poorly projected emissions from international transport (bunker fuels), which were subject to very large changes during this period.

3.1.4 Year 2022 Projection

Globally, we estimate that global fossil CO₂ emissions will grow by 1.1% in 2022 (0.0% to 1.7%) to 10.2 GtC (37.3 GtCO₂), exceeding their 2019 emission levels of 10.0 GtC (36.7 GtCO₂). Global increase in 2022 emissions per fuel types are projected to be +0.8% (range 0.0% to 1.7%) for coal, +2.2% (range -0.7% to 2.9%) for oil, +1.1% (range 0.0% to 2.2%) for natural gas, and -2.8% (range -5.5% to -0.2%) for cement.

For China, projected fossil emissions in 2022 are expected to decline by 1.5% (range -3.0% to +0.1%) compared with 2021 emissions, bringing 2022 emissions for China around 3.0 GtC yr⁻¹ (11.1 GtCO₂ yr⁻¹). Changes in fuel specific projections for China are -0.5% for coal, -2.3% for oil, -1.1% natural gas, and -9.2% for cement.



726 For the USA, the Energy Information Administration (EIA) emissions projection for 2022 combined with
727 cement clinker data from USGS gives an increase of 1.6% (range -0.9% to +4.1%) compared to 2021, bringing
728 USA 2022 emissions to around 1.4 GtC yr⁻¹ (5.1 GtCO₂ yr⁻¹). This is based on separate projections for coal -
729 2.8%, oil +1.9%, natural gas +4.1%, and cement +0.7%.

730 For the European Union, our projection for 2022 is for a decline of 1.0% (range -2.9% to +1.0%) over 2021,
731 with 2022 emissions around 0.8 GtC yr⁻¹ (2.8 GtCO₂ yr⁻¹). This is based on separate projections for coal of
732 +7.5%, oil +0.6%, natural gas -11.0%, and cement unchanged.

733 For India, our projection for 2022 is an increase of 5.6% (range of 3.5% to 7.7%) over 2021, with 2022
734 emissions around 0.8 GtC yr⁻¹ (2.9 GtCO₂ yr⁻¹). This is based on separate projections for coal of +5.0%, oil
735 +8.0%, natural gas -3.0%, and cement +10.0%.

736 For the rest of the world, the expected growth rate for 2022 is 2.5% (range 0.1% to 2.3%). The fuel-specific
737 projected 2022 growth rates for the rest of the world are: +1.4% (range -0.6% to +3.4%) for coal, +3.2% (1.6%
738 to +4.9%) for oil, +2.6% (1.1% to 4.1%) for natural gas, +2.8% (+0.6% to +5.1%) for cement.

739 3.2 Emissions from Land Use Changes

740 3.2.1 Historical period 1850-2021

741 Cumulative CO₂ emissions from land-use changes (E_{LUC}) for 1850-2021 were 205 ± 60 GtC (Table 8; Figure 3;
742 Figure 14). The cumulative emissions from E_{LUC} are particularly uncertain, with large spread among individual
743 estimates of 140 GtC (updated H&N2017), 280 GtC (BLUE), and 190 GtC (OSCAR) for the three bookkeeping
744 models and a similar wide estimate of 185 ± 60 GtC for the DGVMs (all cumulative numbers are rounded to the
745 nearest 5GtC). These estimates are broadly consistent with indirect constraints from vegetation biomass
746 observations, giving a cumulative source of 155 ± 50 GtC over the 1901-2012 period (Li et al., 2017). However,
747 given the large spread, a best estimate is difficult to ascertain.

748 3.2.2 Recent period 1960-2021

749 In contrast to growing fossil emissions, CO₂ emissions from land-use, land-use change, and forestry have
750 remained relatively constant, over the 1960-1999 period, but showing a slight decrease of about 0.1 GtC per
751 decade since the 1990s, reaching 1.2 ± 0.7 GtC yr⁻¹ for the 2012-2021 period (Table 6), but with large spread
752 across estimates (Table 5, Figure 7). Different from the bookkeeping average, the DGVMs model average grows
753 slightly larger over the 1970-2021 period and shows no sign of decreasing emissions in the recent decades
754 (Table 5, Figure 7). This is, however, expected as DGVM-based estimates include the loss of additional sink
755 capacity, which grows with time, while the bookkeeping estimates do not (Appendix D4).

756 E_{LUC} is a net term of various gross fluxes, which comprise emissions and removals. Gross emissions on average
757 over the 1850-2021 period are two (BLUE, OSCAR) to three (updated H&N2017) times larger than the net E_{LUC}
758 emissions, and remained largely constant over the last 60 years, with a moderate increase from an average of 3.2
759 ± 0.9 GtC yr⁻¹ for the decade of the 1960s to an average of 3.8 ± 0.7 GtC yr⁻¹ during 2012-2021 (Figure 7),
760 showing the relevance of land management such as harvesting or rotational agriculture. Increases in gross
761 removals, from 1.8 ± 0.4 GtC yr⁻¹ for the 1960s to 2.6 ± 0.4 GtC yr⁻¹ for 2012-2021, were slightly larger than the



762 increase in gross emissions. Since the processes behind gross removals, foremost forest regrowth and soil
763 recovery, are all slow, while gross emissions include a large instantaneous component, short-term changes in
764 land-use dynamics, such as a temporary decrease in deforestation, influences gross emissions dynamics more
765 than gross removals dynamics. It is these relative changes to each other that explain the small decrease in net
766 E_{LUC} emissions over the last two decades and the last few years. Gross fluxes often differ more across the three
767 bookkeeping estimates than net fluxes, which is expected due to different process representation; in particular,
768 treatment of shifting cultivation, which increases both gross emissions and removals, differs across models.

769 There is a smaller decrease in net CO_2 emissions from land-use change in the last few years (Figure 7) than in
770 our last year's estimate (Friedlingstein et al., 2021), which places our updated estimates between last year's
771 estimate and the estimate from the GCB2020 (Friedlingstein et al., 2020). This change is principally attributable
772 to changes in E_{LUC} estimates from BLUE and OSCAR, which relate to changes in the underlying land-use
773 forcing (see Appendix C.2.2 for details). These changes address issues identified with last year's land-use
774 forcing (see Friedlingstein et al., 2022) and remove/attenuate several emission peaks in Brazil and the DR
775 Congo and lead to higher net emissions in Brazil in the last decades compared to last year's global carbon
776 budget. While we deem these changes in land-use forcing and emissions an improvement, the estimated
777 emissions based on the new land-use forcing still do not fully reflect the rise in Brazilian deforestation in the
778 recent few years (Silva Junior, 2021), and associated increasing emissions from deforestation would have been
779 missed here. Differences still exist, which highlight the need for accurate knowledge of land-use transitions and
780 their spatial and temporal variability. A further caveat is that global land-use change data for model input does
781 not capture forest degradation, which often occurs on small scale or without forest cover changes easily
782 detectable from remote sensing and poses a growing threat to forest area and carbon stocks that may surpass
783 deforestation effects (e.g., Matricardi et al., 2020, Qin et al., 2021).

784 We additionally separate the net E_{LUC} into component fluxes to gain further insight into the drivers of gross
785 sources and sinks and how the bookkeeping models compare to each other (Figure 7; Sec. C.2.1). On average
786 over the 2012-2021 period and over the three bookkeeping estimates, emissions from deforestation amount to
787 $1.8 \pm 0.4 \text{ GtC yr}^{-1}$ and carbon uptake in forests to $-0.9 \pm 0.3 \text{ GtC yr}^{-1}$ (Table 5). Emissions from organic soils
788 caused by peat drainage or peat fires (with $0.2 \pm 0.1 \text{ GtC yr}^{-1}$) and the net flux from other transitions (with $0.1 \pm$
789 0.1 GtC yr^{-1}) are substantially less important globally, but emissions from organic soils contribute over
790 proportionally to interannual variability (related in particular to peat fires in dry years in Southeast Asia).
791 Deforestation is thus the main driver of global gross sources. The relatively small deforestation flux in
792 comparison to the gross source estimate above is explained by the fact that emissions associated with wood
793 harvesting, while they do constitute a source of emissions to the atmosphere, are contained in the component
794 flux on forest, together with the associated carbon uptake in regrowth, because wood harvesting does not change
795 the land cover. For the same reason the flux on forest, being a net flux of sources from slash and product decay
796 following wood harvest and sinks due to regrowth after wood harvest or after abandonment, is smaller than the
797 gross sink estimates above. This split into component fluxes thus clarifies better the potentials for emission
798 reduction and carbon dioxide removal than the gross fluxes do: the emissions from deforestation could be halted
799 (largely) without compromising carbon uptake in other component fluxes and contribute to emissions reduction;
800 reforestation following agricultural abandonment does not directly depend on deforestation and can
801 independently provide carbon dioxide removal. By contrast, reducing wood harvesting to reduce emissions to



802 the atmosphere is associated with less forest regrowth; sinks and sources cannot be decoupled here. Last, we
803 compare our component flux estimates to NGHGI (Grassi et al., 2022b): With 1.1 GtC yr⁻¹ averaged over 2012-
804 2021, deforestation emissions are reported to be smaller by countries than the bookkeeping estimate. A reason
805 for this lies in the fact that country reports do not (fully) capture the carbon flux consequences of shifting
806 cultivation. With 0.3 GtC yr⁻¹ and 0.2 GtC yr⁻¹, emissions from organic soils and the net flux from other
807 transitions, respectively, are similar (slightly larger) than the estimates based on the bookkeeping approach and
808 the external peat drainage and burning datasets. With 1.75 GtC yr⁻¹, carbon uptake in forests is substantially
809 larger, owing to the inclusion of natural CO₂ fluxes on managed land in the NGHGI (see below).

810 Overall, highest land-use emissions occur in the tropical regions of all three continents. The top three emitters
811 (both cumulatively 1959-2021 and on average over 2012-2021) are Brazil (in particular the Amazon Arc of
812 Deforestation), Indonesia and the Democratic Republic of the Congo, with these 3 countries contributing 0.7
813 GtC yr⁻¹ or 58% of the global total land-use emissions (average over 2012-2021) (Figure 6b). This is related to
814 massive expansion of cropland, particularly in the last few decades in Latin America, Southeast Asia, and sub-
815 Saharan Africa Emissions (Hong et al., 2021), to a substantial part for export (Pendrill et al., 2019). Emission
816 intensity is high in many tropical countries, particularly of Southeast Asia, due to high rates of land conversion
817 in regions of carbon-dense and often still pristine, undegraded natural forests (Hong et al., 2021). Emissions are
818 further increased by peat fires in equatorial Asia (GFED4s, van der Werf et al., 2017). Uptake due to land-use
819 change occurs, particularly in Europe, partly related to expanding forest area as a consequence of the forest
820 transition in the 19th and 20th century and subsequent regrowth of forest (Figure 6b) (Mather 2001; McGrath et
821 al., 2015).

822 While the mentioned patterns are supported by independent literature and robust, we acknowledge that model
823 spread is substantially larger on regional than global level, as has been shown for bookkeeping models (Bastos
824 et al., 2021) as well as DGVMs (Obermeier et al., 2021). A detailed analysis of country-level or regional
825 uncertainties is beyond the scope of this study. Assessments for individual regions will be performed as part of
826 REgional Carbon Cycle Assessment and Processes (RECCAP2; Ciais et al., 2020) or already exist for selected
827 regions (e.g., for Europe by Petrescu et al., 2020, for Brazil by Rosan et al., 2021, for 8 selected
828 countries/regions in comparison to inventory data by Schwingshackl et al., *subm.*).

829 National GHG inventory data (NGHGI) under the LULUCF sector or data submitted by countries to FAOSTAT
830 differ from the global models' definition of E_{LUC} we adopt here in that in the NGHGI reporting, the natural
831 fluxes (S_{LAND}) are counted towards E_{LUC} when they occur on managed land (Grassi et al., 2018). In order to
832 compare our results to the NGHGI approach, we perform a re-mapping of our E_{LUC} estimate by including the
833 S_{LAND} over managed forest from the DGVMs simulations (following Grassi et al., 2021) to the bookkeeping
834 E_{LUC} estimate (see Appendix C.2.3). For the 2012-2021 period, we estimate that 1.8 GtC yr⁻¹ of S_{LAND} occurred
835 on managed forests and is then reallocated to E_{LUC} here, as done in the NGHGI method. Doing so, our mean
836 estimate of E_{LUC} is reduced from a source of 1.2 GtC to a sink of 0.6 GtC, very similar to the NGHGI estimate
837 of a 0.5 GtC sink (Table 9). The re-mapping approach has been shown to be generally applicable also on
838 country-level (Schwingshackl et al., *subm.*). Country-level analysis suggests, e.g., that the bookkeeping mean
839 estimates higher deforestation emissions than the national report in Indonesia, but estimates less CO₂ removal
840 by afforestation than the national report in China. The fraction of the natural CO₂ sinks that the NGHGI



841 estimates include differs substantially across countries, related to varying proportions of managed vs all forest
842 areas (Schwingshackl et al., *subm.*).

843 Though estimates between GHGI, FAOSTAT, individual process-based models and the mapped budget
844 estimates still differ in value and need further analysis, the approach taken here provides a possibility to relate
845 the global models' and NGHGI approach to each other routinely and thus link the anthropogenic carbon budget
846 estimates of land CO₂ fluxes directly to the Global Stocktake, as part of UNFCCC Paris Agreement.

847 **3.2.3 Final year 2021**

848 The global CO₂ emissions from land-use change are estimated as 1.1 ± 0.7 GtC in 2021, similar to the 2020
849 estimate. However, confidence in the annual change remains low.

850 Land-use change and related emissions may have been affected by the COVID-19 pandemic (e.g. Poulter et al.,
851 2021). During the period of the pandemic, environmental protection policies and their implementation may have
852 been weakened in Brazil (Vale et al., 2021). In other countries, too, monitoring capacities and legal enforcement
853 of measures to reduce tropical deforestation have been reduced due to budget restrictions of environmental
854 agencies or impairments to ground-based monitoring that prevents land grabs and tenure conflicts (Brancalion et
855 al., 2020, Amador-Jiménez et al., 2020). Effects of the pandemic on trends in fire activity or forest cover
856 changes are hard to separate from those of general political developments and environmental changes and the
857 long-term consequences of disruptions in agricultural and forestry economic activities (e.g., Gruère and Brooks,
858 2020; Golar et al., 2020; Beckman and Countryman, 2021) remain to be seen. Overall, there is limited evidence
859 so far that COVID-19 was a key driver of changes in LULUCF emissions at global scale. Impacts vary across
860 countries and deforestation-curbing and enhancing factors may partly compensate each other (Wunder et al.,
861 2021).

862 **3.2.4 Year 2022 Projection**

863 In Indonesia, peat fire emissions are very low, potentially related to a relatively wet dry season (GFED4.1s, van
864 der Werf et al., 2017). In South America, the trajectory of tropical deforestation and degradation fires resembles
865 the long-term average; global emissions from tropical deforestation and degradation fires were estimated to be
866 116 TgC by August 23 (GFED4.1s, van der Werf et al., 2017). Our preliminary estimate of E_{LUC} for 2022 is
867 substantially lower than the 2012-2021 average, which saw years of anomalously dry conditions in Indonesia
868 and high deforestation fires in South America (Friedlingstein et al., 2022). Based on the fire emissions until
869 August 23, we expect E_{LUC} emissions of around 1.0 GtC in 2022. Note that although our extrapolation is based
870 on tropical deforestation and degradation fires, degradation attributable to selective logging, edge-effects or
871 fragmentation will not be captured. Further, deforestation and fires in deforestation zones may become more
872 disconnected, partly due changes in legislation in some regions. For example, Van Wees et al. (2021) found that
873 the contribution from fires to forest loss decreased in the Amazon and in Indonesia over the period of 2003-
874 2018. More recent years, however, saw an uptick in the Amazon again (Tyukavina et al., 2022 with update) and
875 more work is needed to understand fire-deforestation relations.



876 The fires in Mediterranean Europe in summer 2022 and in the U.S. in spring 2022, though above average for
877 those regions, only contribute a small amount to global emissions. However, they were unrelated to land-use
878 change and are thus not attributed to E_{LUC} , but would be captured by the natural land sink.

879 Land use dynamics may be influenced by the disruption to the global food market associated with the war in
880 Ukraine, but scientific evidence so far is very limited. High food prices, which preceded but were exacerbated
881 by the war (Torero 2022), are generally linked to higher deforestation (Angelsen and Kaimowitz 1999), while
882 high prices on agricultural inputs such as fertilizers and fuel, which are also under pressure from embargoes,
883 may impair yields.

884 3.3 Total anthropogenic emissions

885 Cumulative anthropogenic CO_2 emissions for 1850-2021 totalled 670 ± 65 GtC (2455 ± 240 Gt CO_2), of which
886 70% (470 GtC) occurred since 1960 and 33% (220 GtC) since 2000 (Table 6 and 8). Total anthropogenic
887 emissions more than doubled over the last 60 years, from 4.5 ± 0.7 GtC yr^{-1} for the decade of the 1960s to an
888 average of 10.9 ± 0.8 GtC yr^{-1} during 2012-2021, and reaching 11.1 ± 0.9 GtC (40.8 ± 3.3 Gt CO_2) in 2021. For
889 2022, we project global total anthropogenic CO_2 emissions from fossil and land use changes to be also around
890 11.1 GtC (40.9 Gt CO_2).

891 During the historical period 1850-2021, 30% of historical emissions were from land use change and 79% from
892 fossil emissions. However, fossil emissions have grown significantly since 1960 while land use changes have
893 not, and consequently the contributions of land use change to total anthropogenic emissions were smaller during
894 recent periods (18% during the period 1960-2021 and 11% during 2012-2021).

895 3.4 Atmospheric CO_2

896 3.4.1 Historical period 1850-2021

897 Atmospheric CO_2 concentration was approximately 277 parts per million (ppm) in 1750 (Joos and Spahni,
898 2008), reaching 300 ppm in the 1910s, 350 ppm in the late 1980s, and reaching 414.71 ± 0.1 ppm in 2021
899 (Dlugokencky and Tans, 2022); Figure 1). The mass of carbon in the atmosphere increased by 48% from 590
900 GtC in 1750 to 879 GtC in 2021. Current CO_2 concentrations in the atmosphere are unprecedented in the last 2
901 million years and the current rate of atmospheric CO_2 increase is at least 10 times faster than at any other time
902 during the last 800,000 years (Canadell et al., 2021).

903 3.4.2 Recent period 1960-2021

904 The growth rate in atmospheric CO_2 level increased from 1.7 ± 0.07 GtC yr^{-1} in the 1960s to 5.2 ± 0.02 GtC yr^{-1}
905 during 2012-2022 with important decadal variations (Table 6, Figure 3 and Figure 4). During the last decade
906 (2012-2021), the growth rate in atmospheric CO_2 concentration continued to increase, albeit with large
907 interannual variability (Figure 4).

908 The airborne fraction (AF), defined as the ratio of atmospheric CO_2 growth rate to total anthropogenic
909 emissions:

$$910 \quad AF = G_{ATM} / (E_{FOS} + E_{LUC}) \quad (2)$$



911 provides a diagnostic of the relative strength of the land and ocean carbon sinks in removing part of the
912 anthropogenic CO₂ perturbation. The evolution of AF over the last 60 years shows no significant trend,
913 remaining at around 44%, albeit showing a large interannual and decadal variability driven by the year-to-year
914 variability in G_{ATM} (Figure 9). The observed stability of the airborne fraction over the 1960-2020 period
915 indicates that the ocean and land CO₂ sinks have been removing on average about 55% of the anthropogenic
916 emissions (see sections 3.5 and 3.6).

917 **3.4.3 Final year 2021**

918 The growth rate in atmospheric CO₂ concentration was 5.2 ± 0.2 GtC (2.46 ± 0.08 ppm) in 2021 (Figure 4;
919 Dlugokencky and Tans, 2022), slightly above the 2020 growth rate (5.0 GtC) but similar to the 2011-2020
920 average (5.2 GtC).

921 **3.4.4 Year 2022 Projection**

922 The 2022 growth in atmospheric CO₂ concentration (G_{ATM}) is projected to be about 5.5 GtC (2.58 ppm) based
923 on GLO observations until August 2022, bringing the atmospheric CO₂ concentration to an expected level of
924 417.3 ppm averaged over the year, 51% over the pre-industrial level.

925 **3.5 Ocean Sink**

926 **3.5.1 Historical period 1850-2021**

927 Cumulated since 1850, the ocean sink adds up to 175 ± 35 GtC, with more than two thirds of this amount (120
928 GtC) being taken up by the global ocean since 1960. Over the historical period, the ocean sink increased in pace
929 with the anthropogenic emissions exponential increase (Figure 3b). Since 1850, the ocean has removed 26% of
930 total anthropogenic emissions.

931 **3.5.2 Recent period 1960-2021**

932 The ocean CO₂ sink increased from 1.1 ± 0.4 GtC yr⁻¹ in the 1960s to 2.9 ± 0.4 GtC yr⁻¹ during 2012-2021
933 (Table 6), with interannual variations of the order of a few tenths of GtC yr⁻¹ (Figure 10). The ocean-borne
934 fraction ($S_{\text{OCEAN}}/(E_{\text{FOS}}+E_{\text{LUC}})$) has been remarkably constant around 25% on average (Figure 9). Variations
935 around this mean illustrate decadal variability of the ocean carbon sink. So far, there is no indication of a
936 decrease in the ocean-borne fraction from 1960 to 2021. The increase of the ocean sink is primarily driven by
937 the increased atmospheric CO₂ concentration, with the strongest CO₂ induced signal in the North Atlantic and
938 the Southern Ocean (Figure 11a). The effect of climate change is much weaker, reducing the ocean sink globally
939 by 0.11 ± 0.09 GtC yr⁻¹ or 4.2% (2012-2021, nine models simulate a weakening of the ocean sink by climate
940 change, range -3.2 to -8.9% and one model a strengthening by 4.8%), and does not show clear spatial patterns
941 across the GOBMs ensemble (Figure 11b). This is the combined effect of change and variability in all
942 atmospheric forcing fields, previously attributed to wind and temperature changes in one model (LeQuéré et al.,
943 2010).

944 The global net air-sea CO₂ flux is a residual of large natural and anthropogenic CO₂ fluxes into and out of the
945 ocean with distinct regional and seasonal variations (Figure 6 and B1). Natural fluxes dominate on regional



946 scales, but largely cancel out when integrated globally (Gruber et al., 2009). Mid-latitudes in all basins and the
947 high-latitude North Atlantic dominate the ocean CO₂ uptake where low temperatures and high wind speeds
948 facilitate CO₂ uptake at the surface (Takahashi et al., 2009). In these regions, formation of mode, intermediate
949 and deep-water masses transport anthropogenic carbon into the ocean interior, thus allowing for continued CO₂
950 uptake at the surface. Outgassing of natural CO₂ occurs mostly in the tropics, especially in the equatorial
951 upwelling region, and to a lesser extent in the North Pacific and polar Southern Ocean, mirroring a well-
952 established understanding of regional patterns of air-sea CO₂ exchange (e.g., Takahashi et al., 2009, Gruber et
953 al., 2009). These patterns are also noticeable in the Surface Ocean CO₂ Atlas (SOCAT) dataset, where an ocean
954 fCO₂ value above the atmospheric level indicates outgassing (Figure B1). This map further illustrates the data-
955 sparsity in the Indian Ocean and the southern hemisphere in general.

956 Interannual variability of the ocean carbon sink is driven by climate variability with a first-order effect from a
957 stronger ocean sink during large El Niño events (e.g., 1997-1998) (Figure 10; Rödenbeck et al., 2014, Hauck et
958 al., 2020). The GOBMs show the same patterns of decadal variability as the mean of the fCO₂-based data
959 products, with a stagnation of the ocean sink in the 1990s and a strengthening since the early 2000s (Figure 10,
960 Le Quéré et al., 2007; Landschützer et al., 2015, 2016; DeVries et al., 2017; Hauck et al., 2020; McKinley et al.,
961 2020). Different explanations have been proposed for this decadal variability, ranging from the ocean's response
962 to changes in atmospheric wind and pressure systems (e.g., Le Quéré et al., 2007, Keppler and Landschützer,
963 2019), including variations in upper ocean overturning circulation (DeVries et al., 2017) to the eruption of
964 Mount Pinatubo and its effects on sea surface temperature and slowed atmospheric CO₂ growth rate in the 1990s
965 (McKinley et al., 2020). The main origin of the decadal variability is a matter of debate with a number of studies
966 initially pointing to the Southern Ocean (see review in Canadell et al., 2021), but also contributions from the
967 North Atlantic and North Pacific (Landschützer et al., 2016, DeVries et al., 2019), or a global signal (McKinley
968 et al., 2020) were proposed.

969 Although all individual GOBMs and data-products fall within the observational constraint, the ensemble means
970 of GOBMs, and data-products adjusted for the riverine flux diverge over time with a mean offset increasing
971 from 0.28 GtC yr⁻¹ in the 1990s to 0.61 GtC yr⁻¹ in the decade 2012-2021 and reaching 0.79 GtC yr⁻¹ in 2021.
972 The S_{OCEAN} positive trend over time diverges by a factor two since 2002 (GOBMs: 0.28 ± 0.07 GtC yr⁻¹ per
973 decade, data-products: 0.61 ± 0.17 GtC yr⁻¹ per decade, S_{OCEAN}: 0.45 GtC yr⁻¹ per decade) and by a factor of
974 three since 2010 (GOBMs: 0.21 ± 0.14 GtC yr⁻¹ per decade, data-products: 0.66 ± 0.38 GtC yr⁻¹ per decade
975 S_{OCEAN}: 0.44 GtC yr⁻¹ per decade). The GOBMs estimate is slightly higher (<0.1 GtC yr⁻¹) than in the previous
976 global carbon budget (Friedlingstein et al., 2022), because one new model is included (CESM2) and four models
977 revised their estimate upwards (CESM-ETHZ, CNRM, FESOM2-REcoM, PlankTOM). The data-product
978 estimate is higher by about 0.1 GtC yr⁻¹ compared to Friedlingstein et al. (2022) as a result of an upward
979 correction in three products (Jena-MLS, MPI-SOMFFN, OS-ETHZ-Gracer), the submission of LDEO-HPD
980 which is above average, the non-availability of the CSIR product, and the small upward correction of the river
981 flux adjustment.

982 The discrepancy between the two types of estimates stems mostly from a larger Southern Ocean sink in the data-
983 products prior to 2001, and from a larger S_{OCEAN} trend in the northern and southern extra-tropics since then
984 (Figure 13). Note that the location of the mean offset (but not its trend) depends strongly on the choice of



985 regional river flux adjustment and would occur in the tropics rather than in the Southern Ocean when using the
986 dataset of Lacroix et al. (2020) instead of Aumont et al. (2001). Other possible explanations for the discrepancy
987 in the Southern Ocean could be missing winter observations and data sparsity in general (Bushinsky et al., 2019,
988 Gloege et al., 2021), or model biases (as indicated by the large model spread in the South, Figure 13, and the
989 larger model-data mismatch, Figure B2).

990 In GCB releases until 2021, the ocean sink 1959-1989 was only estimated by GOBMs due to the absence of
991 $f\text{CO}_2$ observations. Now, the first data-based estimates extending back to 1957/58 are becoming available (Jena-
992 MLS, Rödenbeck et al., 2022, LDEO-HPD, Bennington et al., 2022; Gloege et al. 2022). These are based on a
993 multi-linear regression of $p\text{CO}_2$ with environmental predictors (Rödenbeck et al., 2022, included here) or on
994 model-data $p\text{CO}_2$ misfits and their relation to environmental predictors (Bennington et al., 2022). The Jena-MLS
995 estimate falls well within the range of GOBM estimates and has a correlation of 0.98 with S_{OCEAN} (1959-2021 as
996 well as 1959-1989). It agrees well on the mean S_{OCEAN} estimate since 1977 with a slightly higher amplitude of
997 variability (Figure 10). Until 1976, Jena-MLS is $0.2\text{--}0.3 \text{ GtCyr}^{-1}$ below the central S_{OCEAN} estimate. The
998 agreement especially on phasing of variability is impressive, and the discrepancies in the mean flux 1959-1976
999 could be explained by an overestimated trend of Jena-MLS (Rödenbeck et al., 2022). Bennington et al. (2022)
1000 report a larger flux into the pre-1990 ocean than in Jena-MLS.

1001 The reported S_{OCEAN} estimate from GOBMs and data-products is $2.1 \pm 0.4 \text{ GtC yr}^{-1}$ over the period 1994 to
1002 2007, which is in agreement with the ocean interior estimate of $2.2 \pm 0.4 \text{ GtC yr}^{-1}$ which accounts for the
1003 climate effect on the natural CO_2 flux of $-0.4 \pm 0.24 \text{ GtC yr}^{-1}$ (Gruber et al., 2019) to match the definition of
1004 S_{OCEAN} used here (Hauck et al., 2020). This comparison depends critically on the estimate of the climate effect
1005 on the natural CO_2 flux, which is smaller from the GOBMs (-0.1 GtC yr^{-1}) than in Gruber et al. (2019).
1006 Uncertainties of these two estimates would also overlap when using the GOBM estimate of the climate effect on
1007 the natural CO_2 flux.

1008 During 2010-2016, the ocean CO_2 sink appears to have intensified in line with the expected increase from
1009 atmospheric CO_2 (McKinley et al., 2020). This effect is stronger in the $f\text{CO}_2$ -based data products (Figure 10,
1010 ocean sink 2016 minus 2010, GOBMs: $+0.42 \pm 0.09 \text{ GtC yr}^{-1}$, data-products: $+0.52 \pm 0.22 \text{ GtC yr}^{-1}$). The
1011 reduction of $-0.09 \text{ GtC yr}^{-1}$ (range: -0.39 to $+0.01 \text{ GtC yr}^{-1}$) in the ocean CO_2 sink in 2017 is consistent with the
1012 return to normal conditions after the El Niño in 2015/16, which caused an enhanced sink in previous years.
1013 After 2017, the GOBMs ensemble mean suggests the ocean sink levelling off at about 2.6 GtC yr^{-1} , whereas the
1014 data-products' estimate increases by $0.24 \pm 0.17 \text{ GtC yr}^{-1}$ over the same period.

1015 **3.5.3 Final year 2021**

1016 The estimated ocean CO_2 sink was $2.9 \pm 0.4 \text{ GtC}$ in 2021. This is a decrease of 0.12 GtC compared to 2020, in
1017 line with the expected sink weakening from persistent La Niña conditions. GOBM and data-product estimates
1018 consistently result in a stagnation of S_{OCEAN} (GOBMs: $-0.09 \pm 0.15 \text{ GtC}$, data-products: $-0.15 \pm 0.24 \text{ GtC}$). Seven
1019 models and six data products show a decrease in S_{OCEAN} (GOBMs down to -0.31 GtC , data-products down to $-$
1020 0.58 GtC), while three models and two data products show an increase in S_{OCEAN} (GOBMs up to 0.15 GtC , data-
1021 products up to 0.12 GtC ; Figure 10). The data-products have a larger uncertainty at the tails of the reconstructed
1022 time series (e.g., Watson et al., 2020). Specifically, the data-products' estimate of the last year is regularly



1023 adjusted in the following release owing to the tail effect and an incrementally increasing data availability with 1-
1024 5 years lag (Figure 10 inset).

1025 **3.5.4 Year 2022 Projection**

1026 Using a feed-forward neural network method (see section 2.4) we project an ocean sink of 2.9 GtC for 2022.
1027 This is similar to the year 2021 as the La Niña conditions persist in 2022.

1028 **3.5.5 Model Evaluation**

1029 The additional simulation D allows to separate the anthropogenic carbon component (steady state and non-
1030 steady state, sim D - sim A) and to compare the model flux and DIC inventory change directly to the interior
1031 ocean estimate of Gruber et al. (2019) without further assumptions. The GOBMs ensemble average of
1032 anthropogenic carbon inventory changes 1994-2007 amounts to 2.2 GtC yr⁻¹ and is thus lower than the 2.6 ± 0.3
1033 GtC yr⁻¹ estimated by Gruber et al (2019). Only four models with the highest sink estimate fall within the range
1034 reported by Gruber et al. (2019). This suggests that most of the GOBMs underestimate anthropogenic carbon
1035 uptake by the ocean. Analysis of Earth System Models indicate that this may be due to biases in ocean carbon
1036 transport and mixing from the surface mixed layer to the ocean interior (Goris et al., 2018, Terhaar et al., 2021,
1037 Bourgeois et al., 2022, Terhaar et al., 2022,), biases in the chemical buffer capacity (Revelle factor) of the ocean
1038 (Vaittinada Ayar et al., 2022; Terhaar et al., 2022) and partly due to a late starting date of the simulations
1039 (mirrored in atmospheric CO₂ chosen for the preindustrial control simulation, Table A2, Bronselaer et al., 2017,
1040 Terhaar et al., 2022). Interestingly, and in contrast to the uncertainties in the surface CO₂ flux, we find the
1041 largest mismatch in interior ocean carbon accumulation in the tropics (93% of the mismatch), with minor
1042 contribution from the north (1%) and the south (6%). This highlights the role of interior ocean carbon
1043 redistribution for those inventories (Khatiwala et al., 2009).

1044 The evaluation of the ocean estimates (Figure B2) shows an RMSE from annually detrended data of 0.4 to 2.6
1045 μatm for the seven fCO₂-based data products over the globe, relative to the fCO₂ observations from the SOCAT
1046 v2022 dataset for the period 1990-2021. The GOBMs RMSEs are larger and range from 3.0 to 4.8 μatm. The
1047 RMSEs are generally larger at high latitudes compared to the tropics, for both the data products and the
1048 GOBMs. The data products have RMSEs of 0.4 to 3.2 μatm in the tropics, 0.8 to 2.8 μatm in the north, and 0.8
1049 to 3.6 μatm in the south. Note that the data products are based on the SOCAT v2022 database, hence the
1050 SOCAT is not an independent dataset for the evaluation of the data products. The GOBMs RMSEs are more
1051 spread across regions, ranging from 2.5 to 3.9 μatm in the tropics, 3.1 to 6.5 μatm in the North, and 5.4 to 7.9
1052 μatm in the South. The higher RMSEs occur in regions with stronger climate variability, such as the northern
1053 and southern high latitudes (poleward of the subtropical gyres). The upper range of the model RMSEs have
1054 decreased somewhat relative to Friedlingstein et al. (2022).



1055 **3.6 Land Sink**

1056 **3.6.1 Historical period 1850-2021**

1057 Cumulated since 1850, the terrestrial CO₂ sink amounts to 210 ± 45 GtC, 31% of total anthropogenic emissions.
1058 Over the historical period, the sink increased in pace with the anthropogenic emissions exponential increase
1059 (Figure 3b).

1060 **3.6.2 Recent period 1960-2021**

1061 The terrestrial CO₂ sink increased from 1.2 ± 0.4 GtC yr⁻¹ in the 1960s to 3.1 ± 0.6 GtC yr⁻¹ during 2012-2021,
1062 with important interannual variations of up to 2 GtC yr⁻¹ generally showing a decreased land sink during El
1063 Niño events (Figure 8), responsible for the corresponding enhanced growth rate in atmospheric CO₂
1064 concentration. The larger land CO₂ sink during 2012-2021 compared to the 1960s is reproduced by all the
1065 DGVMs in response to the increase in both atmospheric CO₂ and nitrogen deposition, and the changes in
1066 climate, and is consistent with constraints from the other budget terms (Table 5).

1067 Over the period 1960 to present the increase in the global terrestrial CO₂ sink is largely attributed to the CO₂
1068 fertilisation effect (Prentice et al., 2001, Piao et al., 2009), directly stimulating plant photosynthesis and
1069 increased plant water use in water limited systems, with a small negative contribution of climate change (Figure
1070 11). There is a range of evidence to support a positive terrestrial carbon sink in response to increasing
1071 atmospheric CO₂, albeit with uncertain magnitude (Walker et al., 2021). As expected from theory, the greatest
1072 CO₂ effect is simulated in the tropical forest regions, associated with warm temperatures and long growing
1073 seasons (Hickler et al., 2008) (Figure 11a). However, evidence from tropical intact forest plots indicate an
1074 overall decline in the land sink across Amazonia (1985-2011), attributed to enhanced mortality offsetting
1075 productivity gains (Brienen et al., 2005, Hubau et al., 2020). During 2012-2021 the land sink is positive in all
1076 regions (Figure 6) with the exception of eastern Brazil, Southwest USA, Southeast Europe and Central Asia,
1077 North and South Africa, and eastern Australia, where the negative effects of climate variability and change (i.e.
1078 reduced rainfall) counterbalance CO₂ effects. This is clearly visible on Figure 11 where the effects of CO₂
1079 (Figure 11a) and climate (Figure 11b) as simulated by the DGVMs are isolated. The negative effect of climate is
1080 the strongest in most of South America, Central America, Southwest US, Central Europe, western Sahel,
1081 southern Africa, Southeast Asia and southern China, and eastern Australia (Figure 11b). Globally, climate
1082 change reduces the land sink by 0.63 ± 0.52 GtC yr⁻¹ or 17% (2012-2021).

1083 Since 2020 the globe has experienced La Niña conditions which would be expected to lead to an increased land
1084 carbon sink. A clear peak in the global land sink is not evident in S_{LAND}, and we find that a La Niña- driven
1085 increase in tropical land sink is offset by a reduced high latitude extra-tropical land sink, which may be linked to
1086 the land response to recent climate extremes. In the past years several regions experienced record-setting fire
1087 events. While global burned area has declined over the past decades mostly due to declining fire activity in
1088 savannas (Andela et al., 2017), forest fire emissions are rising and have the potential to counter the negative fire
1089 trend in savannas (Zheng et al., 2021). Noteworthy events include the 2019-2020 Black Summer event in
1090 Australia (emissions of roughly 0.2 GtC; van der Velde et al., 2021) and Siberia in 2021 where emissions
1091 approached 0.4 GtC or three times the 1997-2020 average according to GFED4s. While other regions, including



1092 Western US and Mediterranean Europe, also experienced intense fire seasons in 2021 their emissions are
1093 substantially lower.

1094 Despite these regional negative effects of climate change on S_{LAND} , the efficiency of land to remove
1095 anthropogenic CO_2 emissions has remained broadly constant over the last six decades, with a land-borne
1096 fraction ($S_{\text{LAND}}/(E_{\text{FOS}}+E_{\text{LUC}})$) of ~30% (Figure 9).

1097 **3.6.3 Final year 2021**

1098 The terrestrial CO_2 sink from the DGVMs ensemble was $3.5 \pm 0.9 \text{ GtC}$ in 2021, slightly above the decadal
1099 average of $3.1 \pm 0.6 \text{ GtC yr}^{-1}$ (Figure 4, Table 6). We note that the DGVMs estimate for 2021 is larger, but
1100 within the uncertainty, than the $2.8 \pm 0.9 \text{ GtC yr}^{-1}$ estimate from the residual sink from the global budget
1101 ($E_{\text{FOS}}+E_{\text{LUC}}-G_{\text{ATM}}-S_{\text{OCEAN}}$) (Table 5).

1102 **3.6.4 Year 2022 Projection**

1103 Using a feed-forward neural network method we project a land sink of 3.4 GtC for 2022, very similar to the
1104 2021 estimate. As for the ocean sink, we attribute this to the persistence of La Niña conditions in 2022.

1105 **3.6.5 Model Evaluation**

1106 The evaluation of the DGVMs (Figure B3) shows generally high skill scores across models for runoff, and to a
1107 lesser extent for vegetation biomass, GPP, and ecosystem respiration (Figure B3, left panel). Skill score was
1108 lowest for leaf area index and net ecosystem exchange, with a widest disparity among models for soil carbon.
1109 These conclusions are supported by a more comprehensive analysis of DGVM performance in comparison with
1110 benchmark data (Seiler et al., 2022). Furthermore, results show how DGVM differences are often of similar
1111 magnitude compared with the range across observational datasets.
1112

1113 **3.7 Partitioning the carbon sinks**

1114 **3.7.1 Global sinks and spread of estimates**

1115 In the period 2012-2021, the bottom-up view of total global carbon sinks provided by the GCB, S_{OCEAN} for the
1116 ocean and $S_{\text{LAND}}-E_{\text{LUC}}$ for the land (to be comparable to inversions), agrees closely with the top-down global
1117 carbon sinks delivered by the atmospheric inversions. Figure 12 shows both total sink estimates of the last
1118 decade split by ocean and land (including E_{LUC}), which match the difference between G_{ATM} and E_{FOS} to within
1119 $0.01\text{-}0.12 \text{ GtC yr}^{-1}$ for inverse systems, and to 0.34 GtC yr^{-1} for the GCB mean. The latter represents the B_{IM}
1120 discussed in Section 3.8, which by design is minimal for the inverse systems.

1121 The distributions based on the individual models and data products reveal substantial spread but converge near
1122 the decadal means quoted in Tables 5 and 6. Sink estimates for S_{OCEAN} and from inverse systems are mostly
1123 non-Gaussian, while the ensemble of DGVMs appears more normally distributed justifying the use of a multi-
1124 model mean and standard deviation for their errors in the budget. Noteworthy is that the tails of the distributions
1125 provided by the land and ocean bottom-up estimates would not agree with the global constraint provided by the



1126 fossil fuel emissions and the observed atmospheric CO₂ growth rate ($E_{\text{FOS}} - G_{\text{ATM}}$). This illustrates the power of
1127 the atmospheric joint constraint from G_{ATM} and the global CO₂ observation network it derives from.

1128 **3.7.2 Total atmosphere-to-land fluxes**

1129 The total atmosphere-to-land fluxes ($S_{\text{LAND}} - E_{\text{LUC}}$), calculated here as the difference between S_{LAND} from the
1130 DGVMs and E_{LUC} from the bookkeeping models, amounts to a 1.9 ± 0.9 GtC yr⁻¹ sink during 2012-2021 (Table
1131 5). Estimates of total atmosphere-to-land fluxes ($S_{\text{LAND}} - E_{\text{LUC}}$) from the DGVMs alone (1.5 ± 0.5 GtC yr⁻¹) are
1132 consistent with this estimate and also with the global carbon budget constraint ($E_{\text{FOS}} - G_{\text{ATM}} - S_{\text{OCEAN}}$, 1.5 ± 0.6
1133 GtC yr⁻¹ Table 5). For the last decade (2012-2021), the inversions estimate the net atmosphere-to-land uptake to
1134 lie within a range of 1.1 to 1.7 GtC yr⁻¹, consistent with the GCB and DGVMs estimates of $S_{\text{LAND}} - E_{\text{LUC}}$ (Figure
1135 13 top row).

1136 **3.7.3 Total atmosphere-to-ocean fluxes**

1137 For the 2012-2021 period, the GOBMs (2.6 ± 0.5 GtC yr⁻¹) produce a lower estimate for the ocean sink than the
1138 fCO₂-based data products (3.2 ± 0.6 GtC yr⁻¹), which shows up in Figure 12 as a separate peak in the
1139 distribution from the GOBMs (triangle symbols pointing right) and from the fCO₂-based products (triangle
1140 symbols pointing left). Atmospheric inversions (2.7 to 3.3 GtC yr⁻¹) also suggest higher ocean uptake in the
1141 recent decade (Figure 13 top row). In interpreting these differences, we caution that the riverine transport of
1142 carbon taken up on land and outgassing from the ocean is a substantial (0.65 GtC yr⁻¹) and uncertain term that
1143 separates the various methods. A recent estimate of decadal ocean uptake from observed O₂/N₂ ratios (Tohjima
1144 et al., 2019) also points towards a larger ocean sink, albeit with large uncertainty (2012-2016: 3.1 ± 1.5 GtC yr⁻¹).
1145

1146 **3.7.4 Regional breakdown and interannual variability**

1147 Figure 13 also shows the latitudinal partitioning of the total atmosphere-to-surface fluxes excluding fossil CO₂
1148 emissions ($S_{\text{OCEAN}} + S_{\text{LAND}} - E_{\text{LUC}}$) according to the multi-model average estimates from GOBMs and ocean
1149 fCO₂-based products (S_{OCEAN}) and DGVMs ($S_{\text{LAND}} - E_{\text{LUC}}$), and from atmospheric inversions (S_{OCEAN} and S_{LAND}
1150 $- E_{\text{LUC}}$).

1151 **3.7.4.1 North**

1152 Despite being one of the most densely observed and studied regions of our globe, annual mean carbon sink
1153 estimates in the northern extra-tropics (north of 30°N) continue to differ. The atmospheric inversions suggest an
1154 atmosphere-to-surface sink ($S_{\text{OCEAN}} + S_{\text{LAND}} - E_{\text{LUC}}$) for 2012-2021 of 2.0 to 3.2 GtC yr⁻¹, which is higher than
1155 the process models' estimate of 2.2 ± 0.4 GtC yr⁻¹ (Figure 13). The GOBMs (1.2 ± 0.2 GtC yr⁻¹), fCO₂-based
1156 data products (1.4 ± 0.1 GtC yr⁻¹), and inversion systems (0.9 to 1.4 GtC yr⁻¹) produce consistent estimates of
1157 the ocean sink. Thus, the difference mainly arises from the total land flux ($S_{\text{LAND}} - E_{\text{LUC}}$) estimate, which is 1.0
1158 ± 0.4 GtC yr⁻¹ in the DGVMs compared to 0.6 to 2.0 GtC yr⁻¹ in the atmospheric inversions (Figure 13, second
1159 row).

1160 Discrepancies in the northern land fluxes conforms with persistent issues surrounding the quantification of the
1161 drivers of the global net land CO₂ flux (Arneeth et al., 2017; Huntzinger et al., 2017; O'Sullivan et al., 2022) and



1162 the distribution of atmosphere-to-land fluxes between the tropics and high northern latitudes (Baccini et al.,
1163 2017; Schimel et al., 2015; Stephens et al., 2007; Ciais et al. 2019; Gaubert et al., 2019).

1164 In the northern extratropics, the process models, inversions, and fCO₂-based data products consistently suggest
1165 that most of the variability stems from the land (Figure 13). Inversions generally estimate similar interannual
1166 variations (IAV) over land to DGVMs (0.30 – 0.37 vs 0.17 – 0.69 GtC yr⁻¹, averaged over 1990-2021), and they
1167 have higher IAV in ocean fluxes (0.05 – 0.09 GtC yr⁻¹) relative to GOBMs (0.02 – 0.06 GtC yr⁻¹, Figure B2),
1168 and fCO₂-based data products (0.03 – 0.09 GtC yr⁻¹).

1169 3.7.4.2 Tropics

1170 In the tropics (30°S-30°N), both the atmospheric inversions and process models estimate a total carbon balance
1171 ($S_{\text{OCEAN}}+S_{\text{LAND}}-E_{\text{LUC}}$) that is close to neutral over the past decade. The GOBMs (0.06 ± 0.34 GtC yr⁻¹), fCO₂-
1172 based data products (0.00 ± 0.06 GtC yr⁻¹), and inversion systems (-0.2 to 0.5 GtC yr⁻¹) all indicate an
1173 approximately neutral tropical ocean flux (see Figure B1 for spatial patterns). DGVMs indicate a net land sink
1174 ($S_{\text{LAND}}-E_{\text{LUC}}$) of 0.5 ± 0.3 GtC yr⁻¹, whereas the inversion systems indicate a net land flux between -0.9 and 0.7
1175 GtC yr⁻¹, though with high uncertainty (Figure 13, third row).

1176 The tropical lands are the origin of most of the atmospheric CO₂ interannual variability (Ahlström et al., 2015),
1177 consistently among the process models and inversions (Figure 13). The interannual variability in the tropics is
1178 similar among the ocean data products (0.07 – 0.16 GtC yr⁻¹) and the GOBMs (0.07 – 0.16 GtC yr⁻¹, Figure
1179 B2), which is the highest ocean sink variability of all regions. The DGVMs and inversions indicate that
1180 atmosphere-to-land CO₂ fluxes are more variable than atmosphere-to-ocean CO₂ fluxes in the tropics, with
1181 interannual variability of 0.5 to 1.1 and 0.8 to 1.0 GtC yr⁻¹ for DGVMs and inversions, respectively.

1182 3.7.4.3 South

1183 In the southern extra-tropics (south of 30°S), the atmospheric inversions suggest a total atmosphere-to-surface
1184 sink ($S_{\text{OCEAN}}+S_{\text{LAND}}-E_{\text{LUC}}$) for 2012-2021 of 1.6 to 1.9 GtC yr⁻¹, slightly higher than the process models'
1185 estimate of 1.4 ± 0.3 GtC yr⁻¹ (Figure 13). An approximately neutral total land flux ($S_{\text{LAND}}-E_{\text{LUC}}$) for the
1186 southern extra-tropics is estimated by both the DGVMs (0.02 ± 0.06 GtC yr⁻¹) and the inversion systems (sink of
1187 -0.2 to 0.2 GtC yr⁻¹). This means nearly all carbon uptake is due to oceanic sinks south of 30°S. The Southern
1188 Ocean flux in the fCO₂-based data products (1.8 ± 0.1 GtC yr⁻¹) and inversion estimates (1.6 to 1.9 GtCyr-1) is
1189 higher than in the GOBMs (1.4 ± 0.3 GtC yr⁻¹) (Figure 13, bottom row). This discrepancy in the mean flux is
1190 likely explained by the uncertainty in the regional distribution of the river flux adjustment (Aumont et al., 2001,
1191 Lacroix et al., 2020) applied to fCO₂-based data products and inverse systems to isolate the anthropogenic
1192 S_{OCEAN} flux. Other possibly contributing factors are that the data-products potentially underestimate the winter
1193 CO₂ outgassing south of the Polar Front (Bushinsky et al., 2019) and model biases. CO₂ fluxes from this region
1194 are more sparsely sampled by all methods, especially in wintertime (Figure B1).

1195 The interannual variability in the southern extra-tropics is low because of the dominance of ocean areas with
1196 low variability compared to land areas. The split between land ($S_{\text{LAND}}-E_{\text{LUC}}$) and ocean (S_{OCEAN}) shows a
1197 substantial contribution to variability in the south coming from the land, with no consistency between the
1198 DGVMs and the inversions or among inversions. This is expected due to the difficulty of separating exactly the



1199 land and oceanic fluxes when viewed from atmospheric observations alone. The S_{OCEAN} interannual variability
1200 was found to be higher in the $f\text{CO}_2$ -based data products (0.09 to 0.19 GtC yr^{-1}) compared to GOBMs (0.03 to
1201 0.06 GtC yr^{-1}) in 1990-2021 (Figure B2). Model subsampling experiments recently illustrated that observation-
1202 based products may overestimate decadal variability in the Southern Ocean carbon sink by 30% due to data
1203 sparsity, based on one data product with the highest decadal variability (Gloege et al., 2021).

1204 **3.7.4.4 Tropical vs northern land uptake**

1205 A continuing conundrum is the partitioning of the global atmosphere-land flux between the northern hemisphere
1206 land and the tropical land (Stephens et al., 2017; Pan et al., 2011; Gaubert et al., 2019). It is of importance
1207 because each region has its own history of land-use change, climate drivers, and impact of increasing
1208 atmospheric CO_2 and nitrogen deposition. Quantifying the magnitude of each sink is a prerequisite to
1209 understanding how each individual driver impacts the tropical and mid/high-latitude carbon balance.

1210 We define the North-South (N-S) difference as net atmosphere-land flux north of 30°N minus the net
1211 atmosphere-land flux south of 30°N . For the inversions, the N-S difference ranges from 0.1 GtC yr^{-1} to 2.9 GtC
1212 yr^{-1} across this year's inversion ensemble with a preference across models for either a smaller Northern land
1213 sink with a near neutral tropical land flux (medium N-S difference), or a large Northern land sink and a tropical
1214 land source (large N-S difference).

1215 In the ensemble of DGVMs the N-S difference is $0.6 \pm 0.5 \text{ GtC yr}^{-1}$, a much narrower range than the one from
1216 inversions. Only two DGVMs have a N-S difference larger than 1.0 GtC yr^{-1} . The larger agreement across
1217 DGVMs than across inversions is to be expected as there is no correlation between Northern and Tropical land
1218 sinks in the DGVMs as opposed to the inversions where the sum of the two regions being well-constrained leads
1219 to an anti-correlation between these two regions. The much smaller spread in the N-S difference between the
1220 DGVMs could help to scrutinise the inverse systems further. For example, a large northern land sink and a
1221 tropical land source in an inversion would suggest a large sensitivity to CO_2 fertilisation (the dominant factor
1222 driving the land sinks) for Northern ecosystems, which would be not mirrored by tropical ecosystems. Such a
1223 combination could be hard to reconcile with the process understanding gained from the DGVMs ensembles and
1224 independent measurements (e.g. Free Air CO_2 Enrichment experiments). Such investigations will be further
1225 pursued in the upcoming assessment from REgional Carbon Cycle Assessment and Processes (RECCAP2; Ciais
1226 et al., 2020).

1227 **3.8 Closing the Global Carbon Cycle**

1228 **3.8.1 Partitioning of Cumulative Emissions and Sink Fluxes**

1229 The global carbon budget over the historical period (1850-2021) is shown in Figure 3.

1230 Emissions during the period 1850-2021 amounted to $670 \pm 65 \text{ GtC}$ and were partitioned among the atmosphere
1231 ($275 \pm 5 \text{ GtC}$; 41%), ocean ($175 \pm 35 \text{ GtC}$; 26%), and the land ($210 \pm 45 \text{ GtC}$; 31%). The cumulative land sink
1232 is almost equal to the cumulative land-use emissions ($200 \pm 60 \text{ GtC}$), making the global land nearly neutral over
1233 the whole 1850-2021 period.



1234 The use of nearly independent estimates for the individual terms of the global carbon budget shows a cumulative
1235 budget imbalance of 15 GtC (2% of total emissions) during 1850-2021 (Figure 3, Table 8), which, if correct,
1236 suggests that emissions could be slightly too high by the same proportion (2%) or that the combined land and
1237 ocean sinks are slightly underestimated (by about 3%), although these are well within the uncertainty range of
1238 each component of the budget. Nevertheless, part of the imbalance could originate from the estimation of
1239 significant increase in E_{FOS} and E_{LUC} between the mid 1920s and the mid 1960s which is unmatched by a similar
1240 growth in atmospheric CO_2 concentration as recorded in ice cores (Figure 3). However, the known loss of
1241 additional sink capacity of 30-40 GtC (over the 1850-2020 period) due to reduced forest cover has not been
1242 accounted for in our method and would exacerbate the budget imbalance (Section 2.7.4).

1243 For the more recent 1960-2021 period where direct atmospheric CO_2 measurements are available, total
1244 emissions ($E_{\text{FOS}} + E_{\text{LUC}}$) amounted to 470 ± 50 GtC, of which 385 ± 20 GtC (82%) were caused by fossil CO_2
1245 emissions, and 85 ± 45 GtC (18%) by land-use change (Table 8). The total emissions were partitioned among
1246 the atmosphere (210 ± 5 GtC; 45%), ocean (120 ± 25 GtC; 26%), and the land (145 ± 30 GtC; 30%), with a near
1247 zero (-5 GtC) unattributed budget imbalance. All components except land-use change emissions have
1248 significantly grown since 1960, with important interannual variability in the growth rate in atmospheric CO_2
1249 concentration and in the land CO_2 sink (Figure 4), and some decadal variability in all terms (Table 6).
1250 Differences with previous budget releases are documented in Figure B5.

1251 The global carbon budget averaged over the last decade (2012-2021) is shown in Figure 2, Figure 14 (right
1252 panel) and Table 6. For this period, 89% of the total emissions ($E_{\text{FOS}} + E_{\text{LUC}}$) were from fossil CO_2 emissions
1253 (E_{FOS}), and 11% from land-use change (E_{LUC}). The total emissions were partitioned among the atmosphere
1254 (48%), ocean (26%) and land (29%), with a near-zero unattributed budget imbalance ($\sim 3\%$). For single years,
1255 the budget imbalance can be larger (Figure 4). For 2021, the combination of our estimated sources (10.9 ± 0.9
1256 GtC yr^{-1}) and sinks (11.6 ± 1.0 GtC yr^{-1}) leads to a B_{IM} of -0.6 GtC, suggesting a slight underestimation of the
1257 anthropogenic sources, and/or an overestimation of the combined land and ocean sinks

1258 3.8.2 Carbon Budget Imbalance trend and variability

1259 The carbon budget imbalance (B_{IM} ; Eq. 1, Figure 4) quantifies the mismatch between the estimated total
1260 emissions and the estimated changes in the atmosphere, land, and ocean reservoirs. The mean budget imbalance
1261 from 1960 to 2021 is very small (4.6 GtC over the period, i.e. average of 0.07 GtC yr^{-1}) and shows no trend over
1262 the full time series (Figure 4). The process models (GOBMs and DGVMs) and data-products have been selected
1263 to match observational constraints in the 1990s, but no further constraints have been applied to their
1264 representation of trend and variability. Therefore, the near-zero mean and trend in the budget imbalance is seen
1265 as evidence of a coherent community understanding of the emissions and their partitioning on those time scales
1266 (Figure 4). However, the budget imbalance shows substantial variability of the order of ± 1 GtC yr^{-1} , particularly
1267 over semi-decadal time scales, although most of the variability is within the uncertainty of the estimates. The
1268 positive carbon imbalance during the 1960s, and early 1990s, indicates that either the emissions were
1269 overestimated, or the sinks were underestimated during these periods. The reverse is true for the 1970s, and to a
1270 lower extent for the 1980s and 2012-2021 period (Figure 4, Table 6).

1271 We cannot attribute the cause of the variability in the budget imbalance with our analysis, we only note that the
1272 budget imbalance is unlikely to be explained by errors or biases in the emissions alone because of its large semi-



1273 decadal variability component, a variability that is untypical of emissions and has not changed in the past 60
1274 years despite a near tripling in emissions (Figure 4). Errors in S_{LAND} and S_{OCEAN} are more likely to be the main
1275 cause for the budget imbalance, especially on interannual to semi-decadal timescales. For example,
1276 underestimation of the S_{LAND} by DGVMs has been reported following the eruption of Mount Pinatubo in 1991
1277 possibly due to missing responses to changes in diffuse radiation (Mercado et al., 2009). Although since
1278 GCB2021 we accounted for aerosol effects on solar radiation quantity and quality (diffuse vs direct), most
1279 DGVMs only used the former as input (i.e., total solar radiation) (Table A1). Thus, the ensemble mean may not
1280 capture the full effects of volcanic eruptions, i.e. associated with high light scattering sulphate aerosols, on the
1281 land carbon sink (O'Sullivan et al., 2021). DGVMs are suspected to overestimate the land sink in response to
1282 the wet decade of the 1970s (Sitch et al., 2008). Quasi-decadal variability in the ocean sink has also been
1283 reported, with all methods agreeing on a smaller than expected ocean CO_2 sink in the 1990s and a larger than
1284 expected sink in the 2000s (Figure 10; Landschützer et al., 2016, DeVries et al., 2019, Hauck et al., 2020,
1285 McKinley et al., 2020). Errors in sink estimates could also be driven by errors in the climatic forcing data,
1286 particularly precipitation for S_{LAND} and wind for S_{OCEAN} . Also, the B_{IM} shows substantial departure from zero on
1287 yearly time scales (Figure 4e), highlighting unresolved variability of the carbon cycle, likely in the land sink
1288 (S_{LAND}), given its large year to year variability (Figure 4d and 8).

1289 Both the budget imbalance (B_{IM} , Table 6) and the residual land sink from the global budget ($E_{\text{FOS}}+E_{\text{LUC}}-G_{\text{ATM}}-$
1290 S_{OCEAN} , Table 5) include an error term due to the inconsistencies that arises from using E_{LUC} from bookkeeping
1291 models, and S_{LAND} from DGVMs, most notably the loss of additional sink capacity (see section 2.7). Other
1292 differences include a better accounting of land use changes practices and processes in bookkeeping models than
1293 in DGVMs, or the bookkeeping models error of having present-day observed carbon densities fixed in the past.
1294 That the budget imbalance shows no clear trend towards larger values over time is an indication that these
1295 inconsistencies probably play a minor role compared to other errors in S_{LAND} or S_{OCEAN} .

1296 Although the budget imbalance is near zero for the recent decades, it could be due to compensation of errors.
1297 We cannot exclude an overestimation of CO_2 emissions, particularly from land-use change, given their large
1298 uncertainty, as has been suggested elsewhere (Piao et al., 2018), combined with an underestimate of the sinks. A
1299 larger DGVM ($S_{\text{LAND}}-E_{\text{LUC}}$) over the extra-tropics would reconcile model results with inversion estimates for
1300 fluxes in the total land during the past decade (Figure 13; Table 5). Likewise, a larger S_{OCEAN} is also possible
1301 given the higher estimates from the data-products (see section 3.1.2, Figure 10 and Figure 13), the
1302 underestimation of interior ocean anthropogenic carbon accumulation in the GOBMs (section 3.5.5), and the
1303 recently suggested upward adjustments of the ocean carbon sink in Earth System Models (Terhaar et al., 2022),
1304 and in data-products, here related to a potential temperature bias and skin effects (Watson et al., 2020, Dong et
1305 al., 2022, Figure 10). If S_{OCEAN} were to be based on data-products alone, with all data-products including this
1306 adjustment, this would result in a 2012-2021 S_{OCEAN} of 3.8 GtC yr^{-1} (Dong et al., 2022) or $>4 \text{ GtC yr}^{-1}$ (Watson
1307 et al., 2020), i.e., outside of the range supported by the atmospheric inversions and with an implied negative B_{IM}
1308 of more than -1 GtC yr^{-1} indicating that a closure of the budget could only be achieved with either anthropogenic
1309 emissions being significantly larger and/or the net land sink being substantially smaller than estimated here.
1310 More integrated use of observations in the Global Carbon Budget, either on their own or for further constraining
1311 model results, should help resolve some of the budget imbalance (Peters et al., 2017).

1312



1313 4 Tracking progress towards mitigation targets

1314 The average growth in global fossil CO₂ emissions peaked at +3% per year during the 2000s, driven by the rapid
1315 growth in emissions in China. In the last decade, however, the global growth rate has slowly declined, reaching
1316 a low +0.5% per year over 2012-2021 (including the 2020 global decline and the 2021 emissions rebound).

1317 While this slowdown in global fossil CO₂ emissions growth is welcome, it is far from the emission decrease
1318 needed to be consistent with the temperature goals of the Paris Agreement.

1319 Since the 1990s, the average growth rate of fossil CO₂ emissions has continuously declined across the group of
1320 developed countries of the Organisation for Economic Co-operation and Development (OECD), with emissions
1321 peaking in around 2005 and now declining at around 1% yr⁻¹ (Le Quéré et al., 2021). In the decade 2012-2021,
1322 territorial fossil CO₂ emissions decreased significantly (at the 95% confidence level) in 24 countries whose
1323 economies grew significantly (also at the 95% confidence level): Belgium, Croatia, Czech Republic, Denmark,
1324 Estonia, Finland, France, Germany, Hong Kong, Israel, Italy, Japan, Luxembourg, Malta, Mexico, Netherlands,
1325 Norway, Singapore, Slovenia, Sweden, Switzerland, United Kingdom, USA, and Uruguay (updated from Le
1326 Quéré et al., 2019). Altogether, these 24 countries emitted 2.4 GtC yr⁻¹ (8.8 GtCO₂ yr⁻¹) on average over the last
1327 decade, about one quarter of world CO₂ fossil emissions. Consumption-based emissions also fell significantly
1328 during the final decade for which estimates are available (2011-2020) in 15 of these countries: Belgium,
1329 Denmark, Estonia, Finland, France, Germany, Hong Kong, Israel, Japan, Luxembourg, Mexico, Netherlands,
1330 Singapore, Sweden, United Kingdom, and Uruguay. Figure 15 shows that the emission declines in the USA and
1331 the EU27 are primarily driven by increased decarbonisation (CO₂ emissions per unit energy) in the last decade
1332 compared to the previous, with smaller contributions in the EU27 from slightly weaker economic growth and
1333 slightly larger declines in energy per GDP. These countries have stable or declining energy use and so
1334 decarbonisation policies replace existing fossil fuel infrastructure (Le Quéré et al. 2019).

1335 In contrast, fossil CO₂ emissions continue to grow in non-OECD countries, although the growth rate has slowed
1336 from almost 6% yr⁻¹ during the 2000s to less than 2% yr⁻¹ in the last decade. Representing 47% of non-OECD
1337 emissions in 2021, a large part of this slowdown is due to China, which has seen emissions growth decline from
1338 nearly 10% yr⁻¹ in the 2000s to 1.5% yr⁻¹ in the last decade. Excluding China, non-OECD emissions grew at
1339 3.3% yr⁻¹ in the 2000s compared to 1.6% yr⁻¹ in the last decade. Figure 15 shows that, compared to the previous
1340 decade, China has had weaker economic growth in the last decade and a higher decarbonisation rate, with more
1341 rapid declines in energy per GDP that are now back to levels seen during the 1990s. India and the rest of the
1342 world have strong economic growth that is not offset by decarbonisation or declines in energy per GDP, driving
1343 up fossil CO₂ emissions. Despite the high deployment of renewables in some countries (e.g., India), fossil
1344 energy sources continue to grow to meet growing energy demand (Le Quéré et al. 2019).

1345 Globally, fossil CO₂ emissions growth is slowing, and this is due to the emergence of climate policy (Eskander
1346 and Fankhauser 2020; Le Quere et al 2019) and technological change, which is leading to a shift from coal to
1347 gas and growth in renewable energies, and reduced expansion of coal capacity. At the aggregated global level,
1348 decarbonisation shows a strong and growing signal in the last decade, with smaller contributions from lower
1349 economic growth and declines in energy per GDP. Despite the slowing growth in global fossil CO₂ emissions,
1350 emissions are still growing, far from the reductions needed to meet the ambitious climate goals of the UNFCCC
1351 Paris agreement.



1352 We update the remaining carbon budget assessed by the IPCC AR6 (Canadell et al., 2021), accounting for the
1353 2020 to 2022 estimated emissions from fossil fuel combustion (E_{FOS}) and land use changes (E_{LUC}). From
1354 January 2023, the remaining carbon (50% likelihood) for limiting global warming to 1.5°C, 1.7°C and 2°C is
1355 estimated to amount to 105, 200, and 335 GtC (380, 730, 1230 GtCO₂). These numbers include an uncertainty
1356 based on model spread (as in IPCC AR6), which is reflected through the percent likelihood of exceeding the
1357 given temperature threshold. These remaining amounts correspond respectively to about 9, 18 and 30 years from
1358 the beginning of 2023, at the 2022 level of total CO₂ emissions. Reaching net zero CO₂ emissions by 2050
1359 entails cutting total anthropogenic CO₂ emissions by about 0.4 GtC (1.4 GtCO₂) each year on average,
1360 comparable to the decrease observed in 2020 during the COVID-19 pandemic.

1361

1362 5 Discussion

1363 Each year when the global carbon budget is published, each flux component is updated for all previous years to
1364 consider corrections that are the result of further scrutiny and verification of the underlying data in the primary
1365 input data sets. Annual estimates may be updated with improvements in data quality and timeliness (e.g., to
1366 eliminate the need for extrapolation of forcing data such as land-use). Of all terms in the global budget, only the
1367 fossil CO₂ emissions and the growth rate in atmospheric CO₂ concentration are based primarily on empirical
1368 inputs supporting annual estimates in this carbon budget. The carbon budget imbalance, yet an imperfect
1369 measure, provides a strong indication of the limitations in observations in understanding and representing
1370 processes in models, and/or in the integration of the carbon budget components.

1371 The persistent unexplained variability in the carbon budget imbalance limits our ability to verify reported
1372 emissions (Peters et al., 2017) and suggests we do not yet have a complete understanding of the underlying
1373 carbon cycle dynamics on annual to decadal timescales. Resolving most of this unexplained variability should
1374 be possible through different and complementary approaches. First, as intended with our annual updates, the
1375 imbalance as an error term is reduced by improvements of individual components of the global carbon budget
1376 that follow from improving the underlying data and statistics and by improving the models through the
1377 resolution of some of the key uncertainties detailed in Table 10. Second, additional clues to the origin and
1378 processes responsible for the variability in the budget imbalance could be obtained through a closer scrutiny of
1379 carbon variability in light of other Earth system data (e.g., heat balance, water balance), and the use of a wider
1380 range of biogeochemical observations to better understand the land-ocean partitioning of the carbon imbalance
1381 (e.g. oxygen, carbon isotopes). Finally, additional information could also be obtained through higher resolution
1382 and process knowledge at the regional level, and through the introduction of inferred fluxes such as those based
1383 on satellite CO₂ retrievals. The limit of the resolution of the carbon budget imbalance is yet unclear, but most
1384 certainly not yet reached given the possibilities for improvements that lie ahead.

1385 Estimates of global fossil CO₂ emissions from different datasets are in relatively good agreement when the
1386 different system boundaries of these datasets are considered (Andrew, 2020a). But while estimates of E_{FOS} are
1387 derived from reported activity data requiring much fewer complex transformations than some other components
1388 of the budget, uncertainties remain, and one reason for the apparently low variation between datasets is
1389 precisely the reliance on the same underlying reported energy data. The budget excludes some sources of fossil



1390 CO₂ emissions, which available evidence suggests are relatively small (<1%). We have added emissions from
1391 lime production in China and the US, but these are still absent in most other non-Annex I countries, and before
1392 1990 in other Annex I countries.

1393 Estimates of E_{LUC} suffer from a range of intertwined issues, including the poor quality of historical land-cover
1394 and land-use change maps, the rudimentary representation of management processes in most models, and the
1395 confusion in methodologies and boundary conditions used across methods (e.g., Arneeth et al., 2017; Pongratz et
1396 al., 2014, see also Section 2.7.4 on the loss of sink capacity; Bastos et al., 2021). Uncertainties in current and
1397 historical carbon stocks in soils and vegetation also add uncertainty in the E_{LUC} estimates. Unless a major effort
1398 to resolve these issues is made, little progress is expected in the resolution of E_{LUC}. This is particularly
1399 concerning given the growing importance of E_{LUC} for climate mitigation strategies, and the large issues in the
1400 quantification of the cumulative emissions over the historical period that arise from large uncertainties in E_{LUC}.

1401 By adding the DGVMs estimates of CO₂ fluxes due to environmental change from countries' managed forest
1402 areas (part of S_{LAND} in this budget) to the budget E_{LUC} estimate, we successfully reconciled the large gap
1403 between our E_{LUC} estimate and the land use flux from NGHGs using the approach described in Grassi et al.
1404 (2021) for future scenario and in Grassi et al. (2022b) using data from the Global Carbon Budget 2021. The
1405 updated data presented here can be used as potential adjustment in the policy context, e.g., to help assessing the
1406 collective countries' progress towards the goal of the Paris Agreement and avoiding double-accounting for the
1407 sink in managed forests. In the absence of this adjustment, collective progress would hence appear better than it
1408 is (Grassi et al. 2021). The need of such adjustment whenever a comparison between LULUCF fluxes reported
1409 by countries and the global emission estimates of the IPCC is attempted is recommended also in the recent
1410 UNFCCC Synthesis report for the first Global Stocktake (UNFCCC, 2022). However, this adjustment should be
1411 seen as a short-term and pragmatic fix based on existing data, rather than a definitive solution to bridge the
1412 differences between global models and national inventories. Additional steps are needed to understand and
1413 reconcile the remaining differences, some of which are relevant at the country level (Grassi, et al. 2022b,
1414 Schwingshackl, et al., *subm.*).

1415 The comparison of GOBMs, data products and inversions highlights substantial discrepancy in the Southern
1416 Ocean (Figure 13, Hauck et al., 2020). A large part of the uncertainty in the mean fluxes stems from the regional
1417 distribution of the river flux adjustment term. The current distribution (Aumont et al., 2001) is based on one
1418 model study yielding the largest riverine outgassing flux south of 20°S, whereas a recent study, also based on
1419 one model, simulates the largest share of the outgassing to occur in the tropics (Lacroix et al., 2020). The long-
1420 standing sparse data coverage of fCO₂ observations in the Southern compared to the Northern Hemisphere (e.g.,
1421 Takahashi et al., 2009) continues to exist (Bakker et al., 2016, 2022, Figure B1) and to lead to substantially
1422 higher uncertainty in the S_{OCEAN} estimate for the Southern Hemisphere (Watson et al., 2020, Gloege et al.,
1423 2021). This discrepancy, which also hampers model improvement, points to the need for increased high-quality
1424 fCO₂ observations especially in the Southern Ocean. At the same time, model uncertainty is illustrated by the
1425 large spread of individual GOBM estimates (indicated by shading in Figure 13) and highlights the need for
1426 model improvement. The diverging trends in S_{OCEAN} from different methods is a matter of concern, which is
1427 unresolved. The assessment of the net land-atmosphere exchange from DGVMs and atmospheric inversions also
1428 shows substantial discrepancy, particularly for the estimate of the total land flux over the northern extra-tropic.



1429 This discrepancy highlights the difficulty to quantify complex processes (CO₂ fertilisation, nitrogen deposition
1430 and fertilisers, climate change and variability, land management, etc.) that collectively determine the net land
1431 CO₂ flux. Resolving the differences in the Northern Hemisphere land sink will require the consideration and
1432 inclusion of larger volumes of observations.

1433 We provide metrics for the evaluation of the ocean and land models and the atmospheric inversions (Figs. B2 to
1434 B4). These metrics expand the use of observations in the global carbon budget, helping 1) to support
1435 improvements in the ocean and land carbon models that produce the sink estimates, and 2) to constrain the
1436 representation of key underlying processes in the models and to allocate the regional partitioning of the CO₂
1437 fluxes. However, GOBMs skills have changed little since the introduction of the ocean model evaluation. The
1438 additional simulation allows for direct comparison with interior ocean anthropogenic carbon estimates and
1439 suggests that the models underestimate anthropogenic carbon uptake and storage. This is an initial step towards
1440 the introduction of a broader range of observations that we hope will support continued improvements in the
1441 annual estimates of the global carbon budget.

1442 We assessed before that a sustained decrease of -1% in global emissions could be detected at the 66%
1443 likelihood level after a decade only (Peters et al., 2017). Similarly, a change in behaviour of the land and/or
1444 ocean carbon sink would take as long to detect, and much longer if it emerges more slowly. To continue
1445 reducing the carbon imbalance on annual to decadal time scales, regionalising the carbon budget, and integrating
1446 multiple variables are powerful ways to shorten the detection limit and ensure the research community can
1447 rapidly identify issues of concern in the evolution of the global carbon cycle under the current rapid and
1448 unprecedented changing environmental conditions.

1449

1450 **6 Conclusions**

1451 The estimation of global CO₂ emissions and sinks is a major effort by the carbon cycle research community that
1452 requires a careful compilation and synthesis of measurements, statistical estimates, and model results. The
1453 delivery of an annual carbon budget serves two purposes. First, there is a large demand for up-to-date
1454 information on the state of the anthropogenic perturbation of the climate system and its underpinning causes. A
1455 broad stakeholder community relies on the data sets associated with the annual carbon budget including
1456 scientists, policy makers, businesses, journalists, and non-governmental organisations engaged in adapting to
1457 and mitigating human-driven climate change. Second, over the last decades we have seen unprecedented
1458 changes in the human and biophysical environments (e.g., changes in the growth of fossil fuel emissions, impact
1459 of COVID-19 pandemic, Earth's warming, and strength of the carbon sinks), which call for frequent
1460 assessments of the state of the planet, a better quantification of the causes of changes in the contemporary global
1461 carbon cycle, and an improved capacity to anticipate its evolution in the future. Building this scientific
1462 understanding to meet the extraordinary climate mitigation challenge requires frequent, robust, transparent, and
1463 traceable data sets and methods that can be scrutinised and replicated. This paper via 'living data' helps to keep
1464 track of new budget updates.

1465



1466 **7 Data availability**

1467 The data presented here are made available in the belief that their wide dissemination will lead to greater
1468 understanding and new scientific insights of how the carbon cycle works, how humans are altering it, and how
1469 we can mitigate the resulting human-driven climate change. Full contact details and information on how to cite
1470 the data shown here are given at the top of each page in the accompanying database and summarised in Table 2.

1471 The accompanying database includes two Excel files organised in the following spreadsheets:

1472 File `Global_Carbon_Budget_2022v0.1.xlsx` includes the following:

- 1473 1. Summary
- 1474 2. The global carbon budget (1959-2021);
- 1475 3. The historical global carbon budget (1750-2021);
- 1476 4. Global CO₂ emissions from fossil fuels and cement production by fuel type, and the per-capita emissions
1477 (1850-2021);
- 1478 5. CO₂ emissions from land-use change from the individual methods and models (1959-2021);
- 1479 6. Ocean CO₂ sink from the individual ocean models and fCO₂-based products (1959-2021);
- 1480 7. Terrestrial CO₂ sink from the individual DGVMs (1959-2021);
- 1481 8. Cement carbonation CO₂ sink (1959-2021).

1482

1483 File `National_Carbon_Emissions_2022v0.1.xlsx` includes the following:

- 1484 1. Summary
- 1485 2. Territorial country CO₂ emissions from fossil CO₂ emissions (1850-2021);
- 1486 3. Consumption country CO₂ emissions from fossil CO₂ emissions and emissions transfer from the
1487 international trade of goods and services (1990-2020) using CDIAC/UNFCCC data as reference;
- 1488 4. Emissions transfers (Consumption minus territorial emissions; 1990-2020);
- 1489 5. Country definitions.

1490

1491 Both spreadsheets are published by the Integrated Carbon Observation System (ICOS) Carbon Portal and are
1492 available at <https://doi.org/10.18160/GCP-2022> (Friedlingstein et al., 2022b). National emissions data are also
1493 available from the Global Carbon Atlas (<http://www.globalcarbonatlas.org/>, last access: 25 September 2022) and
1494 from Our World in Data (<https://ourworldindata.org/co2-emissions>, last access: 25 September 2022).

1495

1496 **8 Author contributions**

1497 PF, MOS, MWJ, RMA, LGr, JH, CLQ, ITL, AO, GPP, WP, JP, CIS, and SS designed the study, conducted the
1498 analysis, and wrote the paper with input from JGC, PC and RBJ. RMA, GPP and JIK produced the fossil fuel
1499 emissions and their uncertainties and analysed the emissions data. MH and GM provided fossil fuel emission
1500 data. JP, TGa, CIS and RAH provided the bookkeeping land-use change emissions with synthesis by JP and



1501 CIS, JH, LB, ÖG, NG, TI, KL, NMa, LR, JS, RS, HiT, and ReW provided an update of the global ocean
1502 biogeochemical models, MG, LGI, LGr, YI, AJ, ChR, JDS, and JZ provided an update of the ocean fCO₂ data
1503 products, with synthesis on both streams by JH, LGr and NMa. SRA, NRB, MB, HCB, MC, WE, RAF, TGk,
1504 KK, NL, NMe, NMM, DRM, SN, TO, DP, KP, ChR, IS, TS, AJS, CoS, ST, TT, BT, RiW, CW, AW provided
1505 ocean fCO₂ measurements for the year 2021, with synthesis by AO and KO. AA, VKA, SF, AKJ, EK, DK, JK,
1506 MJM, MOS, BP, QS, HaT, APW, WY, XY, and SZ provided an update of the Dynamic Global Vegetation
1507 Models, with synthesis by SS and MOS. WP, ITL, FC, JL, YN, PIP, ChR, XT, and BZ provided an updated
1508 atmospheric inversion, WP, FC, and ITL developed the protocol and produced the evaluation. RMA provided
1509 predictions of the 2022 emissions and atmospheric CO₂ growth rate. PL provided the predictions of the 2022
1510 ocean and land sinks. LPC, GCH, KKG, TMR and GRvdW provided forcing data for land-use change. RA, GG,
1511 FT, and CY provided data for the land-use change NGHGI mapping. PPT provided key atmospheric CO₂ data.
1512 MWJ produced the model atmospheric CO₂ forcing and the atmospheric CO₂ growth rate. MOS and NB
1513 produced the aerosol diffuse radiative forcing for the DGVMs. IH provided the climate forcing data for the
1514 DGVMs. ER provided the evaluation of the DGVMs. MWJ provided the emissions prior for use in the inversion
1515 systems. ZL provided seasonal emissions data for most recent years for the emission prior. MWJ and MOS
1516 developed the new data management pipeline which automates many aspects of the data collation, analysis,
1517 plotting and synthesis. PF, MOS and MMJ coordinated the effort, revised all figures, tables, text and/or numbers
1518 to ensure the update was clear from the 2021 edition and in line with the globalcarbonatlas.org.

1519

1520 **Competing interests.** The authors declare that they have no conflict of interest.

1521

1522 **9 Acknowledgements**

1523 We thank all people and institutions who provided the data used in this global carbon budget 2022 and the Global
1524 Carbon Project members for their input throughout the development of this publication. We thank Nigel Hawtin
1525 for producing Figure 2 and Figure 14. We thank Thomas Hawes for technical support with the data management
1526 pipeline. We thank Ed Dlugokencky for providing atmospheric CO₂ measurements. We thank Ian G. C. Ashton,
1527 Fatemeh Cheginig, Trang T. Chau, Sam Ditkovsky, Christian Ethé, Amanda R. Fay, Lonneke Goddijn-Murphy,
1528 T. Holding, Fabrice Lacroix, Enhui Liao, Galen A. McKinley, Shijie Shu, Richard Sims, Jade Skye, Andrew J.
1529 Watson, David Willis, and David K. Woolf for their involvement in the development, use and analysis of the
1530 models and data-products used here. Daniel Kennedy thanks all the scientists, software engineers, and



1531 administrators who contributed to the development of CESM2. We thank Joe Salisbury, Doug Vandemark,
1532 Christopher W. Hunt, and Peter Landschützer who contributed to the provision of surface ocean CO₂ observations
1533 for the year 2021 (see Table A5). We also thank Benjamin Pfeil, Rocío Castaño-Primo, and Stephen D. Jones of
1534 the Ocean Thematic Centre of the EU Integrated Carbon Observation System (ICOS) Research Infrastructure,
1535 Eugene Burger of NOAA's Pacific Marine Environmental Laboratory and Alex Kozyr of NOAA's National
1536 Centers for Environmental Information, for their contribution to surface ocean CO₂ data and metadata
1537 management. This is PMEL contribution 5434. We thank the scientists, institutions, and funding agencies
1538 responsible for the collection and quality control of the data in SOCAT as well as the International Ocean Carbon
1539 Coordination Project (IOCCP), the Surface Ocean Lower Atmosphere Study (SOLAS) and the Integrated Marine
1540 Biosphere Research (IMBeR) program for their support. We thank data providers ObsPack GLOBALVIEWplus
1541 v7.0 and NRT v7.2 for atmospheric CO₂ observations. We thank the individuals and institutions that provided the
1542 databases used for the model evaluations used here. We thank Fortunat Joos, Samar Khatiwala and Timothy
1543 DeVries for providing historical data. Matthew J. McGrath thanks the whole ORCHIDEE group. Ian Harris thanks
1544 the Japan Meteorological Agency (JMA) for producing the Japanese 55-year Reanalysis (JRA-55). Anthony P.
1545 Walker thanks ORNL which is managed by UT-Battelle, LLC, for the DOE under contract DE-AC05-1008
1546 00OR22725. Yosuke Niwa thanks CSIRO, EC, EMPA, FMI, IPEN, JMA, LSCE, NCAR, NIES, NILU, NIWA,
1547 NOAA, SIO, and TU/NIPR for providing data for NISMON-CO₂. Xiangjun Tian thanks Zhe Jin, Yilong Wang,
1548 Tao Wang and Shilong Piao for their contributions to the GONGGA inversion system. Bo Zheng thanks the
1549 comments and suggestions from Philippe Ciais and Frédéric Chevallier. Frédéric Chevallier thanks Marine
1550 Remaud who maintained the atmospheric transport model for the CAMS inversion. Paul I. Palmer thanks Liang
1551 Feng and acknowledges ongoing support from the National Centre for Earth Observation. Junjie Liu thanks the
1552 Jet Propulsion Laboratory, California Institute of Technology. Wiley Evans thanks the Tula Foundation for
1553 funding support. Australian ocean CO₂ data were sourced from Australia's Integrated Marine Observing System
1554 (IMOS); IMOS is enabled by the National Collaborative Research Infrastructure Strategy (NCRIS). Margot
1555 Cronin thanks Anthony English, Clynt Gregory and Gordon Furey (P&O Maritime Services) for their support.
1556 Nathalie Lefèvre thanks the crew of the Cap San Lorenzo and the US IMAGO of IRD Brest for technical support.
1557 Henry C. Bittig is grateful for the skillful technical support of M. Glockzin and B. Sadkowiak. Meike Becker and
1558 Are Olsen thank Sparebanken Vest/Agenda Vestlandet for their support for the observations on the Statsraad
1559 Lehmkuhl. Thanos Gkritzalis thanks the personnel and crew of Simon Stevin. Matthew W. Jones thanks Anthony
1560 J. De-Gol for his technical and conceptual assistance with the development of GCP-GridFED. FAOSTAT is



1561 funded by FAO member states through their contributions to the FAO Regular Programme, data contributions by
1562 national experts are greatly acknowledged. The views expressed in this paper are the authors' only and do not
1563 necessarily reflect those of FAO. Finally, we thank all funders who have supported the individual and joint
1564 contributions to this work (see Table A9), as well as the reviewers of this manuscript and previous versions, and
1565 the many researchers who have provided feedback.

1566

1567 **References**

- 1568 Ahlström, A., Raupach, M. R., Schurgers, G., Smith, B., Arneth, A., Jung, M., Reichstein, M., Canadell, J. G.,
1569 Friedlingstein, P., Jain, A. K., Kato, E., Poulter, B., Sitch, S., Stocker, B. D., Viovy, N., Wang, Y. P., Wiltshire,
1570 A., Zaehle, S., and Zeng, N.: The dominant role of semi-arid ecosystems in the trend and variability of the land
1571 CO₂ sink, 348, 895–899, <https://doi.org/10.1126/science.aaa1668>, 2015.
- 1572 Amador-Jiménez, M., Millner, N., Palmer, C., Pennington, R. T., and Sileci, L.: The Unintended Impact of
1573 Colombia's Covid-19 Lockdown on Forest Fires, *Environ Resource Econ*, 76, 1081–1105,
1574 <https://doi.org/10.1007/s10640-020-00501-5>, 2020.
- 1575 Amante, C. and Eakins, B. W.: ETOPO1 Global Relief Model converted to PanMap layer format,
1576 <https://doi.org/10.1594/PANGAEA.769615>, 2009.
- 1577 Andela, N., Morton, D. C., Giglio, L., Chen, Y., van der Werf, G. R., Kasibhatla, P. S., DeFries, R. S., Collatz,
1578 G. J., Hantson, S., Kloster, S., Bachelet, D., Forrest, M., Lasslop, G., Li, F., Mangeon, S., Melton, J. R., Yue, C.,
1579 and Randerson, J. T.: A human-driven decline in global burned area, *Science*, 356, 1356–1362,
1580 <https://doi.org/10.1126/science.aal4108>, 2017.
- 1581 Andres, R. J., Boden, T. A., Bréon, F.-M., Ciais, P., Davis, S., Erickson, D., Gregg, J. S., Jacobson, A., Marland,
1582 G., Miller, J., Oda, T., Olivier, J. G. J., Raupach, M. R., Rayner, P., and Treanton, K.: A synthesis of carbon
1583 dioxide emissions from fossil-fuel combustion, *Biogeosciences*, 9, 1845–1871, [https://doi.org/10.5194/bg-9-](https://doi.org/10.5194/bg-9-1845-2012)
1584 1845-2012, 2012.
- 1585 Andres, R. J., Boden, T. A., and Higdon, D.: A new evaluation of the uncertainty associated with CDIAC
1586 estimates of fossil fuel carbon dioxide emission, *Tellus B: Chemical and Physical Meteorology*, 66, 23616,
1587 <https://doi.org/10.3402/tellusb.v66.23616>, 2014.
- 1588 Andrew, R. M.: A comparison of estimates of global carbon dioxide emissions from fossil carbon sources, *Earth*
1589 *Syst. Sci. Data*, 12, 1437–1465, <https://doi.org/10.5194/essd-12-1437-2020>, 2020a.
- 1590 Andrew, R. M.: Timely estimates of India's annual and monthly fossil CO₂ emissions, *Earth Syst. Sci. Data*, 12,
1591 2411–2421, <https://doi.org/10.5194/essd-12-2411-2020>, 2020b.
- 1592 Andrew, R. M.: Towards near real-time, monthly fossil CO₂ emissions estimates for the European Union with
1593 current-year projections, *Atmospheric Pollution Research*, 101229, <https://doi.org/10.1016/j.apr.2021.101229>,



- 1594 2021.
- 1595 Andrew, R. M. and Peters, G. P.: A multi-region input–output table based on the global trade analysis project
1596 database (GTAP-MRIO), *Economic Systems Research*, 25, 99–121,
1597 <https://doi.org/10.1080/09535314.2012.761953>, 2013.
- 1598 Andrew, R. M. and Peters, G. P.: The Global Carbon Project’s fossil CO₂ emissions dataset (2021v34),
1599 <https://doi.org/10.5281/ZENODO.5569235>, 2021.
- 1600 Angelsen, A. and Kaimowitz, D.: Rethinking the Causes of Deforestation: Lessons from Economic Models,
1601 *World Bank Res. Obs.*, 14, 73–98, <https://doi.org/10.1093/wbro/14.1.73>, 1999.
- 1602 Aragão, L. E. O. C., Anderson, L. O., Fonseca, M. G., Rosan, T. M., Vedovato, L. B., Wagner, F. H., Silva, C.
1603 V. J., Silva Junior, C. H. L., Arai, E., Aguiar, A. P., Barlow, J., Berenguer, E., Deeter, M. N., Domingues, L. G.,
1604 Gatti, L., Gloor, M., Malhi, Y., Marengo, J. A., Miller, J. B., Phillips, O. L., and Saatchi, S.: 21st Century
1605 drought-related fires counteract the decline of Amazon deforestation carbon emissions, *Nat Commun*, 9, 536,
1606 <https://doi.org/10.1038/s41467-017-02771-y>, 2018.
- 1607 Archer, D., Eby, M., Brovkin, V., Ridgwell, A., Cao, L., Mikolajewicz, U., Caldeira, K., Matsumoto, K.,
1608 Munhoven, G., Montenegro, A., and Tokos, K.: Atmospheric Lifetime of Fossil Fuel Carbon Dioxide, *Annu.*
1609 *Rev. Earth Planet. Sci.*, 37, 117–134, <https://doi.org/10.1146/annurev.earth.031208.100206>, 2009.
- 1610 Arneth, A., Sitch, S., Pongratz, J., Stocker, B. D., Ciais, P., Poulter, B., Bayer, A. D., Bondeau, A., Calle, L.,
1611 Chini, L. P., Gasser, T., Fader, M., Friedlingstein, P., Kato, E., Li, W., Lindeskog, M., Nabel, J. E. M. S., Pugh,
1612 T. A. M., Robertson, E., Viovy, N., Yue, C., and Zaehle, S.: Historical carbon dioxide emissions caused by
1613 land-use changes are possibly larger than assumed, *Nature Geosci*, 10, 79–84, <https://doi.org/10.1038/ngeo2882>,
1614 2017.
- 1615 Arora, V. K., Boer, G. J., Christian, J. R., Curry, C. L., Denman, K. L., Zahariev, K., Flato, G. M., Scinocca, J.
1616 F., Merryfield, W. J., and Lee, W. G.: The Effect of Terrestrial Photosynthesis Down Regulation on the
1617 Twentieth-Century Carbon Budget Simulated with the CCCma Earth System Model, 22, 6066–6088,
1618 <https://doi.org/10.1175/2009JCLI3037.1>, 2009.
- 1619 Asaadi, A., Arora, V. K., Melton, J. R., and Bartlett, P.: An improved parameterization of leaf area index (LAI)
1620 seasonality in the Canadian Land Surface Scheme (CLASS) and Canadian Terrestrial Ecosystem Model
1621 (CTEM) modelling framework, 15, 6885–6907, <https://doi.org/10.5194/bg-15-6885-2018>, 2018.
- 1622 Aumont, O., Orr, J. C., Monfray, P., Ludwig, W., Amiotte-Suchet, P., and Probst, J.-L.: Riverine-driven
1623 interhemispheric transport of carbon, *Global Biogeochem. Cycles*, 15, 393–405,
1624 <https://doi.org/10.1029/1999GB001238>, 2001.
- 1625 Aumont, O., Ethé, C., Tagliabue, A., Bopp, L., and Gehlen, M.: PISCES-v2: an ocean biogeochemical model
1626 for carbon and ecosystem studies, 8, 2465–2513, <https://doi.org/10.5194/gmd-8-2465-2015>, 2015.
- 1627 Avitabile, V., Herold, M., Heuvelink, G. B. M., Lewis, S. L., Phillips, O. L., Asner, G. P., Armston, J., Ashton,



- 1628 P. S., Banin, L., Bayol, N., Berry, N. J., Boeckx, P., de Jong, B. H. J., DeVries, B., Girardin, C. A. J., Kearsley,
1629 E., Lindsell, J. A., Lopez-Gonzalez, G., Lucas, R., Malhi, Y., Morel, A., Mitchard, E. T. A., Nagy, L., Qie, L.,
1630 Quinones, M. J., Ryan, C. M., Ferry, S. J. W., Sunderland, T., Laurin, G. V., Gatti, R. C., Valentini, R.,
1631 Verbeeck, H., Wijaya, A., and Willcock, S.: An integrated pan-tropical biomass map using multiple reference
1632 datasets, *Glob Change Biol*, 22, 1406–1420, <https://doi.org/10.1111/gcb.13139>, 2016.
- 1633 Baccini, A., Walker, W., Carvalho, L., Farina, M., Sulla-Menashe, D., and Houghton, R. A.: Tropical forests are
1634 a net carbon source based on aboveground measurements of gain and loss, *Science*, 358, 230–234,
1635 <https://doi.org/10.1126/science.aam5962>, 2017.
- 1636 Bakker, D. C. E., Pfeil, B., Landa, C. S., Metzl, N., O'Brien, K. M., Olsen, A., Smith, K., Cosca, C., Harasawa,
1637 S., Jones, S. D., Nakaoka, S., Nojiri, Y., Schuster, U., Steinhoff, T., Sweeney, C., Takahashi, T., Tilbrook, B.,
1638 Wada, C., Wanninkhof, R., Alin, S. R., Balestrini, C. F., Barbero, L., Bates, N. R., Bianchi, A. A., Bonou, F.,
1639 Boutin, J., Bozec, Y., Burger, E. F., Cai, W.-J., Castle, R. D., Chen, L., Chierici, M., Currie, K., Evans, W.,
1640 Featherstone, C., Feely, R. A., Fransson, A., Goyet, C., Greenwood, N., Gregor, L., Hankin, S., Hardman-
1641 Mountford, N. J., Harlay, J., Hauck, J., Hoppema, M., Humphreys, M. P., Hunt, C. W., Huss, B., Ibáñez, J. S.
1642 P., Johannessen, T., Keeling, R., Kitidis, V., Körtzinger, A., Kozyr, A., Krasakopoulou, E., Kuwata, A.,
1643 Landschützer, P., Lauvset, S. K., Lefèvre, N., Lo Monaco, C., Manke, A., Mathis, J. T., Merlivat, L., Millero, F.
1644 J., Monteiro, P. M. S., Munro, D. R., Murata, A., Newberger, T., Omar, A. M., Ono, T., Paterson, K., Pearce,
1645 D., Pierrot, D., Robbins, L. L., Saito, S., Salisbury, J., Schlitzer, R., Schneider, B., Schweitzer, R., Sieger, R.,
1646 Skjelvan, I., Sullivan, K. F., Sutherland, S. C., Sutton, A. J., Tadokoro, K., Telszewski, M., Tuma, M., van
1647 Heuven, S. M. A. C., Vandemark, D., Ward, B., Watson, A. J., and Xu, S.: A multi-decade record of high-
1648 quality CO₂ data in version 3 of the Surface Ocean CO₂ Atlas (SOCAT), *Earth Syst. Sci. Data*, 8, 383–413,
1649 <https://doi.org/10.5194/essd-8-383-2016>, 2016.
- 1650 Bakker, Dorothee C. E.; Alin, Simone R.; Becker, Meike; Bittig, Henry C.; Castaño-Primo, Rocío; Feely,
1651 Richard A.; Gkritzalis, Thanos; Kadono, Koji; Kozyr, Alex; Lauvset, Siv K.; Metzl, Nicolas; Munro, David R.;
1652 Nakaoka, Shin-ichiro; Nojiri, Yukihiko; O'Brien, Kevin M.; Olsen, Are; Pfeil, Benjamin; Pierrot, Denis;
1653 Steinhoff, Tobias; Sullivan, Kevin F.; Sutton, Adrienne J.; Sweeney, Colm; Tilbrook, Bronte; Wada, Chisato;
1654 Wanninkhof, Rik; Willstrand Wranne, Anna; Akl, John; Apelthun, Lisa B.; Bates, Nicholas; Beatty, Cory M.;
1655 Burger, Eugene F.; Cai, Wei-Jun; Cosca, Catherine E.; Corredor, Jorge E.; Cronin, Margot; Cross, Jessica N.;
1656 De Carlo, Eric H.; DeGrandpre, Michael D.; Emerson, Steven; Enright, Matt P.; Enyo, Kazutaka; Evans, Wiley;
1657 Frangoulis, Constantin; Fransson, Agneta; García-Ibáñez, Maribel I.; Gehrung, Martina; Giannoudi, Louisa;
1658 Glockzin, Michael; Hales, Burke; Howden, Stephan D.; Hunt, Christopher W.; Ibáñez, J. Severino P.; Jones,
1659 Steve D.; Kamb, Linus; Körtzinger, Arne; Landa, Camilla S.; Landschützer, Peter; Lefèvre, Nathalie; Lo
1660 Monaco, Claire; Macovei, Vlad A.; Maenner Jones, Stacy; Meinig, Christian; Millero, Frank J.; Monacci,
1661 Natalie M.; Mordy, Calvin; Morell, Julio M.; Murata, Akihiko; Musielewicz, Sylvia; Neill, Craig; Newberger,
1662 Tim; Nomura, Daiki; Ohman, Mark; Ono, Tsuneo; Passmore, Abe; Petersen, Wilhelm; Petihakis, George;
1663 Perivoliotis, Leonidas; Plueddemann, Albert J.; Rehder, Gregor; Reynaud, Thierry; Rodriguez, Carmen; Ross,
1664 Andrew; Rutgersson, Anna; Sabine, Christopher L.; Salisbury, Joseph E.; Schlitzer, Reiner; Send, Uwe;
1665 Skjelvan, Ingunn; Stamatakis, Natalia; Sutherland, Stewart C.; Sweeney, Colm; Tadokoro, Kazuaki; Tanhua,
1666 Toste; Telszewski, Maciej; Trull, Tom; Vandemark, Douglas; van Ooijen, Erik; Voynova, Yoana G.; Wang,



- 1667 Hongjie; Weller, Robert A.; Whitehead, Chris; Wilson, Doug (2022). Surface Ocean CO2 Atlas Database
1668 Version 2022 (SOCATv2022) (NCEI Accession 0253659). NOAA National Centers for Environmental
1669 Information. <https://doi.org/10.25921/1h9f-nb73>.
- 1670 Ballantyne, A. P., Alden, C. B., Miller, J. B., Tans, P. P., and White, J. W. C.: Increase in observed net carbon
1671 dioxide uptake by land and oceans during the past 50 years, *Nature*, 488, 70–72,
1672 <https://doi.org/10.1038/nature11299>, 2012.
- 1673 Ballantyne, A. P., Andres, R., Houghton, R., Stocker, B. D., Wanninkhof, R., Anderegg, W., Cooper, L. A.,
1674 DeGrandpre, M., Tans, P. P., Miller, J. B., Alden, C., and White, J. W. C.: Audit of the global carbon budget:
1675 estimate errors and their impact on uptake uncertainty, *Biogeosciences*, 12, 2565–2584,
1676 <https://doi.org/10.5194/bg-12-2565-2015>, 2015.
- 1677 Bastos, A., O’Sullivan, M., Ciais, P., Makowski, D., Sitch, S., Friedlingstein, P., Chevallier, F., Rödenbeck, C.,
1678 Pongratz, J., Luijkx, I. T., Patra, P. K., Peylin, P., Canadell, J. G., Lauerwald, R., Li, W., Smith, N. E., Peters,
1679 W., Goll, D. S., Jain, A. K., Kato, E., Lienert, S., Lombardozzi, D. L., Haverd, V., Nabel, J. E. M. S., Poulter,
1680 B., Tian, H., Walker, A. P., and Zaehle, S.: Sources of Uncertainty in Regional and Global Terrestrial CO₂
1681 Exchange Estimates, *Global Biogeochem. Cycles*, 34, <https://doi.org/10.1029/2019GB006393>, 2020.
- 1682 Bastos, A., Hartung, K., Nützel, T. B., Nabel, J. E. M. S., Houghton, R. A., and Pongratz, J.: Comparison of
1683 uncertainties in land-use change fluxes from bookkeeping model parameterisation, 12, 745–762,
1684 <https://doi.org/10.5194/esd-12-745-2021>, 2021.
- 1685 Basu, S., Baker, D. F., Chevallier, F., Patra, P. K., Liu, J., and Miller, J. B.: The impact of transport model
1686 differences on CO₂ surface flux estimates from OCO-2 retrievals of column average CO₂, *Atmos. Chem. Phys.*,
1687 18, 7189–7215, <https://doi.org/10.5194/acp-18-7189-2018>, 2018.
- 1688 Bauer, J. E., Cai, W.-J., Raymond, P. A., Bianchi, T. S., Hopkinson, C. S., and Regnier, P. A. G.: The changing
1689 carbon cycle of the coastal ocean, *Nature*, 504, 61–70, <https://doi.org/10.1038/nature12857>, 2013.
- 1690 Beckman, J. and Countryman, A. M.: The Importance of Agriculture in the Economy: Impacts from COVID-19,
1691 103, 1595–1611, <https://doi.org/10.1111/ajae.12212>, 2021.
- 1692 Bellouin, N., Rae, J., Jones, A., Johnson, C., Haywood, J., and Boucher, O.: Aerosol forcing in the Climate
1693 Model Intercomparison Project (CMIP5) simulations by HadGEM2-ES and the role of ammonium nitrate, 116,
1694 <https://doi.org/10.1029/2011JD016074>, 2011.
- 1695 Bennington, V., Gloege, L., and McKinley, G. A.: Variability in the Global Ocean Carbon Sink From 1959 to
1696 2020 by Correcting Models with Observations, *Geophys. Res. Lett.*, 49, e2022GL098632,
1697 <https://doi.org/10.1029/2022GL098632>, 2022.
- 1698 Berthet, S., Séférian, R., Bricaud, C., Chevallier, M., Voltaire, A., and Ethé, C.: Evaluation of an Online Grid-
1699 Coarsening Algorithm in a Global Eddy-Admitting Ocean Biogeochemical Model, 11, 1759–1783,
1700 <https://doi.org/10.1029/2019MS001644>, 2019.



- 1701 Bourgeois, T., Goris, N., Schwinger, J., and Tjiputra, J. F.: Stratification constrains future heat and carbon
1702 uptake in the Southern Ocean between 30°S and 55°S. *Nat Commun* 13, 340, [https://doi.org/10.1038/s41467-](https://doi.org/10.1038/s41467-022-27979-5)
1703 [022-27979-5](https://doi.org/10.1038/s41467-022-27979-5), 2022.
- 1704 Brancalion, P. H. S., Broadbent, E. N., de-Miguel, S., Cardil, A., Rosa, M. R., Almeida, C. T., Almeida, D. R.
1705 A., Chakravarty, S., Zhou, M., Gamarra, J. G. P., Liang, J., Crouzeilles, R., Hérault, B., Aragão, L. E. O. C.,
1706 Silva, C. A., and Almeyda-Zambrano, A. M.: Emerging threats linking tropical deforestation and the COVID-19
1707 pandemic, *Perspectives in Ecology and Conservation*, 18, 243–246,
1708 <https://doi.org/10.1016/j.pecon.2020.09.006>, 2020.
- 1709 Brienen, R. J. W., Phillips, O. L., Feldpausch, T. R., Gloor, E., Baker, T. R., Lloyd, J., Lopez-Gonzalez, G.,
1710 Monteagudo-Mendoza, A., Malhi, Y., Lewis, S. L., Vásquez Martínez, R., Alexiades, M., Álvarez Dávila, E.,
1711 Alvarez-Loayza, P., Andrade, A., Aragão, L. E. O. C., Araujo-Murakami, A., Arets, E. J. M. M., Arroyo, L.,
1712 Aymard C., G. A., Bánki, O. S., Baraloto, C., Barroso, J., Bonal, D., Boot, R. G. A., Camargo, J. L. C., Castilho,
1713 C. V., Chama, V., Chao, K. J., Chave, J., Comiskey, J. A., Cornejo Valverde, F., da Costa, L., de Oliveira, E. A.,
1714 Di Fiore, A., Erwin, T. L., Fauset, S., Forsthofer, M., Galbraith, D. R., Grahame, E. S., Groot, N., Hérault, B.,
1715 Higuchi, N., Honorio Coronado, E. N., Keeling, H., Killeen, T. J., Laurance, W. F., Laurance, S., Licona, J.,
1716 Magnussen, W. E., Marimon, B. S., Marimon-Junior, B. H., Mendoza, C., Neill, D. A., Nogueira, E. M., Núñez,
1717 P., Pallqui Camacho, N. C., Parada, A., Pardo-Molina, G., Peacock, J., Peña-Claros, M., Pickavance, G. C.,
1718 Pitman, N. C. A., Poorter, L., Prieto, A., Quesada, C. A., Ramírez, F., Ramírez-Angulo, H., Restrepo, Z.,
1719 Roopsind, A., Rudas, A., Salomão, R. P., Schwarz, M., Silva, N., Silva-Espejo, J. E., Silveira, M., Stropp, J.,
1720 Talbot, J., ter Steege, H., Teran-Aguilar, J., Terborgh, J., Thomas-Caesar, R., Toledo, M., Torello-Raventos, M.,
1721 Umetsu, R. K., van der Heijden, G. M. F., van der Hout, P., Guimarães Vieira, I. C., Vieira, S. A., Vilanova, E.,
1722 Vos, V. A., and Zagt, R. J.: Long-term decline of the Amazon carbon sink, 519, 344–348,
1723 <https://doi.org/10.1038/nature14283>, 2015.
- 1724 Broecker, W. S.: Ocean chemistry during glacial time, *Geochimica et Cosmochimica Acta*, 46, 1689–1705,
1725 [https://doi.org/10.1016/0016-7037\(82\)90110-7](https://doi.org/10.1016/0016-7037(82)90110-7), 1982.
- 1726 Bruno, M. and Joos, F.: Terrestrial carbon storage during the past 200 years: A Monte Carlo Analysis of CO₂
1727 data from ice core and atmospheric measurements, *Global Biogeochem. Cycles*, 11, 111–124,
1728 <https://doi.org/10.1029/96GB03611>, 1997.
- 1729 Buitenhuis, E. T., Hashioka, T., and Quéré, C. L.: Combined constraints on global ocean primary production
1730 using observations and models: OCEAN PRIMARY PRODUCTION, *Global Biogeochem. Cycles*, 27, 847–
1731 858, <https://doi.org/10.1002/gbc.20074>, 2013.
- 1732 Burton, C., Betts, R., Cardoso, M., Feldpausch, T. R., Harper, A., Jones, C. D., Kelley, D. I., Robertson, E., and
1733 Wiltshire, A.: Representation of fire, land-use change and vegetation dynamics in the Joint UK Land
1734 Environment Simulator vn4.9 (JULES), *Geosci. Model Dev.*, 12, 179–193, [https://doi.org/10.5194/gmd-12-179-](https://doi.org/10.5194/gmd-12-179-2019)
1735 2019, 2019.
- 1736 Bushinsky, S. M., Landschützer, P., Rödenbeck, C., Gray, A. R., Baker, D., Mazloff, M. R., Resplandy, L.,



- 1737 Johnson, K. S., and Sarmiento, J. L.: Reassessing Southern Ocean Air-Sea CO₂ Flux Estimates With the
1738 Addition of Biogeochemical Float Observations, *Global Biogeochem. Cycles*, 33, 1370–1388,
1739 <https://doi.org/10.1029/2019GB006176>, 2019.
- 1740 Canadell, J. G., Le Quere, C., Raupach, M. R., Field, C. B., Buitenhuis, E. T., Ciais, P., Conway, T. J., Gillett,
1741 N. P., Houghton, R. A., and Marland, G.: Contributions to accelerating atmospheric CO₂ growth from economic
1742 activity, carbon intensity, and efficiency of natural sinks, *Proceedings of the National Academy of Sciences*,
1743 104, 18866–18870, <https://doi.org/10.1073/pnas.0702737104>, 2007.
- 1744 Canadell, J. G., Monteiro, P. M. S., Costa, M. H., Cotrim da Cunha, L., Cox, P. M., Eliseev, A. V., Henson, S.,
1745 Ishii, M., Jaccard, S., Koven, C., Lohila, A., Patra, P. K., Piao, S., Rogelj, J., Syampungani, S., Zaehle, S., and
1746 Zickfeld, K.: Global Carbon and other Biogeochemical Cycles and Feedbacks. In: *Climate Change 2021: The
1747 Physical Science Basis. Contribution of Working Group I to the Sixth Assessment Report of the
1748 Intergovernmental Panel on Climate Change* [Masson-Delmotte, V., P. Zhai, A. Pirani, S. L. Connors, C. Péan,
1749 S. Berger, N. Caud, Y. Chen, L. Goldfarb, M. I. Gomis, M. Huang, K. Leitzell, E. Lonnoy, J.B.R. Matthews, T.
1750 K. Maycock, T. Waterfield, O. Yelekçi, R. Yu and B. Zhou (eds.)]. Cambridge University Press, 2021.
- 1751 Cao, Z., Myers, R. J., Lupton, R. C., Duan, H., Sacchi, R., Zhou, N., Reed Miller, T., Cullen, J. M., Ge, Q., and
1752 Liu, G.: The sponge effect and carbon emission mitigation potentials of the global cement cycle, *Nat Commun*,
1753 11, 3777, <https://doi.org/10.1038/s41467-020-17583-w>, 2020.
- 1754 Carbon Monitor: CO₂ Emissions Variation, available at: <https://carbonmonitor.org/>, last access: 25 September
1755 2022., 2022.
- 1756 Chatfield, C.: The Holt-Winters Forecasting Procedure, 27, 264–279, <https://doi.org/10.2307/2347162>, 1978.
- 1757 Chau, T. T. T., Gehlen, M., and Chevallier, F.: QUALITY INFORMATION DOCUMENT for Global Ocean
1758 Surface Carbon Product MULTIOBS_GLO_BIO CARBON_SURFACE_REP_015_008, Le Laboratoire des
1759 Sciences du Climat et de l'Environnement, 2020.
- 1760 Chau, T. T. T., Gehlen, M., and Chevallier, F.: A seamless ensemble-based reconstruction of surface ocean
1761 *p*CO₂ and air–sea CO₂ fluxes over the global coastal and open oceans, *Biogeosciences*, 19, 1087–1109,
1762 <https://doi.org/10.5194/bg-19-1087-2022>, 2022.
- 1763 Chevallier, F.: On the parallelization of atmospheric inversions of CO₂ surface fluxes within a variational
1764 framework, 6, 783–790, <https://doi.org/10.5194/gmd-6-783-2013>, 2013.
- 1765 Chevallier, F., Fisher, M., Peylin, P., Serrar, S., Bousquet, P., Bréon, F.-M., Chédin, A., and Ciais, P.: Inferring
1766 CO₂ sources and sinks from satellite observations: Method and application to TOVS data, *J. Geophys. Res.*,
1767 110, D24309, <https://doi.org/10.1029/2005JD006390>, 2005.
- 1768 Chevallier, F., Remaud, M., O'Dell, C. W., Baker, D., Peylin, P., and Cozic, A.: Objective evaluation of
1769 surface- and satellite-driven carbon dioxide atmospheric inversions, *Atmos. Chem. Phys.*, 19, 14233–14251,
1770 <https://doi.org/10.5194/acp-19-14233-2019>, 2019.



- 1771 Chini, L., Hurtt, G., Sahajpal, R., Frolking, S., Klein Goldewijk, K., Sitch, S., Ganzenmüller, R., Ma, L., Ott, L.,
1772 Pongratz, J., and Poulter, B.: Land-use harmonization datasets for annual global carbon budgets, 13, 4175–4189,
1773 <https://doi.org/10.5194/essd-13-4175-2021>, 2021.
- 1774 Ciais, P., Sabine, C., Bala, G., Bopp, L., Brovkin, V., Canadell, J. G., Chhabra, A., DeFries, R., Galloway, J.,
1775 Heimann, M., Jones, C., Le Quéré, C., Myneni, R., Piao, S., Thornton, P., Willem, J., Friedlingstein, P., and
1776 Munhoven, G.: Carbon and Other Biogeochemical Cycles, in *Climate Change 2013: The Physical Science*
1777 *Basis, Contribution of Working Group I to the Fifth Assessment Report of the Intergovernmental Panel on*
1778 *Climate Change*, edited by: Intergovernmental Panel on Climate Change, Cambridge University Press,
1779 Cambridge, UK, 465–570, 2013.
- 1780 Ciais, P., Tan, J., Wang, X., Roedenbeck, C., Chevallier, F., Piao, S.-L., Moriarty, R., Broquet, G., Le Quéré, C.,
1781 Canadell, J. G., Peng, S., Poulter, B., Liu, Z., and Tans, P.: Five decades of northern land carbon uptake
1782 revealed by the interhemispheric CO₂ gradient, *Nature*, 568, 221–225, [https://doi.org/10.1038/s41586-019-](https://doi.org/10.1038/s41586-019-1078-6)
1783 1078-6, 2019.
- 1784 Ciais, P., Bastos, A., Chevallier, F., Lauerwald, R., Poulter, B., Canadell, P., Hugelius, G., Jackson, R. B., Jain,
1785 A., Jones, M., Kondo, M., Lujikx, I., Patra, P. K., Peters, W., Pongratz, J., Petrescu, A. M. R., Piao, S., Qiu, C.,
1786 Von Randow, C., Regnier, P., Saunois, M., Scholes, R., Shvidenko, A., Tian, H., Yang, H., Wang, X., and
1787 Zheng, B.: Definitions and methods to estimate regional land carbon fluxes for the second phase of the REgional
1788 Carbon Cycle Assessment and Processes Project (RECCAP-2), 1–46, <https://doi.org/10.5194/gmd-2020-259>,
1789 2020.
- 1790 Collier, N., Hoffman, F. M., Lawrence, D. M., Keppel-Aleks, G., Koven, C. D., Riley, W. J., Mu, M., and
1791 Randerson, J. T.: The International Land Model Benchmarking (ILAMB) System: Design, Theory, and
1792 Implementation, *J. Adv. Model. Earth Syst.*, 10, 2731–2754, <https://doi.org/10.1029/2018MS001354>, 2018.
- 1793 Conchedda, G. and Tubiello, F. N.: Drainage of organic soils and GHG emissions: Validation with country data,
1794 *Biosphere – Biogeosciences*, <https://doi.org/10.5194/essd-2020-202>, 2020.
- 1795 Cooper, D. J., Watson, A. J., and Ling, R. D.: Variation of pCO₂ along a North Atlantic shipping route (U.K. to
1796 the Caribbean): A year of automated observations, *Marine Chemistry*, 60, 147–164,
1797 [https://doi.org/10.1016/S0304-4203\(97\)00082-0](https://doi.org/10.1016/S0304-4203(97)00082-0), 1998.
- 1798 Cox, A., Vermeulen, A., Manning, A., Beyersdorf, A., Zahn, A., Manning, A., Watson, A., Karion, A., Hensen,
1799 A., Arlyn Andrews, Frumau, A., Colomb, A., Scheeren, B., Law, B., Baier, B., Munger, B., Paplawsky, B.,
1800 Viner, B., Stephens, B., Daube, B., Labuschagne, C., Myhre, C. L., Hanson, C., Miller, C. E., Plass-Duelmer,
1801 C., Plass-Duelmer, C., Gerbig, C., Sloop, C. D., Sweeney, C., Kubistin, D., Goto, D., Jaffe, D., Say, D., Van
1802 Dinter, D., Bowling, D., Lam, D. H. Y., Dickon Young, Worthly, D., Dlugokencky, E., Kozlova, E., Gloor, E.,
1803 Cuevas, E., Reyes-Sanchez, E., Hintsa, E., Kort, E., Morgan, E., Obersteiner, F., Apadula, F., Francois Gheusi,
1804 Meinhardt, F., Moore, F., Vitkova, G., Chen, G., Bentz, G., Manca, G., Brailsford, G., Forster, G., Boenisch, H.,
1805 Riris, H., Meijer, H., Timas, H., Matsueda, H., Huilin Chen, Levin, I., Lehner, I., Mammarella, I., Bartyzel, J.,
1806 Abshire, J. B., Elkins, J. W., Levula, J., Jaroslaw Necki, Pichon, J. M., Peischl, J., Müller-Williams, J., Turnbull,



- 1807 J., Miller, J. B., Lee, J., Lin, J., Josep-Anton Morgui, DiGangi, J. P., Hatakka, J., Coletta, J. D., Worsley, J.,
1808 Holst, J., Kominkova, K., McKain, K., Saito, K., Aikin, K., Davis, K., Thoning, K., Tørseth, K., Haszpra, L.,
1809 Mitchell, L., Gatti, L. V., Emmenegger, L., Lukasz Chmura, Merchant, L., Sha, M. K., Delmotte, M., et al.:
1810 Multi-laboratory compilation of atmospheric carbon dioxide data for the period 1957-2019;
1811 obspack_co2_1_GLOBALVIEWplus_v6.1_2021-03-01, <https://doi.org/10.25925/20201204>, 2021.
- 1812 Cox, P. M., Pearson, D., Booth, B. B., Friedlingstein, P., Huntingford, C., Jones, C. D., and Luke, C. M.:
1813 Sensitivity of tropical carbon to climate change constrained by carbon dioxide variability, *Nature*, 494, 341–344,
1814 <https://doi.org/10.1038/nature11882>, 2013.
- 1815 Crippa, M., Janssens-Maenhout, G., Guizzardi, D., Van Dingenen, R., and Dentener, F.: Contribution and
1816 uncertainty of sectorial and regional emissions to regional and global PM_{2.5} health impacts, 19, 5165–5186,
1817 <https://doi.org/10.5194/acp-19-5165-2019>, 2019.
- 1818 Dai, A. and Trenberth, K. E.: Estimates of Freshwater Discharge from Continents: Latitudinal and Seasonal
1819 Variations, 3, 660–687, [https://doi.org/10.1175/1525-7541\(2002\)003<0660:EOFDfC>2.0.CO;2](https://doi.org/10.1175/1525-7541(2002)003<0660:EOFDfC>2.0.CO;2), 2002.
- 1820 Davis, S. J. and Caldeira, K.: Consumption-based accounting of CO₂ emissions, *Proceedings of the National*
1821 *Academy of Sciences*, 107, 5687–5692, <https://doi.org/10.1073/pnas.0906974107>, 2010.
- 1822 De Kauwe, M. G., Disney, M. I., Quaife, T., Lewis, P., and Williams, M.: An assessment of the MODIS
1823 collection 5 leaf area index product for a region of mixed coniferous forest, *Remote Sensing of Environment*,
1824 115, 767–780, <https://doi.org/10.1016/j.rse.2010.11.004>, 2011.
- 1825 De Kauwe, M. G., Medlyn, B. E., Zaehle, S., Walker, A. P., Dietze, M. C., Wang, Y.-P., Luo, Y., Jain, A. K.,
1826 El-Masri, B., Hickler, T., Wårlind, D., Weng, E., Parton, W. J., Thornton, P. E., Wang, S., Prentice, I. C., Asao,
1827 S., Smith, B., McCarthy, H. R., Iversen, C. M., Hanson, P. J., Warren, J. M., Oren, R., and Norby, R. J.: Where
1828 does the carbon go? A model–data intercomparison of vegetation carbon allocation and turnover processes at
1829 two temperate forest free-air CO₂ enrichment sites, *New Phytol.*, 203, 883–899,
1830 <https://doi.org/10.1111/nph.12847>, 2014.
- 1831 Decharme, B., Delire, C., Minvielle, M., Colin, J., Vergnes, J.-P., Alias, A., Saint-Martin, D., Séférian, R.,
1832 Sénési, S., and Voldoire, A.: Recent Changes in the ISBA-CTRIP Land Surface System for Use in the CNRM-
1833 CM6 Climate Model and in Global Off-Line Hydrological Applications, 11, 1207–1252,
1834 <https://doi.org/10.1029/2018MS001545>, 2019.
- 1835 Delire, C., Séférian, R., Decharme, B., Alkama, R., Calvet, J.-C., Carrer, D., Gibelin, A.-L., Joetzer, E., Morel,
1836 X., Rocher, M., and Tzanos, D.: The Global Land Carbon Cycle Simulated With ISBA-CTRIP: Improvements
1837 Over the Last Decade, 12, e2019MS001886, <https://doi.org/10.1029/2019MS001886>, 2020.
- 1838 Denman, K. L., Brasseur, G., Chidthaisong, A., Ciais, P., Cox, P. M., Dickinson, R. E., Hauglustaine, D.,
1839 Heinze, C., Holland, E., Jacob, D., Lohmann, U., Ramachandran, S., Leite da Silva Dias, P., Wofsy, S. C., and
1840 Zhang, X.: Couplings Between Changes in the Climate System and Biogeochemistry, in: *Climate Change 2007:*
1841 *The Physical Science Basis. Contribution of Working Group I to the Fourth Assessment Report of the*



- 1842 Intergovernmental Panel on Climate Change, edited by: Solomon, S., Qin, D., Manning, M., Marquis, M.,
1843 Averyt, K., Tignor, M. M. B., Miller, H. L., and Chen, Z. L., Cambridge University Press, Cambridge, UK and
1844 New York, USA, 499–587, 2007.
- 1845 Denning, A. S., Fung, I. Y., and Randall, D.: Latitudinal gradient of atmospheric CO₂ due to seasonal exchange
1846 with land biota, *Nature*, 376, 240–243, <https://doi.org/10.1038/376240a0>, 1995.
- 1847 Denvil-Sommer, A., Gehlen, M., Vrac, M., and Mejia, C.: LSCE-FFNN-v1: a two-step neural network model
1848 for the reconstruction of surface ocean pCO₂ over the global ocean, 12, 2091–2105,
1849 <https://doi.org/10.5194/gmd-12-2091-2019>, 2019.
- 1850 DeVries, T.: The oceanic anthropogenic CO₂ sink: Storage, air-sea fluxes, and transports over the industrial
1851 era, *Global Biogeochem. Cycles*, 28, 631–647, <https://doi.org/10.1002/2013GB004739>, 2014.
- 1852 DeVries, T., Holzer, M., and Primeau, F.: Recent increase in oceanic carbon uptake driven by weaker upper-
1853 ocean overturning, *Nature*, 542, 215–218, <https://doi.org/10.1038/nature21068>, 2017.
- 1854 DeVries, T., Quéré, C. L., Andrews, O., Berthet, S., Hauck, J., Ilyina, T., Landschützer, P., Lenton, A., Lima, I.
1855 D., Nowicki, M., Schwinger, J., and Séférian, R.: Decadal trends in the ocean carbon sink, *PNAS*, 116, 11646–
1856 11651, <https://doi.org/10.1073/pnas.1900371116>, 2019.
- 1857 Di Sarra, A. G., Karion, A., Arlyn Andrews, Colomb, A., Scheeren, B., Viner, B., Myhre, C. L., Miller, C. E.,
1858 Plass-Duelmer, C., Plass-Duelmer, C., Sloop, C. D., Sweeney, C., Kubistin, D., Jaffe, D., Dlugokencky, E.,
1859 Vitkova, G., Manca, G., Huilin Chen, Lehner, I., Mammarella, I., Pichon, J. M., Müller-Williams, J., Miller, J.
1860 B., Lee, J., Hatakka, J., Holst, J., Kominkova, K., McKain, K., Thoning, K., Tørseth, K., Emmenegger, L., Sha,
1861 M. K., Delmotte, M., Fischer, M. L., Schumacher, M., Leuenberger, M., Steinbacher, M., De Mazière, M.,
1862 Lindauer, M., Mölder, M., Heliasz, M., Marek, M. V., Ramonet, M., Lopez, M., Laurent, O., Hermanssen, O.,
1863 Trisolino, P., Cristofanelli, P., Smith, P., Bakwin, P., Bergamaschi, P., Keronen, P., Tans, P., Piacentino, S.,
1864 Biraud, S. C., Conil, S., De Wekker, S., Biermann, T., Laurila, T., Aalto, T., and Kazan, V.: Multi-laboratory
1865 compilation of atmospheric carbon dioxide data for the years 2020–2021; obspack_co2_1_NRT_v6.1.1_2021-
1866 05-17, <https://doi.org/10.25925/20210517>, 2021.
- 1867 Dickson, A. G., Sabine, C. L., and Christian, J. R.: Guide to best practices for ocean CO₂ measurement. Sidney,
1868 British Columbia, North Pacific Marine Science Organization, 191pp. (PICES Special Publication 3; IOCCP
1869 Report 8). DOI: <https://doi.org/10.25607/OBP-1342>, 2007.
- 1870 Dlugokencky, E. and Tans, P.: Trends in atmospheric carbon dioxide, National Oceanic and Atmospheric
1871 Administration, Earth System Research Laboratory (NOAA/ESRL), available at:
1872 <http://www.esrl.noaa.gov/gmd/ccgg/trends/global.html>, accessed: 16 November 2020., 2020.
- 1873 Dlugokencky, E. and Tans, P.: Trends in atmospheric carbon dioxide, National Oceanic and Atmospheric
1874 Administration, Earth System Research Laboratory (NOAA/ESRL), available at:
1875 <http://www.esrl.noaa.gov/gmd/ccgg/trends/global.html>, last access: 25 September 2022., 2022.



- 1876 Doney, S. C., Lima, I., Feely, R. A., Glover, D. M., Lindsay, K., Mahowald, N., Moore, J. K., and Wanninkhof,
1877 R.: Mechanisms governing interannual variability in upper-ocean inorganic carbon system and air–sea CO₂
1878 fluxes: Physical climate and atmospheric dust, *Deep Sea Research Part II: Topical Studies in Oceanography*, 56,
1879 640–655, <https://doi.org/10.1016/j.dsr2.2008.12.006>, 2009.
- 1880 Dong, Y., Bakker, D. C. E., Bell, T. G., Huang, B., Landschützer, P., Liss, P. S., and Yang, M.: Update on the
1881 Temperature Corrections of Global Air-Sea CO₂ Flux Estimates, *Glob. Biogeochem. Cycles*, 36,
1882 e2022GB007360, <https://doi.org/10.1029/2022GB007360>, 2022.
- 1883 Dou, X., Wang, Y., Ciais, P., Chevallier, F., Davis, S. J., Crippa, M., Janssens-Maenhout, G., Guizzardi, D.,
1884 Solazzo, E., Yan, F., Huo, D., Zheng, B., Zhu, B., Cui, D., Ke, P., Sun, T., Wang, H., Zhang, Q., Gentine, P.,
1885 Deng, Z., and Liu, Z.: Near-real-time global gridded daily CO₂ emissions, *The Innovation*, 3, 100182,
1886 <https://doi.org/10.1016/j.xinn.2021.100182>, 2022.
- 1887 Duce, R. A., LaRoche, J., Altieri, K., Arrigo, K. R., Baker, A. R., Capone, D. G., Cornell, S., Dentener, F.,
1888 Galloway, J., Ganeshram, R. S., Geider, R. J., Jickells, T., Kuypers, M. M., Langlois, R., Liss, P. S., Liu, S. M.,
1889 Middelburg, J. J., Moore, C. M., Nickovic, S., Oschlies, A., Pedersen, T., Prospero, J., Schlitzer, R., Seitzinger,
1890 S., Sorensen, L. L., Uematsu, M., Ulloa, O., Voss, M., Ward, B., and Zamora, L.: Impacts of Atmospheric
1891 Anthropogenic Nitrogen on the Open Ocean, *Science*, 320, 893–897, <https://doi.org/10.1126/science.1150369>,
1892 2008.
- 1893 Dufour, C. O., Sommer, J. L., Gehlen, M., Orr, J. C., Molines, J., Simeon, J., and Barnier, B.: Eddy
1894 compensation and controls of the enhanced sea-to-air CO₂ flux during positive phases of the Southern Annular
1895 Mode, *Global Biogeochem. Cycles*, 27, 950–961, <https://doi.org/10.1002/gbc.20090>, 2013.
- 1896 Eakins, B. W. and Sharman, G. F.: National Geophysical Data Center: Volumes of the World’s Oceans from
1897 ETOPO1, available at: https://www.ngdc.noaa.gov/mgg/global/etopo1_ocean_volumes.html, last access: 25
1898 September 2022, U.S. Department of Commerce, 2010.
- 1899 Eggleston, H. S., Buendia, L., Miwa, K., Ngara, T., and Tanabe, K.: Volume 4: Agriculture, forestry and land
1900 use. in: 2006 IPCC guidelines for national greenhouse gas inventories., 2006.
- 1901 EIA: U.S. Energy Information Administration: Short-Term Energy Outlook, available at:
1902 <http://www.eia.gov/forecasts/steo/outlook>, last access: 25 September 2022., 2022.
- 1903 Erb, K.-H., Kastner, T., Luyssaert, S., Houghton, R. A., Kuemmerle, T., Olofsson, P., and Haberl, H.: Bias in
1904 the attribution of forest carbon sinks, *Nature Clim Change*, 3, 854–856, <https://doi.org/10.1038/nclimate2004>,
1905 2013.
- 1906 Erb, K.-H., Kastner, T., Plutzer, C., Bais, A. L. S., Carvalhais, N., Fetzel, T., Gingrich, S., Haberl, H., Lauk, C.,
1907 Niedertscheider, M., Pongratz, J., Thurner, M., and Luyssaert, S.: Unexpectedly large impact of forest
1908 management and grazing on global vegetation biomass, *Nature*, 553, 73–76,
1909 <https://doi.org/10.1038/nature25138>, 2018.
- 1910 Eskander, S. M. S. U. and Fankhauser, S.: Reduction in greenhouse gas emissions from national climate



- 1911 legislation, *Nat. Clim. Chang.*, 10, 750–756, <https://doi.org/10.1038/s41558-020-0831-z>, 2020.
- 1912 Etheridge, D. M., Steele, L. P., Langenfelds, R. L., Francey, R. J., Barnola, J.-M., and Morgan, V. I.: Natural
1913 and anthropogenic changes in atmospheric CO₂ over the last 1000 years from air in Antarctic ice and firn, *J.*
1914 *Geophys. Res.*, 101, 4115–4128, <https://doi.org/10.1029/95JD03410>, 1996.
- 1915 Eyring, V., Bony, S., Meehl, G. A., Senior, C. A., Stevens, B., Stouffer, R. J., and Taylor, K. E.: Overview of
1916 the Coupled Model Intercomparison Project Phase 6 (CMIP6) experimental design and organization, *Geosci.*
1917 *Model Dev.*, 9, 1937–1958, <https://doi.org/10.5194/gmd-9-1937-2016>, 2016.
- 1918 FAO: Global Forest Resources Assessment 2020: Main report, FAO, Rome, Italy, 184 pp.,
1919 <https://doi.org/10.4060/ca9825en>, 2020.
- 1920 FAO: FAOSTAT Statistical Database, domains Climate Change, available at:
1921 <http://www.fao.org/faostat/en/#data/GT>, last access: 25 September 2022, 2021.
- 1922 FAOSTAT: FAOSTAT: Food and Agriculture Organization Statistics Division, available at:
1923 <http://faostat.fao.org/>, last access: 25 September 2022), 2021.
- 1924 FAO/UNEP: Food and Agriculture Organisation / United Nations Environment Programme: The state of food
1925 and agriculture 1981, available at: <https://www.fao.org/3/ap661e/ap661e.pdf>, last access: 25 September 2022,
1926 1981.
- 1927 Fan, L., Wigneron, J.-P., Ciaï, P., Chave, J., Brandt, M., Fensholt, R., Saatchi, S. S., Bastos, A., Al-Yaari, A.,
1928 Hufkens, K., Qin, Y., Xiao, X., Chen, C., Myneni, R. B., Fernandez-Moran, R., Mialon, A., Rodriguez-
1929 Fernandez, N. J., Kerr, Y., Tian, F., and Peñuelas, J.: Satellite-observed pantropical carbon dynamics, *Nat.*
1930 *Plants*, 5, 944–951, <https://doi.org/10.1038/s41477-019-0478-9>, 2019.
- 1931 Fay, A. R. and McKinley, G. A.: Global open-ocean biomes: mean and temporal variability, 6, 273–284,
1932 <https://doi.org/10.5194/essd-6-273-2014>, 2014.
- 1933 Fay, A. R., Gregor, L., Landschützer, P., McKinley, G. A., Gruber, N., Gehlen, M., Iida, Y., Laruelle, G. G.,
1934 Rödenbeck, C., and Zeng, J.: Harmonization of global surface ocean pCO₂ mapped products and their flux
1935 calculations; an improved estimate of the ocean carbon sink, 1–32, <https://doi.org/10.5194/essd-2021-16>, 2021a.
- 1936 Fay, A. R., Gregor, L., Landschützer, P., McKinley, G. A., Gruber, N., Gehlen, M., Iida, Y., Laruelle, G. G.,
1937 Rödenbeck, C., Roobaert, A., and Zeng, J.: SeaFlux: harmonization of air–sea CO₂ fluxes from surface pCO₂
1938 data products using a standardized approach, 13, 4693–4710, <https://doi.org/10.5194/essd-13-4693-2021>, 2021b.
- 1939 Feng, L., Palmer, P. I., Bosch, H., and Dance, S.: Estimating surface CO₂ fluxes from space-borne CO₂ dry air
1940 mole fraction observations using an ensemble Kalman Filter, 15, 2009.
- 1941 Feng, L., Palmer, P. I., Parker, R. J., Deutscher, N. M., Feist, D. G., Kivi, R., Morino, I., and Sussmann, R.:
1942 Estimates of European uptake of CO₂ inferred from GOSAT XCO₂ retrievals: sensitivity to measurement bias
1943 inside and outside Europe, *Atmos. Chem. Phys.*, 16, 1289–1302, <https://doi.org/10.5194/acp-16-1289-2016>,



- 1944 2016.
- 1945 Feng, Y., Zeng, Z., Searchinger, T. D., Ziegler, A. D., Wu, J., Wang, D., He, X., Elsen, P. R., Ciais, P., Xu, R.,
1946 Guo, Z., Peng, L., Tao, Y., Spracklen, D. V., Holden, J., Liu, X., Zheng, Y., Xu, P., Chen, J., Jiang, X., Song,
1947 X.-P., Lakshmi, V., Wood, E. F., and Zheng, C.: Doubling of annual forest carbon loss over the tropics during
1948 the early twenty-first century, *Nat. Sustain.*, 1–8, <https://doi.org/10.1038/s41893-022-00854-3>, 2022.
- 1949 Friedlingstein, P., Houghton, R. A., Marland, G., Hackler, J., Boden, T. A., Conway, T. J., Canadell, J. G.,
1950 Raupach, M. R., Ciais, P., and Le Quéré, C.: Update on CO₂ emissions, *Nature Geosci*, 3, 811–812,
1951 <https://doi.org/10.1038/ngeo1022>, 2010.
- 1952 Friedlingstein, P., Andrew, R. M., Rogelj, J., Peters, G. P., Canadell, J. G., Knutti, R., Luderer, G., Raupach, M.
1953 R., Schaeffer, M., van Vuuren, D. P., and Le Quéré, C.: Persistent growth of CO₂ emissions and implications
1954 for reaching climate targets, *Nature Geosci*, 7, 709–715, <https://doi.org/10.1038/ngeo2248>, 2014.
- 1955 Friedlingstein, P., Jones, M. W., O’Sullivan, M., Andrew, R. M., Hauck, J., Peters, G. P., Peters, W., Pongratz,
1956 J., Sitch, S., Le Quéré, C., Bakker, D. C. E., Canadell, J. G., Ciais, P., Jackson, R. B., Anthoni, P., Barbero, L.,
1957 Bastos, A., Bastrikov, V., Becker, M., Bopp, L., Buitenhuis, E., Chandra, N., Chevallier, F., Chini, L. P., Currie,
1958 K. I., Feely, R. A., Gehlen, M., Gilfillan, D., Gkritzalis, T., Goll, D. S., Gruber, N., Gutekunst, S., Harris, I.,
1959 Haverd, V., Houghton, R. A., Hurtt, G., Ilyina, T., Jain, A. K., Joetzjer, E., Kaplan, J. O., Kato, E., Klein
1960 Goldewijk, K., Korsbakken, J. I., Landschützer, P., Lauvset, S. K., Lefèvre, N., Lenton, A., Lienert, S.,
1961 Lombardozi, D., Marland, G., McGuire, P. C., Melton, J. R., Metzl, N., Munro, D. R., Nabel, J. E. M. S.,
1962 Nakaoka, S.-I., Neill, C., Omar, A. M., Ono, T., Peregón, A., Pierrot, D., Poulter, B., Rehder, G., Resplandy, L.,
1963 Robertson, E., Rödenbeck, C., Séférian, R., Schwinger, J., Smith, N., Tans, P. P., Tian, H., Tilbrook, B.,
1964 Tubiello, F. N., van der Werf, G. R., Wiltshire, A. J., and Zaehle, S.: Global Carbon Budget 2019, *Earth Syst.*
1965 *Sci. Data*, 11, 1783–1838, <https://doi.org/10.5194/essd-11-1783-2019>, 2019.
- 1966 Friedlingstein, P., O’Sullivan, M., Jones, M. W., Andrew, R. M., Hauck, J., Olsen, A., Peters, G. P., Peters, W.,
1967 Pongratz, J., Sitch, S., Le Quéré, C., Canadell, J. G., Ciais, P., Jackson, R. B., Alin, S., Aragão, L. E. O. C.,
1968 Arneeth, A., Arora, V., Bates, N. R., Becker, M., Benoit-Cattin, A., Bittig, H. C., Bopp, L., Bultan, S., Chandra,
1969 N., Chevallier, F., Chini, L. P., Evans, W., Florentie, L., Forster, P. M., Gasser, T., Gehlen, M., Gilfillan, D.,
1970 Gkritzalis, T., Gregor, L., Gruber, N., Harris, I., Hartung, K., Haverd, V., Houghton, R. A., Ilyina, T., Jain, A.
1971 K., Joetzjer, E., Kadono, K., Kato, E., Kitidis, V., Korsbakken, J. I., Landschützer, P., Lefèvre, N., Lenton, A.,
1972 Lienert, S., Liu, Z., Lombardozi, D., Marland, G., Metzl, N., Munro, D. R., Nabel, J. E. M. S., Nakaoka, S.-I.,
1973 Niwa, Y., O’Brien, K., Ono, T., Palmer, P. I., Pierrot, D., Poulter, B., Resplandy, L., Robertson, E., Rödenbeck,
1974 C., Schwinger, J., Séférian, R., Skjelvan, I., Smith, A. J. P., Sutton, A. J., Tanhua, T., Tans, P. P., Tian, H.,
1975 Tilbrook, B., van der Werf, G., Vuichard, N., Walker, A. P., Wanninkhof, R., Watson, A. J., Willis, D.,
1976 Wiltshire, A. J., Yuan, W., Yue, X., and Zaehle, S.: Global Carbon Budget 2020, *Earth Syst. Sci. Data*, 12,
1977 3269–3340, <https://doi.org/10.5194/essd-12-3269-2020>, 2020.
- 1978 Friedlingstein, P., Jones, M. W., O’Sullivan, M., Andrew, R. M., Bakker, D. C. E., Hauck, J., Le Quéré, C.,
1979 Peters, G. P., Peters, W., Pongratz, J., Sitch, S., Canadell, J. G., Ciais, P., Jackson, R. B., Alin, S. R., Anthoni,
1980 P., Bates, N. R., Becker, M., Bellouin, N., Bopp, L., Chau, T. T. T., Chevallier, F., Chini, L. P., Cronin, M.,



- 1981 Currie, K. I., Decharme, B., Djeutchouang, L. M., Dou, X., Evans, W., Feely, R. A., Feng, L., Gasser, T.,
1982 Gilfillan, D., Gkritzalis, T., Grassi, G., Gregor, L., Gruber, N., Gürses, Ö., Harris, I., Houghton, R. A., Hurtt, G.
1983 C., Iida, Y., Ilyina, T., Luijckx, I. T., Jain, A., Jones, S. D., Kato, E., Kennedy, D., Klein Goldewijk, K., Knauer,
1984 J., Korsbakken, J. I., Körtzinger, A., Landschützer, P., Lauvset, S. K., Lefèvre, N., Lienert, S., Liu, J., Marland,
1985 G., McGuire, P. C., Melton, J. R., Munro, D. R., Nabel, J. E. M. S., Nakaoka, S.-I., Niwa, Y., Ono, T., Pierrot,
1986 D., Poulter, B., Rehder, G., Resplandy, L., Robertson, E., Rödenbeck, C., Rosan, T. M., Schwinger, J.,
1987 Schwingshackl, C., Séférian, R., Sutton, A. J., Sweeney, C., Tanhua, T., Tans, P. P., Tian, H., Tilbrook, B.,
1988 Tubiello, F., van der Werf, G. R., Vuichard, N., Wada, C., Wanninkhof, R., Watson, A. J., Willis, D., Wiltshire,
1989 A. J., Yuan, W., Yue, C., Yue, X., Zaehle, S., and Zeng, J.: Global Carbon Budget 2021, *Earth Syst. Sci. Data*,
1990 14, 1917–2005, <https://doi.org/10.5194/essd-14-1917-2022>, 2022a.
- 1991 Friedlingstein, P., O’Sullivan, M., Jones, M. W., Andrew, R. M., Gregor, L., Hauck, L., Le Quéré, C., Luijckx, I.
1992 T., Olsen, A., Peters, G. P., Peters, W., Pongratz, J., Schwingshackl, C., Sitch, S., Canadell, J. G., Ciais, P.,
1993 Jackson, R. B., Alin, S., Alkama, R., Arneeth, A., Arora, V. K., Bates, N. R., Becker, M., Bellouin, N., Bittig, H.
1994 C., Bopp, L., Chevallier, F., Chini, L. P., Cronin, M., Evans, W., Falk, S., Feely, R. A., Gasser, T., Gehlen, M.,
1995 Gkritzalis, T., Gloege, L., Grassi, G., Gruber, N., Gürses, Ö., Harris, I., Hefner, M., Houghton, R. A., Hurtt, G.
1996 C., Iida, Y., Ilyina, T., Jain, A. T., Jersild, A., Kadono, K., Kato, E., Kennedy, D., Klein Goldewijk, K., Knauer,
1997 J., Korsbakken, J. I., Landschützer, P., Lefèvre, N., Lindsay, Keith., Liu, J., Marland, G., Mayot, N., McGrath,
1998 M. J., Metzl, N., Monacci, N. M., Munro, D. R., Nakaoka, S.-I., Niwa, Y., O’Brien, K., Ono, T., Palmer, P. I.,
1999 Pan, N., Pierrot, D., Pockock, K., Poulter, B., Resplandy, L., Robertson, E., Rödenbeck, C., Rodriguez, C.,
2000 Rosan, T. M., Schwinger, J., Séférian, R., Shutler, J. D., Skjelvan, I., Steinhoff, T., Sun, Q., Sutton, A. J.,
2001 Sweeney, C., Takao, S., Tanhua, T., Tans, P. P., Tian, X., Tian, H., Tilbrook, B., Tsujino, H., Tubiello, F., van
2002 der Werf, G. R., Walker, A. P., Wanninkhof, R., Whitehead, C., Wranne, A., Wright, R. M., Yuan, W., Yue, C.,
2003 Yue, X., Zaehle, S., Zeng, J., Zheng, B. and Zhu, L.: Supplemental data of the Global Carbon Budget 2022,
2004 ICOS-ERIC Carbon Portal, <https://doi.org/10.18160/GCP-2022>, 2022b.
- 2005 Ganzenmüller, R., Bultan, S., Winkler, K., Fuchs, R., Zabel, F., and Pongratz, J.: Land-use change emissions
2006 based on high-resolution activity data substantially lower than previously estimated, *Environ. Res. Lett.*, 17,
2007 064050, <https://doi.org/10.1088/1748-9326/ac70d8>, 2022.
- 2008 Gasser, T. and Ciais, P.: A theoretical framework for the net land-to-atmosphere CO₂ flux and its implications
2009 in the definition of "emissions from land-use change", *Earth Syst. Dynam.*, 4, 171–186,
2010 <https://doi.org/10.5194/esd-4-171-2013>, 2013.
- 2011 Gasser, T., Crepin, L., Quilcaille, Y., Houghton, R. A., Ciais, P., and Obersteiner, M.: Historical CO₂ emissions
2012 from land use and land cover change and their uncertainty, *Biogeosciences*, 17, 4075–4101,
2013 <https://doi.org/10.5194/bg-17-4075-2020>, 2020.
- 2014 Gaubert, B., Stephens, B. B., Basu, S., Chevallier, F., Deng, F., Kort, E. A., Patra, P. K., Peters, W., Rödenbeck,
2015 C., Saeki, T., Schimel, D., Van der Laan-Luijckx, I., Wofsy, S., and Yin, Y.: Global atmospheric CO₂ inverse
2016 models converging on neutral tropical land exchange, but disagreeing on fossil fuel and atmospheric growth
2017 rate, *Biogeosciences*, 16, 117–134, <https://doi.org/10.5194/bg-16-117-2019>, 2019.



- 2018 Gaubert, B., Emmons, L. K., Raeder, K., Tilmes, S., Miyazaki, K., Arellano Jr., A. F., Elguindi, N., Granier, C.,
2019 Tang, W., Barré, J., Worden, H. M., Buchholz, R. R., Edwards, D. P., Franke, P., Anderson, J. L., Saunio, M.,
2020 Schroeder, J., Woo, J.-H., Simpson, I. J., Blake, D. R., Meinardi, S., Wennberg, P. O., Crounse, J., Teng, A.,
2021 Kim, M., Dickerson, R. R., He, H., Ren, X., Pusede, S. E., and Diskin, G. S.: Correcting model biases of CO in
2022 East Asia: impact on oxidant distributions during KORUS-AQ, 20, 14617–14647, [https://doi.org/10.5194/acp-](https://doi.org/10.5194/acp-20-14617-2020)
2023 20-14617-2020, 2020.
- 2024 GCCA, 2021. Concrete Future: The GCCA 2050 Cement and Concrete Industry Roadmap for Net Zero
2025 Concrete, available at: <https://gccassociation.org/concretefuture/>, last access: 2 August 2022.
- 2026 Giglio, L., Schroeder, W., and Justice, C. O.: The collection 6 MODIS active fire detection algorithm and fire
2027 products, *Remote Sensing of Environment*, 178, 31–41, <https://doi.org/10.1016/j.rse.2016.02.054>, 2016.
- 2028 Gilfillan, D. and Marland, G.: CDIAC-FF: global and national CO₂ emissions from fossil fuel combustion and
2029 cement manufacture: 1751–2017, 13, 1667–1680, <https://doi.org/10.5194/essd-13-1667-2021>, 2021.
- 2030 Gloege, L., McKinley, G. A., Landschützer, P., Fay, A. R., Frölicher, T. L., Fyfe, J. C., Ilyina, T., Jones, S.,
2031 Lovenduski, N. S., Rodgers, K. B., Schlunegger, S., and Takano, Y.: Quantifying Errors in Observationally
2032 Based Estimates of Ocean Carbon Sink Variability, 35, e2020GB006788,
2033 <https://doi.org/10.1029/2020GB006788>, 2021.
- 2034 Gloege, L., Yan, M., Zheng, T., and McKinley, G. A.: Improved Quantification of Ocean Carbon Uptake by
2035 Using Machine Learning to Merge Global Models and pCO₂ Data, *J. Adv. Model. Earth Syst.*, 14,
2036 e2021MS002620, <https://doi.org/10.1029/2021MS002620>, 2022.
- 2037 Goddijn-Murphy, L. M., Woolf, D. K., Land, P. E., Shutler, J. D., and Donlon, C.: The OceanFlux Greenhouse
2038 Gases methodology for deriving a sea surface climatology of CO₂ fugacity in support of air–sea gas flux
2039 studies, 11, 519–541, <https://doi.org/10.5194/os-11-519-2015>, 2015.
- 2040 Golar, G., Malik, A., Muis, H., Herman, A., Nurudin, N., and Lukman, L.: The social-economic impact of
2041 COVID-19 pandemic: implications for potential forest degradation, *Heliyon*, 6, e05354,
2042 <https://doi.org/10.1016/j.heliyon.2020.e05354>, 2020.
- 2043 Goris, N., Tjiputra, J. F., Olsen, A., Schwinger, J., Lauvset, S. K., & Jeansson, E.: Constraining Projection-
2044 Based Estimates of the Future North Atlantic Carbon Uptake, *Journal of Climate*, 31(10), 3959–3978. Retrieved
2045 Sep 25, 2022, from <https://journals.ametsoc.org/view/journals/clim/31/10/jcli-d-17-0564.1.xml>, 2018.
- 2046 Grassi, G., House, J., Kurz, W. A., Cescatti, A., Houghton, R. A., Peters, G. P., Sanz, M. J., Viñas, R. A.,
2047 Alkama, R., Arneeth, A., Bondeau, A., Dentener, F., Fader, M., Federici, S., Friedlingstein, P., Jain, A. K., Kato,
2048 E., Koven, C. D., Lee, D., Nabel, J. E. M. S., Nassikas, A. A., Perugini, L., Rossi, S., Sitch, S., Viovy, N.,
2049 Wiltshire, A., and Zaehle, S.: Reconciling global-model estimates and country reporting of anthropogenic forest
2050 CO₂ sinks, *Nature Clim Change*, 8, 914–920, <https://doi.org/10.1038/s41558-018-0283-x>, 2018.
- 2051 Grassi, G., Stehfest, E., Rogelj, J., van Vuuren, D., Cescatti, A., House, J., Nabuurs, G.-J., Rossi, S., Alkama,



- 2052 R., Viñas, R. A., Calvin, K., Ceccherini, G., Federici, S., Fujimori, S., Gusti, M., Hasegawa, T., Havlik, P.,
2053 Humpenöder, F., Korosuo, A., Perugini, L., Tubiello, F. N., and Popp, A.: Critical adjustment of land mitigation
2054 pathways for assessing countries' climate progress, *Nat. Clim. Chang.*, 11, 425–434,
2055 <https://doi.org/10.1038/s41558-021-01033-6>, 2021.
- 2056 Grassi, G., Conchedda, G., Federici, S., Abad Viñas, R., Korosuo, A., Melo, J., Rossi, S., Sandker, M.,
2057 Somogyi, Z., and Tubiello, F. N.: Carbon Fluxes from Land 2000–2020: Bringing Clarity on Countries'
2058 Reporting, *Earth System Science Data*, April. <https://doi.org/https://doi.org/10.5194/essd-2022-104>, 2022a.
- 2059 Grassi, G., Schwingshackl, C., Gasser, T., Houghton, R. A., Sitch, S., Canadell, J. G., Cescatti, A., Ciais, P.,
2060 Federici, S., Friedlingstein, P., Kurz, W. A., Sanz Sanchez, M. J., Abad Viñas, R., Alkama, R., Ceccherini, G.,
2061 Kato, E., Kennedy, D., Knauer, J., Korosuo, A., McGrath, M. J., Nabel, J., Poulter, B., Rossi, S., Walker, A. P.,
2062 Yuan, W., Yue, X., and Pongratz, J.: Mapping land-use fluxes for 2001–2020 from global models to national
2063 inventories, *Earth Syst. Sci. Data Discuss.* [preprint], <https://doi.org/10.5194/essd-2022-245>, in review, 2022b.
- 2064 Gregg, J. S., Andres, R. J., and Marland, G.: China: Emissions pattern of the world leader in CO₂ emissions
2065 from fossil fuel consumption and cement production, *Geophys. Res. Lett.*, 35, L08806,
2066 <https://doi.org/10.1029/2007GL032887>, 2008.
- 2067 Gregor, L. and Gruber, N.: OceanSODA-ETHZ: a global gridded data set of the surface ocean carbonate system
2068 for seasonal to decadal studies of ocean acidification, 13, 777–808, <https://doi.org/10.5194/essd-13-777-2021>,
2069 2021.
- 2070 Gregor, L., Lebehoh, A. D., Kok, S., and Scheel Monteiro, P. M.: A comparative assessment of the uncertainties
2071 of global surface ocean CO₂ estimates using a machine-learning ensemble (CSIR-ML6 version 2019a) – have
2072 we hit the wall?, 12, 5113–5136, <https://doi.org/10.5194/gmd-12-5113-2019>, 2019.
- 2073 Gruber, N., Gloor, M., Mikaloff Fletcher, S. E., Doney, S. C., Dutkiewicz, S., Follows, M. J., Gerber, M.,
2074 Jacobson, A. R., Joos, F., Lindsay, K., Menemenlis, D., Mouchet, A., Müller, S. A., Sarmiento, J. L., and
2075 Takahashi, T.: Oceanic sources, sinks, and transport of atmospheric CO₂, 23,
2076 <https://doi.org/10.1029/2008GB003349>, 2009.
- 2077 Gruber, N., Clement, D., Carter, B. R., Feely, R. A., van Heuven, S., Hoppema, M., Ishii, M., Key, R. M.,
2078 Kozyr, A., Lauvset, S. K., Lo Monaco, C., Mathis, J. T., Murata, A., Olsen, A., Perez, F. F., Sabine, C. L.,
2079 Tanhua, T., and Wanninkhof, R.: The oceanic sink for anthropogenic CO₂ from 1994 to 2007, 363, 1193–1199,
2080 <https://doi.org/10.1126/science.aau5153>, 2019.
- 2081 Gruère, G. and Brooks, J.: Viewpoint: Characterising early agricultural and food policy responses to the
2082 outbreak of COVID-19, *Food Policy*, 100, 102017, <https://doi.org/10.1016/j.foodpol.2020.102017>, 2021.
- 2083 Guan, D., Liu, Z., Geng, Y., Lindner, S., and Hubacek, K.: The gigatonne gap in China's carbon dioxide
2084 inventories, *Nature Clim Change*, 2, 672–675, <https://doi.org/10.1038/nclimate1560>, 2012.
- 2085 Guo, R., Wang, J., Bing, L., Tong, D., Ciais, P., Davis, S. J., Andrew, R. M., Xi, F., and Liu, Z.: Global CO₂



- 2086 uptake by cement from 1930 to 2019, 13, 1791–1805, <https://doi.org/10.5194/essd-13-1791-2021>, 2021.
- 2087 Gütschow, J., Jeffery, M. L., Gieseke, R., Gebel, R., Stevens, D., Krapp, M., and Rocha, M.: The PRIMAP-hist
2088 national historical emissions time series, 8, 571–603, <https://doi.org/10.5194/essd-8-571-2016>, 2016.
- 2089 Gütschow, J., Günther, A., and Pflüger, M.: The PRIMAP-hist national historical emissions time series (1750-
2090 2019) v2.3.1, <https://doi.org/10.5281/zenodo.5494497>, 2021.
- 2091 Hall, B. D., Crotwell, A. M., Kitzis, D. R., Mefford, T., Miller, B. R., Schibig, M. F., and Tans, P. P.: Revision
2092 of the World Meteorological Organization Global Atmosphere Watch (WMO/GAW) CO₂ calibration scale, 14,
2093 3015–3032, <https://doi.org/10.5194/amt-14-3015-2021>, 2021.
- 2094 Hansen, M. C., Potapov, P. V., Moore, R., Hancher, M., Turubanova, S. A., Tyukavina, A., Thau, D., Stehman,
2095 S. V., Goetz, S. J., Loveland, T. R., Kommareddy, A., Egorov, A., Chini, L., Justice, C. O., and Townshend, J.
2096 R. G.: High-Resolution Global Maps of 21st-Century Forest Cover Change, *Science*, 342, 850–853,
2097 <https://doi.org/10.1126/science.1244693>, 2013.
- 2098 Hansis, E., Davis, S. J., and Pongratz, J.: Relevance of methodological choices for accounting of land use
2099 change carbon fluxes, *Global Biogeochem. Cycles*, 29, 1230–1246, <https://doi.org/10.1002/2014GB004997>,
2100 2015.
- 2101 Harris, I., Jones, P. D., Osborn, T. J., and Lister, D. H.: Updated high-resolution grids of monthly climatic
2102 observations - the CRU TS3.10 Dataset, *Int. J. Climatol.*, 34, 623–642, <https://doi.org/10.1002/joc.3711>, 2014.
- 2103 Harris, I., Osborn, T. J., Jones, P., and Lister, D.: Version 4 of the CRU TS monthly high-resolution gridded
2104 multivariate climate dataset, *Sci Data*, 7, 109, <https://doi.org/10.1038/s41597-020-0453-3>, 2020.
- 2105 Hauck, J., Zeising, M., Le Quéré, C., Gruber, N., Bakker, D. C. E., Bopp, L., Chau, T. T. T., Gürses, Ö., Ilyina,
2106 T., Landschützer, P., Lenton, A., Resplandy, L., Rödenbeck, C., Schwinger, J., and Séférian, R.: Consistency
2107 and Challenges in the Ocean Carbon Sink Estimate for the Global Carbon Budget, *Front. Mar. Sci.*, 7, 571720,
2108 <https://doi.org/10.3389/fmars.2020.571720>, 2020.
- 2109 Haverd, V., Smith, B., Nieradzik, L., Briggs, P. R., Woodgate, W., Trudinger, C. M., Canadell, J. G., and Cuntz,
2110 M.: A new version of the CABLE land surface model (Subversion revision r4601) incorporating land use and
2111 land cover change, woody vegetation demography, and a novel optimisation-based approach to plant
2112 coordination of photosynthesis, *Geosci. Model Dev.*, 11, 2995–3026, [https://doi.org/10.5194/gmd-11-2995-](https://doi.org/10.5194/gmd-11-2995-2018)
2113 2018, 2018.
- 2114 Heinemann, A., Mertz, O., Frohling, S., Christensen, A. E., Hurni, K., Sedano, F., Chini, L. P., Sahajpal, R.,
2115 Hansen, M., and Hurtt, G.: A global view of shifting cultivation: Recent, current, and future extent, *PLOS ONE*,
2116 12, e0184479, <https://doi.org/10.1371/journal.pone.0184479>, 2017.
- 2117 Hertwich, E. G. and Peters, G. P.: Carbon Footprint of Nations: A Global, Trade-Linked Analysis, *Environ. Sci.*
2118 *Technol.*, 43, 6414–6420, <https://doi.org/10.1021/es803496a>, 2009.



- 2119 Hickler, T., Smith, B., Prentice, I. C., Mjöfors, K., Miller, P., Arneth, A., and Sykes, M. T.: CO₂ fertilization in
2120 temperate FACE experiments not representative of boreal and tropical forests, 14, 1531–1542,
2121 <https://doi.org/10.1111/j.1365-2486.2008.01598.x>, 2008.
- 2122 Ho, D. T., Wanninkhof, R., Schlosser, P., Ullman, D. S., Hebert, D., and Sullivan, K. F.: Toward a universal
2123 relationship between wind speed and gas exchange: Gas transfer velocities measured with ³He/SF₆ during the
2124 Southern Ocean Gas Exchange Experiment, 116, <https://doi.org/10.1029/2010JC006854>, 2011.
- 2125 Hoesly, R. M., Smith, S. J., Feng, L., Klimont, Z., Janssens-Maenhout, G., Pitkanen, T., Seibert, J. J., Vu, L.,
2126 Andres, R. J., Bolt, R. M., Bond, T. C., Dawidowski, L., Kholod, N., Kurokawa, J., Li, M., Liu, L., Lu, Z.,
2127 Moura, M. C. P., O'Rourke, P. R., and Zhang, Q.: Historical (1750–2014) anthropogenic emissions of reactive
2128 gases and aerosols from the Community Emissions Data System (CEDS), *Geosci. Model Dev.*, 11, 369–408,
2129 <https://doi.org/10.5194/gmd-11-369-2018>, 2018.
- 2130 Hong, C., Burney, J. A., Pongratz, J., Nabel, J. E. M. S., Mueller, N. D., Jackson, R. B., and Davis, S. J.: Global
2131 and regional drivers of land-use emissions in 1961–2017, 589, 554–561, [https://doi.org/10.1038/s41586-020-](https://doi.org/10.1038/s41586-020-03138-y)
2132 03138-y, 2021.
- 2133 Hooijer, A., Page, S., Canadell, J. G., Silvius, M., Kwadijk, J., Wösten, H., and Jauhiainen, J.: Current and
2134 future CO₂ emissions from drained peatlands in Southeast Asia, *Biogeosciences*, 7, 1505–1514,
2135 <https://doi.org/10.5194/bg-7-1505-2010>, 2010.
- 2136 Houghton, R. A.: Why are estimates of the terrestrial carbon balance so different?, 9, 500–509,
2137 <https://doi.org/10.1046/j.1365-2486.2003.00620.x>, 2003.
- 2138 Houghton, R. A. and Nassikas, A. A.: Global and regional fluxes of carbon from land use and land cover change
2139 1850–2015: Carbon Emissions From Land Use, *Global Biogeochem. Cycles*, 31, 456–472,
2140 <https://doi.org/10.1002/2016GB005546>, 2017.
- 2141 Houghton, R. A., House, J. I., Pongratz, J., van der Werf, G. R., DeFries, R. S., Hansen, M. C., Le Quéré, C.,
2142 and Ramankutty, N.: Carbon emissions from land use and land-cover change, *Biogeosciences*, 9, 5125–5142,
2143 <https://doi.org/10.5194/bg-9-5125-2012>, 2012.
- 2144 Hubau, W., Lewis, S. L., Phillips, O. L., Affum-Baffoe, K., Beeckman, H., Cunf-Sanchez, A., Daniels, A. K.,
2145 Ewango, C. E. N., Fauset, S., Mukinzi, J. M., Sheil, D., Sonké, B., Sullivan, M. J. P., Sunderland, T. C. H.,
2146 Taedoumg, H., Thomas, S. C., White, L. J. T., Abernethy, K. A., Adu-Bredu, S., Amani, C. A., Baker, T. R.,
2147 Banin, L. F., Baya, F., Begne, S. K., Bennett, A. C., Benedet, F., Bitariho, R., Bocko, Y. E., Boeckx, P.,
2148 Boundja, P., Brienen, R. J. W., Brncic, T., Chezeaux, E., Chuyong, G. B., Clark, C. J., Collins, M., Comiskey, J.
2149 A., Coomes, D. A., Dargie, G. C., de Haulleville, T., Kamdem, M. N. D., Doucet, J.-L., Esquivel-Muelbert, A.,
2150 Feldpausch, T. R., Fofanah, A., Foli, E. G., Gilpin, M., Gloor, E., Gonmadje, C., Gourlet-Fleury, S., Hall, J. S.,
2151 Hamilton, A. C., Harris, D. J., Hart, T. B., Hockemba, M. B. N., Hladik, A., Ifo, S. A., Jeffery, K. J., Jucker, T.,
2152 Yakusu, E. K., Kearsley, E., Kenfack, D., Koch, A., Leal, M. E., Levesley, A., Lindsell, J. A., Lisingo, J.,
2153 Lopez-Gonzalez, G., Lovett, J. C., Makana, J.-R., Malhi, Y., Marshall, A. R., Martin, J., Martin, E. H., Mbayu,
2154 F. M., Medjibe, V. P., Mihindou, V., Mitchard, E. T. A., Moore, S., Munishi, P. K. T., Bengone, N. N., Ojo, L.,



- 2155 Ondo, F. E., Peh, K. S.-H., Pickavance, G. C., Poulsen, A. D., Poulsen, J. R., Qie, L., Reitsma, J., Rovero, F.,
2156 Swaine, M. D., Talbot, J., Taplin, J., Taylor, D. M., Thomas, D. W., Toirambe, B., Mukendi, J. T., Tuagben, D.,
2157 Umunay, P. M., et al.: Asynchronous carbon sink saturation in African and Amazonian tropical forests, 579, 80–
2158 87, <https://doi.org/10.1038/s41586-020-2035-0>, 2020.
- 2159 Hugelius, G., Bockheim, J. G., Camill, P., Elberling, B., Grosse, G., Harden, J. W., Johnson, K., Jorgenson, T.,
2160 Koven, C. D., Kuhry, P., Michaelson, G., Mishra, U., Palmtag, J., Ping, C.-L., O'Donnell, J., Schirmer, L.,
2161 Schuur, E. A. G., Sheng, Y., Smith, L. C., Strauss, J., and Yu, Z.: A new data set for estimating organic carbon
2162 storage to 3 m depth in soils of the northern circumpolar permafrost region, *Earth Syst. Sci. Data*, 5, 393–402,
2163 <https://doi.org/10.5194/essd-5-393-2013>, 2013.
- 2164 Humphrey, V., Zscheischler, J., Ciais, P., Gudmundsson, L., Sitch, S., and Seneviratne, S. I.: Sensitivity of
2165 atmospheric CO₂ growth rate to observed changes in terrestrial water storage, 560, 628–631,
2166 <https://doi.org/10.1038/s41586-018-0424-4>, 2018.
- 2167 Humphrey, V., Berg, A., Ciais, P., Gentine, P., Jung, M., Reichstein, M., Seneviratne, S. I., and Frankenberg,
2168 C.: Soil moisture–atmosphere feedback dominates land carbon uptake variability, 592, 65–69,
2169 <https://doi.org/10.1038/s41586-021-03325-5>, 2021.
- 2170 Huntzinger, D. N., Michalak, A. M., Schwalm, C., Ciais, P., King, A. W., Fang, Y., Schaefer, K., Wei, Y.,
2171 Cook, R. B., Fisher, J. B., Hayes, D., Huang, M., Ito, A., Jain, A. K., Lei, H., Lu, C., Maignan, F., Mao, J.,
2172 Parazoo, N., Peng, S., Poulter, B., Ricciuto, D., Shi, X., Tian, H., Wang, W., Zeng, N., and Zhao, F.:
2173 Uncertainty in the response of terrestrial carbon sink to environmental drivers undermines carbon-climate
2174 feedback predictions, *Sci Rep*, 7, 4765, <https://doi.org/10.1038/s41598-017-03818-2>, 2017.
- 2175 Hurtt, G., Chini, L., Sahajpal, R., Frolking, S., Bodirsky, B. L., Calvin, K., Doelman, J., Fisk, J., Fujimori, S.,
2176 Klein Goldewijk, K., Hasegawa, T., Havlik, P., Heinemann, A., Humpenöder, F., Jungclaus, J., Kaplan, J.,
2177 Krisztin, T., Lawrence, D., Lawrence, P., Mertz, O., Pongratz, J., Popp, A., Riahi, K., Shevliakova, E., Stehfest,
2178 E., Thornton, P., van Vuuren, D., and Zhang, X.: input4MIPs.CMIP6.CMIP.UofMD.UofMD-landState-2-1-h,
2179 <https://doi.org/10.22033/ESGF/input4MIPs.1127>, 2017.
- 2180 Hurtt, G. C., Chini, L. P., Frolking, S., Betts, R. A., Feddema, J., Fischer, G., Fisk, J. P., Hibbard, K., Houghton,
2181 R. A., Janetos, A., Jones, C. D., Kindermann, G., Kinoshita, T., Klein Goldewijk, K., Riahi, K., Shevliakova, E.,
2182 Smith, S., Stehfest, E., Thomson, A., Thornton, P., van Vuuren, D. P., and Wang, Y. P.: Harmonization of land-
2183 use scenarios for the period 1500–2100: 600 years of global gridded annual land-use transitions, wood harvest,
2184 and resulting secondary lands, *Climatic Change*, 109, 117–161, <https://doi.org/10.1007/s10584-011-0153-2>,
2185 2011.
- 2186 Hurtt, G. C., Chini, L., Sahajpal, R., Frolking, S., Bodirsky, B. L., Calvin, K., Doelman, J. C., Fisk, J., Fujimori,
2187 S., Klein Goldewijk, K., Hasegawa, T., Havlik, P., Heinemann, A., Humpenöder, F., Jungclaus, J., Kaplan, J. O.,
2188 Kennedy, J., Krisztin, T., Lawrence, D., Lawrence, P., Ma, L., Mertz, O., Pongratz, J., Popp, A., Poulter, B.,
2189 Riahi, K., Shevliakova, E., Stehfest, E., Thornton, P., Tubiello, F. N., van Vuuren, D. P., and Zhang, X.:
2190 Harmonization of global land use change and management for the period 850–2100 (LUH2) for CMIP6, *Geosci.*



- 2191 Model Dev., 13, 5425–5464, <https://doi.org/10.5194/gmd-13-5425-2020>, 2020.
- 2192 IEA: International Energy Agency: Global Energy Review, available at: [https://www.iea.org/reports/global-](https://www.iea.org/reports/global-energy-review-2021)
2193 [energy-review-2021](https://www.iea.org/reports/global-energy-review-2021), last access: 25 September 2022, 2021a.
- 2194 IEA: International Energy Agency: World Energy Outlook, available at: [https://www.iea.org/reports/world-](https://www.iea.org/reports/world-energy-outlook-2021)
2195 [energy-outlook-2021](https://www.iea.org/reports/world-energy-outlook-2021), last access: 25 September 2022, 2021b.
- 2196 IEA/OECD: International Energy Agency/Organisation for Economic Cooperation and Development: CO2
2197 emissions from fuel combustion, available at: [https://webstore.iea.org/co2-emissions-from-fuel-combustion-](https://webstore.iea.org/co2-emissions-from-fuel-combustion-2019-highlights)
2198 [2019-highlights](https://webstore.iea.org/co2-emissions-from-fuel-combustion-2019-highlights), last access: 25 September 2022, 2019.
- 2199 Iida, Y., Kojima, A., Takatani, Y., Nakano, T., Sugimoto, H., Midorikawa, T., and Ishii, M.: Trends in pCO₂
2200 and sea–air CO₂ flux over the global open oceans for the last two decades, *J Oceanogr*, 71, 637–661,
2201 <https://doi.org/10.1007/s10872-015-0306-4>, 2015.
- 2202 Iida, Y., Takatani, Y., Kojima, A., and Ishii, M.: Global trends of ocean CO₂ sink and ocean acidification: an
2203 observation-based reconstruction of surface ocean inorganic carbon variables, *J Oceanogr*, 77, 323–358,
2204 <https://doi.org/10.1007/s10872-020-00571-5>, 2021.
- 2205 Ilyina, T., Six, K. D., Segsneider, J., Maier-Reimer, E., Li, H., and Núñez-Riboni, I.: Global ocean
2206 biogeochemistry model HAMOCC: Model architecture and performance as component of the MPI-Earth system
2207 model in different CMIP5 experimental realizations: The Model Hamocc within Mpi-Esm in Cmp5, *J. Adv.*
2208 *Model. Earth Syst.*, 5, 287–315, <https://doi.org/10.1029/2012MS000178>, 2013.
- 2209 IMF: International Monetary Fund: World Economic Outlook, available at: <http://www.imf.org>, last access: 25
2210 September 2022, 2022.
- 2211 Inness, A., Ades, M., Agustí-Panareda, A., Barré, J., Benedictow, A., Blechschmidt, A.-M., Dominguez, J. J.,
2212 Engelen, R., Eskes, H., Flemming, J., Huijnen, V., Jones, L., Kipling, Z., Massart, S., Parrington, M., Peuch, V.-
2213 H., Razinger, M., Remy, S., Schulz, M., and Suttie, M.: The CAMS reanalysis of atmospheric composition, 19,
2214 3515–3556, <https://doi.org/10.5194/acp-19-3515-2019>, 2019.
- 2215 IPCC: Summary for Policymakers. In: *Climate Change 2021: The Physical Science Basis. Contribution of*
2216 *Working Group I to the Sixth Assessment Report of the Intergovernmental Panel on Climate Change* [Masson-
2217 Delmotte, V., P. Zhai, A. Pirani, S.L. Connors, C. Péan, S. Berger, N. Caud, Y. Chen, L. Goldfarb, M.I. Gomis,
2218 M. Huang, K. Leitzell, E. Lonnoy, J.B.R. Matthews, T.K. Maycock, T. Waterfield, O. Yelekçi, R. Yu, and B.
2219 Zhou (eds.)]. Cambridge University Press, 2021.
- 2220 Ito, A. and Inatomi, M.: Use of a process-based model for assessing the methane budgets of global terrestrial
2221 ecosystems and evaluation of uncertainty, 9, 759–773, <https://doi.org/10.5194/bg-9-759-2012>, 2012.
- 2222 Jackson, R. B., Canadell, J. G., Le Quéré, C., Andrew, R. M., Korsbakken, J. I., Peters, G. P., and Nakicenovic,
2223 N.: Reaching peak emissions, *Nature Clim Change*, 6, 7–10, <https://doi.org/10.1038/nclimate2892>, 2016.



- 2224 Jackson, R. B., Le Quéré, C., Andrew, R. M., Canadell, J. G., Korsbakken, J. I., Liu, Z., Peters, G. P., and
2225 Zheng, B.: Global energy growth is outpacing decarbonization, *Environ. Res. Lett.*, 13, 120401,
2226 <https://doi.org/10.1088/1748-9326/aaf303>, 2018.
- 2227 Jackson, R. B., Friedlingstein, P., Andrew, R. M., Canadell, J. G., Le Quéré, C., and Peters, G. P.: Persistent
2228 fossil fuel growth threatens the Paris Agreement and planetary health, *Environ. Res. Lett.*, 14, 121001,
2229 <https://doi.org/10.1088/1748-9326/ab57b3>, 2019.
- 2230 Jackson, R. B., Friedlingstein, P., Quéré, C. L., Abernethy, S., Andrew, R. M., Canadell, J. G., Ciais, P., Davis,
2231 S. J., Deng, Z., Liu, Z., Korsbakken, J. I., and Peters, G. P.: Global fossil carbon emissions rebound near pre-
2232 COVID-19 levels, *Environ. Res. Lett.*, 17, 031001, <https://doi.org/10.1088/1748-9326/ac55b6>, 2022.
- 2233 Jacobson, A. R., Mikaloff Fletcher, S. E., Gruber, N., Sarmiento, J. L., and Gloor, M.: A joint atmosphere-ocean
2234 inversion for surface fluxes of carbon dioxide: 1. Methods and global-scale fluxes: JOINT INVERSION-
2235 METHODS AND GLOBAL FLUXES, *Global Biogeochem. Cycles*, 21,
2236 <https://doi.org/10.1029/2005GB002556>, 2007.
- 2237 Jähne, B.: Air-sea gas exchange. *Elements of Physical Oceanography: A Derivative of the Encyclopedia of*
2238 *Ocean Sciences*, 160–169. <https://doi.org/10.1016/B978-0-12-409548-9.11613-6>, 2019.
- 2239 Jähne, B., Haussecker, H.: Air-water exchange, *Annual reviews of fluid mechanics*, doi:
2240 10.1146/annurev.fluid.30.1.443, <https://www.annualreviews.org/doi/10.1146/annurev.fluid.30.1.443>, 1998.
- 2241 Jain, A. K., Meiyappan, P., Song, Y., and House, J. I.: CO₂ emissions from land-use change affected more by
2242 nitrogen cycle, than by the choice of land-cover data, 19, 2893–2906, <https://doi.org/10.1111/gcb.12207>, 2013.
- 2243 Janssens-Maenhout, G., Crippa, M., Guizzardi, D., Muntean, M., Schaaf, E., Dentener, F., Bergamaschi, P.,
2244 Pagliari, V., Olivier, J. G. J., Peters, J. A. H. W., van Aardenne, J. A., Monni, S., Doering, U., Petrescu, A. M.
2245 R., Solazzo, E., and Oreggioni, G. D.: EDGAR v4.3.2 Global Atlas of the three major greenhouse gas emissions
2246 for the period 1970–2012, *Earth Syst. Sci. Data*, 11, 959–1002, <https://doi.org/10.5194/essd-11-959-2019>, 2019.
- 2247 Jin, Z., Wang, T., Zhang, H., Wang, Y., Ding, J., and Tian, X.: Constraint of satellite CO₂ retrieval on the global
2248 carbon cycle from a Chinese atmospheric inversion system, under review, *Sci. China Earth Sci.*, 2022.
- 2249 JODI: Joint Organisations Data Initiative, available at: <https://www.jodidata.org>, last access: 25 September
2250 2022, 2022.
- 2251 Jones, M. W., Andrew, R. M., Peters, G. P., Janssens-Maenhout, G., De-Gol, A. J., Ciais, P., Patra, P. K.,
2252 Chevallier, F., and Le Quéré, C.: Gridded fossil CO₂ emissions and related O₂ combustion consistent with
2253 national inventories 1959–2018, *Sci Data*, 8, 2, <https://doi.org/10.1038/s41597-020-00779-6>, 2021.
- 2254 Jones, M. W., Andrew, R. M., Peters, G. P., Janssens-Maenhout, G., De-Gol, A. J., Dou, X., Liu, Z., Pickers, P.,
2255 Ciais, P., Patra, P. K., Chevallier, F., and Le Quéré, C.: Gridded fossil CO₂ emissions and related O₂
2256 combustion consistent with national inventories 1959–2021, <https://doi.org/10.5281/zenodo.4277266>, 2022.



- 2257 Joos, F. and Spahni, R.: Rates of change in natural and anthropogenic radiative forcing over the past 20,000
2258 years, *Proceedings of the National Academy of Sciences*, 105, 1425–1430,
2259 <https://doi.org/10.1073/pnas.0707386105>, 2008.
- 2260 Joos, F., Spahni, R., Stocker, B. D., Lienert, S., Müller, J., Fischer, H., Schmitt, J., Prentice, I. C., Otto-Bliesner,
2261 B., and Liu, Z.: N₂O changes from the Last Glacial Maximum to the preindustrial – Part 2: terrestrial N₂O
2262 emissions and carbon–nitrogen cycle interactions, *Biogeosciences*, 17, 3511–3543, [https://doi.org/10.5194/bg-](https://doi.org/10.5194/bg-17-3511-2020)
2263 17-3511-2020, 2020.
- 2264 Jung, M., Reichstein, M., Ciais, P., Seneviratne, S. I., Sheffield, J., Goulden, M. L., Bonan, G., Cescatti, A.,
2265 Chen, J., de Jeu, R., Dolman, A. J., Eugster, W., Gerten, D., Gianelle, D., Gobron, N., Heinke, J., Kimball, J.,
2266 Law, B. E., Montagnani, L., Mu, Q., Mueller, B., Oleson, K., Papale, D., Richardson, A. D., Rouspard, O.,
2267 Running, S., Tomelleri, E., Viovy, N., Weber, U., Williams, C., Wood, E., Zaehle, S., and Zhang, K.: Recent
2268 decline in the global land evapotranspiration trend due to limited moisture supply, *Nature*, 467, 951–954,
2269 <https://doi.org/10.1038/nature09396>, 2010.
- 2270 Jung, M., Reichstein, M., Schwalm, C. R., Huntingford, C., Sitch, S., Ahlström, A., Arneth, A., Camps-Valls,
2271 G., Ciais, P., Friedlingstein, P., Gans, F., Ichii, K., Jain, A. K., Kato, E., Papale, D., Poulter, B., Raduly, B.,
2272 Rödenbeck, C., Tramontana, G., Viovy, N., Wang, Y.-P., Weber, U., Zaehle, S., and Zeng, N.: Compensatory
2273 water effects link yearly global land CO₂ sink changes to temperature, *Nature*, 541, 516–520,
2274 <https://doi.org/10.1038/nature20780>, 2017.
- 2275 Kalnay, E., Kanamitsu, M., Kistler, R., Collins, W., Deaven, D., Gandin, L., Iredell, M., Saha, S., White, G.,
2276 Woollen, J., Zhu, Y., Chelliah, M., Ebisuzaki, W., Higgins, W., Janowiak, J., Mo, K. C., Ropelewski, C., Wang,
2277 J., Leetmaa, A., Reynolds, R., Jenne, R., and Joseph, D.: The NCEP/NCAR 40-Year Reanalysis Project, 77,
2278 437–472, [https://doi.org/10.1175/1520-0477\(1996\)077<0437:TNYRP>2.0.CO;2](https://doi.org/10.1175/1520-0477(1996)077<0437:TNYRP>2.0.CO;2), 1996.
- 2279 Kato, E., Kinoshita, T., Ito, A., Kawamiya, M., and Yamagata, Y.: Evaluation of spatially explicit emission
2280 scenario of land-use change and biomass burning using a process-based biogeochemical model, 8, 104–122,
2281 <https://doi.org/10.1080/1747423X.2011.628705>, 2013.
- 2282 Keeling, C. D., Bacastow, R. B., Bainbridge, A. E., Ekdahl, C. A., Guenther, P. R., Waterman, L. S., and Chin,
2283 J. F. S.: Atmospheric carbon dioxide variations at Mauna Loa Observatory, Hawaii, 28, 538–551,
2284 <https://doi.org/10.1111/j.2153-3490.1976.tb00701.x>, 1976.
- 2285 Keeling, R. F. and Manning, A. C.: 5.15 - Studies of Recent Changes in Atmospheric O₂ Content, in: *Treatise*
2286 *on Geochemistry* (Second Edition), edited by: Holland, H. D. and Turekian, K. K., Elsevier, Oxford, 385–404,
2287 <https://doi.org/10.1016/B978-0-08-095975-7.00420-4>, 2014.
- 2288 Keppler, L. and Landschützer, P.: Regional Wind Variability Modulates the Southern Ocean Carbon Sink, *Sci*
2289 *Rep.*, 9, 7384, <https://doi.org/10.1038/s41598-019-43826-y>, 2019.
- 2290 Khatiwala, S., Primeau, F., and Hall, T.: Reconstruction of the history of anthropogenic CO₂ concentrations in
2291 the ocean, *Nature*, 462, 346–349, <https://doi.org/10.1038/nature08526>, 2009.



- 2292 Khatiwala, S., Tanhua, T., Mikaloff Fletcher, S., Gerber, M., Doney, S. C., Graven, H. D., Gruber, N.,
2293 McKinley, G. A., Murata, A., Ríos, A. F., and Sabine, C. L.: Global ocean storage of anthropogenic carbon,
2294 *Biogeosciences*, 10, 2169–2191, <https://doi.org/10.5194/bg-10-2169-2013>, 2013.
- 2295 Klein Goldewijk, K., Beusen, A., Doelman, J., and Stehfest, E.: Anthropogenic land use estimates for the
2296 Holocene – HYDE 3.2, *Earth Syst. Sci. Data*, 9, 927–953, <https://doi.org/10.5194/essd-9-927-2017>, 2017a.
- 2297 Klein Goldewijk, K., Dekker, S. C., and van Zanden, J. L.: Per-capita estimations of long-term historical land
2298 use and the consequences for global change research, *Journal of Land Use Science*, 1747423X.2017.1354938,
2299 <https://doi.org/10.1080/1747423X.2017.1354938>, 2017b.
- 2300 Kobayashi, S., Ota, Y., Harada, Y., Ebita, A., Moriya, M., Onoda, H., Onogi, K., Kamahori, H., Kobayashi, C.,
2301 Endo, H., Miyaoka, K., and Takahashi, K.: The JRA-55 Reanalysis: General Specifications and Basic
2302 Characteristics, *Journal of the Meteorological Society of Japan*, 93, 5–48, <https://doi.org/10.2151/jmsj.2015->
2303 001, 2015.
- 2304 Kong, Y., Zheng, B., Zhang, Q., and He, K.: Global and regional carbon budget for 2015–2020 inferred from
2305 OCO-2 based on an ensemble Kalman filter coupled with GEOS-Chem, *Atmospheric Chem. Phys.*, 22, 10769–
2306 10788, <https://doi.org/10.5194/acp-22-10769-2022>, 2022.
- 2307 Korsbakken, J. I., Peters, G. P., and Andrew, R. M.: Uncertainties around reductions in China’s coal use and
2308 CO₂ emissions, *Nature Clim Change*, 6, 687–690, <https://doi.org/10.1038/nclimate2963>, 2016.
- 2309 Krinner, G., Viovy, N., de Noblet-Ducoudré, N., Ogée, J., Polcher, J., Friedlingstein, P., Ciais, P., Sitch, S., and
2310 Prentice, I. C.: A dynamic global vegetation model for studies of the coupled atmosphere-biosphere system:
2311 DVGM for coupled climate studies, *Global Biogeochem. Cycles*, 19, <https://doi.org/10.1029/2003GB002199>,
2312 2005.
- 2313 Lacroix, F., Ilyina, T., and Hartmann, J.: Oceanic CO₂ outgassing and biological production hotspots induced
2314 by pre-industrial river loads of nutrients and carbon in a global modeling approach, *Biogeosciences*, 17, 55–88,
2315 <https://doi.org/10.5194/bg-17-55-2020>, 2020.
- 2316 Lacroix, F., Ilyina, T., Mathis, M., Laruelle, G. G., and Regnier, P.: Historical increases in land-derived nutrient
2317 inputs may alleviate effects of a changing physical climate on the oceanic carbon cycle, *Glob Change Biol*, 27,
2318 5491–5513, <https://doi.org/10.1111/gcb.15822>, 2021.
- 2319 Landschützer, P., Gruber, N., Bakker, D. C. E., Schuster, U., Nakaoka, S., Payne, M. R., Sasse, T. P., and Zeng,
2320 J.: A neural network-based estimate of the seasonal to inter-annual variability of the Atlantic Ocean carbon sink,
2321 *Biogeosciences*, 10, 7793–7815, <https://doi.org/10.5194/bg-10-7793-2013>, 2013.
- 2322 Landschützer, P., Gruber, N., Bakker, D. C. E., and Schuster, U.: Recent variability of the global ocean carbon
2323 sink, *Global Biogeochem. Cycles*, 28, 927–949, <https://doi.org/10.1002/2014GB004853>, 2014.
- 2324 Landschützer, P., Gruber, N., Haumann, F. A., Rödenbeck, C., Bakker, D. C. E., van Heuven, S., Hoppema, M.,
2325 Metzl, N., Sweeney, C., Takahashi, T., Tilbrook, B., and Wanninkhof, R.: The reinvigoration of the Southern



- 2326 Ocean carbon sink, *Science*, 349, 1221–1224, <https://doi.org/10.1126/science.aab2620>, 2015.
- 2327 Landschützer, P., Gruber, N., and Bakker, D. C. E.: Decadal variations and trends of the global ocean carbon
2328 sink: decadal air-sea CO₂ flux variability, *Global Biogeochem. Cycles*, 30, 1396–1417,
2329 <https://doi.org/10.1002/2015GB005359>, 2016.
- 2330 Landschützer, P., Laruelle, G. G., Roobaert, A., and Regnier, P.: A uniform pCO₂ climatology combining open
2331 and coastal oceans, *12*, 2537–2553, <https://doi.org/10.5194/essd-12-2537-2020>, 2020.
- 2332 Lang, F., Ackermann, L., Huang, Y., Truong, S. C. H., Siems, S. T., and Manton, M. J.: A climatology of open
2333 and closed mesoscale cellular convection over the Southern Ocean derived from Himawari-8 observations, 1–
2334 27, <https://doi.org/10.5194/acp-2021-681>, 2021.
- 2335 Lasslop, G., Reichstein, M., Papale, D., Richardson, A. D., Arneeth, A., Barr, A., Stoy, P., and Wohlfahrt, G.:
2336 Separation of net ecosystem exchange into assimilation and respiration using a light response curve approach:
2337 critical issues and global evaluation: Separation of NEE into GPP and RECO, *16*, 187–208,
2338 <https://doi.org/10.1111/j.1365-2486.2009.02041.x>, 2010.
- 2339 Lawrence, D. M., Fisher, R. A., Koven, C. D., Oleson, K. W., Swenson, S. C., Bonan, G., Collier, N., Ghimire,
2340 B., van Kampenhout, L., Kennedy, D., Kluzek, E., Lawrence, P. J., Li, F., Li, H., Lombardozzi, D., Riley, W. J.,
2341 Sacks, W. J., Shi, M., Vertenstein, M., Wieder, W. R., Xu, C., Ali, A. A., Badger, A. M., Bisht, G., van den
2342 Broeke, M., Brunke, M. A., Burns, S. P., Buzan, J., Clark, M., Craig, A., Dahlin, K., Drewniak, B., Fisher, J. B.,
2343 Flanner, M., Fox, A. M., Gentine, P., Hoffman, F., Keppel-Aleks, G., Knox, R., Kumar, S., Lenaerts, J., Leung,
2344 L. R., Lipscomb, W. H., Lu, Y., Pandey, A., Pelletier, J. D., Perket, J., Randerson, J. T., Ricciuto, D. M.,
2345 Sanderson, B. M., Slater, A., Subin, Z. M., Tang, J., Thomas, R. Q., Val Martin, M., and Zeng, X.: The
2346 Community Land Model Version 5: Description of New Features, Benchmarking, and Impact of Forcing
2347 Uncertainty, *11*, 4245–4287, <https://doi.org/10.1029/2018MS001583>, 2019.
- 2348 Le Quéré, C., Rödenbeck, C., Buitenhuis, E. T., Conway, T. J., Langenfelds, R., Gomez, A., Labuschagne, C.,
2349 Ramonet, M., Nakazawa, T., Metzl, N., Gillett, N., and Heimann, M.: Saturation of the Southern Ocean CO₂
2350 Sink Due to Recent Climate Change, *316*, 1735–1738, <https://doi.org/10.1126/science.1136188>, 2007.
- 2351 Le Quéré, C., Raupach, M. R., Canadell, J. G., Marland, G., Bopp, L., Ciais, P., Conway, T. J., Doney, S. C.,
2352 Feely, R. A., Foster, P., Friedlingstein, P., Gurney, K., Houghton, R. A., House, J. I., Huntingford, C., Levy, P.
2353 E., Lomas, M. R., Majkut, J., Metzl, N., Ometto, J. P., Peters, G. P., Prentice, I. C., Randerson, J. T., Running,
2354 S. W., Sarmiento, J. L., Schuster, U., Sitch, S., Takahashi, T., Viovy, N., van der Werf, G. R., and Woodward,
2355 F. I.: Trends in the sources and sinks of carbon dioxide, *Nature Geosci*, 2, 831–836,
2356 <https://doi.org/10.1038/ngeo689>, 2009.
- 2357 Le Quéré, C., Andres, R. J., Boden, T., Conway, T., Houghton, R. A., House, J. I., Marland, G., Peters, G. P.,
2358 van der Werf, G. R., Ahlström, A., Andrew, R. M., Bopp, L., Canadell, J. G., Ciais, P., Doney, S. C., Enright,
2359 C., Friedlingstein, P., Huntingford, C., Jain, A. K., Jourdain, C., Kato, E., Keeling, R. F., Klein Goldewijk, K.,
2360 Levis, S., Levy, P., Lomas, M., Poulter, B., Raupach, M. R., Schwinger, J., Sitch, S., Stocker, B. D., Viovy, N.,
2361 Zaehle, S., and Zeng, N.: The global carbon budget 1959–2011, *Earth Syst. Sci. Data*, 5, 165–185,



- 2362 <https://doi.org/10.5194/essd-5-165-2013>, 2013.
- 2363 Le Quéré, C., Peters, G. P., Andres, R. J., Andrew, R. M., Boden, T. A., Ciais, P., Friedlingstein, P., Houghton,
2364 R. A., Marland, G., Moriarty, R., Sitch, S., Tans, P., Arneeth, A., Arvanitis, A., Bakker, D. C. E., Bopp, L.,
2365 Canadell, J. G., Chini, L. P., Doney, S. C., Harper, A., Harris, I., House, J. I., Jain, A. K., Jones, S. D., Kato, E.,
2366 Keeling, R. F., Klein Goldewijk, K., Körtzinger, A., Koven, C., Lefèvre, N., Maignan, F., Omar, A., Ono, T.,
2367 Park, G.-H., Pfiel, B., Poulter, B., Raupach, M. R., Regnier, P., Rödenbeck, C., Saito, S., Schwinger, J.,
2368 Segschneider, J., Stocker, B. D., Takahashi, T., Tilbrook, B., van Heuven, S., Viovy, N., Wanninkhof, R.,
2369 Wiltshire, A., and Zaehle, S.: Global carbon budget 2013, *Earth Syst. Sci. Data*, 6, 235–263,
2370 <https://doi.org/10.5194/essd-6-235-2014>, 2014.
- 2371 Le Quéré, C., Moriarty, R., Andrew, R. M., Peters, G. P., Ciais, P., Friedlingstein, P., Jones, S. D., Sitch, S.,
2372 Tans, P., Arneeth, A., Boden, T. A., Bopp, L., Bozec, Y., Canadell, J. G., Chini, L. P., Chevallier, F., Cosca, C.
2373 E., Harris, I., Hoppema, M., Houghton, R. A., House, J. I., Jain, A. K., Johannessen, T., Kato, E., Keeling, R. F.,
2374 Kitidis, V., Klein Goldewijk, K., Koven, C., Landa, C. S., Landschützer, P., Lenton, A., Lima, I. D., Marland,
2375 G., Mathis, J. T., Metz, N., Nojiri, Y., Olsen, A., Ono, T., Peng, S., Peters, W., Pfiel, B., Poulter, B., Raupach,
2376 M. R., Regnier, P., Rödenbeck, C., Saito, S., Salisbury, J. E., Schuster, U., Schwinger, J., Séférian, R.,
2377 Segschneider, J., Steinhoff, T., Stocker, B. D., Sutton, A. J., Takahashi, T., Tilbrook, B., van der Werf, G. R.,
2378 Viovy, N., Wang, Y.-P., Wanninkhof, R., Wiltshire, A., and Zeng, N.: Global carbon budget 2014, *Earth Syst.*
2379 *Sci. Data*, 7, 47–85, <https://doi.org/10.5194/essd-7-47-2015>, 2015a.
- 2380 Le Quéré, C., Moriarty, R., Andrew, R. M., Canadell, J. G., Sitch, S., Korsbakken, J. I., Friedlingstein, P.,
2381 Peters, G. P., Andres, R. J., Boden, T. A., Houghton, R. A., House, J. I., Keeling, R. F., Tans, P., Arneeth, A.,
2382 Bakker, D. C. E., Barbero, L., Bopp, L., Chang, J., Chevallier, F., Chini, L. P., Ciais, P., Fader, M., Feely, R. A.,
2383 Gkritzalis, T., Harris, I., Hauck, J., Ilyina, T., Jain, A. K., Kato, E., Kitidis, V., Klein Goldewijk, K., Koven, C.,
2384 Landschützer, P., Lauvset, S. K., Lefèvre, N., Lenton, A., Lima, I. D., Metz, N., Millero, F., Munro, D. R.,
2385 Murata, A., Nabel, J. E. M. S., Nakaoka, S., Nojiri, Y., O'Brien, K., Olsen, A., Ono, T., Pérez, F. F., Pfiel, B.,
2386 Pierrot, D., Poulter, B., Rehder, G., Rödenbeck, C., Saito, S., Schuster, U., Schwinger, J., Séférian, R.,
2387 Steinhoff, T., Stocker, B. D., Sutton, A. J., Takahashi, T., Tilbrook, B., van der Laan-Luijckx, I. T., van der Werf,
2388 G. R., van Heuven, S., Vandemark, D., Viovy, N., Wiltshire, A., Zaehle, S., and Zeng, N.: Global Carbon
2389 Budget 2015, *Earth Syst. Sci. Data*, 7, 349–396, <https://doi.org/10.5194/essd-7-349-2015>, 2015b.
- 2390 Le Quéré, C., Andrew, R. M., Canadell, J. G., Sitch, S., Korsbakken, J. I., Peters, G. P., Manning, A. C., Boden,
2391 T. A., Tans, P. P., Houghton, R. A., Keeling, R. F., Alin, S., Andrews, O. D., Anthoni, P., Barbero, L., Bopp, L.,
2392 Chevallier, F., Chini, L. P., Ciais, P., Currie, K., Delire, C., Doney, S. C., Friedlingstein, P., Gkritzalis, T.,
2393 Harris, I., Hauck, J., Haverd, V., Hoppema, M., Klein Goldewijk, K., Jain, A. K., Kato, E., Körtzinger, A.,
2394 Landschützer, P., Lefèvre, N., Lenton, A., Lienert, S., Lombardozi, D., Melton, J. R., Metz, N., Millero, F.,
2395 Monteiro, P. M. S., Munro, D. R., Nabel, J. E. M. S., Nakaoka, S., O'Brien, K., Olsen, A., Omar, A. M., Ono,
2396 T., Pierrot, D., Poulter, B., Rödenbeck, C., Salisbury, J., Schuster, U., Schwinger, J., Séférian, R., Skjelvan, I.,
2397 Stocker, B. D., Sutton, A. J., Takahashi, T., Tian, H., Tilbrook, B., van der Laan-Luijckx, I. T., van der Werf, G.
2398 R., Viovy, N., Walker, A. P., Wiltshire, A. J., and Zaehle, S.: Global Carbon Budget 2016, *Earth Syst. Sci. Data*,
2399 8, 605–649, <https://doi.org/10.5194/essd-8-605-2016>, 2016.



- 2400 Le Quéré, C., Andrew, R. M., Friedlingstein, P., Sitch, S., Pongratz, J., Manning, A. C., Korsbakken, J. I.,
2401 Peters, G. P., Canadell, J. G., Jackson, R. B., Boden, T. A., Tans, P. P., Andrews, O. D., Arora, V. K., Bakker,
2402 D. C. E., Barbero, L., Becker, M., Betts, R. A., Bopp, L., Chevallier, F., Chini, L. P., Ciais, P., Cosca, C. E.,
2403 Cross, J., Currie, K., Gasser, T., Harris, I., Hauck, J., Haverd, V., Houghton, R. A., Hunt, C. W., Hurtt, G.,
2404 Ilyina, T., Jain, A. K., Kato, E., Kautz, M., Keeling, R. F., Klein Goldewijk, K., Körtzinger, A., Landschützer,
2405 P., Lefèvre, N., Lenton, A., Lienert, S., Lima, I., Lombardozi, D., Metzl, N., Millero, F., Monteiro, P. M. S.,
2406 Munro, D. R., Nabel, J. E. M. S., Nakaoka, S., Nojiri, Y., Padin, X. A., Peregon, A., Pfeil, B., Pierrot, D.,
2407 Poulter, B., Rehder, G., Reimer, J., Rödenbeck, C., Schwinger, J., Séférian, R., Skjelvan, I., Stocker, B. D.,
2408 Tian, H., Tilbrook, B., Tubiello, F. N., van der Laan-Luijkx, I. T., van der Werf, G. R., van Heuven, S., Viovy,
2409 N., Vuichard, N., Walker, A. P., Watson, A. J., Wiltshire, A. J., Zaehle, S., and Zhu, D.: Global Carbon Budget
2410 2017, *Earth Syst. Sci. Data*, 10, 405–448, <https://doi.org/10.5194/essd-10-405-2018>, 2018a.
- 2411 Le Quéré, C., Andrew, R. M., Friedlingstein, P., Sitch, S., Hauck, J., Pongratz, J., Pickers, P. A., Korsbakken, J.
2412 I., Peters, G. P., Canadell, J. G., Arneeth, A., Arora, V. K., Barbero, L., Bastos, A., Bopp, L., Chevallier, F.,
2413 Chini, L. P., Ciais, P., Doney, S. C., Gkritzalis, T., Goll, D. S., Harris, I., Haverd, V., Hoffman, F. M.,
2414 Hoppema, M., Houghton, R. A., Hurtt, G., Ilyina, T., Jain, A. K., Johannessen, T., Jones, C. D., Kato, E.,
2415 Keeling, R. F., Klein Goldewijk, K., Landschützer, P., Lefèvre, N., Lienert, S., Liu, Z., Lombardozi, D., Metzl,
2416 N., Munro, D. R., Nabel, J. E. M. S., Nakaoka, S., Neill, C., Olsen, A., Ono, T., Patra, P., Peregon, A., Peters,
2417 W., Peylin, P., Pfeil, B., Pierrot, D., Poulter, B., Rehder, G., Resplandy, L., Robertson, E., Rocher, M.,
2418 Rödenbeck, C., Schuster, U., Schwinger, J., Séférian, R., Skjelvan, I., Steinhoff, T., Sutton, A., Tans, P. P.,
2419 Tian, H., Tilbrook, B., Tubiello, F. N., van der Laan-Luijkx, I. T., van der Werf, G. R., Viovy, N., Walker, A.
2420 P., Wiltshire, A. J., Wright, R., Zaehle, S., and Zheng, B.: Global Carbon Budget 2018, *Earth Syst. Sci. Data*,
2421 10, 2141–2194, <https://doi.org/10.5194/essd-10-2141-2018>, 2018b.
- 2422 Le Quéré, C., Korsbakken, J. I., Wilson, C., Tosun, J., Andrew, R., Andres, R. J., Canadell, J. G., Jordan, A.,
2423 Peters, G. P., and van Vuuren, D. P.: Drivers of declining CO₂ emissions in 18 developed economies, *Nat.*
2424 *Clim. Chang.*, 9, 213–217, <https://doi.org/10.1038/s41558-019-0419-7>, 2019.
- 2425 Le Quéré, C., Peters, G. P., Friedlingstein, P., Andrew, R. M., Canadell, J. G., Davis, S. J., Jackson, R. B., and
2426 Jones, M. W.: Fossil CO₂ emissions in the post-COVID-19 era, *Nat. Clim. Chang.*, 11, 197–199,
2427 <https://doi.org/10.1038/s41558-021-01001-0>, 2021.
- 2428 Li, H. and Ilyina, T.: Current and Future Decadal Trends in the Oceanic Carbon Uptake Are Dominated by
2429 Internal Variability, *Geophys. Res. Lett.*, 45, 916–925, <https://doi.org/10.1002/2017GL075370>, 2018.
- 2430 Li, W., Ciais, P., Peng, S., Yue, C., Wang, Y., Thurner, M., Saatchi, S. S., Arneeth, A., Avitabile, V., Carvalhais,
2431 N., Harper, A. B., Kato, E., Koven, C., Liu, Y. Y., Nabel, J. E. M. S., Pan, Y., Pongratz, J., Poulter, B., Pugh, T.
2432 A. M., Santoro, M., Sitch, S., Stocker, B. D., Viovy, N., Wiltshire, A., Yousefpour, R., and Zaehle, S.: Land-use
2433 and land-cover change carbon emissions between 1901 and 2012 constrained by biomass observations,
2434 *Biogeosciences*, 14, 5053–5067, <https://doi.org/10.5194/bg-14-5053-2017>, 2017.
- 2435 Liao, E., Resplandy, L., Liu, J., and Bowman, K. W.: Amplification of the Ocean Carbon Sink During El Niños:
2436 Role of Poleward Ekman Transport and Influence on Atmospheric CO₂, 34, e2020GB006574,



- 2437 <https://doi.org/10.1029/2020GB006574>, 2020.
- 2438 Lienert, S. and Joos, F.: A Bayesian ensemble data assimilation to constrain model parameters and land-use
2439 carbon emissions, *Biogeosciences*, 15, 2909–2930, <https://doi.org/10.5194/bg-15-2909-2018>, 2018.
- 2440 Liu, J., Baskaran, L., Bowman, K., Schimel, D., Bloom, A. A., Parazoo, N. C., Oda, T., Carroll, D.,
2441 Menemenlis, D., Joiner, J., Commane, R., Daube, B., Gatti, L. V., McKain, K., Miller, J., Stephens, B. B.,
2442 Sweeney, C., and Wofsy, S.: Carbon Monitoring System Flux Net Biosphere Exchange 2020 (CMS-Flux NBE
2443 2020), 13, 299–330, <https://doi.org/10.5194/essd-13-299-2021>, 2021.
- 2444 Liu, Z., Guan, D., Wei, W., Davis, S. J., Ciais, P., Bai, J., Peng, S., Zhang, Q., Hubacek, K., Marland, G.,
2445 Andres, R. J., Crawford-Brown, D., Lin, J., Zhao, H., Hong, C., Boden, T. A., Feng, K., Peters, G. P., Xi, F.,
2446 Liu, J., Li, Y., Zhao, Y., Zeng, N., and He, K.: Reduced carbon emission estimates from fossil fuel combustion
2447 and cement production in China, *Nature*, 524, 335–338, <https://doi.org/10.1038/nature14677>, 2015.
- 2448 Liu, Z., Ciais, P., Deng, Z., Davis, S. J., Zheng, B., Wang, Y., Cui, D., Zhu, B., Dou, X., Ke, P., Sun, T., Guo,
2449 R., Zhong, H., Boucher, O., Bréon, F.-M., Lu, C., Guo, R., Xue, J., Boucher, E., Tanaka, K., and Chevallier, F.:
2450 Carbon Monitor, a near-real-time daily dataset of global CO₂ emission from fossil fuel and cement production,
2451 *Sci Data*, 7, 392, <https://doi.org/10.1038/s41597-020-00708-7>, 2020a.
- 2452 Liu, Z., Ciais, P., Deng, Z., Lei, R., Davis, S. J., Feng, S., Zheng, B., Cui, D., Dou, X., Zhu, B., Guo, R., Ke, P.,
2453 Sun, T., Lu, C., He, P., Wang, Y., Yue, X., Wang, Y., Lei, Y., Zhou, H., Cai, Z., Wu, Y., Guo, R., Han, T., Xue,
2454 J., Boucher, O., Boucher, E., Chevallier, F., Tanaka, K., Wei, Y., Zhong, H., Kang, C., Zhang, N., Chen, B., Xi,
2455 F., Liu, M., Bréon, F.-M., Lu, Y., Zhang, Q., Guan, D., Gong, P., Kammen, D. M., He, K., and Schellnhuber, H.
2456 J.: Near-real-time monitoring of global CO₂ emissions reveals the effects of the COVID-19 pandemic, *Nat*
2457 *Commun*, 11, 5172, <https://doi.org/10.1038/s41467-020-18922-7>, 2020b.
- 2458 Long, M. C., Moore, J. K., Lindsay, K., Levy, M., Doney, S. C., Luo, J. Y., et al., 2021. Simulations with the
2459 Marine Biogeochemistry Library (MARBL). *Journal of Advances in Modeling Earth Systems*, 13,
2460 e2021MS002647, <https://doi.org/10.1029/2021MS002647>.
- 2461 Ma, L., Hurtt, G. C., Chini, L. P., Sahajpal, R., Pongratz, J., Frohking, S., Stehfest, E., Klein Goldewijk, K.,
2462 O’Leary, D., and Doelman, J. C.: Global rules for translating land-use change (LUH2) to land-cover change for
2463 CMIP6 using GLM2, *Geosci. Model Dev.*, 13, 3203–3220, <https://doi.org/10.5194/gmd-13-3203-2020>, 2020.
- 2464 Maki, T., Ikegami, M., Fujita, T., Hirahara, T., Yamada, K., Mori, K., Takeuchi, A., Tsutsumi, Y., Suda, K., and
2465 Conway, T. J.: New technique to analyse global distributions of CO₂ concentrations and fluxes from non-
2466 processed observational data, 62, 797–809, <https://doi.org/10.1111/j.1600-0889.2010.00488.x>, 2010.
- 2467 MapBiomass: MapBiomass Collection 6, available at: <https://plataforma.brasil.mapbiomas.org/>, last access: 25
2468 September 2022, 2022.
- 2469 Marland, G.: Uncertainties in Accounting for CO₂ From Fossil Fuels, 12, 136–139,
2470 <https://doi.org/10.1111/j.1530-9290.2008.00014.x>, 2008.



- 2471 Marland, G., Hamal, K., and Jonas, M.: How Uncertain Are Estimates of CO₂ Emissions?, 13, 4–7,
2472 <https://doi.org/10.1111/j.1530-9290.2009.00108.x>, 2009.
- 2473 Masarie, K. A. and Tans, P. P.: Extension and integration of atmospheric carbon dioxide data into a globally
2474 consistent measurement record, *J. Geophys. Res.*, 100, 11593, <https://doi.org/10.1029/95JD00859>, 1995.
- 2475 Mather, A.: The transition from deforestation to reforestation in Europe., 35–52, 2001.
- 2476 Matricardi, E. A. T., Skole, D. L., Costa, O. B., Pedlowski, M. A., Samek, J. H., and Miguel, E. P.: Long-term
2477 forest degradation surpasses deforestation in the Brazilian Amazon, 369, 1378–1382,
2478 <https://doi.org/10.1126/science.abb3021>, 2020.
- 2479 Mauritsen, T., Bader, J., Becker, T., Behrens, J., Bittner, M., Brokopf, R., Brovkin, V., Claussen, M., Crueger,
2480 T., Esch, M., Fast, I., Fiedler, S., Fläschner, D., Gayler, V., Giorgetta, M., Goll, D. S., Haak, H., Hagemann, S.,
2481 Hedemann, C., Hohenegger, C., Ilyina, T., Jahns, T., Jimenez-de-la-Cuesta, D., Jungclaus, J., Kleinen, T.,
2482 Kloster, S., Kracher, D., Kinne, S., Kleberg, D., Lasslop, G., Kornbluh, L., Marotzke, J., Matei, D., Meraner,
2483 K., Mikolajewicz, U., Modali, K., Möbis, B., Müller, W. A., Nabel, J. E. M. S., Nam, C. C. W., Notz, D.,
2484 Nyawira, S.-S., Paulsen, H., Peters, K., Pincus, R., Pohlmann, H., Pongratz, J., Popp, M., Raddatz, T. J., Rast,
2485 S., Redler, R., Reick, C. H., Rohrschneider, T., Schemann, V., Schmidt, H., Schnur, R., Schulzweida, U., Six,
2486 K. D., Stein, L., Stemmler, I., Stevens, B., von Storch, J.-S., Tian, F., Voigt, A., Vrese, P., Wieners, K.-H.,
2487 Wilkenskjaeld, S., Winkler, A., and Roeckner, E.: Developments in the MPI-M Earth System Model version 1.2
2488 (MPI-ESM1.2) and Its Response to Increasing CO₂, 11, 998–1038, <https://doi.org/10.1029/2018MS001400>,
2489 2019.
- 2490 McGrath, M. J., Luyssaert, S., Meyfroidt, P., Kaplan, J. O., Bürgi, M., Chen, Y., Erb, K., Gimmi, U.,
2491 McInerney, D., Naudts, K., Otto, J., Pasztor, F., Ryder, J., Schelhaas, M.-J., and Valade, A.: Reconstructing
2492 European forest management from 1600 to 2010, 12, 4291–4316, <https://doi.org/10.5194/bg-12-4291-2015>,
2493 2015.
- 2494 McKinley, G. A., Pilcher, D. J., Fay, A. R., Lindsay, K., Long, M. C., and Lovenduski, N. S.: Timescales for
2495 detection of trends in the ocean carbon sink, *Nature*, 530, 469–472, <https://doi.org/10.1038/nature16958>, 2016.
- 2496 McKinley, G. A., Fay, A. R., Eddebbbar, Y. A., Gloege, L., and Lovenduski, N. S.: External Forcing Explains
2497 Recent Decadal Variability of the Ocean Carbon Sink, *AGU Advances*, 1,
2498 <https://doi.org/10.1029/2019AV000149>, 2020.
- 2499 McNeil, B. I.: Anthropogenic CO₂ Uptake by the Ocean Based on the Global Chlorofluorocarbon Data Set, 299,
2500 235–239, <https://doi.org/10.1126/science.1077429>, 2003.
- 2501 Meiyappan, P., Jain, A. K., and House, J. I.: Increased influence of nitrogen limitation on CO₂ emissions from
2502 future land use and land use change, *Global Biogeochem. Cycles*, 29, 1524–1548,
2503 <https://doi.org/10.1002/2015GB005086>, 2015.
- 2504 Melton, J. R., Arora, V. K., Wisernig-Cojoc, E., Seiler, C., Fortier, M., Chan, E., and Teckentrup, L.: CLASSIC



- 2505 v1.0: the open-source community successor to the Canadian Land Surface Scheme (CLASS) and the Canadian
2506 Terrestrial Ecosystem Model (CTEM) – Part 1: Model framework and site-level performance, *Geosci. Model*
2507 *Dev.*, 13, 2825–2850, <https://doi.org/10.5194/gmd-13-2825-2020>, 2020.
- 2508 Mercado, L. M., Bellouin, N., Sitch, S., Boucher, O., Huntingford, C., Wild, M., and Cox, P. M.: Impact of
2509 changes in diffuse radiation on the global land carbon sink, *Nature*, 458, 1014–1017,
2510 <https://doi.org/10.1038/nature07949>, 2009.
- 2511 Merchant, C. J., Embury, O., Bulgin, C. E., Block, T., Corlett, G. K., Fiedler, E., Good, S. A., Mittaz, J.,
2512 Rayner, N. A., Berry, D., Eastwood, S., Taylor, M., Tsushima, Y., Waterfall, A., Wilson, R., and Donlon, C.:
2513 Satellite-based time-series of sea-surface temperature since 1981 for climate applications, *Sci. Data*, 6, 223,
2514 <https://doi.org/10.1038/s41597-019-0236-x>, 2019.
- 2515 Mikaloff Fletcher, S. E., Gruber, N., Jacobson, A. R., Doney, S. C., Dutkiewicz, S., Gerber, M., Follows, M.,
2516 Joos, F., Lindsay, K., Menemenlis, D., Mouchet, A., Müller, S. A., and Sarmiento, J. L.: Inverse estimates of
2517 anthropogenic CO₂ uptake, transport, and storage by the ocean: air-sea exchange of anthropogenic carbon,
2518 *Global Biogeochem. Cycles*, 20, <https://doi.org/10.1029/2005GB002530>, 2006.
- 2519 Müller, J. and Joos, F.: Committed and projected future changes in global peatlands – continued transient model
2520 simulations since the Last Glacial Maximum, *Biogeosciences*, 18, 3657–3687, [https://doi.org/10.5194/bg-18-](https://doi.org/10.5194/bg-18-3657-2021)
2521 [3657-2021](https://doi.org/10.5194/bg-18-3657-2021), 2021.
- 2522 Myneni, R. B., Ramakrishna, R., Nemani, R., and Running, S. W.: Estimation of global leaf area index and
2523 absorbed par using radiative transfer models, *IEEE Trans. Geosci. Remote Sensing*, 35, 1380–1393,
2524 <https://doi.org/10.1109/36.649788>, 1997.
- 2525 Naegler, T.: Reconciliation of excess 14C-constrained global CO₂ piston velocity estimates, 61, 372–384,
2526 <https://doi.org/10.1111/j.1600-0889.2008.00408.x>, 2009.
- 2527 Nakamura, T., Yamazaki, K., Iwamoto, K., Honda, M., Miyoshi, Y., Ogawa, Y., and Ukita, J.: A negative phase
2528 shift of the winter AO/NAO due to the recent Arctic sea-ice reduction in late autumn, 120, 3209–3227,
2529 <https://doi.org/10.1002/2014JD022848>, 2015.
- 2530 Nakano, H., Tsujino, H., Hirabara, M., Yasuda, T., Motoi, T., Ishii, M., and Yamanaka, G.: Uptake mechanism
2531 of anthropogenic CO₂ in the Kuroshio Extension region in an ocean general circulation model, *J. Oceanogr.*, 67,
2532 765–783, <https://doi.org/10.1007/s10872-011-0075-7>, 2011.
- 2533 Narayanan, B., Aguiar, A., and McDougall, R.: Global Trade, Assistance, and Production: The GTAP 9 Data
2534 Base, *Cent. Glob. Trade Anal. Purdue Univ.*, available at: [https://](https://www.gtapecon.purdue.edu/databases/v9/default.asp)
2535 www.gtapecon.purdue.edu/databases/v9/default.asp, last access: 25 September 2022, 2015.
- 2536 NBS: National Bureau of Statistics of China: Statistical Communiqué of the People’s Republic of China on the
2537 2021 National Economic and Social Development, available at:
2538 http://www.stats.gov.cn/english/PressRelease/202202/t20220227_1827963.html, last access: 25 September



- 2539 2022, 2022.
- 2540 NCEP: National Centers for Environmental Prediction. ONI Index. Cold & Warm Episodes by Season, available
2541 at: https://origin.cpc.ncep.noaa.gov/products/analysis_monitoring/ensostuff/ONI_v5.php, last access: 25
2542 September 2022, 2022.
- 2543 Nightingale, P. D., Liss, P. S., and Schlosser, P.: Measurements of air-sea gas transfer during an open ocean
2544 algal bloom, 27, 2117–2120, <https://doi.org/10.1029/2000GL011541>, 2000.
- 2545 Niwa, Y., Ishijima, K., Ito, A., and Iida, Y.: Toward a long-term atmospheric CO₂ inversion for elucidating
2546 natural carbon fluxes: technical notes of NISMON-CO₂ v2021.1, Prog. Earth Planet Sci., 9, 42,
2547 <https://doi.org/10.1186/s40645-022-00502-6>, 2022.
- 2548 Niwa, Y., Langenfelds, R., Krummel, P., Loh, Zoe, Worthy, Doug, Hatakka, Juha, Aalto, Tuula, Ramonet,
2549 Michel, Delmotte, Marc, Schmidt, Martina, Gheusi, Francois, Mihalopoulos, N., Morgui, J.A., Andrews, Arlyn,
2550 Dlugokencky, Ed, Lee, John, Sweeney, Colm, Thoning, Kirk, Tans, Pieter, De Wekker, Stephan, Fischer, Marc
2551 L., Jaffe, Dan, McKain, Kathryn, Viner, Brian, Miller, John B., Karion, Anna, Miller, Charles, Sloop,
2552 Christopher D., Saito, Kazuyuki, Aoki, Shuji, Morimoto, Shinji, Goto, Daisuke, Steinbacher, Martin, Myhre,
2553 Cathrine Lund, Hermanssen, Ove, Stephens, Britton, Keeling, Ralph, Afshar, Sara, Paplawsky, Bill, Cox, Adam,
2554 Walker, Stephen, Schuldt, Kenneth, Mukai, Hitoshi, Machida, Toshinobu, Sasakawa, Motoki, Nomura, Shohei,
2555 Ito, Akihiko, Iida, Yosuke, and Jones, Matthew W.: Long-term global CO₂ fluxes estimated by NICAM-based
2556 Inverse Simulation for Monitoring CO₂ (NISMON-CO₂) (ver.2022.1), <https://doi.org/10.17595/20201127.001>,
2557 2020.
- 2558 Obermeier, W. A., Nabel, J. E. M. S., Loughran, T., Hartung, K., Bastos, A., Havermann, F., Anthoni, P.,
2559 Arneth, A., Goll, D. S., Lienert, S., Lombardozi, D., Luyssaert, S., McGuire, P. C., Melton, J. R., Poulter, B.,
2560 Sitch, S., Sullivan, M. O., Tian, H., Walker, A. P., Wiltshire, A. J., Zaehle, S., and Pongratz, J.: Modelled land
2561 use and land cover change emissions – a spatio-temporal comparison of different approaches, 12, 635–670,
2562 <https://doi.org/10.5194/esd-12-635-2021>, 2021.
- 2563 O’Rourke, P. R., Smith, S. J., Mott, A., Ahsan, H., McDuffie, E. E., Crippa, M., Klimont, Z., McDonald, B.,
2564 Wang, S., Nicholson, M. B., Feng, L., and Hoesly, R. M.: CEDS v_2021_04_21 Release Emission Data,
2565 <https://doi.org/10.5281/zenodo.4741285>, 2021.
- 2566 Orr, J. C., Najjar, R. G., Aumont, O., Bopp, L., Bullister, J. L., Danabasoglu, G., Doney, S. C., Dunne, J. P.,
2567 Dutay, J.-C., Graven, H., Griffies, S. M., John, J. G., Joos, F., Levin, I., Lindsay, K., Matear, R. J., McKinley,
2568 G. A., Mouchet, A., Oschlies, A., Romanou, A., Schlitzer, R., Tagliabue, A., Tanhua, T., and Yool, A.:
2569 Biogeochemical protocols and diagnostics for the CMIP6 Ocean Model Intercomparison Project (OMIP), 10,
2570 2169–2199, <https://doi.org/10.5194/gmd-10-2169-2017>, 2017.
- 2571 O’Sullivan, M., Zhang, Y., Bellouin, N., Harris, I., Mercado, L. M., Sitch, S., Ciais, P., and Friedlingstein, P.:
2572 Aerosol–light interactions reduce the carbon budget imbalance, Environ. Res. Lett., 16, 124072,
2573 <https://doi.org/10.1088/1748-9326/ac3b77>, 2021.



- 2574 O'Sullivan, M., Friedlingstein, P., Sitch, S., Anthoni, P., Arneth, A., Arora, V. K., Bastrikov, V., Delire, C.,
2575 Goll, D. S., Jain, A., Kato, E., Kennedy, D., Knauer, J., Lienert, S., Lombardozi, D., McGuire, P. C., Melton, J.
2576 R., Nabel, J. E. M. S., Pongratz, J., Poulter, B., Séférian, R., Tian, H., Vuichard, N., Walker, A. P., Yuan, W.,
2577 Yue, X., and Zaehle, S.: Process-oriented analysis of dominant sources of uncertainty in the land carbon sink,
2578 *Nat. Commun.*, 13, 4781, <https://doi.org/10.1038/s41467-022-32416-8>, 2022.
- 2579 Palmer, P. I., Feng, L., Baker, D., Chevallier, F., Bösch, H., and Somkuti, P.: Net carbon emissions from
2580 African biosphere dominate pan-tropical atmospheric CO₂ signal, *Nat Commun*, 10, 3344,
2581 <https://doi.org/10.1038/s41467-019-11097-w>, 2019.
- 2582 Pan, Y., Birdsey, R. A., Fang, J., Houghton, R., Kauppi, P. E., Kurz, W. A., Phillips, O. L., Shvidenko, A.,
2583 Lewis, S. L., Canadell, J. G., Ciais, P., Jackson, R. B., Pacala, S. W., McGuire, A. D., Piao, S., Rautiainen, A.,
2584 Sitch, S., and Hayes, D.: A Large and Persistent Carbon Sink in the World's Forests, *Science*, 333, 988–993,
2585 <https://doi.org/10.1126/science.1201609>, 2011.
- 2586 Patra, P. K., Takigawa, M., Watanabe, S., Chandra, N., Ishijima, K., and Yamashita, Y.: Improved Chemical
2587 Tracer Simulation by MIROC4.0-based Atmospheric Chemistry-Transport Model (MIROC4-ACTM), *SOLA*,
2588 14, 91–96, <https://doi.org/10.2151/sola.2018-016>, 2018.
- 2589 Pendrill, F., Persson, U. M., Godar, J., Kastner, T., Moran, D., Schmidt, S., and Wood, R.: Agricultural and
2590 forestry trade drives large share of tropical deforestation emissions, *Global Environmental Change*, 56, 1–10,
2591 <https://doi.org/10.1016/j.gloenvcha.2019.03.002>, 2019.
- 2592 Peters, G. P., Andrew, R., and Lennox, J.: Constructing an environmentally-extended multi-regional input–
2593 output table using the GTAP database, *Economic Systems Research*, 23, 131–152,
2594 <https://doi.org/10.1080/09535314.2011.563234>, 2011a.
- 2595 Peters, G. P., Minx, J. C., Weber, C. L., and Edenhofer, O.: Growth in emission transfers via international trade
2596 from 1990 to 2008, *Proceedings of the National Academy of Sciences*, 108, 8903–8908,
2597 <https://doi.org/10.1073/pnas.1006388108>, 2011b.
- 2598 Peters, G. P., Davis, S. J., and Andrew, R.: A synthesis of carbon in international trade, *Biogeosciences*, 9,
2599 3247–3276, <https://doi.org/10.5194/bg-9-3247-2012>, 2012a.
- 2600 Peters, G. P., Marland, G., Le Quéré, C., Boden, T., Canadell, J. G., and Raupach, M. R.: Rapid growth in CO₂
2601 emissions after the 2008–2009 global financial crisis, *Nature Clim Change*, 2, 2–4,
2602 <https://doi.org/10.1038/nclimate1332>, 2012b.
- 2603 Peters, G. P., Andrew, R. M., Boden, T., Canadell, J. G., Ciais, P., Le Quéré, C., Marland, G., Raupach, M. R.,
2604 and Wilson, C.: The challenge to keep global warming below 2 °C, *Nature Clim Change*, 3, 4–6,
2605 <https://doi.org/10.1038/nclimate1783>, 2013.
- 2606 Peters, G. P., Le Quéré, C., Andrew, R. M., Canadell, J. G., Friedlingstein, P., Ilyina, T., Jackson, R. B., Joos,
2607 F., Korsbakken, J. I., McKinley, G. A., Sitch, S., and Tans, P.: Towards real-time verification of CO₂ emissions,



- 2608 Nature Clim Change, 7, 848–850, <https://doi.org/10.1038/s41558-017-0013-9>, 2017.
- 2609 Peters, G. P., Andrew, R. M., Canadell, J. G., Friedlingstein, P., Jackson, R. B., Korsbakken, J. I., Le Quéré, C.,
2610 and Peregón, A.: Carbon dioxide emissions continue to grow amidst slowly emerging climate policies, Nat.
2611 Clim. Chang., 10, 3–6, <https://doi.org/10.1038/s41558-019-0659-6>, 2020.
- 2612 Petrescu, A. M. R., Peters, G. P., Janssens-Maenhout, G., Ciais, P., Tubiello, F. N., Grassi, G., Nabuurs, G.-J.,
2613 Leip, A., Carmona-Garcia, G., Winiwarter, W., Höglund-Isaksson, L., Günther, D., Solazzo, E., Kiesow, A.,
2614 Bastos, A., Pongratz, J., Nabel, J. E. M. S., Conchedda, G., Pilli, R., Andrew, R. M., Schelhaas, M.-J., and
2615 Dolman, A. J.: European anthropogenic AFOLU greenhouse gas emissions: a review and benchmark data, Earth
2616 Syst. Sci. Data, 12, 961–1001, <https://doi.org/10.5194/essd-12-961-2020>, 2020.
- 2617 Pfeil, B., Olsen, A., Bakker, D. C. E., Hankin, S., Koyuk, H., Kozyr, A., Malczyk, J., Manke, A., Metz, N.,
2618 Sabine, C. L., Akl, J., Alin, S. R., Bates, N., Bellerby, R. G. J., Borges, A., Boutin, J., Brown, P. J., Cai, W.-J.,
2619 Chavez, F. P., Chen, A., Cosca, C., Fassbender, A. J., Feely, R. A., González-Dávila, M., Goyet, C., Hales, B.,
2620 Hardman-Mountford, N., Heinze, C., Hood, M., Hoppema, M., Hunt, C. W., Hydes, D., Ishii, M., Johannessen,
2621 T., Jones, S. D., Key, R. M., Körtzinger, A., Landschützer, P., Lauvset, S. K., Lefèvre, N., Lenton, A.,
2622 Lourantou, A., Merlivat, L., Midorikawa, T., Mintrop, L., Miyazaki, C., Murata, A., Nakadate, A., Nakano, Y.,
2623 Nakaoka, S., Nojiri, Y., Omar, A. M., Padin, X. A., Park, G.-H., Paterson, K., Perez, F. F., Pierrot, D., Poisson,
2624 A., Ríos, A. F., Santana-Casiano, J. M., Salisbury, J., Sarma, V. V. S. S., Schlitzer, R., Schneider, B., Schuster,
2625 U., Sieger, R., Skjelvan, I., Steinhoff, T., Suzuki, T., Takahashi, T., Tedesco, K., Telszewski, M., Thomas, H.,
2626 Tilbrook, B., Tjiputra, J., Vandemark, D., Veness, T., Wanninkhof, R., Watson, A. J., Weiss, R., Wong, C. S.,
2627 and Yoshikawa-Inoue, H.: A uniform, quality controlled Surface Ocean CO₂ Atlas (SOCAT), Earth Syst. Sci.
2628 Data, 5, 125–143, <https://doi.org/10.5194/essd-5-125-2013>, 2013.
- 2629 Piao, S., Ciais, P., Friedlingstein, P., de Noblet-Ducoudré, N., Cadule, P., Viovy, N., and Wang, T.:
2630 Spatiotemporal patterns of terrestrial carbon cycle during the 20th century, 23,
2631 <https://doi.org/10.1029/2008GB003339>, 2009.
- 2632 Piao, S., Huang, M., Liu, Z., Wang, X., Ciais, P., Canadell, J. G., Wang, K., Bastos, A., Friedlingstein, P.,
2633 Houghton, R. A., Le Quéré, C., Liu, Y., Myneni, R. B., Peng, S., Pongratz, J., Sitch, S., Yan, T., Wang, Y., Zhu,
2634 Z., Wu, D., and Wang, T.: Lower land-use emissions responsible for increased net land carbon sink during the
2635 slow warming period, Nature Geosci, 11, 739–743, <https://doi.org/10.1038/s41561-018-0204-7>, 2018.
- 2636 Pongratz, J., Reick, C. H., Houghton, R. A., and House, J. I.: Terminology as a key uncertainty in net land use
2637 and land cover change carbon flux estimates, Earth Syst. Dynam., 5, 177–195, <https://doi.org/10.5194/esd-5-177-2014>, 2014.
- 2639 Potapov, P., Hansen, M. C., Laestadius, L., Turubanova, S., Yaroshenko, A., Thies, C., Smith, W., Zhuravleva,
2640 I., Komarova, A., Minnemeyer, S., and Esipova, E.: The last frontiers of wilderness: Tracking loss of intact
2641 forest landscapes from 2000 to 2013, 3, e1600821, <https://doi.org/10.1126/sciadv.1600821>, 2017.
- 2642 Poulter, B., Frank, D. C., Hodson, E. L., and Zimmermann, N. E.: Impacts of land cover and climate data
2643 selection on understanding terrestrial carbon dynamics and the CO₂ airborne fraction, Biogeosciences, 8, 2027–



- 2644 2036, <https://doi.org/10.5194/bg-8-2027-2011>, 2011.
- 2645 Poulter, B., Freeborn, P. H., Jolly, W. M., and Varner, J. M.: COVID-19 lockdowns drive decline in active fires
2646 in southeastern United States, *PNAS*, 118, <https://doi.org/10.1073/pnas.2105666118>, 2021.
- 2647 Prather, M.: Interactive comment on “Carbon dioxide and climate impulse response functions for the
2648 computation of greenhouse gas metrics: a multi-model analysis” by F. Joos et al., 6, 2012.
- 2649 Prentice, I. C., Farquhar, G. D., Fasham, M. J. R., Goulden, M. L., Heimann, M., Jaramillo, V. J., Kheshgi, H.
2650 S., Le Quéré, C., Scholes, R. J., and Wallace, D. W. R.: The Carbon Cycle and Atmospheric Carbon Dioxide, in
2651 *Climate Change 2001: The Scientific Basis. Contribution of Working Group I to the Third Assessment Report*
2652 *of the Intergovernmental Panel on Climate Change*, edited by: Houghton, J. T., Ding, Y., Griggs, D. J., Noguera,
2653 M., van der Linden, P. J., Dai, X., Maskell, K., and Johnson, C. A., Cambridge University Press, Cambridge,
2654 United Kingdom and New York, NY, USA, 183–237, 2001.
- 2655 Price, J. T. and Warren, R.: Literature Review of the Potential of “Blue Carbon” Activities to Reduce Emissions,
2656 available at: [https://avoid-net-uk.cc.ic.ac.uk/wp-content/uploads/delightful-downloads/2016/03/Literature-](https://avoid-net-uk.cc.ic.ac.uk/wp-content/uploads/delightful-downloads/2016/03/Literature-review-of-the-potential-of-blue-carbon-activities-to-reduce-emissions-AVOID2-WPE2.pdf)
2657 [review-of-the-potential-of-blue-carbon-activities-to-reduce-emissions-AVOID2-WPE2.pdf](https://avoid-net-uk.cc.ic.ac.uk/wp-content/uploads/delightful-downloads/2016/03/Literature-review-of-the-potential-of-blue-carbon-activities-to-reduce-emissions-AVOID2-WPE2.pdf), last access: 25
2658 September 2022, 2016.
- 2659 Qin, Y., Xiao, X., Wigneron, J.-P., Ciais, P., Brandt, M., Fan, L., Li, X., Crowell, S., Wu, X., Doughty, R.,
2660 Zhang, Y., Liu, F., Sitch, S., and Moore, B.: Carbon loss from forest degradation exceeds that from
2661 deforestation in the Brazilian Amazon, *Nat. Clim. Chang.*, 11, 442–448, [https://doi.org/10.1038/s41558-021-](https://doi.org/10.1038/s41558-021-01026-5)
2662 [01026-5](https://doi.org/10.1038/s41558-021-01026-5), 2021.
- 2663 Qiu, C., Ciais, P., Zhu, D., Guenet, B., Peng, S., Petrescu, A. M. R., Lauerwald, R., Makowski, D., Gallego-
2664 Sala, A. V., Charman, D. J., and Brewer, S. C.: Large historical carbon emissions from cultivated northern
2665 peatlands, 7, eabf1332, <https://doi.org/10.1126/sciadv.abf1332>, 2021.
- 2666 Raupach, M. R., Marland, G., Ciais, P., Le Quere, C., Canadell, J. G., Klepper, G., and Field, C. B.: Global and
2667 regional drivers of accelerating CO₂ emissions, *Proceedings of the National Academy of Sciences*, 104, 10288–
2668 10293, <https://doi.org/10.1073/pnas.0700609104>, 2007.
- 2669 Regnier, P., Friedlingstein, P., Ciais, P., Mackenzie, F. T., Gruber, N., Janssens, I. A., Laruelle, G. G.,
2670 Lauerwald, R., Luysaert, S., Andersson, A. J., Arndt, S., Arnosti, C., Borges, A. V., Dale, A. W., Gallego-Sala,
2671 A., Goddérís, Y., Goossens, N., Hartmann, J., Heinze, C., Ilyina, T., Joos, F., LaRowe, D. E., Leifeld, J.,
2672 Meysman, F. J. R., Munhoven, G., Raymond, P. A., Spahni, R., Suntharalingam, P., and Thullner, M.:
2673 Anthropogenic perturbation of the carbon fluxes from land to ocean, *Nature Geosci.*, 6, 597–607,
2674 <https://doi.org/10.1038/ngeo1830>, 2013.
- 2675 Regnier, P., Resplandy, L., Najjar, R. G., and Ciais, P.: The land-to-ocean loops of the global carbon cycle,
2676 *Nature*, 603, 401–410, <https://doi.org/10.1038/s41586-021-04339-9>, 2022.
- 2677 Reick, C. H., Gayler, V., Goll, D., Hagemann, S., Heidkamp, M., Nabel, J. E. M. S., Raddatz, T., Roeckner, E.,



- 2678 Schnur, R., and Wilkenskjaeld, S.: JSBACH 3 - The land component of the MPI Earth System Model:
2679 documentation of version 3.2, <https://doi.org/10.17617/2.3279802>, 2021.
- 2680 Remaud, M., Chevallier, F., Cozic, A., Lin, X., and Bousquet, P.: On the impact of recent developments of the
2681 LMDz atmospheric general circulation model on the simulation of CO₂ transport, 11, 4489,
2682 <https://doi.org/10.5194/gmd-11-4489-2018>, 2018.
- 2683 Resplandy, L., Keeling, R. F., Rödenbeck, C., Stephens, B. B., Khatiwala, S., Rodgers, K. B., Long, M. C.,
2684 Bopp, L., and Tans, P. P.: Revision of global carbon fluxes based on a reassessment of oceanic and riverine
2685 carbon transport, *Nature Geosci*, 11, 504–509, <https://doi.org/10.1038/s41561-018-0151-3>, 2018.
- 2686 Reynolds, R. W., Rayner, N. A., Smith, T. M., Stokes, D. C., and Wang, W.: An Improved In Situ and Satellite
2687 SST Analysis for Climate, *J. Clim.*, 15, 1609–1625, [https://doi.org/10.1175/1520-0442\(2002\)015<1609:AIISAS>2.0.CO;2](https://doi.org/10.1175/1520-0442(2002)015<1609:AIISAS>2.0.CO;2), 2002.
- 2689 Rhein, M., Rintoul, S. R., Aoki, S., Campos, E., Chambers, D., Feely, R. A., Gulev, S., Johnson, G. C., Josey, S.
2690 A., Kostianoy, A., Mauritzen, C., Roemmich, D., and Talley, L. D.: *Observations: Ocean*, edited by: Stocker, T.
2691 F., Qin, D., Plattner, G.-K., Tignor, M., Allen, S. K., Boschung, J., Nauels, A., Xia, Y., Bex, V., and Midgley, P.
2692 M., Cambridge University Press, 255–316, 2013.
- 2693 Rödenbeck, C., Houweling, S., Gloor, M., and Heimann, M.: CO₂ flux history 1982–2001 inferred from
2694 atmospheric data using a global inversion of atmospheric transport, 46, 2003.
- 2695 Rödenbeck, C., Keeling, R. F., Bakker, D. C. E., Metzl, N., Olsen, A., Sabine, C., and Heimann, M.: Global
2696 surface-ocean pCO₂ and sea–air CO₂ flux variability from an observation-driven ocean mixed-layer scheme, 9,
2697 193–216, <https://doi.org/10.5194/os-9-193-2013>, 2013.
- 2698 Rödenbeck, C., Bakker, D. C. E., Metzl, N., Olsen, A., Sabine, C., Cassar, N., Reum, F., Keeling, R. F., and
2699 Heimann, M.: Interannual sea–air CO₂ flux variability from an observation-driven ocean mixed-layer scheme,
2700 11, 4599–4613, <https://doi.org/10.5194/bg-11-4599-2014>, 2014.
- 2701 Rödenbeck, C., Bakker, D. C. E., Gruber, N., Iida, Y., Jacobson, A. R., Jones, S., Landschützer, P., Metzl, N.,
2702 Nakaoka, S., Olsen, A., Park, G.-H., Peylin, P., Rodgers, K. B., Sasse, T. P., Schuster, U., Shutler, J. D.,
2703 Valsala, V., Wanninkhof, R., and Zeng, J.: Data-based estimates of the ocean carbon sink variability – first
2704 results of the Surface Ocean CO₂ Mapping intercomparison (SOCOM), *Biogeosciences*, 12, 7251–7278,
2705 <https://doi.org/10.5194/bg-12-7251-2015>, 2015.
- 2706 Rödenbeck, C., Zaehle, S., Keeling, R., and Heimann, M.: History of El Niño impacts on the global carbon
2707 cycle 1957–2017: a quantification from atmospheric CO₂ data, 373, 20170303,
2708 <https://doi.org/10.1098/rstb.2017.0303>, 2018.
- 2709 Rödenbeck, C., DeVries, T., Hauck, J., Le Quéré, C., and Keeling, R. F.: Data-based estimates of interannual
2710 sea–air CO₂ flux variations 1957–2020 and their relation to environmental drivers, *Biogeosciences*, 19, 2627–
2711 2652, <https://doi.org/10.5194/bg-19-2627-2022>, 2022.



- 2712 Roobaert, A., Laruelle, G. G., Landschützer, P., and Regnier, P.: Uncertainty in the global oceanic CO₂ uptake
2713 induced by wind forcing: quantification and spatial analysis, 15, 1701–1720, [https://doi.org/10.5194/bg-15-](https://doi.org/10.5194/bg-15-1701-2018)
2714 1701-2018, 2018.
- 2715 Rosan, T. M., Klein Goldewijk, K., Ganzenmüller, R., O’Sullivan, M., Pongratz, J., Mercado, L. M., Aragao, L.
2716 E. O. C., Heinrich, V., Randow, C. V., Wiltshire, A., Tubiello, F. N., Bastos, A., Friedlingstein, P., and Sitch,
2717 S.: A multi-data assessment of land use and land cover emissions from Brazil during 2000–2019, *Environ. Res.*
2718 *Lett.*, 16, 074004, <https://doi.org/10.1088/1748-9326/ac08c3>, 2021.
- 2719 Rypdal, K., Paciorek, N., Eggleston, S., Goodwin, J., Irving, W., Penman, J., and Woodfield, M.: Volume 1:
2720 Introduction to the 2006 Guidelines in: 2006 IPCC guidelines for national greenhouse gas inventories., 2006.
- 2721 Saatchi, S. S., Harris, N. L., Brown, S., Lefsky, M., Mitchard, E. T. A., Salas, W., Zutta, B. R., Buermann, W.,
2722 Lewis, S. L., Hagen, S., Petrova, S., White, L., Silman, M., and Morel, A.: Benchmark map of forest carbon
2723 stocks in tropical regions across three continents, *Proceedings of the National Academy of Sciences*, 108, 9899–
2724 9904, <https://doi.org/10.1073/pnas.1019576108>, 2011.
- 2725 Sabine, C. L., Feely, R. A., Gruber, N., Key, R. M., Lee, K., Bullister, J. L., Wanninkhof, R., Wong, C. S.,
2726 Wallace, D. W. R., Tilbrook, B., Millero, F. J., Peng, T.-H., Kozyr, A., Ono, T., and Rios, A. F.: The Oceanic
2727 Sink for Anthropogenic CO₂, 305, 367–371, <https://doi.org/10.1126/science.1097403>, 2004.
- 2728 Sarmiento, J. L., Orr, J. C., and Siegenthaler, U.: A perturbation simulation of CO₂ uptake in an ocean general
2729 circulation model, 97, 3621–3645, <https://doi.org/10.1029/91JC02849>, 1992.
- 2730 Sato, M., Hansen, J. E., McCormick, M. P., and Pollack, J. B.: Stratospheric aerosol optical depths, 1850–1990,
2731 98, 22987–22994, <https://doi.org/10.1029/93JD02553>, 1993.
- 2732 Saunio, M., Stavert, A. R., Poulter, B., Bousquet, P., Canadell, J. G., Jackson, R. B., Raymond, P. A.,
2733 Dlugokencky, E. J., Houweling, S., Patra, P. K., Ciais, P., Arora, V. K., Bastviken, D., Bergamaschi, P., Blake,
2734 D. R., Brailsford, G., Bruhwiler, L., Carlson, K. M., Carrol, M., Castaldi, S., Chandra, N., Crevoisier, C., Crill,
2735 P. M., Covey, K., Curry, C. L., Etiope, G., Frankenberg, C., Gedney, N., Hegglin, M. I., Höglund-Isaksson, L.,
2736 Hugelius, G., Ishizawa, M., Ito, A., Janssens-Maenhout, G., Jensen, K. M., Joos, F., Kleinen, T., Krummel, P.
2737 B., Langenfelds, R. L., Laruelle, G. G., Liu, L., Machida, T., Maksyutov, S., McDonald, K. C., McNorton, J.,
2738 Müller, P. A., Melton, J. R., Morino, I., Müller, J., Murguía-Flores, F., Naik, V., Niwa, Y., Noce, S., O’Doherty,
2739 S., Parker, R. J., Peng, C., Peng, S., Peters, G. P., Prigent, C., Prinn, R., Ramonet, M., Regnier, P., Riley, W. J.,
2740 Rosentreter, J. A., Segers, A., Simpson, I. J., Shi, H., Smith, S. J., Steele, L. P., Thornton, B. F., Tian, H.,
2741 Tohjima, Y., Tubiello, F. N., Tsuruta, A., Viovy, N., Voulgarakis, A., Weber, T. S., van Weele, M., van der
2742 Werf, G. R., Weiss, R. F., Worthy, D., Wunch, D., Yin, Y., Yoshida, Y., Zhang, W., Zhang, Z., Zhao, Y.,
2743 Zheng, B., Zhu, Q., Zhu, Q., and Zhuang, Q.: The Global Methane Budget 2000–2017, *Earth Syst. Sci. Data*, 12,
2744 1561–1623, <https://doi.org/10.5194/essd-12-1561-2020>, 2020.
- 2745 Schimel, D., Alves, D., Enting, I. G., Heimann, M., Joos, F., Raynaud, D., Wigley, T., Prater, M., Derwent, R.,
2746 Ehhalt, D., Fraser, P., Sanhueza, E., Zhou, X., Jonas, P., Charlson, R., Rodhe, H., Sadasivan, S., Shine, K. P.,
2747 Fouquart, Y., Ramaswamy, V., Solomon, S., Srinivasan, J., Albritton, D., Derwent, R., Isaksen, I., Lal, M., and



- 2748 Wuebbles, D.: Radiative Forcing of Climate Change, in: *Climate Change 1995 The Science of Climate Change*,
2749 Contribution of Working Group I to the Second Assessment Report of the Intergovernmental Panel on Climate
2750 Change, edited by: Houghton, J. T., Meira Rillo, L. G., Callander, B. A., Harris, N., Kattenberg, A., and
2751 Maskell, K., Cambridge University Press, Cambridge, United Kingdom and New York, NY, USA, 1995.
- 2752 Schimel, D., Stephens, B. B., and Fisher, J. B.: Effect of increasing CO₂ on the terrestrial carbon cycle, *Proc*
2753 *Natl Acad Sci USA*, 112, 436–441, <https://doi.org/10.1073/pnas.1407302112>, 2015.
- 2754 Schourup-Kristensen, V., Sidorenko, D., Wolf-Gladrow, D. A., and Völker, C.: A skill assessment of the
2755 biogeochemical model REcoM2 coupled to the Finite Element Sea Ice–Ocean Model (FESOM 1.3), *Geosci.*
2756 *Model Dev.*, 7, 2769–2802, <https://doi.org/10.5194/gmd-7-2769-2014>, 2014.
- 2757 Schuh, A. E., Jacobson, A. R., Basu, S., Weir, B., Baker, D., Bowman, K., Chevallier, F., Crowell, S., Davis, K.
2758 J., Deng, F., Denning, S., Feng, L., Jones, D., Liu, J., and Palmer, P. I.: Quantifying the Impact of Atmospheric
2759 Transport Uncertainty on CO₂ Surface Flux Estimates, *Global Biogeochem. Cycles*, 33, 484–500,
2760 <https://doi.org/10.1029/2018GB006086>, 2019.
- 2761 Schuldt et al. Multi-laboratory compilation of atmospheric carbon dioxide data for the period 1957-2020.
2762 <https://doi.org/10.25925/20210801>
- 2763 Schuldt et al. Multi-laboratory compilation of atmospheric carbon dioxide data for the period 2021-2022.
2764 <http://doi.org/10.25925/20220624>
- 2765 Schwinger, J., Goris, N., Tjiputra, J. F., Kriest, I., Bentsen, M., Bethke, I., Ilicak, M., Assmann, K. M., and
2766 Heinze, C.: Evaluation of NorESM-OC (versions 1 and 1.2), the ocean carbon-cycle stand-alone configuration
2767 of the Norwegian Earth System Model (NorESM1), *Geosci. Model Dev.*, 9, 2589–2622,
2768 <https://doi.org/10.5194/gmd-9-2589-2016>, 2016.
- 2769 Schwingshackl, C., Obermeier, W., Bultan, S., Grassi, G., Canadell, J. G., Friedlingstein, P., Gasser, T.,
2770 Houghton, R. A., Kurz, W. A., Sitch, S., and Pongratz, J.: Separating natural and land-use CO₂ fluxes at
2771 country-level to reconcile land-based mitigation estimates, submitted, *One Earth*, 2022.
- 2772 Séférian, R., Nabat, P., Michou, M., Saint-Martin, D., Voltaire, A., Colin, J., Decharme, B., Delire, C., Berthet,
2773 S., Chevallier, M., Sénési, S., Franchisteguy, L., Vial, J., Mallet, M., Joetzjer, E., Geoffroy, O., Guérémy, J.-F.,
2774 Moine, M.-P., Msadek, R., Ribes, A., Rocher, M., Roehrig, R., Salas-y-Méllia, D., Sanchez, E., Terray, L.,
2775 Valcke, S., Waldman, R., Aumont, O., Bopp, L., Deshayes, J., Éthé, C., and Madec, G.: Evaluation of CNRM
2776 Earth System Model, CNRM-ESM2-1: Role of Earth System Processes in Present-Day and Future Climate,
2777 *Journal of Advances in Modeling Earth Systems*, 11, 4182–4227, <https://doi.org/10.1029/2019MS001791>, 2019.
- 2778 Seiler, C., Melton, J. R., Arora, V. K., Sitch, S., Friedlingstein, P., Anthoni, P., Goll, D., Jain, A. K., Joetzjer, E.,
2779 Lienert, S., Lombardozzi, D., Luyssaert, S., Nabel, J. E. M. S., Tian, H., Vuichard, N., Walker, A. P., Yuan, W.:
2780 Are terrestrial biosphere models fit for simulating the global land carbon sink? *Journal of Advances in Modeling*
2781 *Earth Systems*, 14, e2021MS002946 <https://doi.org/10.1029/2021MS002946>, 2022



- 2782 Sellar, A. A., Jones, C. G., Mulcahy, J. P., Tang, Y., Yool, A., Wiltshire, A., O'Connor, F. M., Stringer, M.,
2783 Hill, R., Palmieri, J., Woodward, S., Mora, L., Kuhlbrodt, T., Rumbold, S. T., Kelley, D. I., Ellis, R., Johnson,
2784 C. E., Walton, J., Abraham, N. L., Andrews, M. B., Andrews, T., Archibald, A. T., Berthou, S., Burke, E.,
2785 Blockley, E., Carslaw, K., Dalvi, M., Edwards, J., Folberth, G. A., Gedney, N., Griffiths, P. T., Harper, A. B.,
2786 Hendry, M. A., Hewitt, A. J., Johnson, B., Jones, A., Jones, C. D., Keeble, J., Liddicoat, S., Morgenstern, O.,
2787 Parker, R. J., Predoi, V., Robertson, E., Siahhan, A., Smith, R. S., Swaminathan, R., Woodhouse, M. T., Zeng,
2788 G., and Zerroukat, M.: UKESM1: Description and Evaluation of the U.K. Earth System Model, *J. Adv. Model.*
2789 *Earth Syst.*, 11, 4513–4558, <https://doi.org/10.1029/2019MS001739>, 2019.
- 2790 Shu, S., Jain, A. K., Koven, C. D., and Mishra, U.: Estimation of Permafrost SOC Stock and Turnover Time
2791 Using a Land Surface Model With Vertical Heterogeneity of Permafrost Soils, 34, e2020GB006585,
2792 <https://doi.org/10.1029/2020GB006585>, 2020.
- 2793 Silva Junior, C. H. L., Pessôa, A. C. M., Carvalho, N. S., Reis, J. B. C., Anderson, L. O., and Aragão, L. E. O.
2794 C.: The Brazilian Amazon deforestation rate in 2020 is the greatest of the decade, *Nat Ecol Evol*, 5, 144–145,
2795 <https://doi.org/10.1038/s41559-020-01368-x>, 2021.
- 2796 Sitch, S., Huntingford, C., Gedney, N., Levy, P. E., Lomas, M., Piao, S. L., Betts, R., Ciais, P., Cox, P.,
2797 Friedlingstein, P., Jones, C. D., Prentice, I. C., and Woodward, F. I.: Evaluation of the terrestrial carbon cycle,
2798 future plant geography and climate-carbon cycle feedbacks using five Dynamic Global Vegetation Models
2799 (DGVMs): Uncertainty In Land Carbon Cycle Feedbacks, 14, 2015–2039, [https://doi.org/10.1111/j.1365-](https://doi.org/10.1111/j.1365-2486.2008.01626.x)
2800 [2486.2008.01626.x](https://doi.org/10.1111/j.1365-2486.2008.01626.x), 2008.
- 2801 Smith, B., Wärlind, D., Arneth, A., Hickler, T., Leadley, P., Siltberg, J., and Zaehle, S.: Implications of
2802 incorporating N cycling and N limitations on primary production in an individual-based dynamic vegetation
2803 model, *Biogeosciences*, 11, 2027–2054, <https://doi.org/10.5194/bg-11-2027-2014>, 2014.
- 2804 Stephens, B. B., Gurney, K. R., Tans, P. P., Sweeney, C., Peters, W., Bruhwiler, L., Ciais, P., Ramonet, M.,
2805 Bousquet, P., Nakazawa, T., Aoki, S., Machida, T., Inoue, G., Vinnichenko, N., Lloyd, J., Jordan, A., Heimann,
2806 M., Shibistova, O., Langenfelds, R. L., Steele, L. P., Francey, R. J., and Denning, A. S.: Weak Northern and
2807 Strong Tropical Land Carbon Uptake from Vertical Profiles of Atmospheric CO₂, *Science*, 316, 1732–1735,
2808 <https://doi.org/10.1126/science.1137004>, 2007.
- 2809 Stocker, T., Qin, D., and Platner, G.-K.: Climate Change 2013: The Physical Science Basis. Contribution of
2810 Working Group I to the Fifth Assessment Report of the Intergovernmental Panel on Climate Change, edited by:
2811 Intergovernmental Panel on Climate Change, Cambridge University Press, Cambridge, 2013.
- 2812 Sweeney, C., Gloor, E., Jacobson, A. R., Key, R. M., McKinley, G., Sarmiento, J. L., and Wanninkhof, R.:
2813 Constraining global air-sea gas exchange for CO₂ with recent bomb 14C measurements, 21,
2814 <https://doi.org/10.1029/2006GB002784>, 2007.
- 2815 SX Coal: Monthly coal consumption estimates, <http://www.sxcoal.com/> (last access: 25 September 2022), 2022.
- 2816 Takahashi, T., Sutherland, S. C., Wanninkhof, R., Sweeney, C., Feely, R. A., Chipman, D. W., Hales, B.,



- 2817 Friederich, G., Chavez, F., Sabine, C., Watson, A., Bakker, D. C. E., Schuster, U., Metzler, N., Yoshikawa-Inoue,
2818 H., Ishii, M., Midorikawa, T., Nojiri, Y., Körtzinger, A., Steinhoff, T., Hoppema, M., Olafsson, J., Arnarson, T.
2819 S., Tilbrook, B., Johannessen, T., Olsen, A., Bellerby, R., Wong, C. S., Delille, B., Bates, N. R., and de Baar, H.
2820 J. W.: Climatological mean and decadal change in surface ocean pCO₂, and net sea–air CO₂ flux over the
2821 global oceans, *Deep Sea Research Part II: Topical Studies in Oceanography*, 56, 554–577,
2822 <https://doi.org/10.1016/j.dsr2.2008.12.009>, 2009.
- 2823 Terhaar, J., Frölicher, T., and Joos, F.: Southern Ocean anthropogenic carbon sink constrained by sea surface
2824 salinity, *Sci. Adv.*, 7, 5964–5992, <https://doi.org/10.1126/sciadv.abd5964>, 2021.
- 2825 Terhaar, J., Frölicher, T. L., and Joos, F.: Observation-constrained estimates of the global ocean carbon sink
2826 from Earth system models, *Biogeosciences*, 19, 4431–4457, <https://doi.org/10.5194/bg-19-4431-2022>, 2022.
- 2827 Thomason, L. W., Ernest, N., Millán, L., Rieger, L., Bourassa, A., Vernier, J.-P., Manney, G., Luo, B.,
2828 Arfeuille, F., and Peter, T.: A global space-based stratospheric aerosol climatology: 1979–2016, 10, 469–492,
2829 <https://doi.org/10.5194/essd-10-469-2018>, 2018.
- 2830 Tian, H., Xu, X., Lu, C., Liu, M., Ren, W., Chen, G., Melillo, J., and Liu, J.: Net exchanges of CO₂, CH₄, and
2831 N₂O between China’s terrestrial ecosystems and the atmosphere and their contributions to global climate
2832 warming, 116, <https://doi.org/10.1029/2010JG001393>, 2011.
- 2833 Tian, H., Chen, G., Lu, C., Xu, X., Hayes, D. J., Ren, W., Pan, S., Huntzinger, D. N., and Wofsy, S. C.: North
2834 American terrestrial CO₂ uptake largely offset by CH₄ and N₂O emissions: toward a full accounting of the
2835 greenhouse gas budget, *Climatic Change*, 129, 413–426, <https://doi.org/10.1007/s10584-014-1072-9>, 2015.
- 2836 Todd-Brown, K. E. O., Randerson, J. T., Post, W. M., Hoffman, F. M., Tarnocai, C., Schuur, E. A. G., and
2837 Allison, S. D.: Causes of variation in soil carbon simulations from CMIP5 Earth system models and comparison
2838 with observations, *Biogeosciences*, 10, 1717–1736, <https://doi.org/10.5194/bg-10-1717-2013>, 2013.
- 2839 Tohjima, Y., Mukai, H., Machida, T., Hoshina, Y., and Nakaoka, S.-I.: Global carbon budgets estimated from
2840 atmospheric O₂N₂ and CO₂ observations in the western Pacific region over a 15-year period, 19, 9269–9285,
2841 <https://doi.org/10.5194/acp-19-9269-2019>, 2019.
- 2842 Torero, M. and FAO: Impact of the Ukraine-Russia conflict on global food security and related matters under
2843 the mandate of the Food and Agriculture Organization of the United Nations (FAO), available at:
2844 <https://www.fao.org/3/njl164en/njl164en.pdf>, last access: 25 Sept 2022, 2022.
- 2845 Tubiello, F. N., Conchedda, G., Wanner, N., Federici, S., Rossi, S., and Grassi, G.: Carbon emissions and
2846 removals from forests: new estimates, 1990–2020, *Earth Syst. Sci. Data*, 13, 1681–1691,
2847 <https://doi.org/10.5194/essd-13-1681-2021>, 2021.
- 2848 Tyukavina A., Potapov P., Hansen M. C., Pickens A. H., Stehman S. V., Turubanova S., Parker D., Zalles V.,
2849 Lima A., Kommareddy I., Song X.-P., Wang L., Harris N.: Global Trends of Forest Loss Due to Fire From 2001
2850 to 2019, *Frontiers in Remote Sensing*, 3, <https://www.frontiersin.org/articles/10.3389/frsen.2022.825190>



- 2851 UN: United Nations Statistics Division: National Accounts Main Aggregates Database, available at:
2852 <http://unstats.un.org/unsd/snaama/Introduction.asp>, last access: 25 September 2022, 2021.
- 2853 UNFCCC: Synthesis report for the technical assessment component of the first global stocktake,
2854 <https://unfccc.int/documents/461466>, last access: 25 September 2022 2022
- 2855 Urakawa, L. S., Tsujino, H., Nakano, H., Sakamoto, K., Yamanaka, G., and Toyoda, T.: The sensitivity of a
2856 depth-coordinate model to diapycnal mixing induced by practical implementations of the isopycnal tracer
2857 diffusion scheme, *Ocean Model.*, 154, 101693, <https://doi.org/10.1016/j.ocemod.2020.101693>, 2020.
- 2858 Vale, M. M., Berenguer, E., Argollo de Menezes, M., Viveiros de Castro, E. B., Pugliese de Siqueira, L., and
2859 Portela, R. de C. Q.: The COVID-19 pandemic as an opportunity to weaken environmental protection in Brazil,
2860 *Biological Conservation*, 255, 108994, <https://doi.org/10.1016/j.biocon.2021.108994>, 2021.
- 2861 van der Laan-Luijkx, I. T., van der Velde, I. R., van der Veen, E., Tsuruta, A., Stanislawski, K.,
2862 Babenhausheide, A., Zhang, H. F., Liu, Y., He, W., Chen, H., Masarie, K. A., Krol, M. C., and Peters, W.:
2863 The CarbonTracker Data Assimilation Shell (CTDAS) v1.0: implementation and global carbon balance 2001–
2864 2015, *Geosci. Model Dev.*, 10, 2785–2800, <https://doi.org/10.5194/gmd-10-2785-2017>, 2017.
- 2865 van der Velde, I. R., Miller, J. B., Schaefer, K., van der Werf, G. R., Krol, M. C., and Peters, W.: Terrestrial
2866 cycling of ^{13}C by photosynthesis, respiration, and biomass burning in SiBCASA, 11, 6553–6571,
2867 <https://doi.org/10.5194/bg-11-6553-2014>, 2014.
- 2868 van der Velde, I. R., van der Werf, G. R., Houweling, S., Maasakkers, J. D., Borsdorff, T., Landgraf, J., Tol, P.,
2869 van Kempen, T. A., van Hees, R., Hoogeveen, R., Veeffkind, J. P., and Aben, I.: Vast CO_2 release from
2870 Australian fires in 2019–2020 constrained by satellite, 597, 366–369, [https://doi.org/10.1038/s41586-021-](https://doi.org/10.1038/s41586-021-03712-y)
2871 03712-y, 2021.
- 2872 van der Werf, G. R., Randerson, J. T., Giglio, L., Collatz, G. J., Mu, M., Kasibhatla, P. S., Morton, D. C.,
2873 DeFries, R. S., Jin, Y., and van Leeuwen, T. T.: Global fire emissions and the contribution of deforestation,
2874 savanna, forest, agricultural, and peat fires (1997–2009), *Atmos. Chem. Phys.*, 10, 11707–11735,
2875 <https://doi.org/10.5194/acp-10-11707-2010>, 2010.
- 2876 van der Werf, G. R., Randerson, J. T., Giglio, L., van Leeuwen, T. T., Chen, Y., Rogers, B. M., Mu, M., van
2877 Marle, M. J. E., Morton, D. C., Collatz, G. J., Yokelson, R. J., and Kasibhatla, P. S.: Global fire emissions
2878 estimates during 1997–2016, *Earth Syst. Sci. Data*, 9, 697–720, <https://doi.org/10.5194/essd-9-697-2017>, 2017.
- 2879 van Wees, D., van der Werf, G. R., Randerson, J. T., Andela, N., Chen, Y., and Morton, D. C.: The role of fire
2880 in global forest loss dynamics, *Glob. Change Biol.*, 27, 2377–2391, <https://doi.org/10.1111/gcb.15591>, 2021.
- 2881 Vaittinada Ayar, P., Bopp, L., Christian, J. R., Ilyina, T., Krasting, J. P., Séférian, R., Tsujino, H., Watanabe,
2882 M., Yool, A., and Tjiputra, J.: Contrasting projections of the ENSO-driven CO_2 flux variability in the equatorial
2883 Pacific under high-warming scenario, *Earth Syst. Dynam.*, 13, 1097–1118, [https://doi.org/10.5194/esd-13-1097-](https://doi.org/10.5194/esd-13-1097-2022)
2884 2022, 2022.



- 2885 Viovy, N.: CRUNCEP data set, available at:
2886 ftp://nacp.ornl.gov/synthesis/2009/frescati/temp/land_use_change/original/readme.htm, last access: 25
2887 September 2022, 2016.
- 2888 Vuichard, N., Messina, P., Luysaert, S., Guenet, B., Zaehle, S., Ghattas, J., Bastrikov, V., and Peylin, P.:
2889 Accounting for carbon and nitrogen interactions in the global terrestrial ecosystem model ORCHIDEE (trunk
2890 version, rev 4999): multi-scale evaluation of gross primary production, *Geosci. Model Dev.*, 12, 4751–4779,
2891 <https://doi.org/10.5194/gmd-12-4751-2019>, 2019.
- 2892 Walker, A. P., Quaife, T., Bodegom, P. M., De Kauwe, M. G., Keenan, T. F., Joiner, J., Lomas, M. R.,
2893 MacBean, N., Xu, C., Yang, X., and Woodward, F. I.: The impact of alternative trait-scaling hypotheses for the
2894 maximum photosynthetic carboxylation rate (V_{cmax}) on global gross primary production, *New Phytol.*, 215,
2895 1370–1386, <https://doi.org/10.1111/nph.14623>, 2017.
- 2896 Walker, A. P., De Kauwe, M. G., Bastos, A., Belmecheri, S., Georgiou, K., Keeling, R. F., McMahon, S. M.,
2897 Medlyn, B. E., Moore, D. J. P., Norby, R. J., Zaehle, S., Anderson-Teixeira, K. J., Battipaglia, G., Brienen, R. J.
2898 W., Cabugao, K. G., Cailleret, M., Campbell, E., Canadell, J. G., Ciais, P., Craig, M. E., Ellsworth, D. S.,
2899 Farquhar, G. D., Faticchi, S., Fisher, J. B., Frank, D. C., Graven, H., Gu, L., Haverd, V., Heilman, K., Heimann,
2900 M., Hungate, B. A., Iversen, C. M., Joos, F., Jiang, M., Keenan, T. F., Knauer, J., Körner, C., Leshyk, V. O.,
2901 Leuzinger, S., Liu, Y., MacBean, N., Malhi, Y., McVicar, T. R., Penuelas, J., Pongratz, J., Powell, A. S., Riutta,
2902 T., Sabot, M. E. B., Schleucher, J., Sitch, S., Smith, W. K., Sulman, B., Taylor, B., Terrer, C., Torn, M. S.,
2903 Treseder, K. K., Trugman, A. T., Trumbore, S. E., van Mantgem, P. J., Voelker, S. L., Whelan, M. E., and
2904 Zuidema, P. A.: Integrating the evidence for a terrestrial carbon sink caused by increasing atmospheric CO₂,
2905 229, 2413–2445, <https://doi.org/10.1111/nph.16866>, 2021.
- 2906 Wanninkhof, R.: Relationship between wind speed and gas exchange over the ocean, 97, 7373–7382,
2907 <https://doi.org/10.1029/92JC00188>, 1992.
- 2908 Wanninkhof, R.: Relationship between wind speed and gas exchange over the ocean revisited, 12, 351–362,
2909 <https://doi.org/10.4319/lom.2014.12.351>, 2014.
- 2910 Wanninkhof, R., Park, G.-H., Takahashi, T., Sweeney, C., Feely, R., Nojiri, Y., Gruber, N., Doney, S. C.,
2911 McKinley, G. A., Lenton, A., Le Quéré, C., Heinze, C., Schwinger, J., Graven, H., and Khattiwala, S.: Global
2912 ocean carbon uptake: magnitude, variability and trends, *Biogeosciences*, 10, 1983–2000,
2913 <https://doi.org/10.5194/bg-10-1983-2013>, 2013.
- 2914 Watson, A. J., Schuster, U., Shutler, J. D., Holding, T., Ashton, I. G. C., Landschützer, P., Woolf, D. K., and
2915 Goddijn-Murphy, L.: Revised estimates of ocean-atmosphere CO₂ flux are consistent with ocean carbon
2916 inventory, *Nat Commun.*, 11, 4422, <https://doi.org/10.1038/s41467-020-18203-3>, 2020.
- 2917 Watson, R. T., Rohde, H., Oeschger, H., and Siegenthaler, U.: Greenhouse Gases and Aerosols, in: *Climate*
2918 *Change: The IPCC Scientific Assessment*. Intergovernmental Panel on Climate Change (IPCC), edited by:
2919 Houghton, J. T., Jenkins, G. J., and Ephraums, J. J., Cambridge University Press, Cambridge, 140, 1990.



- 2920 Weiss, R. F. and Price, B. A.: Nitrous oxide solubility in water and seawater, *Marine Chemistry*, 8, 347–359,
2921 [https://doi.org/10.1016/0304-4203\(80\)90024-9](https://doi.org/10.1016/0304-4203(80)90024-9), 1980.
- 2922 Wenzel, S., Cox, P. M., Eyring, V., and Friedlingstein, P.: Projected land photosynthesis constrained by changes
2923 in the seasonal cycle of atmospheric CO₂, *Nature*, 538, 499–501, <https://doi.org/10.1038/nature19772>, 2016.
- 2924 Wilkenskjeld, S., Kloster, S., Pongratz, J., Raddatz, T., and Reick, C. H.: Comparing the influence of net and
2925 gross anthropogenic land-use and land-cover changes on the carbon cycle in the MPI-ESM, *Biogeosciences*, 11,
2926 4817–4828, <https://doi.org/10.5194/bg-11-4817-2014>, 2014.
- 2927 Wiltshire, A. J., Burke, E. J., Chadburn, S. E., Jones, C. D., Cox, P. M., Davies-Barnard, T., Friedlingstein, P.,
2928 Harper, A. B., Liddicoat, S., Sitch, S., and Zaehle, S.: JULES-CN: a coupled terrestrial carbon–nitrogen scheme
2929 (JULES vn5.1), 14, 2161–2186, <https://doi.org/10.5194/gmd-14-2161-2021>, 2021.
- 2930 Woodward, F. I. and Lomas, M. R.: Vegetation dynamics – simulating responses to climatic change, *Biol. Rev.*,
2931 79, 643–670, <https://doi.org/10.1017/S1464793103006419>, 2004.
- 2932 Wright, R. M., Le Quéré, C., Buitenhuis, E., Pitois, S., and Gibbons, M. J.: Role of jellyfish in the plankton
2933 ecosystem revealed using a global ocean biogeochemical model, 18, 1291–1320, [https://doi.org/10.5194/bg-18-](https://doi.org/10.5194/bg-18-1291-2021)
2934 1291-2021, 2021.
- 2935 Wunder, S., Kaimowitz, D., Jensen, S., and Feder, S.: Coronavirus, macroeconomy, and forests: What likely
2936 impacts?, *For. Policy Econ.*, 131, 102536, <https://doi.org/10.1016/j.forpol.2021.102536>, 2021.
- 2937 Xi, F., Davis, S. J., Ciais, P., Crawford-Brown, D., Guan, D., Pade, C., Shi, T., Syddall, M., Lv, J., Ji, L., Bing,
2938 L., Wang, J., Wei, W., Yang, K.-H., Lagerblad, B., Galan, I., Andrade, C., Zhang, Y., and Liu, Z.: Substantial
2939 global carbon uptake by cement carbonation, *Nature Geosci.*, 9, 880–883, <https://doi.org/10.1038/ngeo2840>,
2940 2016.
- 2941 Xia, J., Chen, Y., Liang, S., Liu, D., and Yuan, W.: Global simulations of carbon allocation coefficients for
2942 deciduous vegetation types, 67, 28016, <https://doi.org/10.3402/tellusb.v67.28016>, 2015.
- 2943 Yeager, S. G., Rosenbloom, N., Glanville, A. A., Wu, X., Simpson, I., Li, H., Molina, M. J., Krumhardt, K.,
2944 Mogen, S., Lindsay, K., Lombardozzi, D., Wieder, W., Kim, W. M., Richter, J. H., Long, M., Danabasoglu, G.,
2945 Bailey, D., Holland, M., Lovenduski, N., Strand, W. G., and King, T.: The Seasonal-to-Multiyear Large
2946 Ensemble (SMYLE) prediction system using the Community Earth System Model version 2, *Geoscientific*
2947 *Model Development*, 15, 6451–6493, <https://doi.org/10.5194/gmd-15-6451-2022>, 2022.
- 2948 Yin, X.: Responses of leaf nitrogen concentration and specific leaf area to atmospheric CO₂ enrichment: a
2949 retrospective synthesis across 62 species: Leaf response to atmospheric CO₂ enrichment, 8, 631–642,
2950 <https://doi.org/10.1046/j.1365-2486.2002.00497.x>, 2002.
- 2951 Yu, Z., Ciais, P., Piao, S., Houghton, R. A., Lu, C., Tian, H., Agathokleous, E., Kattal, G. R., Sitch, S., Goll, D.,
2952 Yue, X., Walker, A., Friedlingstein, P., Jain, A. K., Liu, S., and Zhou, G.: Forest expansion dominates China’s
2953 land carbon sink since 1980, *Nat. Commun.*, 13, 5374, <https://doi.org/10.1038/s41467-022-32961-2>, 2022.



- 2954 Yuan, W., Liu, D., Dong, W., Liu, S., Zhou, G., Yu, G., Zhao, T., Feng, J., Ma, Z., Chen, J., Chen, Y., Chen, S.,
2955 Han, S., Huang, J., Li, L., Liu, H., Liu, S., Ma, M., Wang, Y., Xia, J., Xu, W., Zhang, Q., Zhao, X., and Zhao,
2956 L.: Multiyear precipitation reduction strongly decreases carbon uptake over northern China, 119, 881–896,
2957 <https://doi.org/10.1002/2014JG002608>, 2014.
- 2958 Yue, C., Ciais, P., Luysaert, S., Li, W., McGrath, M. J., Chang, J., and Peng, S.: Representing anthropogenic
2959 gross land use change, wood harvest, and forest age dynamics in a global vegetation model ORCHIDEE-MICT
2960 v8.4.2, 11, 409–428, <https://doi.org/10.5194/gmd-11-409-2018>, 2018.
- 2961 Yue, X. and Unger, N.: The Yale Interactive terrestrial Biosphere model version 1.0: description, evaluation and
2962 implementation into NASA GISS ModelE2, *Geosci. Model Dev.*, 8, 2399–2417, [https://doi.org/10.5194/gmd-8-](https://doi.org/10.5194/gmd-8-2399-2015)
2963 [2399-2015](https://doi.org/10.5194/gmd-8-2399-2015), 2015.
- 2964 Zaehle, S. and Friend, A. D.: Carbon and nitrogen cycle dynamics in the O-CN land surface model: 1. Model
2965 description, site-scale evaluation, and sensitivity to parameter estimates: Site-scale evaluation of a C-N model,
2966 *Global Biogeochem. Cycles*, 24, <https://doi.org/10.1029/2009GB003521>, 2010.
- 2967 Zaehle, S., Ciais, P., Friend, A. D., and Prieur, V.: Carbon benefits of anthropogenic reactive nitrogen offset by
2968 nitrous oxide emissions, *Nature Geosci.*, 4, 601–605, <https://doi.org/10.1038/ngeo1207>, 2011.
- 2969 Zaehle, S., Medlyn, B. E., De Kauwe, M. G., Walker, A. P., Dietze, M. C., Hickler, T., Luo, Y., Wang, Y.-P., El-Masri,
2970 B., Thornton, P., Jain, A., Wang, S., Warlind, D., Weng, E., Parton, W., Iversen, C. M., Gallet-Budynek, A.,
2971 McCarthy, H., Finzi, A., Hanson, P. J., Prentice, I. C., Oren, R., and Norby, R. J.: Evaluation of 11 terrestrial
2972 carbon–nitrogen cycle models against observations from two temperate Free-Air CO₂ Enrichment studies,
2973 *New Phytol.*, 202, 803–822, <https://doi.org/10.1111/nph.12697>, 2014.
- 2974 Zeng, J., Nojiri, Y., Landschützer, P., Telszewski, M., and Nakaoka, S.: A Global Surface Ocean fCO₂ Climatology
2975 Based on a Feed-Forward Neural Network, 31, 1838–1849, <https://doi.org/10.1175/JTECH-D-13-00137.1>,
2976 2014.
- 2977 Zheng, B., Chevallier, F., Yin, Y., Ciais, P., Fortems-Cheiney, A., Deeter, M. N., Parker, R. J., Wang, Y., Worden, H.
2978 M., and Zhao, Y.: Global atmospheric carbon monoxide budget 2000–2017 inferred from multi-species
2979 atmospheric inversions, 26, 2019.
- 2980 Zheng, B., Ciais, P., Chevallier, F., Chuvieco, E., Chen, Y., and Yang, H.: Increasing forest fire emissions despite
2981 the decline in global burned area, 7, eabh2646, <https://doi.org/10.1126/sciadv.abh2646>, 2021.
- 2982 Zscheischler, J., Mahecha, M. D., Avitabile, V., Calle, L., Carvalhais, N., Ciais, P., Gans, F., Gruber, N.,
2983 Hartmann, J., Herold, M., Ichii, K., Jung, M., Landschützer, P., Laruelle, G. G., Lauerwald, R., Papale, D.,
2984 Peylin, P., Poulter, B., Ray, D., Regnier, P., Rödenbeck, C., Roman-Cuesta, R. M., Schwalm, C., Tramontana,
2985 G., Tyukavina, A., Valentini, R., van der Werf, G., West, T. O., Wolf, J. E., and Reichstein, M.: Reviews and
2986 syntheses: An empirical spatiotemporal description of the global surface–atmosphere carbon fluxes:



2987 opportunities and data limitations, Biogeosciences, 14, 3685–3703, <https://doi.org/10.5194/bg-14-3685-2017>,
2988 2017.

2989

2990

2991

2992

2993

2994



2995 **Tables**

2996

Table 1. Factors used to convert carbon in various units (by convention, Unit 1 = Unit 2 × conversion).			
Unit 1	Unit 2	Conversion	Source
GtC (gigatonnes of carbon)	ppm (parts per million) (a)	2.124 (b)	Ballantyne et al. (2012)
GtC (gigatonnes of carbon)	PgC (petagrams of carbon)		1 SI unit conversion
GtCO ₂ (gigatonnes of carbon dioxide)	GtC (gigatonnes of carbon)	3.664	44.01/12.011 in mass equivalent
GtC (gigatonnes of carbon)	MtC (megatonnes of carbon)	1000	SI unit conversion
(a) Measurements of atmospheric CO ₂ concentration have units of dry-air mole fraction. ‘ppm’ is an abbreviation for micromole/mol, dry air.			
(b) The use of a factor of 2.124 assumes that all the atmosphere is well mixed within one year. In reality, only the troposphere is well mixed and the growth rate of CO ₂ concentration in the less well-mixed stratosphere is not measured by sites from the NOAA network. Using a factor of 2.124 makes the approximation that the growth rate of CO ₂ concentration in the stratosphere equals that of the troposphere on a yearly basis.			

2997

2998



2999

Table 2. How to cite the individual components of the global carbon budget presented here.	
Component	Primary reference
Global fossil CO ₂ emissions (EFOS), total and by fuel type	Updated from Andrew and Peters (2021)
National territorial fossil CO ₂ emissions (EFOS)	Gilfillan and Marland (2022), UNFCCC (2022)
National consumption-based fossil CO ₂ emissions (EFOS) by country (consumption)	Peters et al. (2011b) updated as described in this paper
Net land-use change flux (ELUC)	This paper (see Table 4 for individual model references).
Growth rate in atmospheric CO ₂ concentration (GATM)	Dlugokencky and Tans (2022)
Ocean and land CO ₂ sinks (SOCEAN and SLAND)	This paper (see Table 4 for individual model and data products references).

3000



Table 3. Main methodological changes in the global carbon budget since 2018. Methodological changes introduced in one year are kept for the following years unless noted. Empty cells mean there were no methodological changes introduced that year. Table A7 lists methodological changes from the first global carbon budget publication up to 2017.

Publication year	Fossil fuel emissions		LUC emissions	Reservoirs			Uncertainty & other changes
	Global	Country (territorial)		Atmosphere	Ocean	Land	
2018 Le Quéré et al. (2018b) GCB2018	Revision in cement emissions; Projection includes EU-specific data	Aggregation of overseas territories into governing nations for total of 213 countries a	Average of two bookkeeping models; use of 16 DGVMs	Use of four atmospheric inversions	Based on seven models	Based on 16 models; revised atmospheric forcing from CRUNCEP to CRUJRA	Introduction of metrics for evaluation of individual models using observations
2019 Friedlingstein et al. (2019) GCB2019	Global emissions calculated as sum of all countries plus bunkers, rather than taken directly from CDIAC.		Average of two bookkeeping models; use of 15 DGVMs	Use of three atmospheric inversions	Based on nine models	Based on 16 models	
2020 Friedlingstein et al. (2020) GCB2020	Cement carbonation now included in the EFOS estimate, reducing EFOS by about 0.2GtC yr ⁻¹ for the last decade	India's emissions from Andrew (2020: India); Corrections to Netherland Antilles and Aruba and Soviet emissions before 1950 as per Andrew (2020: CO ₂); China's coal emissions in 2019 derived from official statistics, emissions now shown for EU27 instead of EU28. Projection for 2020 based on assessment of four	Average of three bookkeeping models; use of 17 DGVMs. Estimate of gross land use sources and sinks provided	Use of six atmospheric inversions	Based on nine models. River flux revised and partitioned NH, Tropics, SH	Based on 17 models	



		approaches.					
2021	Projections are no longer an assessment of four approaches.	Official data included for a number of additional countries, new estimates for South Korea, added emissions from lime production in China.	ELUC estimate compared to the estimates adopted in national GHG inventories (NGHGI)		Average of means of eight models and means of seven data-products. Current year prediction of SOCEAN using a feed-forward neural network method	Current year prediction of SLAND using a feed-forward neural network method	
Friedlingstein et al. (2022a) GCB2021							
2022	This study		ELUC provided at country level. Decomposition into fluxes from deforestation, organic soils, uptake in forests, and other transitions. Change in the methodology to derive LUC maps for Brazil to capture recent upturn in deforestation	Use of nine atmospheric inversions	Average of means of ten models and means of seven data-products	Based on 16 models. Change in the methodology to derive LUC maps for Brazil to capture recent upturn in deforestation	



Table 4. References for the process models, bookkeeping models, ocean data products, and atmospheric inversions. All models and products are updated with new data to the end of year 2021, and the atmospheric forcing for the DGVMs has been updated as described in Section C.2.2.

Model/data name	Reference	Change from Global Carbon Budget 2021 (Friedlingstein et al., 2022a)
<i>Bookkeeping models for land-use change emissions</i>		
BLUE	Hansis et al. (2015)	No change to model, but simulations performed with updated LUH2 forcing. Update in added peat drainage emissions (based on three spatially explicit datasets).
updated H&N2017	Houghton and Nassikas (2017)	Minor bug fix in the fuel harvest estimates, that was causing an overestimation of fuel sink. Update in added peat drainage emissions (based on three spatially explicit datasets).
OSCAR	Gasser et al. (2020)	No change to model, but land use forcing changed to LUH2-GCB2022 and FRA2020 (as used by H&N and extrapolated to 2021), both prescribed at higher spatial resolution (210 instead of 96 regions/countries). Constraining based on last year's budget data for SLAND over 1960-2021. Update in added peat drainage emissions (based on three spatially explicit datasets).
<i>Dynamic global vegetation models</i>		
CABLE-POP	Haverd et al. (2018)	changes in parameterisation. Diffuse fraction of incoming radiation read in as forcing.
CLASSIC	Melton et al. (2020) (a)	Minor bug fixes.
CLM5.0	Lawrence et al. (2019)	No change.
DLEM	Tian et al. (2015) (b)	No change.
IBIS	Yuan et al. (2014) (c)	No change.
ISAM	Meiyappan et al. (2015) (d)	No change.
JSBACH	Reick et al. (2021) (f)	No change.
JULES-ES	Wiltshire et al. (2021) (g)	Minor bug fixes. (Using JULES v6.3, suite u-co002)
LPJ-GUESS	Smith et al. (2014) (h)	No change.
LPJ	Poulter et al. (2011) (i)	No change.
LPX-Bern	Lienert and Joos (2018)	Following the results of Joos et al. (2018), we use modified parameter values which yield a more reasonable (lower) BNF, termed LPX v1.5. This parameter version has increased N immobilization and a stronger N limitation, than the previous version. The N ₂ O Emissions were adjusted accordingly. The parameters



		were obtained by running an ensemble simulation and imposing various observational constraints and subsequently adjusting N immobilization. For the methodology see Lienert et. al. (2018).
OCN	Zaehle and Friend (2010) (j)	No change (uses r294).
ORCHIDEEv3	Vuichard et al. (2019) (k)	No change (ORCHIDEE - V3; revision 7267)
SDGVM	Walker et al. (2017) (l)	No change.
VISIT	Kato et al. (2013) (m)	No change.
YIBs	Yue and Unger (2015)	No change.
<i>Global ocean biogeochemistry models</i>		
NEMO-PlankTOM12	Wright et al. (2021)	Minor bug fixes
MICOM-HAMOCC (NorESM-OCv1.2)	Schwinger et al. (2016)	No change.
MPIOM-HAMOCC6	Lacroix et al. (2021)	No change.
NEMO3.6-PISCESv2-gas (CNRM)	Berthet et al. (2019) (n)	No change.
FESOM-2.1-REcoM2	Hauck et al. (2020) (o)	Extended spin-up, minor bug fixes
MOM6-COBALT (Princeton)	Liao et al. (2020)	No change
CESM-ETHZ	Doney et al. (2009)	Changed salinity restoring in the surface ocean from 700 days to 300 days, except for the Southern Ocean south of 45S, where the restoring timescale was set to 60 days.
NEMO-PISCES (IPSL)	Aumont et al. (2015)	No change.
MRI-ESM2-1	Nakano et al. (2011), Urakawa et al. (2020)	New this year.
CESM2	Long et al. (2021) (p)	New this year.
<i>ocean data products</i>		
MPI-SOMFFN	Landschützer et al. (2016)	update to SOCATv2022 measurements and timeperiod 1982-2021; The estimate now covers the full ocean domain as well as the Arctic Ocean extension described in: Landschützer, P., Laruelle, G. G., Roobaert, A., and Regnier, P.: A uniform pCO ₂



		climatology combining open and coastal oceans, Earth Syst. Sci. Data, 12, 2537–2553, https://doi.org/10.5194/essd-12-2537-2020, 2020.
Jena-MLS	Rödenbeck et al. (2022)	update to SOCATv2022 measurements, time period extended to 1957-2021
CMEMS-LSCE-FFNNv2	Chau et al. (2022)	Update to SOCATv2022 measurements and time period 1985-2021. The CMEMS-LSCE-FFNNv2 product now covers both the open ocean and coastal regions.
LDEO-HPD	Gloege et al. (2022) (q)	New this year
UOEx-Watson	Watson et al. (2020)	Updated to SOCAT v2022 and OISSTv2.1, as recalculated by Holding et al.
NIES-NN	Zeng et al. (2014)	Updated to SOCAT v2022. Small changes in method (gas-exchange coefficient $a = 0.271$; trend calculation 1990-2020, predictors include lon and lat)
JMA-MLR	Iida et al. (2021)	Updated to SOCATv2022 SST fields (MGDSST) updated
OS-ETHZ-GRaCER	Gregor and Gruber (2021)	No change
<i>Atmospheric inversions</i>		
CAMS	Chevallier et al. (2005) (r)	Updated to WMOX2019 scale. Extension to year 2021, revision of the station list, update of the prior fluxes
CarbonTracker Europe (CTE)	van der Laan-Luijkx et al. (2017)	Updated to WMOX2019 scale. Biosphere prior fluxes from the SiB4 model instead of SiBCASA model. Extension to 2021.
Jena CarboScope	Rödenbeck et al. (2018) (s)	Updated to WMOX2019 scale. Extension to 2021.
UoE in-situ	Feng et al., (2016) (t)	Updated to WMOX2019 scale. Updated station list, and refined land-ocean map. Extension to 2021.
NISMOM-CO2	Niwa et al., (2022) (u)	Updated to WMOX2019 scale. Positive definite flux parameters and updated station list. Extension to 2021.
CMS-Flux	Liu et al., (2021)	Updated to WMOX2019 scale. Extension to 2021.
GONGGA	Jin et al. (2022 in review) (v)	New this year.
THU	Kong et al. (2022)	New this year.
CAMS-Satellite	Chevallier et al. (2005) (r)	New this year.
(a) see also Asaadi et al. (2018).		
(b) see also Tian et al. (2011)		
(c) the dynamic carbon allocation scheme was presented by Xia et al. (2015)		
(d) see also Jain et al. (2013). Soil biogeochemistry is updated based on Shu et al. (2020)		



(e) see also Decharme et al. (2019) and Seferian et al. (2019)
(f) see also Mauritsen et al. (2019)
(g) see also Sellar et al. (2019) and Burton et al., (2019). JULES-ES is the Earth System configuration of the Joint UK Land Environment Simulator as used in the UK Earth System Model (UKESM).
(h) to account for the differences between the derivation of shortwave radiation from CRU cloudiness and DSWRF from CRUJRA, the photosynthesis scaling parameter α was modified (-15%) to yield similar results.
(i) compared to published version, decreased LPJ wood harvest efficiency so that 50 % of biomass was removed off-site compared to 85 % used in the 2012 budget. Residue management of managed grasslands increased so that 100 % of harvested grass enters the litter pool.
(j) see also Zaehle et al. (2011).
(k) see also Zaehle and Friend (2010) and Krinner et al. (2005)
(l) see also Woodward and Lomas (2004)
(m) see also Ito and Inatomi (2012).
(n) see also Séférian et al. (2019)
(o) see also Schourup-Kristensen et al (2014)
(p) see also Yeager et al. (2022)
(q) see also Bennington et al. (2022)
(r) see also Remaud (2018)
(s) see also Rödenbeck et al. (2003)
(t) see also Feng et al. (2009) and Palmer et al. (2019)
(u) see also Niwa et al. (2020)
(v) see also Tian et al. (2014)



Table 5. Comparison of results from the bookkeeping method and budget residuals with results from the DGVMs and inverse estimates for different periods, the last decade, and the last year available. All values are in GtCyr⁻¹. See Fig. 7 for explanation of the bookkeeping component fluxes. The DGVM uncertainties represent $\pm 1\sigma$ of the decadal or annual (for 2021) estimates from the individual DGVMs: for the inverse systems the range of available results is given. All values are rounded to the nearest 0.1 GtC and therefore columns do not necessarily add to zero.

		<i>Mean (GtC/yr)</i>						
		1960s	1970s	1980s	1990s	2000s	2012-2021	2021
Land-use change emissions (ELUC)	Bookkeeping (BK) Net flux (1a)	1.5±0.7	1.2±0.7	1.3±0.7	1.5±0.7	1.4±0.7	1.2±0.7	1.1±0.7
	BK - deforestation	1.6±0.4	1.5±0.4	1.6±0.4	1.8±0.3	1.9±0.4	1.8±0.4	1.8±0.4
	BK - organic soils	0.1±0.1	0.1±0.1	0.2±0.1	0.2±0.1	0.2±0.1	0.2±0.1	0.2±0.1
	BK - re-/afforestation and forestry	-0.6±0.1	-0.6±0.1	-0.6±0.2	-0.7±0.1	-0.8±0.2	-0.9±0.3	-1.0±0.3
	BK - other transitions	0.4±0.0	0.2±0.1	0.2±0.1	0.1±0.1	0.1±0.1	0.1±0.1	0.1±0.1
	DGVMs _{net} flux (1b)	1.4±0.5	1.3±0.5	1.5±0.5	1.5±0.6	1.6±0.6	1.6±0.5	1.6±0.5
Terrestrial sink (SLAND)	Residual sink from global budget (EFOS+ELUC(1a)-GATM-SOCEAN) (2a)	1.7±0.8	1.8±0.8	1.6±0.9	2.6±0.9	2.8±0.9	2.8±0.9	2.8±1
	DGVMs (2b)	1.2±0.4	2.2±0.5	1.9±0.7	2.5±0.4	2.7±0.5	3.1±0.6	3.5±0.9
Total land fluxes (SLAND-ELUC)	GCB2022 Budget (2b-1a)	-0.2±0.8	1±0.9	0.5±1	1±0.8	1.4±0.9	1.9±0.9	2.4±1.1
	Budget constraint (2a-1a)	0.2±0.4	0.6±0.5	0.3±0.5	1.1±0.5	1.5±0.6	1.5±0.6	1.7±0.7
	DGVMs _{net} (2b-1b)	-0.1±0.4	0.9±0.5	0.4±0.5	0.9±0.4	1.2±0.3	1.5±0.5	1.9±0.7
	Inversions ^a	---	---	0.3-0.6 (2)	0.7-1.1 (3)	1.2-1.6 (3)	1.1-1.7 (7)	1.5-2.1 (9)

^aEstimates are adjusted for the pre-industrial influence of river fluxes, for the cement carbonation sink, and adjusted to common EFOS (Sect. 2.6). The ranges given include varying numbers (in parentheses) of inversions in each decade (Table A4)



Table 6. Decadal mean in the five components of the anthropogenic CO₂ budget for different periods, and last year available. All values are in GtC yr⁻¹, and uncertainties are reported as ±1σ. Fossil CO₂ emissions include cement carbonation. The table also shows the budget imbalance (B_{IM}), which provides a measure of the discrepancies among the nearly independent estimates. A positive imbalance means the emissions are overestimated and/or the sinks are too small. All values are rounded to the nearest 0.1 GtC and therefore columns do not necessarily add to zero.

		<i>Mean (GtC/yr)</i>							
		1960s	1970s	1980s	1990s	2000s	2012-2021	2021	2022 (Projection)
Total emissions (EFOS + ELUC)	Fossil CO ₂ emissions (EFOS) [*]	3±0.2	4.7±0.2	5.5±0.3	6.3±0.3	7.7±0.4	9.6±0.5	9.9±0.5	10.2±0.5
	Land-use change emissions (ELUC)	1.5±0.7	1.2±0.7	1.3±0.7	1.5±0.7	1.4±0.7	1.2±0.7	1.1±0.7	1±0.7
	Total emissions	4.5±0.7	5.9±0.7	6.8±0.8	7.8±0.8	9.1±0.8	10.8±0.8	10.9±0.9	11.1±0.9
Partitioning	Growth rate in atmos CO ₂ (GATM)	1.7±0.07	2.8±0.07	3.4±0.02	3.1±0.02	4±0.02	5.2±0.02	5.2±0.2	5.5±0.4
	Ocean sink (SOCEAN)	1.1±0.4	1.4±0.4	1.8±0.4	2.1±0.4	2.3±0.4	2.9±0.4	2.9±0.4	2.9±0.4
	Terrestrial sink (SLAND)	1.2±0.4	2.2±0.5	1.9±0.7	2.5±0.4	2.7±0.5	3.1±0.6	3.5±0.9	3.4±0.9
Budget imbalance	B _{IM} = EFOS + ELUC - (GATM + SOCEAN + SLAND)	0.4	-0.4	-0.3	0.1	0.1	-0.3	-0.6	-0.6

^{*}Fossil emissions excluding the cement carbonation sink amount to 3.1±0.2 GtC/yr, 4.7±0.2 GtC/yr, 5.5±0.3 GtC/yr, 6.4±0.3 GtC/yr, 7.9±0.4 GtC/yr, and 9.8±0.5 GtC/yr for the decades 1960s to 2010s respectively and to 10.1±0.5 GtC/yr for 2021.



Table 7. Comparison of the projection with realised fossil CO₂ emissions (EFOS). The ‘Actual’ values are first the estimate available using actual data, and the ‘Projected’ values refers to estimates made before the end of the year for each publication. Projections based on a different method from that described here during 2008-2014 are available in Le Quéré et al., (2016). All values are adjusted for leap years.

	World		China		USA		EU28 / EU27 (i)		India		Rest of World	
	Project ed	Actual	Proje cted	Actual	Proje cted	Actual	Proje cted	Actual	Proje cted	Actual	Proje cted	Actual
2015 (a)	-0.6%	0.06%	-3.9%	-0.7%	-1.5%	-2.5%	-	-	-	-	1.2%	1.2%
	(-1.6 to 0.5)		(-4.6 to -1.1)		(-5.5 to 0.3)		(-0.2 to 2.6)					
2016 (b)	-0.2%	0.20%	-0.5%	-0.3%	-1.7%	-2.1%	-	-	-	-	1.0%	1.3%
	(-1.0 to +1.8)		(-3.8 to +1.3)		(-4.0 to +0.6)		(-0.4 to +2.5)					
2017 (c)	2.0%	1.6%	3.5%	1.5%	-0.4%	-0.5%	-	-	2.00%	3.9%	1.6%	1.9%
	(+0.8 to +3.0)		(+0.7 to +5.4)		(-2.7 to +1.0)		(+0.2 to +3.8)		(0.0 to +3.2)			
2018 (d)	2.7%	2.1%	4.7%	2.3%	2.5%	2.8%	-0.7%	-2.1%	6.3%	8.0%	1.8%	1.7%
	(+1.8 to +3.7)		(+2.0 to +7.4)		(+0.5 to +4.5)		(-2.6 to +1.3)		(+4.3 to +8.3)		(+0.5 to +3.0)	
2019 (e)	0.5%	0.1%	2.6%	2.2%	-2.4%	-2.6%	-1.7%	-4.3%	1.8%	1.0%	0.5%	0.5%
	(-0.3 to +1.4)		(+0.7 to +4.4)		(-4.7 to -0.1)		(-5.1 to +1.8%)		(-0.7 to +3.7)		(-0.8 to +1.8)	
2020 (f)	-6.7%	-5.4%	-1.7%	1.4%	-12.2%	-10.6%	-11.3%	-10.9%	-9.1%	-7.3%	-7.4%	-7.0%
2021 (g)	4.8%	5.1%	4.3%	3.5%	6.8%	6.2%	6.3%	6.8%	11.2%	11.1%	3.2%	4.5%
	(4.2 to 5.4)		(3.0 to 5.4)		(6.6 to 7.0)		(4.3 to 8.3)		(10.7 to 11.7)		(2.0 to 4.3)	
2022 (h)	1.1%	(0% to 1.7%)	-1.5%	(0.1%)	1.6%	(4.1%)	-1.0%	(1.0%)	5.6%	(7.7%)	2.5%	(2.3%)
			(-3.0 to 0.1)		(-0.9 to 4.1)		(-2.9 to 1.0)		(3.5 to 7.7)		(0.1 to 2.3)	

(a) Jackson et al. (2016) and Le Quéré et al. (2015a). (b) Le Quéré et al. (2016). (c) Le Quéré et al. (2018a). (d) Le Quéré et al. (2018b). (e) Friedlingstein et al., (2019), (f) Friedlingstein et al., (2020), (g) Friedlingstein et al., (2022a), (h) This study

(i) EU28 until 2019, EU27 from 2020



Table 8. Cumulative CO₂ for different time periods in gigatonnes of carbon (GtC). Fossil CO₂ emissions include cement carbonation. The budget imbalance (B_{IM}) provides a measure of the discrepancies among the nearly independent estimates. All values are rounded to the nearest 5 GtC and therefore columns do not necessarily add to zero. Uncertainties are reported as follows: E_{FOS} is 5% of cumulative emissions; E_{LUC} prior to 1959 is 1σ spread from the DGVMs, E_{LUC} post-1959 is 0.7*number of years (where 0.7 GtC/yr is the uncertainty on the annual ELUC flux estimate); G_{ATM} uncertainty is held constant at 5 GtC for all time periods; S_{OCEAN} uncertainty is 20% of the cumulative sink (20% relates to the annual uncertainty of 0.4 GtC/yr, which is ~20% of the current ocean sink); and S_{LAND} is the 1σ spread from the DGVMs estimates.

		1750-2021	1850-2014	1850-2021	1960-2021	1850-2022
Emissions	Fossil CO ₂ emissions (E _{FOS})	470±25	400±20	465±25	385±20	475±25
	Land-use change emissions (E _{LUC})	235±70	195±60	205±60	85±45	205±60
	Total emissions	700±75	595±60	670±65	470±50	680±65
Partitioning	Growth rate in atmos CO ₂ (G _{ATM})	295±5	235±5	275±5	210±5	280±5
	Ocean sink (S _{OCEAN})	185±35	155±30	175±35	120±25	180±35
	Terrestrial sink (S _{LAND})	230±50	185±40	210±45	145±30	210±45
Budget imbalance	B _{IM} =E _{FOS} +E _{LUC} -(G _{ATM} +S _{OCEAN} +S _{LAND})	-5	15	15	-5	10

Table 9: Mapping of global carbon cycle models' land flux definitions to the definition of the LULUCF net flux used in national Greenhouse Gas Inventories reported to UNFCCC. See Sec. C.2.3 and Tab. A8 for detail on methodology and comparison to other datasets.

	2002-2011	2012-2021
ELUC from bookkeeping estimates (from Table 5)	1.4	1.2
SLAND on non-intact forest from DGVMs	-1.7	-1.8
ELUC plus SLAND on non-intact forests	-0.3	-0.6
National Greenhouse Gas Inventories	-0.4	-0.5



Table 10. Major known sources of uncertainties in each component of the Global Carbon Budget, defined as input data or processes that have a demonstrated effect of at least ± 0.3 GtC yr⁻¹.

Source of uncertainty	Time scale (years)	Location	Status	Evidence
Fossil CO₂ emissions (EFOS; Section 2.1)				
energy statistics	annual to decadal	global, but mainly China & major developing countries	see Sect. 2.1	(Korsbakken et al., 2016, Guan et al., 2012)
carbon content of coal	annual to decadal	global, but mainly China & major developing countries	see Sect. 2.1	(Liu et al., 2015)
system boundary	annual to decadal	all countries	see Sect. 2.1	(Andrew, 2020)
Net land-use change flux (ELUC; section 2.2)				
land-cover and land-use change statistics	continuous	global; in particular tropics	see Sect. 2.4	(Houghton et al., 2012, Gasser et al., 2020, Ganzenmüller et al., 2022, Yu et al. 2022)
sub-grid-scale transitions	annual to decadal	global	see Sect. 2.4, Table A1	(Wilenskij et al., 2014)
vegetation biomass	annual to decadal	global; in particular tropics	see Sect. 2.4	(Houghton et al., 2012, Bastos et al., 2021)
forest degradation (fire, selective logging)	annual to decadal	tropics	see Sect. 3.2.2, Table A1	(Aragão et al., 2018, Qin et al., 2020)
wood and crop harvest	annual to decadal	global; SE Asia	see Table A1	(Arneeth et al., 2017, Erb et al., 2018)
peat burning (a)	multi-decadal trend	global	see Table A1	(van der Werf et al., 2010, 2017)
loss of additional sink capacity	multi-decadal trend	global	not included; see Appendix D4	(Pongratz et al., 2014, Gasser et al., 2020; Obermeier et al., 2021)
Atmospheric growth rate (GATM; section 2.3) no demonstrated uncertainties larger than ± 0.3 GtC yr⁻¹ (b)				
Ocean sink (SOCEAN; section 2.4)				
sparsity in surface fCO ₂ observations	mean, decadal variability and trend	global, in particular southern hemisphere	see Sect 3.5.2	(Gloege et al., 2021, Denvil-Sommer et al., 2021, Bushinsky et al., 2019)
riverine carbon outgassing and its anthropogenic perturbation	annual to decadal	global, in particular partitioning between Tropics and South	see Sect. 2.4 (anthropogenic perturbations not included)	(Aumont et al., 2001, Resplandy et al., 2018, Lacroix et al., 2020)
Models underestimate interior ocean	annual to decadal	global	see Sect 3.5.5	(Friedlingstein et al., 2021, this study, see also Terhaar et al., 2022)



anthropogenic carbon storage				
near-surface temperature and salinity gradients	mean on all time-scales	global	see Sect. 3.8.2	(Watson et al., 2020, Dong et al., 2022)
Land sink (SLAND; section 2.5)				
strength of CO ₂ fertilisation	multi-decadal trend	global	see Sect. 2.5	(Wenzel et al., 2016; Walker et al., 2021)
response to variability in temperature and rainfall	annual to decadal	global; in particular tropics	see Sect. 2.5	(Cox et al., 2013; Jung et al., 2017; Humphrey et al., 2018; 2021)
nutrient limitation and supply	annual to decadal	global		(Zaehle et al., 2014)
carbon allocation and tissue turnover rates	annual to decadal	global		(De Kauwe et al., 2014; O'Sullivan et al., 2022)
tree mortality	annual	global in particular tropics	see Sect. 2.5	(Hubau et al., 2021; Brienen et al., 2020)
response to diffuse radiation	annual	global	see Sect. 2.5	(Mercado et al., 2009; O'Sullivan et al., 2021)
(a) As result of interactions between land-use and climate				
(b) The uncertainties in GATM have been estimated as ± 0.2 GtC yr ⁻¹ , although the conversion of the growth rate into a global annual flux assuming instantaneous mixing throughout the atmosphere introduces additional errors that have not yet been quantified.				



Figures and Captions

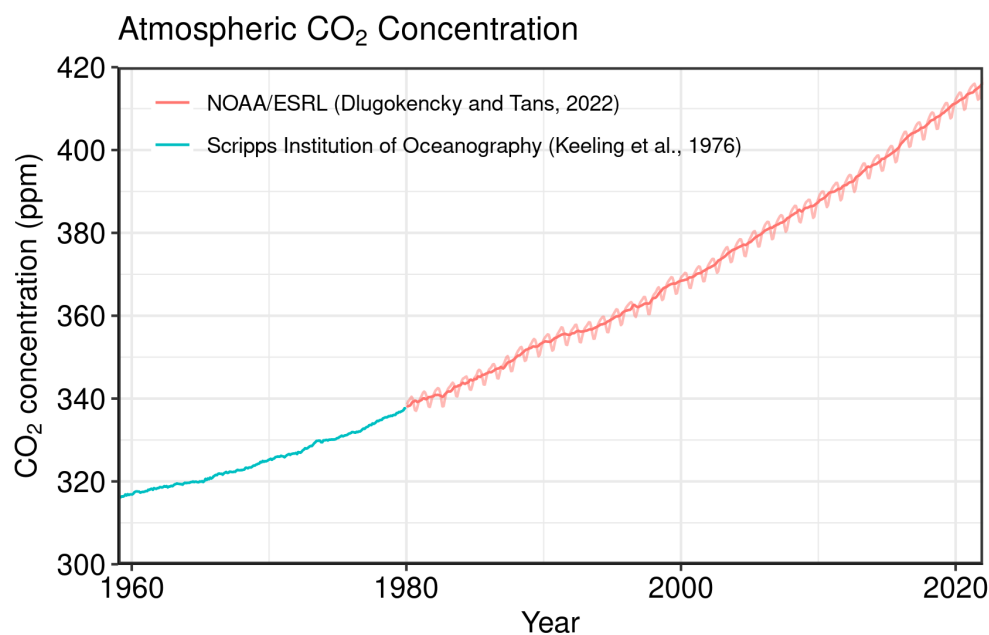


Figure 1. Surface average atmospheric CO₂ concentration (ppm). Since 1980, monthly data are from NOAA/ESRL (Dlugokencky and Tans, 2022) and are based on an average of direct atmospheric CO₂ measurements from multiple stations in the marine boundary layer (Masarie and Tans, 1995). The 1958-1979 monthly data are from the Scripps Institution of Oceanography, based on an average of direct atmospheric CO₂ measurements from the Mauna Loa and South Pole stations (Keeling et al., 1976). To account for the difference of mean CO₂ and seasonality between the NOAA/ESRL and the Scripps station networks used here, the Scripps surface average (from two stations) was de-seasonalised and adjusted to match the NOAA/ESRL surface average (from multiple stations) by adding the mean difference of 0.667 ppm, calculated here from overlapping data during 1980-2012.

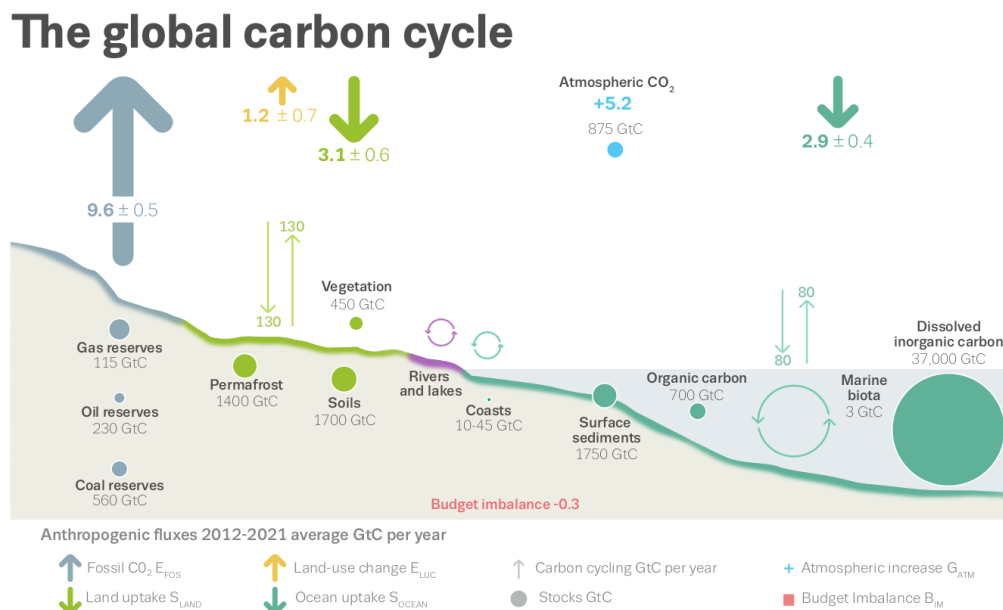


Figure 2. Schematic representation of the overall perturbation of the global carbon cycle caused by anthropogenic activities, averaged globally for the decade 2012-2021. See legends for the corresponding arrows and units. The uncertainty in the atmospheric CO₂ growth rate is very small (± 0.02 GtC yr⁻¹) and is neglected for the figure. The anthropogenic perturbation occurs on top of an active carbon cycle, with fluxes and stocks represented in the background and taken from Canadell et al. (2021) for all numbers, except for the carbon stocks in coasts which is from a literature review of coastal marine sediments (Price and Warren, 2016).

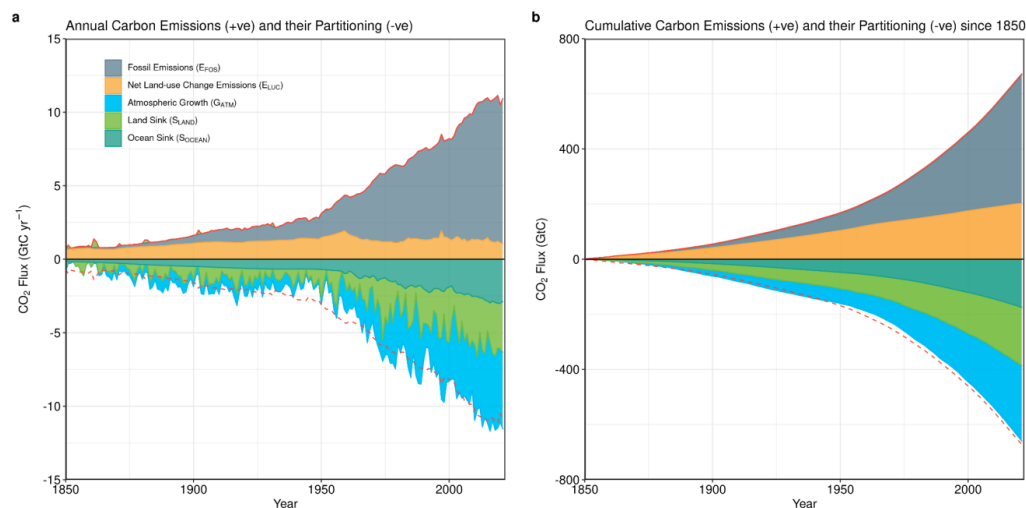


Figure 3. Combined components of the global carbon budget illustrated in Figure 2 as a function of time, for fossil CO₂ emissions (E_{FOS} , including a small sink from cement carbonation; grey) and emissions from land-use change (E_{LUC} ; brown), as well as their partitioning among the atmosphere (G_{ATM} ; cyan), ocean (S_{OCEAN} ; blue), and land (S_{LAND} ; green). Panel (a) shows annual estimates of each flux and panel (b) the cumulative flux (the sum of all prior annual fluxes) since the year 1850. The partitioning is based on nearly independent estimates from observations (for G_{ATM}) and from process model ensembles constrained by data (for S_{OCEAN} and S_{LAND}) and does not exactly add up to the sum of the emissions, resulting in a budget imbalance (BI_M) which is represented by the difference between the bottom red line (mirroring total emissions) and the sum of carbon fluxes in the ocean, land, and atmosphere reservoirs. All data are in $GtC\ yr^{-1}$ (panel a) and GtC (panel b). The E_{FOS} estimate is based on a mosaic of different datasets, and has an uncertainty of $\pm 5\%$ ($\pm 1\sigma$). The E_{LUC} estimate is from three bookkeeping models (Table 4) with uncertainty of $\pm 0.7\ GtC\ yr^{-1}$. The G_{ATM} estimates prior to 1959 are from Joos and Spahni (2008) with uncertainties equivalent to about $\pm 0.1\text{--}0.15\ GtC\ yr^{-1}$ and from Dlugokencky and Tans (2022) since 1959 with uncertainties of about $\pm 0.07\ GtC\ yr^{-1}$ during 1959–1979 and $\pm 0.02\ GtC\ yr^{-1}$ since 1980. The S_{OCEAN} estimate is the average from Khatiwala et al. (2013) and DeVries (2014) with uncertainty of about $\pm 30\%$ prior to 1959, and the average of an ensemble of models and an ensemble of fCO_2 data products (Table 4) with uncertainties of about $\pm 0.4\ GtC\ yr^{-1}$ since 1959. The S_{LAND} estimate is the average of an ensemble of models (Table 4) with uncertainties of about $\pm 1\ GtC\ yr^{-1}$. See the text for more details of each component and their uncertainties.

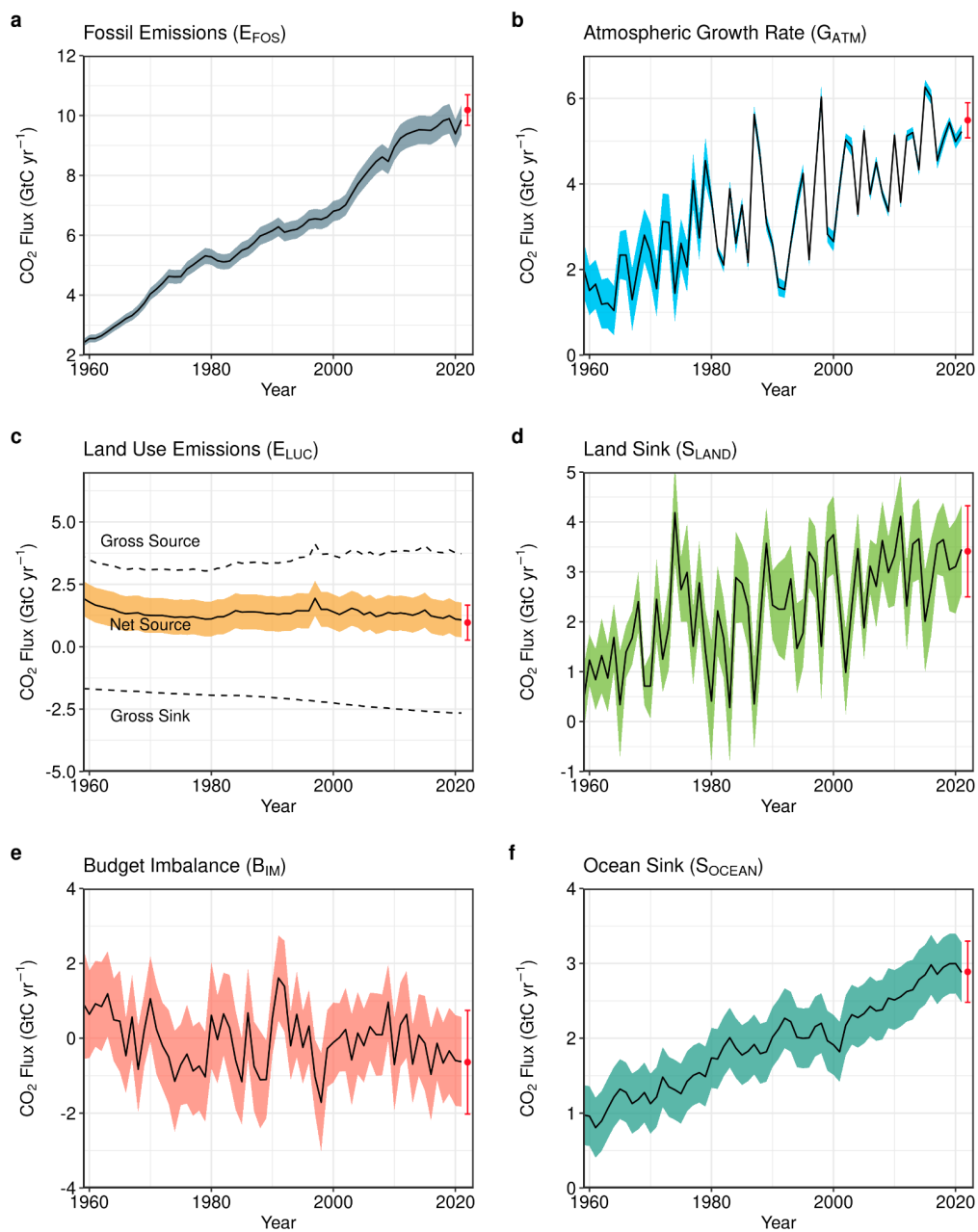




Figure 4. Components of the global carbon budget and their uncertainties as a function of time, presented individually for (a) fossil CO₂ and cement carbonation emissions (E_{FOS}), (b) growth rate in atmospheric CO₂ concentration (G_{ATM}), (c) emissions from land-use change (E_{LUC}), (d) the land CO₂ sink (S_{LAND}), (e) the ocean CO₂ sink (S_{OCEAN}), (f) the budget imbalance that is not accounted for by the other terms. Positive values of S_{LAND} and S_{OCEAN} represent a flux from the atmosphere to land or the ocean. All data are in GtC yr⁻¹ with the uncertainty bounds representing ± 1 standard deviation in shaded colour. Data sources are as in Figure 3. The red dots indicate our projections for the year 2022 and the red error bars the uncertainty in the projections (see methods).

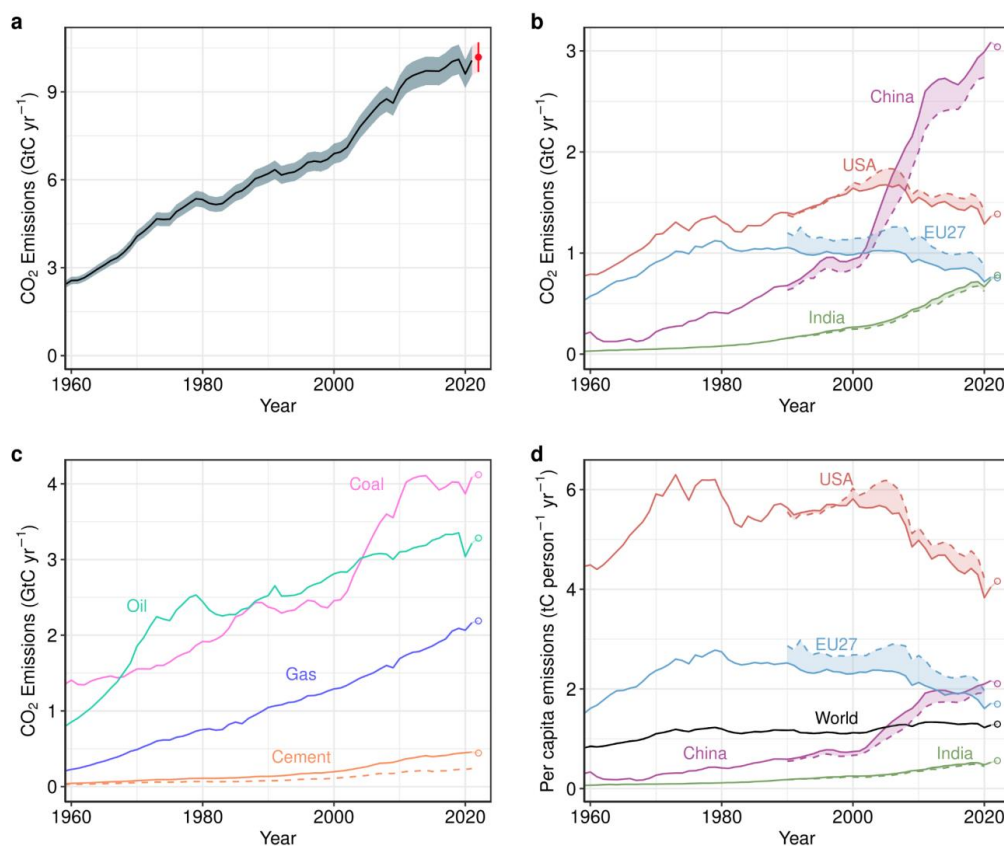




Figure 5. Fossil CO₂ emissions for (a) the globe, including an uncertainty of ± 5% (grey shading) and a projection through the year 2022 (red dot and uncertainty range), (b) territorial (solid lines) and consumption (dashed lines) emissions for the top three country emitters (USA, China, India) and for the European Union (EU27), (c) global emissions by fuel type, including coal, oil, gas, and cement, and cement minus cement carbonation (dashed), and (d) per-capita emissions the world and for the large emitters as in panel (b). Territorial emissions are primarily from a draft update of Gilfillan and Marland (2021) except for national data for Annex I countries for 1990-2020, which are reported to the UNFCCC as detailed in the text, as well as some improvements in individual countries, and extrapolated forward to 2021 using BP Energy Statistics. Consumption-based emissions are updated from Peters et al. (2011b). See Section 2.1 and Appendix C.1 for details of the calculations and data sources.

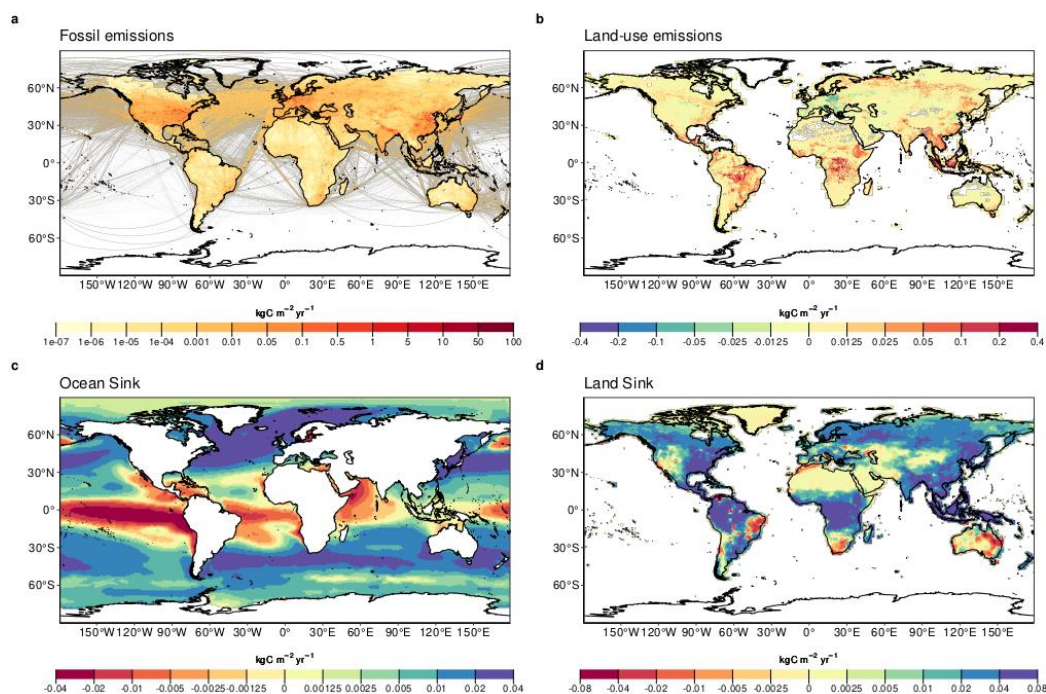


Figure 6. The 2012-2021 decadal mean components of the global carbon budget, presented for (a) fossil CO₂ emissions (E_{FOS}), (b) land-use change emissions (E_{LUC}), (c) the ocean CO₂ sink (S_{OCEAN}), and (d) the land CO₂ sink (S_{LAND}). Positive values for E_{FOS} and E_{LUC} represent a flux to the atmosphere, whereas positive values of S_{OCEAN} and S_{LAND} represent a flux from the atmosphere to the ocean or the land. In all panels, yellow/red (green/blue) colours represent a flux from (into) the land/ocean to (from) the atmosphere. All units are in $\text{kgC m}^{-2} \text{yr}^{-1}$. Note the different scales in each panel. E_{FOS} data shown is from GCP-GridFEDv2022.2. E_{LUC} data shown is only from BLUE as the updated H&N2017 and OSCAR do not resolve gridded fluxes. S_{OCEAN} data shown is the average of GOBMs and data-products means, using GOBMs simulation A, no adjustment for bias and drift applied to the gridded fields (see Section 2.4). S_{LAND} data shown is the average of DGVMs for simulation S2 (see Section 2.5).

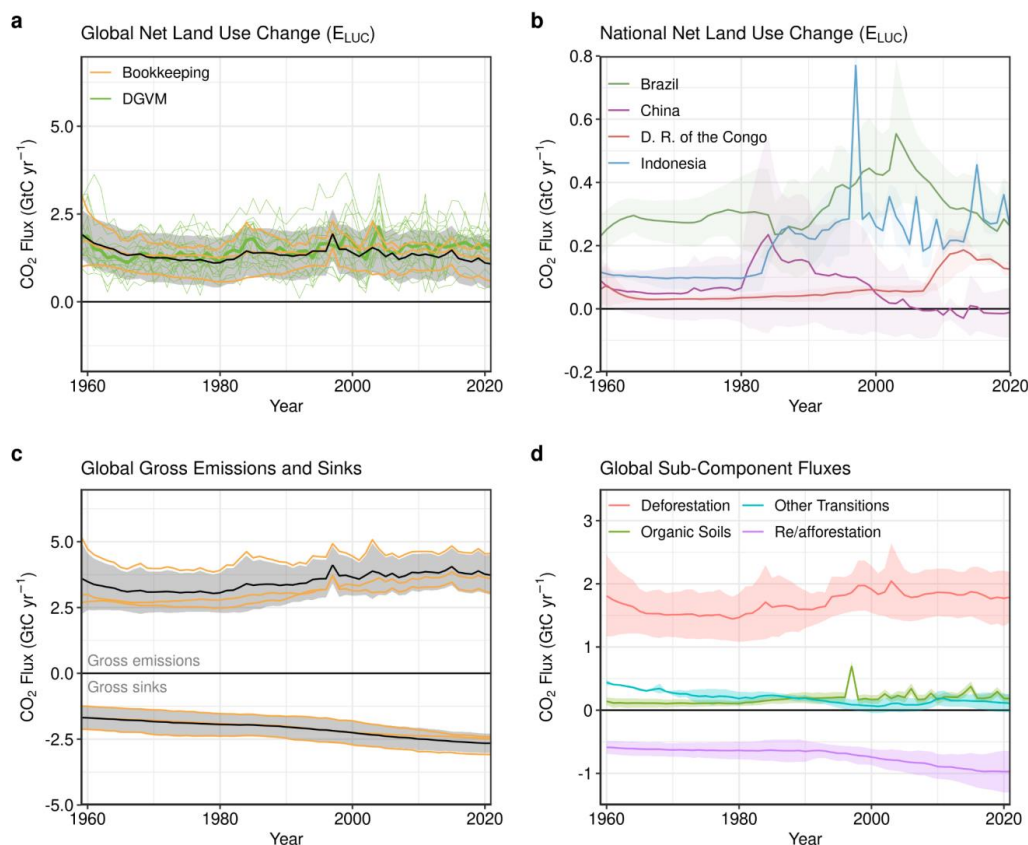


Figure 7. Net CO₂ exchanges between the atmosphere and the terrestrial biosphere related to land use change. (a) Net CO₂ emissions from land-use change (E_{LUC}) with estimates from the three bookkeeping models (yellow lines) and the budget estimate (black with $\pm 1\sigma$ uncertainty), which is the average of the three bookkeeping models. Estimates from individual DGVMs (narrow green lines) and the DGVM ensemble mean (thick green line) are also shown. (b) Net CO₂ emissions from land-use change from the four countries with largest cumulative emissions since 1959. Values shown are the average of the three bookkeeping models. (c) CO₂ gross sinks (negative, from regrowth after agricultural abandonment and wood harvesting) and gross sources (positive, from decaying material left dead on site, products after clearing of natural vegetation for agricultural purposes, wood harvesting, and, for BLUE, degradation from primary to secondary land through usage of natural vegetation as rangeland, and also from emissions from peat drainage and peat burning). Values are shown for the three bookkeeping models (yellow lines) and for their average (black with $\pm 1\sigma$ uncertainty). The sum of the gross sinks and sources is E_{LUC} shown in panel (a). (d) Sources and sinks aggregated into four components that contribute to the net fluxes of CO₂, including: (i) gross sources from deforestation; (ii) net flux on forest lands (slash and product decay following wood harvest; sinks due to regrowth after wood harvest or after abandonment, including reforestation and in shifting cultivation cycles; afforestation), (iii) emissions from organic soils (peat drainage and peat fire, and (iv) sources and sinks related to other land use transitions. The scale of the fluxes shown is smaller than in panel (c) because the substantial gross sources and sinks from wood harvesting are accounted for as net flux under (ii). The sum of the component fluxes is E_{LUC} shown in panel (a).

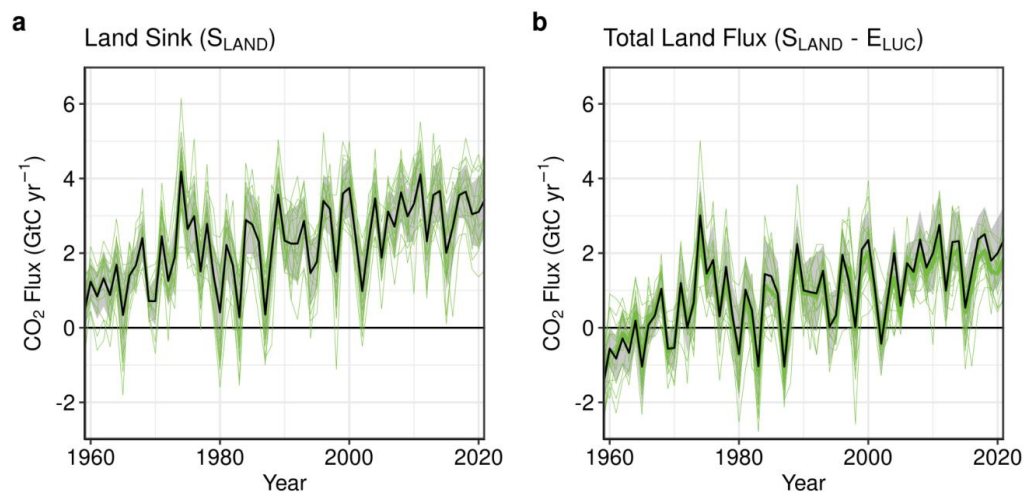


Figure 8: (a) The land CO₂ sink (S_{LAND}) estimated by individual DGVMs estimates (green), as well as the budget estimate (black with $\pm 1\sigma$ uncertainty), which is the average of all DGVMs. (b) Total atmosphere-land CO₂ fluxes ($S_{\text{LAND}} - E_{\text{LUC}}$). The budget estimate of the total land flux (black with $\pm 1\sigma$ uncertainty) combines the DGVM estimate of S_{LAND} from panel (a) with the bookkeeping estimate of E_{LUC} from Figure 7(a). Uncertainties are similarly propagated in quadrature from the budget estimates of S_{LAND} from panel (a) and E_{LUC} from Figure 7(a). DGVMs also provide estimates of E_{LUC} (see Figure 7(a)), which can be combined with their own estimates of the land sink. Hence panel (b) also includes an estimate for the total land flux for individual DGVMs (thin green lines) and their multi-model mean (thick green line).

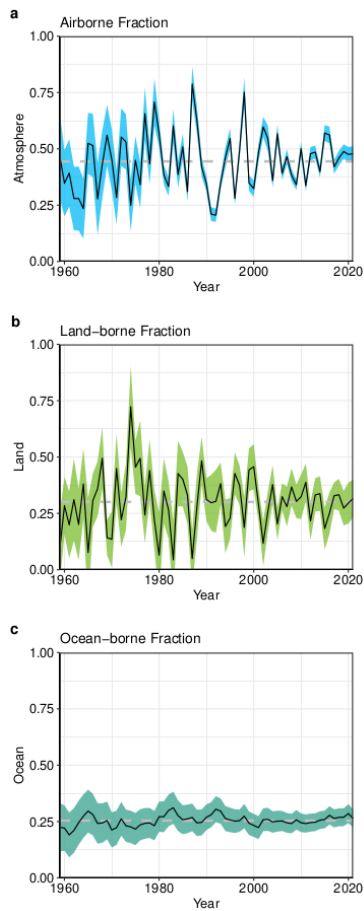


Figure 9. The partitioning of total anthropogenic CO₂ emissions ($E_{FOS} + E_{LUC}$) across (a) the atmosphere (airborne fraction), (b) land (land-borne fraction), and (c) ocean (ocean-borne fraction). Black lines represent the central estimate, and the coloured shading represents the uncertainty. The grey dashed lines represent the long-term average of the airborne (44%), land-borne (30%) and ocean-borne (25%) fractions during 1960-2021.

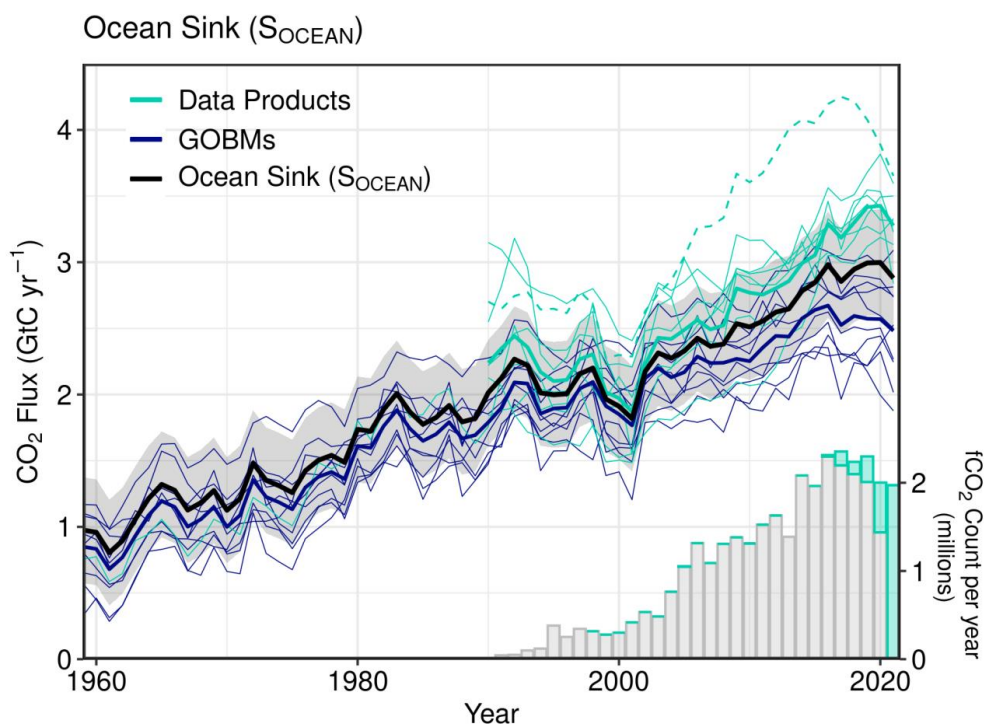


Figure 10. Comparison of the anthropogenic atmosphere-ocean CO_2 flux showing the budget values of S_{OCEAN} (black; with the uncertainty in grey shading), individual ocean models (royal blue), and the ocean fCO_2 -based data products (cyan; with Watson et al. (2020) in dashed line as not used for ensemble mean). Only one data product (Jena-MLS) extends back to 1959 (Rödenbeck et al., 2022). The fCO_2 -based data products were adjusted for the pre-industrial ocean source of CO_2 from river input to the ocean, by subtracting a source of $0.65\ GtC\ yr^{-1}$ to make them comparable to S_{OCEAN} (see Section 2.4). Bar-plot in the lower right illustrates the number of fCO_2 observations in the SOCAT v2022 database (Bakker et al., 2022). Grey bars indicate the number of data points in SOCAT v2021, and coloured bars the newly added observations in v2022.

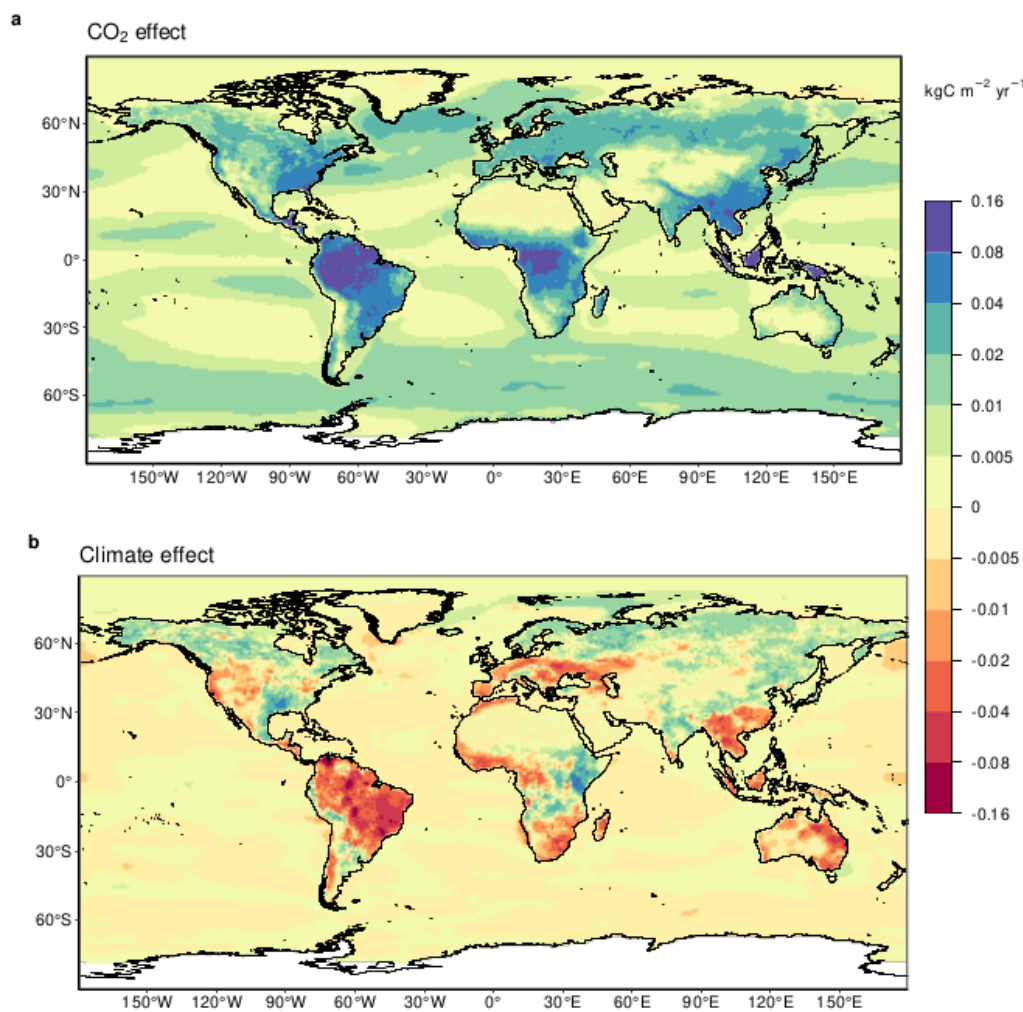


Figure 11. Attribution of the atmosphere-ocean (S_{OCEAN}) and atmosphere-land (S_{LAND}) CO₂ fluxes to (a) increasing atmospheric CO₂ concentrations and (b) changes in climate, averaged over the previous decade 2012-2021. All data shown is from the processed-based GOBMs and DGVMs. The sum of ocean CO₂ and climate effects will not equal the ocean sink shown in Figure 6 which includes the $f\text{CO}_2$ -based data products. See Appendix C.3.2 and C.4.1 for attribution methodology. Units are in kgC m⁻² yr⁻¹ (note the non-linear colour scale).

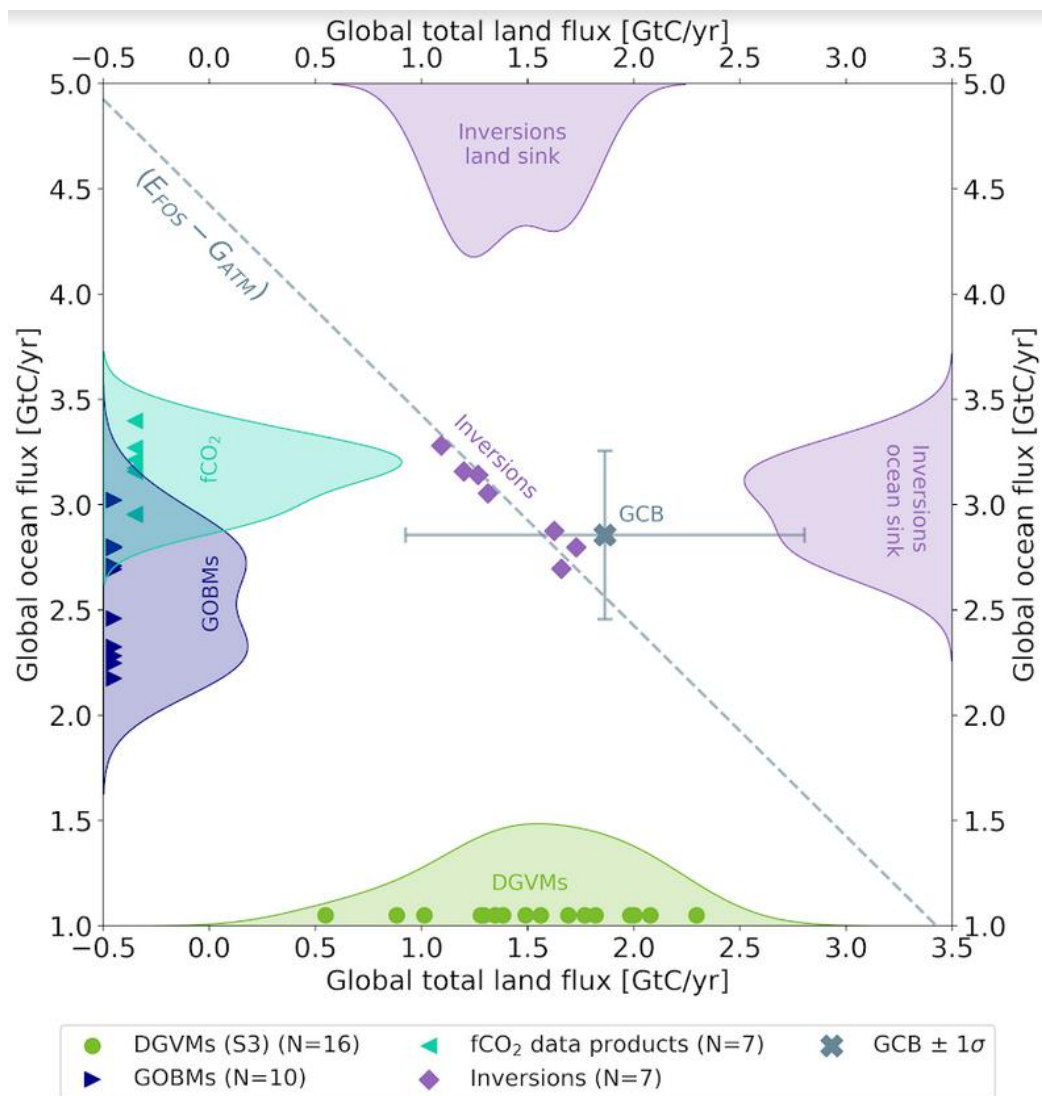


Figure 12. The 2012-2021 decadal mean net atmosphere-ocean and atmosphere-land fluxes derived from the ocean models and fCO_2 products (y-axis, right and left pointing blue triangles respectively), and from the DGVMs (x-axis, green symbols), and the same fluxes estimated from the six inversions (purple symbols on secondary x- and y-axis). The grey central point is the mean ($\pm 1\sigma$) of S_{OCEAN} and $(S_{LAND} - E_{LUC})$ as assessed in this budget. The shaded distributions show the density of the ensemble of individual estimates. The grey diagonal band represents the fossil fuel emissions minus the atmospheric growth rate from this budget ($E_{FOS} - G_{ATM}$). Note that positive values are CO_2 sinks.

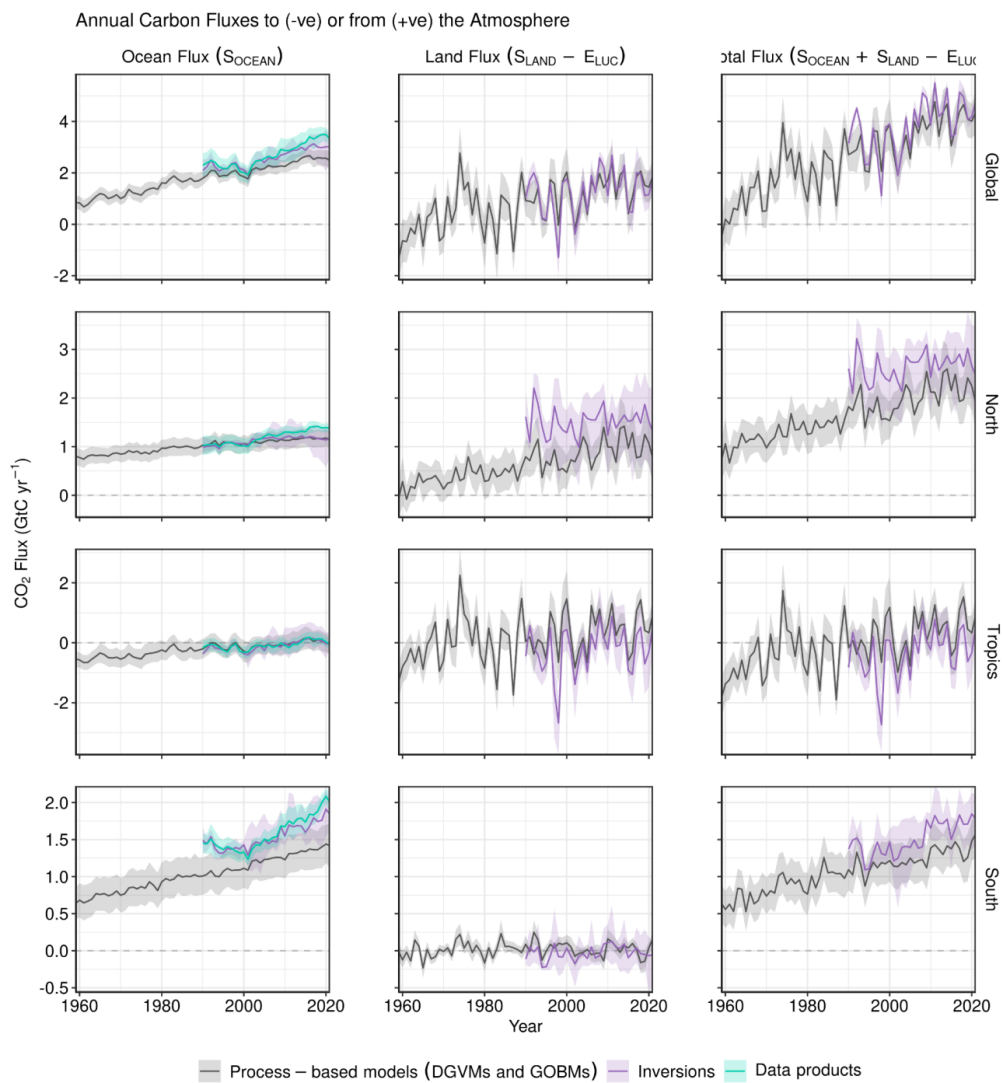




Figure 13. CO₂ fluxes between the atmosphere and the Earth's surface separated between land and oceans, globally and in three latitude bands. The ocean flux is S_{OCEAN} and the land flux is the net atmosphere-land fluxes from the DGVMs. The latitude bands are (top row) global, (2nd row) north (>30°N), (3rd row) tropics (30°S-30°N), and (bottom row) south (<30°S), and over ocean (left column), land (middle column), and total (right column). Estimates are shown for: process-based models (DGVMs for land, GOBMs for oceans); inversion systems (land and ocean); and fCO₂-based data products (ocean only). Positive values indicate a flux from the atmosphere to the land or the ocean. Mean estimates from the combination of the process models for the land and oceans are shown (black line) with ± 1 standard deviation (1σ) of the model ensemble (grey shading). For the total uncertainty in the process-based estimate of the total sink, uncertainties are summed in quadrature. Mean estimates from the atmospheric inversions are shown (purple lines) with their full spread (purple shading). Mean estimates from the fCO₂-based data products are shown for the ocean domain (light blue lines) with their $\pm 1\sigma$ spread (light blue shading). The global S_{OCEAN} (upper left) and the sum of S_{OCEAN} in all three regions represents the anthropogenic atmosphere-to-ocean flux based on the assumption that the preindustrial ocean sink was 0 GtC yr⁻¹ when riverine fluxes are not considered. This assumption does not hold at the regional level, where preindustrial fluxes can be significantly different from zero. Hence, the regional panels for S_{OCEAN} represent a combination of natural and anthropogenic fluxes. Bias-correction and area-weighting were only applied to global S_{OCEAN} ; hence the sum of the regions is slightly different from the global estimate (<0.05 GtC yr⁻¹).



Anthropogenic carbon flows

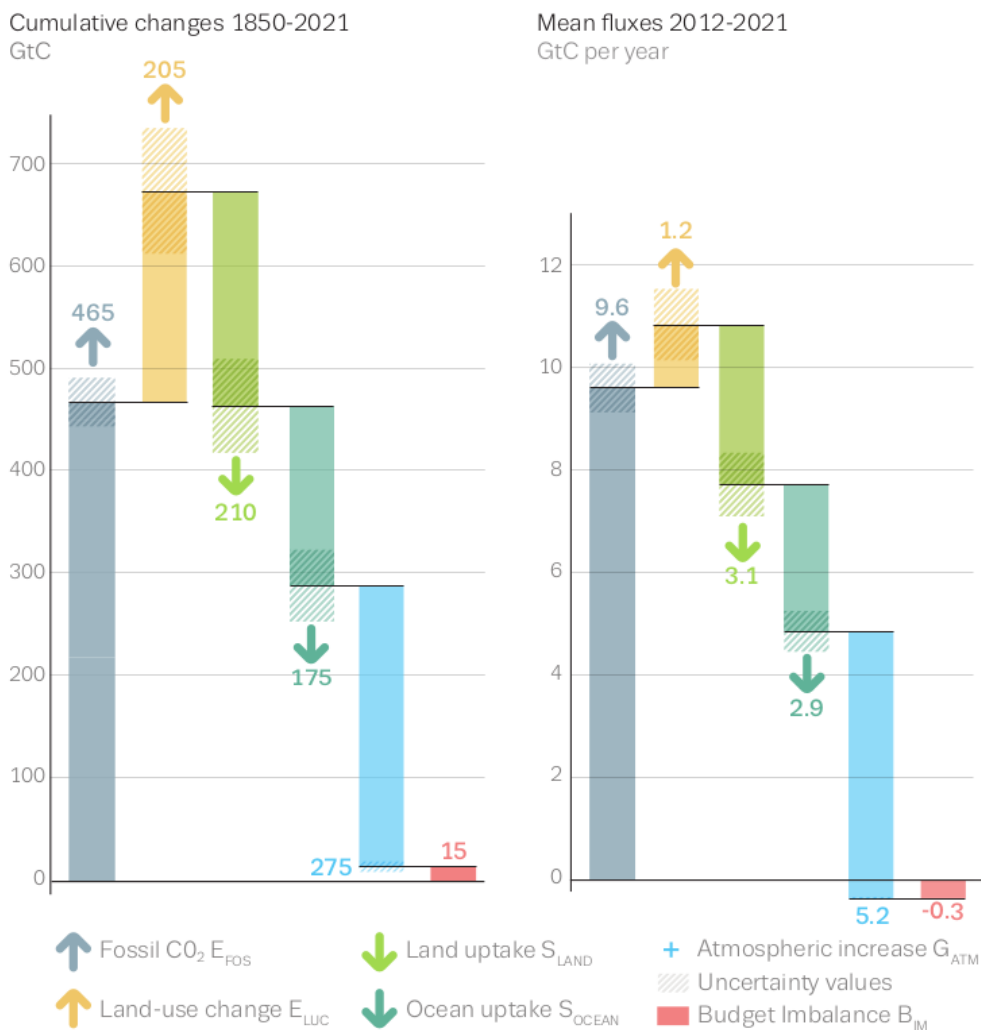


Figure 14. Cumulative changes over the 1850-2021 period (left) and average fluxes over the 2012-2021 period (right) for the anthropogenic perturbation of the global carbon cycle. See the caption of Figure 3 for key information and the methods in text for full details.



Figure 15. Kaya decomposition of the main drivers of fossil CO₂ emissions, considering population, GDP per person, Energy per GDP, and CO₂ emissions per energy, for China (top left), USA (top right), EU27 (middle left), India (middle right), Rest of the World (bottom left), and World (bottom right). Black dots are the annual fossil CO₂ emissions growth rate, coloured bars are the contributions from the different drivers. A general trend is that population and GDP growth put upward pressure on emissions, while energy per GDP and more recently CO₂ emissions per energy put downward pressure on emissions. Both the COVID-19 induced changes during 2020 and the recovery in 2021 led to a stark contrast to previous years, with different drivers in each region.



Appendix A. Supplementary Tables

Table A1. Comparison of the processes included in the bookkeeping method and DGVMs in their estimates of ELUC and SLAND. See Table 4 for model references. All models include deforestation and forest regrowth after abandonment of agriculture (or from afforestation activities on agricultural land). Processes relevant for ELUC are only described for the DGVMs used with land-cover change in this study.

	Bookkeeping Models			DGVMs																
	H&N	BLUE	OSCAR	CABLE-POP	CLASSIC	CLM5.0	DLEM	IBIS	ISAM	JSBACH	JULES-ES	LPJ-GUESS	LPJ	LPJ-Berlin	OCNv2	ORCHIDEEv3	SDGVM	VISIT	YIBs	
Processes relevant for ELUC																				
Wood harvest and forest degradation (a)	yes	yes	yes	yes	no	yes	yes	yes	yes	yes	no	yes	yes	no (d)	yes	yes	no	yes	no	
Shifting cultivation / Subgrid scale transitions	yes (b)	yes	yes	yes	no	yes	no	yes	no	yes	no	yes	yes	no (d)	no	no	no	yes	no	
Cropland harvest (removed, R, or added to litter, L)	yes (R) (j)	yes (R) (j)	yes (R)	yes (R)	yes (L)	yes (R)	yes	yes (R)	yes	yes (R+L)	yes (R)	yes (R)	yes (L)	yes (R)	yes (R+L)	yes (R)	yes (R)	yes (R)	yes (L)	
Peat fires	yes	yes	yes	no	no	yes	no	no	no	no	no	no	no	no	no	no	no	no	no	
fire as a management tool	yes (j)	yes (j)	yes (h)	no	no	no	no	no	no	no	no	no	no	no	no	no	no	no	no	
N fertilisation	yes (j)	yes (j)	yes (h)	no	no	yes	yes	no	yes	no	yes (i)	yes	no	yes	yes	yes	no	no	no	
tillage	yes (j)	yes (j)	yes (h)	no	yes (g)	no	no	no	no	no	no	yes	no	no	no	no	yes (g)	no	no	
irrigation	yes (j)	yes (j)	yes (h)	no	no	yes	yes	no	yes	no	no	yes	no	no	no	no	no	no	no	
wetland drainage	yes (j)	yes (j)	yes (h)	no	no	no	no	no	yes	no	no	no	no	no	no	no	no	no	no	
erosion	yes (j)	yes (j)	yes (h)	no	no	no	yes	no	no	no	no	no	no	no	no	no	no	yes	no	
peat drainage	yes	yes	yes	no	no	no	no	no	no	no	no	no	no	no	no	no	no	no	no	
Grazing and mowing Harvest (removed, r, or added to litter, l)	yes (r) (j)	yes (r) (j)	yes (r)	yes (r)	no	no	no	no	yes (r, l)	yes (l)	no	yes (r)	yes (l)	no	yes (r+l)	no	no	no	no	
Processes also relevant for SLAND (in addition to CO2 fertilisation and climate)																				
Fire simulation and/or suppression	N.A.	N.A.	N.A.	no	yes	yes	no	yes	no	yes	yes	yes	yes	yes	no	no	yes	yes	no	
Carbon-nitrogen interactions, including N deposition	N.A.	N.A.	N.A.	yes	no (f)	yes	yes	no	yes	yes	yes	yes	no	yes	yes	yes	yes (c)	no	no (f)	
Separate treatment of direct and diffuse solar radiation	N.A.	N.A.	N.A.	yes	no	yes	no	no	no	no	yes	no	no	no	no	no	no	no	yes	
(a) Refers to the routine harvest of established managed forests rather than pools of harvested products.																				
(b) No back- and forth-transitions between vegetation types at the country-level, but if forest loss based on FRA exceeded agricultural expansion based on FAO, then this amount of area was cleared for cropland and the same amount of area of old croplands abandoned.																				
(c) Limited. Nitrogen uptake is simulated as a function of soil C, and Vcmax is an empirical function of canopy N. Does not consider N deposition.																				
(d) Available but not active.																				
(e) Simple parameterization of nitrogen limitation based on Yin (2002; assessed on FACE experiments)																				
(f) Although C-N cycle interactions are not represented, the model includes a parameterization of down-regulation of photosynthesis as CO2 increases to emulate nutrient constraints (Arora et al., 2009)																				
(g) Tillage is represented over croplands by increased soil carbon decomposition rate and reduced humification of litter to soil carbon.																				
(h) as far as the DGVMs that OSCAR is calibrated to include it																				
(i) perfect fertilisation assumed, i.e. crops are not nitrogen limited and the implied fertiliser diagnosed																				
(j) Process captured implicitly by use of observed carbon densities.																				



Table A2. Comparison of the processes and model set up for the Global Ocean Biogeochemistry Models for their estimates of SOCEAN. See Table 4 for model references.

	NEMO-PlankTOM 12	NEMO-PISCES (IPSL)	MICOM-HAMOCC (NorESM1-OCv1.2)	MPIOM-HAMOCC 6	FESOM-2.1-REcoM2	NEMO3.6-PISCESv2-gas (CNRM)	MOM6-COBALT (Princeton)	CESM-ETHZ	MRI-ESM2-1	CESM2
Model specifics										
Physical ocean model	NEMOv3.6-ORCA2	NEMOv3.6-eORCA1L75	MICOM (NorESM1-OCv1.2)	MPIOM	FESOM-2.1	NEMOv3.6-GELATOv6-eORCA1L75	MOM6-SIS2	CESMv1.3 (ocean model based on POP2)	MRI.CO Mv4	CESM2-POP2
Biogeochemistry model	PlankTOM 12	PISCESv2	HAMOCC (NorESM1-OCv1.2)	HAMOCC 6	REcoM-2-M	PISCESv2-gas	COBALTv2	BEC (modified & extended)	NPZD	MARBL
Horizontal resolution	2° lon, 0.3 to 1.5° lat	1° lon, 0.3 to 1° lat	1° lon, 0.17 to 0.25 lat	1.5°	unstructured mesh, 20-120 km resolution (CORE mesh)	1° lon, 0.3 to 1° lat	0.5° lon, 0.25 to 0.5° lat	1.125° lon, 0.53° to 0.27° lat	1° lon, 0.3 to 0.5° lat	1.125° lon, 0.53° to 0.27° lat
Vertical resolution	31 levels	75 levels, 1m at the surface	51 isopycnic layers + 2 layers representing a bulk mixed layer	40 levels	46 levels, 10 m spacing in the top 100 m	75 levels, 1m at surface	75 levels hybrid coordinates, 2m at surface	60 levels	60 levels with 1-level bottom boundary layer	60 levels
Total ocean area on native grid (km ²)	3.6080E+08	3.6270E+08	3.6006E+08	3.6598E+08	3.6435E+08	3.6270E+08	3.6111E+08	3.5926E+08	3.6141E+08	3.61E+08
Gas-exchange parameterization	Wanninkhof et al. 1992	Orr et al., 2017	Orr et al., 2017, but with a=0.337	Orr et al., 2017	Orr et al., 2017	Orr et al., 2017	Orr et al., 2017	Wanninkhof (1992, coefficient a scaled down to 0.31)	Orr et al., 2017	Orr et al., 2017
CO ₂ chemistry routines	Following Broecker et al. (1982)	mocsy	Following Dickson et al. 2007	Ilyina et al. (2013) adapted to comply with OMIP protocol (Orr et al., 2017)	mocsy	mocsy	mocsy	OCMIP2 (Orr et al.)	mocsy	OCMIP2 (Orr et al., 2017)
River input (PgC/yr) (organic/inorganic DIC)	0.723 / -	0.61 / -	0	0.77 / -	0 / 0	~0.611 / -	~0.07 / ~0.15	0.33 / -	0 / 0	0.173/0.263
Net flux to sediment (PgC/yr) (organic/other)	0.723 / -	0.59 / -	around 0.54 / -	- / 0.44	0 / 0	~0.656 / -	~0.11 / ~0.07 (CaCO ₃)	0.21 / -	0 / 0	0.345/0.110 (CaCO ₃)
SPIN-UP procedure										
Initialisation of carbon chemistry	GLODAPv1 (preindustrial DIC)	GLODAPv2 (preindustrial DIC)	GLODAPv1 (preindustrial DIC)	initialization from previous simulation	GLODAPv2 (preindustrial DIC)	GLODAPv2	GLODAPv2 (Alkalinity, DIC). DIC	GLODAPv2 (preindustrial DIC)	GLODAPv2 (preindustrial)	GLODAPv2 (preindustrial)



								corrected to 1959 level (simulation A and C) and to pre-industrial level (simulation B and D) using Khatiwala et al 2009		DIC)	DIC)
Preindustrial spin-up prior to 1850	spin-up 1750-1947	spin-up starting in 1836 with 3 loops of JRA55	1000 year spin up	~2000 years	189 years	long spin-up (> 1000 years)	1000 years)	Other bgc tracers initialized from a GFDL-ESM2M spin-up (> 1000 years)	spinup 1655-1849	1661 years with xCO2 = 284.32	spinup 1653-1850, xCO2= 278
Atmospheric forcing fields and CO2											
Atmospheric forcing for (i) pre-industrial spin-up, (ii) spin-up 1850-1958 for simulation B, (iii) simulation B	looping NCEP year 1990 (i, ii, iii)	looping full JRA55 reanalysis	CORE-I (normal year) forcing (i, ii, iii)	OMIP climatology (i), NCEP year 1957 (ii,iii)	JRA55-do v.1.5.0 repeated year 1961 (i, ii, iii)	JRA55-do v1.5.0 full reanalysis (i) cycling year 1958 (ii,iii)	JRA55-do v1.5.0 repeat year 1959 (ii,iii)	GFDL-ESM2M internal forcing (i), JRA55-do v1.5.0 repeat year 1959 (ii,iii)	forcing created from JRA55-do version 1.3 (ii,iii)	JRA55-do v1.5.0 repeat year 1990/91 (i, ii, iii)	(i) repeating JRA 1958-2018 for spinup for A & D, repeating JRA 1990/1991 repeat year forcing for spinup for B & C, (ii) & (iii) JRA 1990/1991 repeat year forcing
Atmospheric CO2 for control spin-up 1850-1958 for simulation B, and for simulation B	constant 278ppm; converted to pCO2 temperature formulation (Sarmiento et al., 1992)	xCO2 of 286.46ppm, converted to pCO2 with constant sea-level pressure and water vapour pressure	xCO2 of 278ppm, converted to pCO2 with sea-level pressure and water vapour pressure	xCO2 of 278ppm, no conversion to pCO2	xCO2 of 278ppm, converted to pCO2 with sea-level pressure and water vapour pressure	xCO2 of 278ppm, converted to pCO2 with sea-level pressure and water vapour pressure	xCO2 of 278ppm, converted to pCO2 with sea-level pressure and water vapour pressure	xCO2 of 278ppm, converted to pCO2 with sea-level pressure and water vapour pressure	xCO2 = 287.4ppm, converted to pCO2 with atmospheric pressure, and water vapour pressure	xCO2 of 284.32ppm (CMIP6 piControl), converted to pCO2 with water vapour and sea-level pressure (JRA55-	xCO2= 278



									do repeat year 1990/91)	
Atmospheric forcing for historical spin-up 1850-1958 for simulation A (i) and for simulation A (ii)	1750-1947: looping NCEP year 1990; 1948-2021: NCEP	1836-1958 : looping full JRA55 reanalysis (i), JRA55-do-v1.4 then 1.5 for 2020-21 (ii)	CORE-I (normal year) forcing; from 1948 onwards NCEP-R1 with CORE-II corrections	NCEP 6 hourly cyclic forcing (10 years starting from 1948, i), 1948-2021: transient NCEP forcing	JRA55-do-v1.5.0 repeated year 1961 (i), transient JRA55-do-v1.5.0 (ii)	JRA55-do cycling year 1958 (i), JRA55-do-v1.5.0 (ii)	JRA55-do-v1.5 repeat year 1959 (i), v1.5.0 (1959-2019, v1.5.0.1b (2020), v1.5.0.1 (2021; ii)	JRA55 version 1.3, repeat cycle between 1958-2018 (i), v1.3 (1959-2018), v.1.5.0.1 (2020-2021)	1653-1957: repeated cycle JRA55-do v1.5.0 1958-2018 (i), v1.5.0 (1958-2018), v1.5.0.1 (2019-2021; ii)	(i) repeating JRA 1958-2018, (ii) JRA 1958-2021
Atmospheric CO2 for historical spin-up 1850-1958 for simulation A (i) and simulation A (ii)	xCO2 provided by the GCB; converted to pCO2 temperature formulation (Sarmiento et al., 1992), monthly resolution (i, ii)	xCO2 as provided by the GCB, global mean, annual resolution, converted to pCO2 with sea-level pressure and water vapour pressure (i, ii)	xCO2 as provided by the GCB, converted to pCO2 with sea level pressure (taken from the atmospheric forcing) and water vapor correction (i, ii)	transient monthly xCO2 provided by GCB, no conversion (i, ii)	xCO2 as provided by the GCB, converted to pCO2 with sea-level pressure and water vapour pressure, global mean, monthly resolution (i, ii)	xCO2 as provided by the GCB, converted to pCO2 with constant sea-level pressure and water vapour pressure, global mean, yearly resolution (i, ii)	xCO2 at year 1959 level (315 ppm, i) and as provided by GCB (ii), both converted to pCO2 with sea-level pressure and water vapour pressure, global mean, yearly resolution (i, ii)	xCO2 as provided by the GCB, converted to pCO2 with locally determined atm. pressure, and water vapour pressure (i, ii)	xCO2 as provided for CMIP6 historical simulations, annual resolution (i), and as provided by GCB (ii), both converted to pCO2 with locally determined atm. pressure, and water vapour and sea-level pressure (1980)	annual global xCO2 provided by GCB, converted to equilibrium CO2* using atmospheric pressure and Weiss and Price (1980)



Table A3: Description of ocean data-products used for assessment of SOCEAN. See Table 4 for references.

	Jena-MLS	MPI-SOMFFN	CMEMS-LSCE-FFNN	Watson et al	NIES-NN	JMA-MLR	OS-ETHZ-GRACER	LDEO HPD
Method	Spatio-temporal interpolation (version oc_v2022). Spatio-temporal field of ocean-internal carbon sources/sinks is fit to the SOCATv2022 pCO ₂ data. Includes a multi-linear regression against environmental drivers to bridge data gaps.	A feed-forward neural network (FFN) determines non-linear relationship between SOCAT pCO ₂ measurements and environmental predictor data for 16 biogeochemical provinces (defined through a self-organizing map, SOM) and is used to fill the existing data gaps.	An ensemble of neural network models trained on 100 subsampled datasets from SOCAT and environmental predictors. The models are used to reconstruct sea surface fugacity of CO ₂ and convert to air-sea CO ₂ fluxes	Modified MPI-SOMFFN with SOCATv2022 pCO ₂ database. Corrected to the subskin temperature of the ocean as measured by satellite (Goddijn-Murphy et al, 2015). Flux calculation corrected for the cool and salty surface skin. Monthly climatology for skin temperature correction derived from ESA CCI product for the period 2003 to 2011 (Merchant et al, 2019).	A feed forward neural network model trained on SOCAT 2021 fCO ₂ and environmental predictor data. The fCO ₂ was normalized to the reference year 2000 by a global fCO ₂ trend: We fitted the dependence of fCO ₂ on year by linear regression. We subtracted the trend from fCO ₂ and used the neural network to model the nonlinear dependence of the residual on predictors. The trend was added to model predictions to reconstruct fCO ₂ .	Fields of total alkalinity (TA) were estimated by using a multiple linear regressions (MLR) method based on GLODAPv2.2021 and satellite observation data. SOCATv2022 fCO ₂ data were converted to dissolved inorganic carbon (DIC) with the TA. Fields of DIC were estimated by using a MLR method based on the DIC and satellite observation data	Geospatial Random Cluster Ensemble Regression is a two-step cluster-regression approach, where multiple clustering instances with slight variations are run to create an ensemble of estimates. We use K-means clustering and a combination of Gradient boosted trees and Feed-forward neural-networks to estimate SOCAT v2022 fCO ₂ .	Based on fCO ₂ -misfit between observed fCO ₂ and eight of the ocean biogeochemical models used in this assessment. The eXtreme Gradient Boosting method links this misfit to environmental observations to reconstruct the model misfit across all space and time., which is then added back to model-based fCO ₂ estimate. The final reconstruction of surface fCO ₂ is the average across the eight reconstructions.
Gas-exchange parameterization	Wanninkhof 1992. Transfer coefficient k scaled to match a global mean transfer rate of 16.5 cm/hr by (Naegler, 2009)	Wanninkhof 1992. Transfer coefficient k scaled to match a global mean transfer rate of 16.5 cm/hr	Wanninkhof 2014. Transfer coefficient k scaled to match a global mean transfer rate of 16.5 cm/hr (Naegler, 2009)	Nightingale et al 2000	Wanninkhof, 2014. Transfer coefficient k scaled to match a global mean transfer rate of 16.5 cm/hr (Naegler, 2009)	Wanninkhof., 2014. Transfer coefficient k scaled to match a global mean transfer rate of 16.5 cm/hr (Naegler, 2009)	Wanninkhof 1992, averaged and scaled for three reanalysis wind data, to a global mean 16.5 cm/hr (after Naegler 2009; Fay & Gregor et al. 2021)	Wanninkhof 1992, averaged and scaled for three reanalysis wind data, to a global mean 16.5 cm/hr (after Naegler 2009; Fay & Gregor et al. 2021)
Wind product	JMA55-do reanalysis	ERA 5	ERA5	Mean and mean square winds monthly 1x1° from CCMP, 0.25x0.25° x 6-hourly,	ERA5	JRA55	JRA55, ERA5, NCEP1	JRA55, ERA5, CCMP2
Spatial resolution	2.5 degrees longitude x 2 degrees latitude	1x1 degree	1x1 degree	1x1 degree	1x1 degree	1x1 degree	1x1 degree	1x1 degree
Temporal resolution	daily	monthly	monthly	monthly	monthly	monthly	monthly	monthly



Atmospheric CO2	Spatially and temporally varying field based on atmospheric CO2 data from 169 stations (Jena CarboScope atmospheric inversion sEXTALL_v2021)	Spatially varying 1x1 degree atmospheric pCO2_wet calculated from the NOAA ESRL marine boundary layer xCO2 and NCEP sea level pressure with the moisture correction by Dickson et al 2007.	Spatially and monthly varying fields of atmospheric pCO2 computed from CO2 mole fraction (CO2 atmospheric inversion from the Copernicus Atmosphere Monitoring Service), and atmospheric dry-air pressure which is derived from monthly surface pressure (ERAS) and water vapour pressure fitted by Weiss and Price 1980	Atmospheric pCO2 (wet) calculated from NOAA marine boundary layer XCO2 and NCEP sea level pressure, with pH2O calculated from Cooper et al, 1998. 2021 XCO2 marine boundary values were not available at submission so we used preliminary values, estimated from 2020 values and increase at Mauna Loa.	NOAA Greenhouse Gas Marine Boundary Layer Reference. https://gml.noaa.gov/ccgg/mbi/mbi.html	Atmospheric xCO2 fields of JMA-GSAM inversion model (Maki et al. 2010; Nakamura et al. 2015) were used. They were converted to pCO2 by using JRA55 sea level pressure. 2021 xCO2 fields were not available at this stage, and we used global xCO2 increments from 2020 to 2021.	NOAA's marine boundary layer product for xCO2 is linearly interpolated onto a 1x1 degree grid and resampled from weekly to monthly. xCO2 is multiplied by ERA5 mean sea level pressure, where the latter corrected for water vapour pressure using Dickson et al. (2007). This results in monthly 1x1 degree pCO2atm.	NOAA's marine boundary layer product for xCO2 is linearly interpolated onto a 1x1 degree grid and resampled from weekly to monthly. xCO2 is multiplied by ERA5 mean sea level pressure, where the latter corrected for water vapour pressure using Dickson et al. (2007). This results in monthly 1x1 degree pCO2atm.
Total ocean area on native grid (km2)	3.63E+08	3.63E+08	3.50E+08	3.52E+08	3.49E+08	3.10E+08 (2.98E+08 to 3.16E+08, depending on ice cover)	3.55E+08	3.61E+08
method to extend product to full global ocean coverage		Arctic and marginal seas added following Landschützer et al. (2020). No coastal cut.				Fay & Gregor et al. 2021	Method has near full coverage	Fay & Gregor et al. 2021. Gaps were filled with monthly climatology. Interannual variability was added to the climatology based on the temporal evolution of 5 products for years 1985 through 2020 and then only using this product for year 2021.



Table A4. Comparison of the inversion set up and input fields for the atmospheric inversions. Atmospheric inversions see the full CO₂ fluxes, including the anthropogenic and pre-industrial fluxes. Hence they need to be adjusted for the pre-industrial flux of CO₂ from the land to the ocean that is part of the natural carbon cycle before they can be compared with SOCEAN and SLAND from process models. See Table 4 for references.

	Copernicus Atmosphere Monitoring Service (CAMS)	Carbon-Tracker Europe (CTE)	Jena CarboScope	UoE	NISMON-CO ₂	CMS-Flux	GONGGA	THU	Copernicus Atmosphere Monitoring Service (CAMS) Satellite
Version number	v21r1	v2022	v2022	UoE v6.1b	v2022.1	v2022	v2022	v2022	FT21r2
Observations									
Atmospheric observations	Hourly resolution (well-mixed conditions) obspack GLOBALVIEWplus v7.0 (a) and NRT_v7.2(b), WDCGG, RAMCES and ICOS ATC	Hourly resolution (well-mixed conditions) obspack GLOBALVIEWplus v7.0 (a) and NRT_v7.2(b)	Flasks and hourly from various institutions (outliers removed by 2σ criterion)	Hourly resolution (well-mixed conditions) obspack GLOBALVIEWplus v7.0(a) and NRT_v7.2(b)	Hourly resolution (well-mixed conditions) obspack GLOBALVIEWplus v7.0(a) and NRT_v7.2(b)	ACOS-GOSAT v9r, OCO-2 v10 scaled to WMO 2019 standard and remote flask observations from ObsPack, GLOBALVIEWplus, v7.0(a) and NRT_v7.2(b)	OCO-2 v10r data that scaled to WMO 2019 standard	OCO-2 v10r data that scaled to WMO 2019 standard	bias-corrected ACOS GOSAT v9 over land until August 2024 + bias-corrected ACOS OCO-2 v10 over land, both rescaled to X2019
Period covered	1979-2021	2001-2021	1957-2021	2001-2021	1990-2021	2010-2021	2015-2021	2015-2021	2010-2021
Prior fluxes									
Biosphere and fires	ORCHIDEE, GFEDv4.1s	SiB4 and GFAS	Zero	CASA v1.0, climatology after 2016 and GFED4.0	VISIT and GFEDv4.1s	CARDAM OM	CASA and GFEDv4.1s	SiB4.2 and GFEDv4.1s	ORCHIDEE, GFEDv4.1s
Ocean	CMEMS-LSCE-FFNN 2021	CarboScope v2021	CarboScope v2022	Takahashi climatology	JMA global ocean mapping (Iida et al., 2015)	MOM6	Takahashi climatology	Takahashi climatology	CMEMS-LSCE-FFNN 2021
Fossil fuels	GridFED 2021.2(c) with an extrapolation to 2021 based on Carbonmonitor and NO ₂	GridFED 2021.3 + GridFED 2022.2 for 2021 (c)	GridFED v2022.2 (c)	GridFED 2022.1 (c)	GridFED v2022.2 (c)	GridFED2 022.2 (c)	GridFED 2021.3 (c) with an extrapolation to 2021 based on Carbonmonitor	GridFED v2022.1 (c)	GridFED 2021.2 (c) with an extrapolation to 2021 based on Carbonmonitor and NO ₂
Transport and optimization									
Transport model	LMDZ v6	TM5	TM3	GEOS-CHEM	NICAM-TM	GEOS-CHEM	GEOS-Chem v12.9.3	GEOS-CHEM	LMDZ v6



Weather forcing	ECMWF	ECMWF	NCEP	MERRA	JRA55	MERRA	MERRA2	GEOS-FP	ECMWF
Horizontal Resolution	Global 3.75°x1.875°	Global 3°x2°, Europe 1°x1°, North America 1°x1°	Global 3.83°x5°	Global 4°x5°	Isocahedral grid: ~225km	Global 4°x5°	Global 2°x2.5°	Global 4°x5°	Global 3.75°x1.875°
Optimization	Variational	Ensemble Kalman filter	Conjugate gradient (re-orthonormalization) (d)	Ensemble Kalman filter	Variational	Variational	Nonlinear least squares four-dimensional variational (NLS-4DVar)	Ensemble Kalman filter	Variational
(a) https://doi.org/10.25925/20210801 . Schuldt et al. Multi-laboratory compilation of atmospheric carbon dioxide data for the period 1957-2020; obspack_co2_1_GLOBALVIEWplus_v7.0_2021-08-18; NOAA Earth System Research Laboratory, Global Monitoring Laboratory. http://doi.org/10.25925/20210801 .									
(b) http://doi.org/10.25925/20220624 . Schuldt et al. Multi-laboratory compilation of atmospheric carbon dioxide data for the period 2021-2022; obspack_co2_1_NRT_v7.2_2022-06-28; NOAA Earth System Research Laboratory, Global Monitoring Laboratory. http://doi.org/10.25925/20220624 .									
(c) GCP-GridFED v2021.2, v2021.3, v2022.1 and v2022.2 (Jones et al., 2022) are updates through the year 2021 of the GCP-GridFED dataset presented by Jones et al. (2021).									
(d) ocean prior not optimised									



Table A5 Attribution of fCO₂ measurements for the year 2021 included in SOCATv2022 (Bakker et al., 2016, 2022) to inform ocean fCO₂-based data products.

Platform Name	Regions	No. of measurements	Principal Investigators	No. of datasets	Platform Type
1 degree	North Atlantic, coastal	71,863	Tanhua, T.	1	Ship
Alawai_158W_21 N	Tropical Pacific	387	Sutton, A.; De Carlo, E. H.; Sabine, C.	1	Mooring
Atlantic Explorer	North Atlantic, tropical Atlantic, coastal	34,399	Bates, N. R.	16	Ship
Atlantic Sail	North Atlantic, coastal	27,496	Steinhoff, T.; Körtzinger, A.	7	Ship
BlueFin	Tropical Pacific	60,606	Alin, S. R.; Feely, R. A.	11	Ship
Cap San Lorenzo	North Atlantic, tropical Atlantic, coastal	44,281	Lefèvre, N.	7	Ship
CCE2_121W_34N	Coastal	1,333	Sutton, A.; Send, U.; Ohman, M.	1	Mooring
Celtic Explorer	North Atlantic, coastal	61,118	Cronin, M.	10	Ship
F.G. Walton Smith	Coastal	38,375	Rodriguez, C.; Millero, F. J.; Pierrot, D.; Wanninkhof, R.	14	Ship
Finnmaid	Coastal	223,438	Rehder, G.; Bittig, H. C.; Glockzin, M.	1	Ship
FRA56	Coastal	5,652	Tanhua, T.	1	Ship
G.O. Sars	Arctic, north Atlantic, coastal	82,607	Skjelvan, I.	9	Ship
GAKOA_149W_60 N	Coastal	402	Monacci, N.; Cross, J.; Musielewicz, S.; Sutton, A.	1	Mooring
Gordon Gunter	North Atlantic, coastal	36,058	Wanninkhof, R.; Pierrot, D.	6	Ship
Gulf Challenger	Coastal	6,375	Salisbury, J.; Vandemark, D.; Hunt, C. W.	6	Ship
Healy	Arctic, north Atlantic, coastal	28,998	Sweeney, C.; Newberger, T.; Sutherland, S. C.; Munro, D. R.	5	Ship
Henry B. Bigelow	North Atlantic, coastal	67,399	Wanninkhof, R.; Pierrot, D.	8	Ship
Heron Island	Coastal	989	Tilbrook, B.; Neill, C.; van Ooijen, E.; Passmore, A.; Black, J.	1	Mooring
Investigator	Southern Ocean, coastal, tropical Pacific, Indian Ocean	120,782	Tilbrook, B.; Akl, J.; Neill, C.	6	Ship
KC_BUOY	Coastal	2,860	Evans, W.; Pockock, K.	1	Mooring
Keifu Maru II	North Pacific, tropical Pacific, coastal	10,053	Kadono, K.	8	Ship
Laurence M. Gould	Southern Ocean	2,604	Sweeney, C.; Newberger, T.; Sutherland, S. C.; Munro, D. R.	1	Ship
Marion Dufresne	Indian Ocean, Southern Ocean, coastal	9,911	Lo Monaco, C.; Metz, N.	1	Ship
Nathaniel B. Palmer	Southern Ocean	2,376	Sweeney, C.; Newberger, T.; Sutherland, S. C.; Munro, D. R.	1	Ship
New Century 2	North Pacific, tropical Pacific, north Atlantic, coastal	198,293	Nakaoka, S.-I.; Takao, S.	10	Ship
Newrest - Art and Fenetres	North Atlantic, tropical Atlantic, south Atlantic, coastal	17,699	Tanhua, T.	2	Ship
Quadra Island Field Station	Coastal	81,201	Evans, W.; Pockock, K.	1	Mooring
Ronald H. Brown	North Atlantic, coastal	31,661	Wanninkhof, R.; Pierrot, D.	3	Ship
Ryofu Maru III	North Pacific, tropical Pacific, coastal	10,464	Kadono, K.	8	Ship
Sea Explorer	Southern Ocean, north Atlantic, coastal, tropical Atlantic	37,027	Landshützer, P.; Tanhua, T.	2	Ship



Sikuliaq	Arctic, north Pacific, coastal	60,549	Sweeney, C.; Newberger, T.; Sutherland, S. C.; Munro, D. R.	13	Ship
Simon Stevin	Coastal	57,055	Gkritzalis, T.; Theetaert, H.; Cattrijsse, A.; T'Jampens, M.	11	Ship
Sitka Tribe of Alaska Environmental Research Laboratory	Coastal	19,086	Whitehead, C.; Evans, W.; Lanphier, K.; Peterson, W.; Kennedy, E.; Hales, B.	1	Mooring
SOFS_14ZE_46S	Southern Ocean	894	Sutton, A.; Trull, T.; Shadwick, E.	1	Mooring
Soyo Maru	Tropical Pacific, coastal	33,234	Ono, T.	3	Ship
Station M	North Atlantic	447	Skjelvan, I.	1	Mooring
Statsraad Lehmkuhl	North Atlantic, tropical Atlantic, coastal	47,881	Becker, M.; Olsen, A.	3	Ship
TAO125W_0N	Tropical Pacific	241	Sutton, A.	1	Mooring
Tavastland	Coastal	48,421	Willstrand Wranne, A.; Steinhoff, T.	17	Ship
Thomas G. Thompson	North Atlantic, tropical Atlantic, north Pacific, tropical Pacific, coastal	47,073	Alin, S. R. ; Feely, R. A.	5	Ship
Trans Future 5	Southern Ocean, north Pacific, tropical Pacific, coastal	257,424	Nakaoka, S.-I.; Takao, S.	22	Ship
Tukuma Arctica	North Atlantic, coastal	70,033	Becker, M.; Olsen, A.	23	Ship
Wakataka Maru	North Pacific, coastal	13,392	Tadokoro, K.	2	Ship



Table A6. Aircraft measurement programs archived by Cooperative Global Atmospheric Data Integration Project (CGADIP; Schuldt et al. 2022a and 2022b) that contribute to the evaluation of the atmospheric inversions (Figure B4).

Site code	Measurement program name in Obspack	Specific doi	Data providers
AAO	Airborne Aerosol Observatory, Bondville, Illinois		Sweeney, C.; Dlugokencky, E.J.
ABOVE	Carbon in Arctic Reservoirs Vulnerability Experiment (CARVE)	https://doi.org/10.3334/ORNLDAAC/1404	Sweeney, C., J.B. Miller, A. Karion, S.J. Dinardo, and C.E. Miller. 2016. CARVE: L2 Atmospheric Gas Concentrations, Airborne Flasks, Alaska, 2012-2015. ORNL DAAC, Oak Ridge, Tennessee, USA.
ACG	Alaska Coast Guard		Sweeney, C.; McKain, K.; Karion, A.; Dlugokencky, E.J.
ACT	Atmospheric Carbon and Transport - America		Sweeney, C.; Dlugokencky, E.J.; Baier, B.; Montzka, S.; Davis, K.
AIRCO RENOA A	NOAA AirCore		Colm Sweeney (NOAA) AND Bianca Baier (NOAA)
ALF	Alta Floresta		Gatti, L.V.; Gloor, E.; Miller, J.B.;
AOA	Aircraft Observation of Atmospheric trace gases by JMA		ghg_obs@met.kishou.go.jp
BGI	Bradgate, Iowa		Sweeney, C.; Dlugokencky, E.J.
BNE	Beaver Crossing, Nebraska		Sweeney, C.; Dlugokencky, E.J.
BRZ	Berezorechka, Russia		Sasakama, N.; Machida, T.
CAR	Briggsdale, Colorado		Sweeney, C.; Dlugokencky, E.J.
CMA	Cape May, New Jersey		Sweeney, C.; Dlugokencky, E.J.
CON	CONTRAIL (Comprehensive Observation Network for TRace gases by AirLiner)	http://dx.doi.org/10.1759/5/20180208.001	Machida, T.; Matsueda, H.; Sawa, Y. Niwa, Y.
CRV	Carbon in Arctic Reservoirs Vulnerability Experiment (CARVE)		Sweeney, C.; Karion, A.; Miller, J.B.; Miller, C.E.; Dlugokencky, E.J.
DND	Dahlen, North Dakota		Sweeney, C.; Dlugokencky, E.J.
ECO	East Coast Outflow		Sweeney, C.; McKain, K.
ESP	Estevan Point, British Columbia		Sweeney, C.; Dlugokencky, E.J.
ETL	East Trout Lake, Saskatchewan		Sweeney, C.; Dlugokencky, E.J.
FWI	Fairchild, Wisconsin		Sweeney, C.; Dlugokencky, E.J.
GSFC	NASA Goddard Space Flight Center Aircraft Campaign		Kawa, S.R.; Abshire, J.B.; Riris, H.
HAA	Molokai Island, Hawaii		Sweeney, C.; Dlugokencky, E.J.
HFM	Harvard University Aircraft Campaign		Wofsy, S.C.
HIL	Homer, Illinois		Sweeney, C.; Dlugokencky, E.J.
HIP	HIPPO (HIAPER Pole-to-Pole Observations)	https://doi.org/10.3334/CDIAC/HIPPO_010	Wofsy, S.C.; Stephens, B.B.; Elkins, J.W.; Hints, E.J.; Moore, F.
IAGOS-CARIBI	In-service Aircraft for a Global Observing System		Obersteiner, F.; Boenisch, H.; Gehrlein, T.; Zahn, A.; Schuck, T.



C			
INX	INFLUX (Indianapolis Flux Experiment)		Sweeney, C.; Dlugokencky, E.J.; Shepson, P.B.; Turnbull, J.
LEF	Park Falls, Wisconsin		Sweeney, C.; Dlugokencky, E.J.
NHA	Offshore Portsmouth, New Hampshire (Isles of Shoals)		Sweeney, C.; Dlugokencky, E.J.
OIL	Oglesby, Illinois		Sweeney, C.; Dlugokencky, E.J.
ORC	ORCAS (O ₂ /N ₂ Ratio and CO ₂ Airborne Southern Ocean Study)	https://doi.org/10.5065/D6S B445X	Stephens, B.B., Sweeney, C., McKain, K., Kort, E.
PFA	Poker Flat, Alaska		Sweeney, C.; Dlugokencky, E.J.
RBA-B	Rio Branco		Gatti, L.V.; Gloor, E.; Miller, J.B.
RTA	Rarotonga		Sweeney, C.; Dlugokencky, E.J.
SCA	Charleston, South Carolina		Sweeney, C.; Dlugokencky, E.J.
SGP	Southern Great Plains, Oklahoma		Sweeney, C.; Dlugokencky, E.J.; Biraud, S.
TAB	Tabatinga		Gatti, L.V.; Gloor, E.; Miller, J.B.
TGC	Offshore Corpus Christi, Texas		Sweeney, C.; Dlugokencky, E.J.
THD	Trinidad Head, California		Sweeney, C.; Dlugokencky, E.J.
WBI	West Branch, Iowa		Sweeney, C.; Dlugokencky, E.J.



Table A7. Main methodological changes in the global carbon budget since first publication. Methodological changes introduced in one year are kept for the following years unless noted. Empty cells mean there were no methodological changes introduced that year.

Publication year	Fossil fuel emissions			LUC emissions	Reservoirs			Uncertainty & other changes
	Global	Country (territorial)	Country (consumption)		Atmosphere	Ocean	Land	
2006 (a)		Split in regions						
2007 (b)				ELUC based on FAO-FRA 2005; constant ELUC for 2006	1959-1979 data from Mauna Loa; data after 1980 from global average	Based on one ocean model tuned to reproduced observed 1990s sink		±1σ provided for all components
2008 (c)				Constant ELUC for 2007				
2009 (d)		Split between Annex B and non-Annex B	Results from an independent study discussed	Fire-based emission anomalies used for 2006-2008		Based on four ocean models normalised to observations with constant delta	First use of five DGVMs to compare with budget residual	
2010 (e)	Projection for current year based on GDP	Emissions for top emitters		ELUC updated with FAO-FRA 2010				
2011 (f)			Split between Annex B and non-Annex B					
2012 (g)		129 countries from 1959	129 countries and regions from 1990-2010 based on GTAP8.0	ELUC for 1997-2011 includes interannual anomalies from fire-based emissions	All years from global average	Based on 5 ocean models normalised to observations with ratio	Ten DGVMs available for SLAND; First use of four models to compare with ELUC	
2013 (h)		250 countriesb	134 countries and regions 1990-2011 based on GTAP8.1, with detailed estimates for years 1997, 2001, 2004, and 2007	ELUC for 2012 estimated from 2001-2010 average		Based on six models compared with two data-products to year 2011	Coordinated DGVM experiments for SLAND and ELUC	Confidence levels; cumulative emissions; budget from 1750



2014 (i)	Three years of BP data	Three years of BP data	Extended to 2012 with updated GDP data	ELUC for 1997-2013 includes interannual anomalies from fire-based emissions		Based on seven models	Based on ten models	Inclusion of breakdown of the sinks in three latitude bands and comparison with three atmospheric inversions
2015 (j)	Projection for current year based Jan-Aug data	National emissions from UNFCCC extended to 2014 also provided	Detailed estimates introduced for 2011 based on GTAP9			Based on eight models	Based on ten models with assessment of minimum realism	The decadal uncertainty for the DGVM ensemble mean now uses $\pm 1\sigma$ of the decadal spread across models
2016 (k)	Two years of BP data	Added three small countries; China's emissions from 1990 from BP data (this release only)		Preliminary ELUC using FRA-2015 shown for comparison; use of five DGVMs		Based on seven models	Based on fourteen models	Discussion of projection for full budget for current year
2017 (l)	Projection includes India-specific data			Average of two bookkeeping models; use of 12 DGVMs		Based on eight models that match the observed sink for the 1990s; no longer normalised	Based on 15 models that meet observation-based criteria (see Sect. 2.5)	Land multi-model average now used in main carbon budget, with the carbon imbalance presented separately; new table of key uncertainties
a Raupach et al. (2007)								
b Canadell et al. (2007)								
c GCP (2008)								
d Le Quéré et al. (2009)								
e Friedlingstein et al. (2010)								
f Peters et al. (2012b)								
g Le Quéré et al. (2013), Peters et al. (2013)								
h Le Quéré et al. (2014)								
i Le Quéré et al. (2015a)								
j Le Quéré et al. (2015b)								
k Le Quéré et al. (2016)								
l Le Quéré et al. (2018a)								



Table A8: Mapping of global carbon cycle models' land flux definitions to the definition of the LULUCF net flux used in national reporting to UNFCCC. Non-intact lands are used here as proxy for "managed lands" in the country reporting, national Greenhouse Gas Inventories (NGHGI) are gap-filled (see Sec. C.2.3 for details). Where available, we provide independent estimates of certain fluxes for comparison.

			2002-2011	2012-2021
ELUC from bookkeeping estimates (from Tab. 5)			1.36	1.24
SLAND	Total (from Tab. 5)	from DGVMs	-2.85	-3.10
	in non-forest lands	from DGVMs	-0.74	-0.83
	in non-intact forest	from DGVMs	-1.67	-1.80
	in intact forests	from DGVMs	-0.44	-0.47
	in intact land	from ORCHIDEE-MICT	-1.34	-1.38
ELUC plus SLAND on non-intact lands	considering non-intact forests only	from bookkeeping ELUC and DGVMs	-0.31	-0.56
	considering all non-intact land	from ORCHIDEE-MICT	0.90	0.60
National Greenhouse Gas Inventories (LULUCF)			-0.37	-0.54
FAOSTAT (LULUCF)			0.39	0.24



Table A9. Funding supporting the production of the various components of the global carbon budget in addition to the authors' supporting institutions (see also acknowledgements).

Funder and grant number (where relevant)	Author Initials
Australia, Integrated Marine Observing System (IMOS)	BT
Australian National Environment Science Program (NESP)	JGC
Belgium, FWO (Flanders Research Foundation, contract GN I001821N)	TGk
BNP Paribas Foundation through Climate & Biodiversity initiative, philanthropic grant for developments of the Global Carbon Atlas	PC
Canada, Tula Foundation	WE, KP
China, National Natural Science Foundation (grant no. 41975155)	XY
China, National Natural Science Foundation (grant no. 42141020)	WY
China, National Natural Science Foundation of China (grant no. 41921005)	BZ
China, Scientific Research Start-up Funds (grant no. QD2021024C) from Tsinghua Shenzhen International Graduate School	BZ
China, Second Tibetan Plateau Scientific Expedition and Research Program (SQ2022QZKK0101)	XT
China, Young Elite Scientists Sponsorship Program by CAST (grant no. YESS20200135)	BZ
EC Copernicus Atmosphere Monitoring Service implemented by ECMWF	FC
EC Copernicus Marine Environment Monitoring Service implemented by Mercator Ocean	MG
EC H2020 (4C; grant no 821003)	PF, MOS, RMA, SS, GPP, PC, JIK, TI, LB, AJ, PL, LGr, NG, NMa, SZ
EC H2020 (CoCO2; grant no. 958927)	RMA, GPP, JIK
EC H2020 (COMFORT; grant no. 820989)	LGr, MG, NG
EC H2020 (CONSTRAIN; grant no 820829)	RS, TGa
EC H2020 (ESM2025 – Earth System Models for the Future; grant agreement No 101003536).	RS, TGa, TI, LB, BD
EC H2020 (JERICO-S3; grant no. 871153)	HCB
EC H2020 (VERIFY; grant no. 776810)	MWJ, RMA, GPP, PC, JIK, MJM
Efg International	TT, MG
European Space Agency Climate Change Initiative ESA-CCI RECCAP2 project 655 (ESRIN/4000123002/18/I-NB)	SS, PC
European Space Agency OceanSODA project (grant no. 4000137603/22/I-DT)	LGr, NG
France, French Oceanographic Fleet (FOF)	NMe
France, ICOS (Integrated Carbon Observation System) France	NL
France, Institut National des Sciences de l'Univers (INSU)	NMe
France, Institut polaire français Paul-Emile Victor(IPEV)	NMe
France, Institut de recherche français sur les ressources marines (IFREMER)	NMe
France, Institut de Recherche pour le Développement (IRD)	NL
France, Observatoire des sciences de l'univers Ecce-Terra (OSU at	NMe



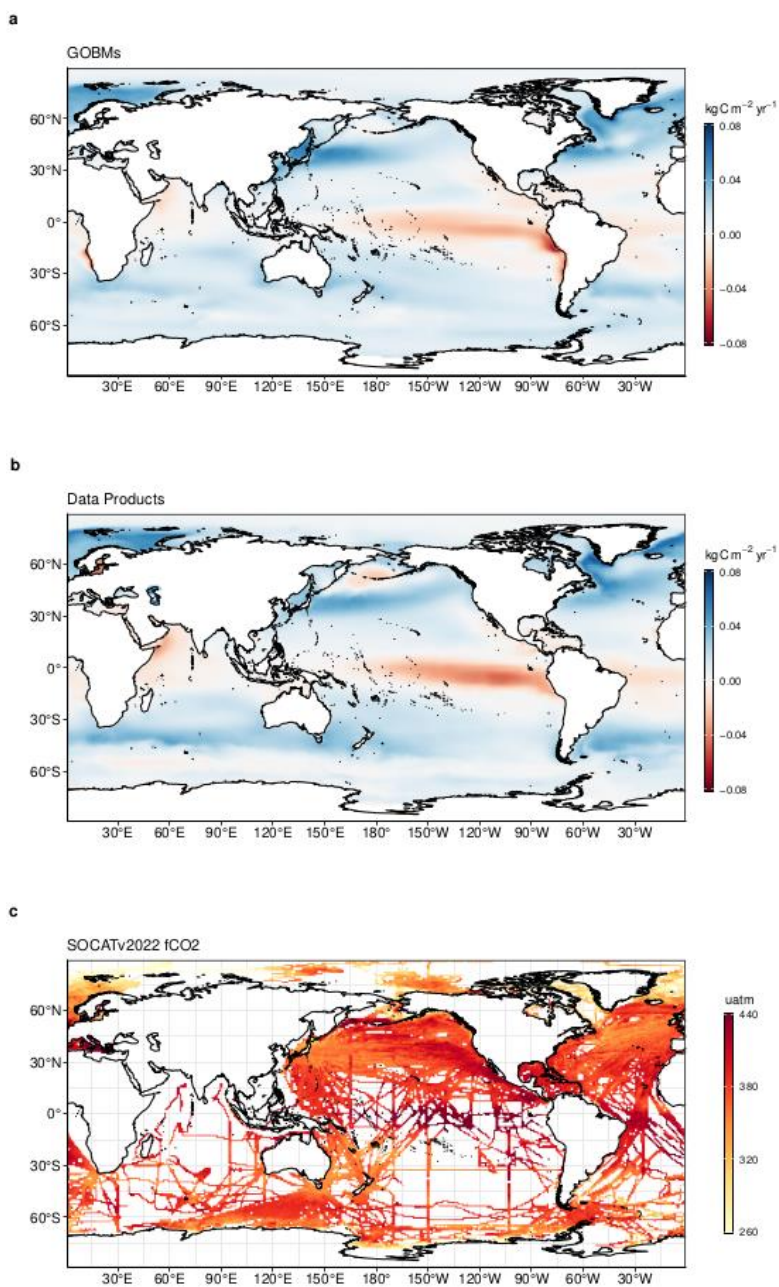
Sorbonne Université)	
Germany, Deutsche Forschungsgemeinschaft (DFG) under Germany's Excellence Strategy – EXC 2037 'Climate, Climatic Change, and Society' – Project Number: 390683824	TI
Germany, Federal Ministry for Education and Research (BMBF)	HCB
Germany, German Federal Ministry of Education and Research under project "DArgo2025" (03F0857C)	TS
Germany, Helmholtz Association ATMO programme	AA
Germany, Helmholtz Young Investigator Group Marine Carbon and Ecosystem Feedbacks in the Earth System (MarESys), grant number VH-NG-1301	JH, OG
Germany, ICOS (Integrated Carbon Observation System) Germany	HCB
Hapag-Lloyd	TT, MG
Ireland, Marine Institute	MC
Japan, Environment Research and Technology Development Fund of the Ministry of the Environment (JPMEERF21S20810)	YN
Japan, Global Environmental Research Coordination System, Ministry of the Environment (grant number E1751)	SN, ST, TO
Japan, Environment Research and Technology Development Fund of the Ministry of the Environment (JPMEERF21S20800)	HT
Japan, Japan Meteorological Agency	KK
Kuehne + Nagel International AG	TT, MG
Mediterranean Shipping Company (MSc)	TT, MG
Monaco, Fondation Prince Albert II de Monaco	TT, MG
Monaco, Yacht Club de Monaco	TT, MG
Netherlands, ICOS (Integrated Carbon Observation System)	WP
Norway, Research Council of Norway (N-ICOS-2, grant no. 296012)	AO, MB, IS
Norway, Norwegian Research Council (grant no. 270061)	JS
Sweden, ICOS (Integrated Carbon Observation System)	AW
Sweden, Swedish Meteorological and Hydrological Institute	AW
Sweden, The Swedish Research Council	AW
Swiss National Science Foundation (grant no. 200020-200511)	QS
Tibet, Second Tibetan Plateau Scientific Expedition and Research Program (SQ2022QZKK0101)	TX
UK Royal Society (grant no. RP\R1\191063)	CLQ
UK, Natural Environment Research Council (SONATA: grant no. NE/P021417/1)	RW
UK, Natural Environmental Research Council (NE/R016518/1)	PIP
UK, Natural Environment Research Council (NE/V01417X/1)	MWJ
UK, Royal Society: The European Space Agency OCEANFLUX projects	JDS
UK Royal Society (grant no. RP\R1\191063)	CLQ
USA, BIA Tribal Resilience	CW
USA, Cooperative Institute for Modeling the Earth System between the National Oceanic and Atmospheric Administration Geophysical	LR



Fluid Dynamics Laboratory and Princeton University and the High Meadows Environmental Institute	
USA, Cooperative Institute for Climate, Ocean, & Ecosystem Studies (CIOCES) under NOAA Cooperative Agreement NA20OAR4320271	KO
USA, Department of Energy, Biological and Environmental Research	APW
USA, Department of Energy, SciDac (DESC0012972)	GCH, LPC
USA, Energy Exascale Earth System Model (E3SM) project, Department of Energy, Office of Science, Office of Biological and Environmental Research	GCH, LPC
USA, EPA Indian General Assistance Program	CW
USA, NASA Carbon Monitoring System program and OCO Science team program (80NM0018F0583) .	JL
USA, NASA Interdisciplinary Research in Earth Science (IDS) (80NSSC17K0348)	GCH, LPC, BP
USA, National Center for Atmospheric Research (NSF Cooperative Agreement No. 1852977)	DK
USA, National Oceanic and Atmospheric Administration, Ocean Acidification Program	DP, RW, SRA, RAF, AJS, NMM
USA, National Oceanic and Atmospheric Administration, Global Ocean Monitoring and Observing Program	DRM, CSw, NRB, CRodr, DP, RW, SRA, RAF, AJS
USA, National Science Foundation (grant number 1903722)	HT
USA, State of Alaska	NMM
Computing resources	
ADA HPC cluster at the University of East Anglia	MWJ
CAMS inversion was granted access to the HPC resources of TGCC under the allocation A0110102201	FC
Cheyenne supercomputer (doi:10.5065/D6RX99HX), were provided by the Computational and Information Systems Laboratory (CISL) at NCAR	DK
HPC cluster Aether at the University of Bremen, financed by DFG within the scope of the Excellence Initiative	ITL
MRI (FUJITSU Server PRIMERGY CX2550M5)	YN
NIES (SX-Aurora)	YN
NIES supercomputer system	EK
UNINETT Sigma2, National Infrastructure for High Performance Computing and Data Storage in Norway (NN2980K/NS2980K)	JS



1 Appendix B. Supplementary Figures

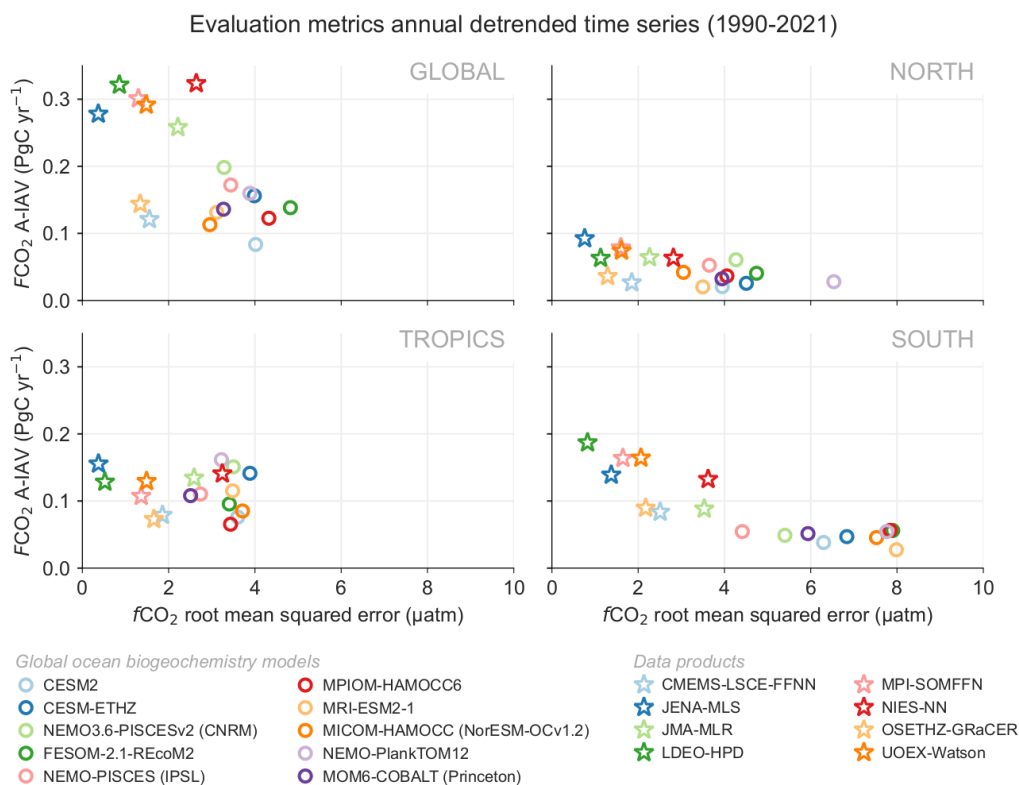


2

3 **Figure B1.** Ensemble mean air-sea CO₂ flux from a) global ocean biogeochemistry models and b) fCO₂ based data products,
4 averaged over 2012-2021 period (kgC m⁻² yr⁻¹). Positive numbers indicate a flux into the ocean. c) gridded SOCAT v2022
5 fCO₂ measurements, averaged over the 2012-2021 period (µatm). In (a) model simulation A is shown. The data-products



- 6 represent the contemporary flux, i.e. including outgassing of riverine carbon, which is estimated to amount to 0.65 GtC yr^{-1}
- 7 globally.
- 8

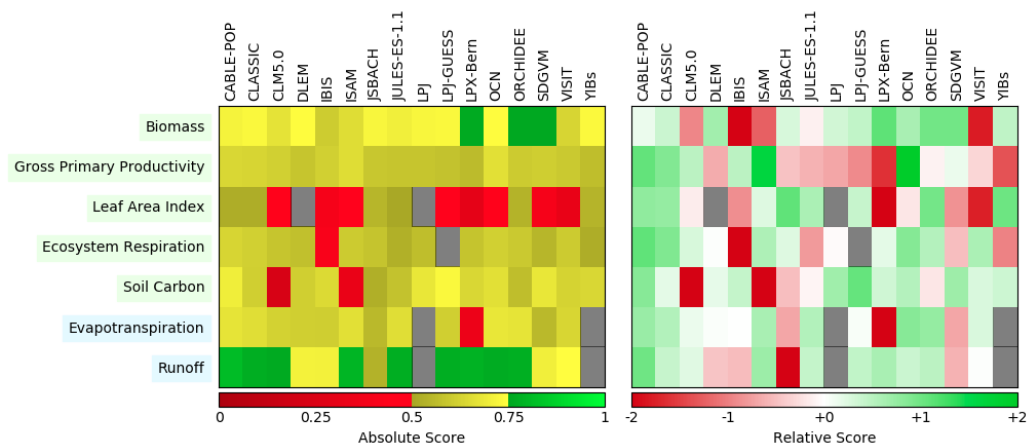


9

10 Figure B2. Evaluation of the GOBMs and data products using the root mean squared error (RMSE) for the period 1990 to 2021,
 11 between the individual surface ocean $f\text{CO}_2$ mapping schemes and the SOCAT v2022 database. The y-axis shows the amplitude of
 12 the interannual variability of the air-sea CO_2 flux (A-IAV, taken as the standard deviation of the detrended annual time series.
 13 Results are presented for the globe, north ($>30^\circ\text{N}$), tropics (30°S - 30°N), and south ($<30^\circ\text{S}$) for the GOBMs (see legend and circle) and
 14 for the $f\text{CO}_2$ -based data products (star symbols). The $f\text{CO}_2$ -based data products use the SOCAT database and therefore are not
 15 independent from the data (see section 2.4.1).

16

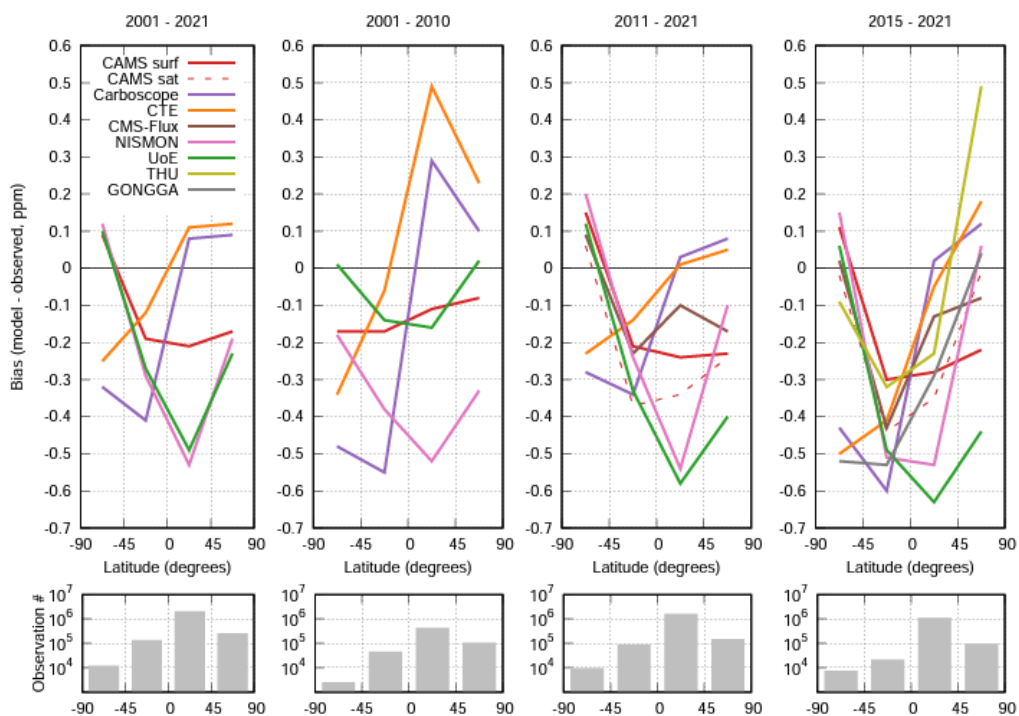
17



18

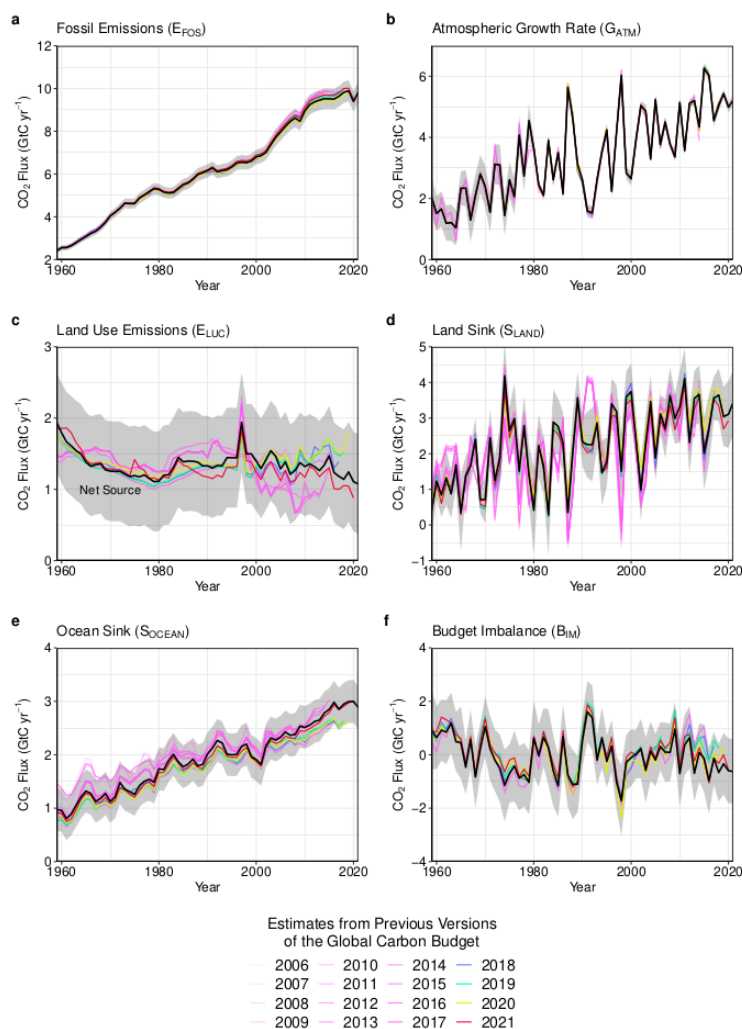
19 **Figure B3.** Evaluation of the DGVMs using the International Land Model Benchmarking system (ILAMB; Collier et al.,
 20 **2018)** (left) absolute skill scores and (right) skill scores relative to other models. The benchmarking is done with observations
 21 for vegetation biomass (Saatchi et al., 2011; and GlobalCarbon unpublished data; Avitabile et al., 2016), GPP (Jung et al.,
 22 2010; Lasslop et al., 2010), leaf area index (De Kauwe et al., 2011; Myneni et al., 1997), ecosystem respiration (Jung et al.,
 23 2010; Lasslop et al., 2010), soil carbon (Hugelius et al., 2013; Todd-Brown et al., 2013), evapotranspiration (De Kauwe et al.,
 24 2011), and runoff (Dai and Trenberth, 2002). For each model-observation comparison a series of error metrics are
 25 calculated, scores are then calculated as an exponential function of each error metric, finally for each variable the multiple
 26 scores from different metrics and observational data sets are combined to give the overall variable scores shown in the left
 27 panel. Overall variable scores increase from 0 to 1 with improvements in model performance. The set of error metrics vary
 28 with data set and can include metrics based on the period mean, bias, root mean squared error, spatial distribution,
 29 interannual variability and seasonal cycle. The relative skill score shown in the right panel is a Z-score, which indicates in
 30 units of standard deviation the model scores relative to the multi-model mean score for a given variable. Grey boxes
 31 represent missing model data.

32



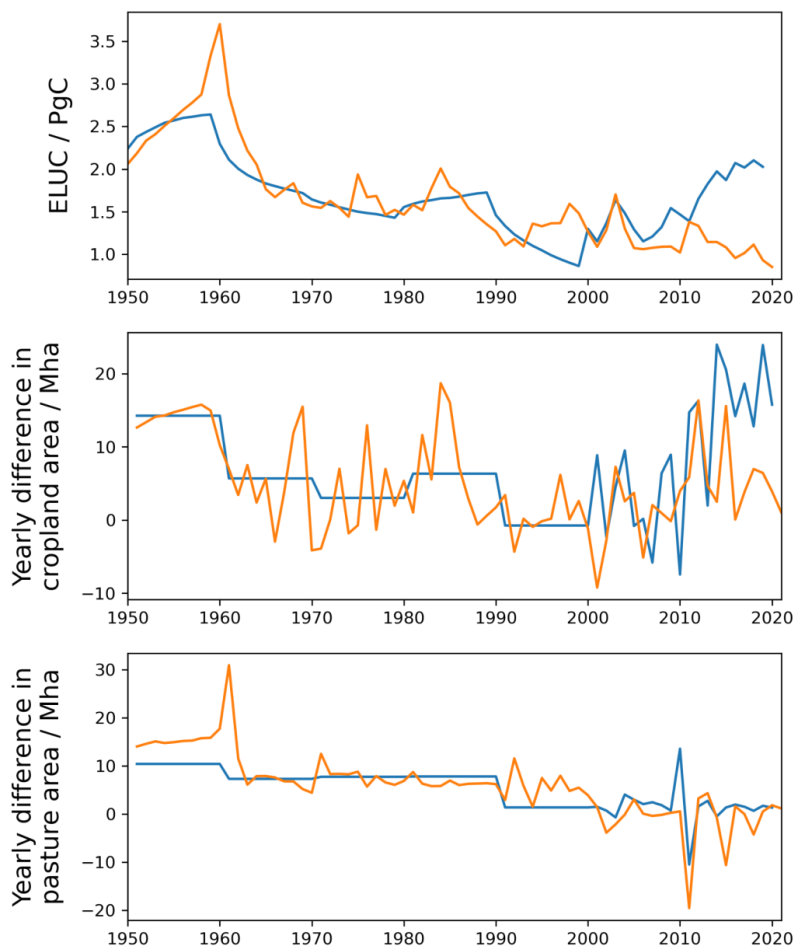
33

34 Figure B4. Evaluation of the atmospheric inversion products. The mean of the model minus observations is shown for four
35 latitude bands in four periods: (first panel) 2001-2021, (second panel) 2001-2010, (third panel) 2011-2021, (fourth panel)
36 2015-2021. The 9 systems are compared to independent CO₂ measurements made onboard aircraft over many places of the
37 world between 2 and 7 km above sea level. Aircraft measurements archived in the Cooperative Global Atmospheric Data
38 Integration Project (Schuldt et al. 2021, Schuldt et al. 2022) from sites, campaigns or programs that have not been
39 assimilated and cover at least 9 months (except for SH programs) between 2001 and 2021, have been used to compute the
40 biases of the differences in four 45° latitude bins. Land and ocean data are used without distinction, and observation density
41 varies strongly with latitude and time as seen on the lower panels.



42

43 **Figure B5.** Comparison of the estimates of each component of the global carbon budget in this study (black line) with the
 44 estimates released annually by the GCP since 2006. Grey shading shows the uncertainty bounds representing ± 1 standard
 45 deviation of the current global carbon budget, based on the uncertainty assessments described in Appendix C. CO₂ emissions
 46 from (a) fossil CO₂ emissions (E_{FOS}), and (b) land-use change (E_{LUC}), as well as their partitioning among (c) the atmosphere
 47 (G_{ATM}), (d) the land (S_{LAND}), and (e) the ocean (S_{OCEAN}). See legend for the corresponding years, and Tables 3 and A7 for
 48 references. The budget year corresponds to the year when the budget was first released. All values are in GtC yr⁻¹.



49

50 **Figure B6.** Differences in the HYDE/LUH2 land-use forcing used for the global carbon budgets GCB2020 (Friedlingstein et
51 al., 2021), and for GCB2021/GCB2022 (Friedlingstein et al., 2022a, Friedlingstein et al., 2022b). Shown are year-to-year
52 changes in cropland area (middle panel) and pasture area (bottom panel). To illustrate the relevance of the update in the
53 land-use forcing to the recent trends in ELUC, the top panel shows the land-use emission estimate from the bookkeeping model
54 BLUE (original model output, i.e. excluding peat fire and drainage emissions).

55



56 **Appendix C. Extended Methodology**

57 **C.1 Methodology Fossil Fuel CO₂ emissions (E_{FOS})**

58 **C.1.1 Cement carbonation**

59 From the moment it is created, cement begins to absorb CO₂ from the atmosphere, a process known as ‘cement
60 carbonation’. We estimate this CO₂ sink, as the average of two studies in the literature (Cao et al., 2020; Guo et al.,
61 2021). Both studies use the same model, developed by Xi et al. (2016), with different parameterisations and input data,
62 with the estimate of Guo and colleagues being a revision of Xi et al (2016). The trends of the two studies are very
63 similar. Modelling cement carbonation requires estimation of a large number of parameters, including the different
64 types of cement material in different countries, the lifetime of the structures before demolition, of cement waste after
65 demolition, and the volumetric properties of structures, among others (Xi et al., 2016). Lifetime is an important
66 parameter because demolition results in the exposure of new surfaces to the carbonation process. The main reasons for
67 differences between the two studies appear to be the assumed lifetimes of cement structures and the geographic
68 resolution, but the uncertainty bounds of the two studies overlap. In the present budget, we include the cement
69 carbonation carbon sink in the fossil CO₂ emission component (E_{FOS}).

70 **C.1.2 Emissions embodied in goods and services**

71 CDIAC, UNFCCC, and BP national emission statistics ‘include greenhouse gas emissions and removals taking place
72 within national territory and offshore areas over which the country has jurisdiction’ (Rypdal et al., 2006), and are called
73 territorial emission inventories. Consumption-based emission inventories allocate emissions to products that are
74 consumed within a country, and are conceptually calculated as the territorial emissions minus the ‘embodied’ territorial
75 emissions to produce exported products plus the emissions in other countries to produce imported products
76 (Consumption = Territorial – Exports + Imports). Consumption-based emission attribution results (e.g. Davis and
77 Caldeira, 2010) provide additional information to territorial-based emissions that can be used to understand emission
78 drivers (Hertwich and Peters, 2009) and quantify emission transfers by the trade of products between countries (Peters
79 et al., 2011b). The consumption-based emissions have the same global total, but reflect the trade-driven movement of
80 emissions across the Earth's surface in response to human activities. We estimate consumption-based emissions from
81 1990-2020 by enumerating the global supply chain using a global model of the economic relationships between
82 economic sectors within and between every country (Andrew and Peters, 2013; Peters et al., 2011a). Our analysis is
83 based on the economic and trade data from the Global Trade and Analysis Project (GTAP; Narayanan et al., 2015), and
84 we make detailed estimates for the years 1997 (GTAP version 5), 2001 (GTAP6), and 2004, 2007, 2011, and 2014
85 (GTAP10.0a), covering 57 sectors and 141 countries and regions. The detailed results are then extended into an annual
86 time series from 1990 to the latest year of the Gross Domestic Product (GDP) data (2020 in this budget), using GDP
87 data by expenditure in current exchange rate of US dollars (USD; from the UN National Accounts main Aggregates
88 database; UN, 2021) and time series of trade data from GTAP (based on the methodology in Peters et al., 2011a). We
89 estimate the sector-level CO₂ emissions using the GTAP data and methodology, add the flaring and cement emissions
90 from our fossil CO₂ dataset, and then scale the national totals (excluding bunker fuels) to match the emission estimates
91 from the carbon budget. We do not provide a separate uncertainty estimate for the consumption-based emissions, but



92 based on model comparisons and sensitivity analysis, they are unlikely to be significantly different than for the
93 territorial emission estimates (Peters et al., 2012a).

94 **C.1.3 Uncertainty assessment for E_{FOS}**

95 We estimate the uncertainty of the global fossil CO₂ emissions at $\pm 5\%$ (scaled down from the published $\pm 10\%$ at $\pm 2\sigma$
96 to the use of $\pm 1\sigma$ bounds reported here; Andres et al., 2012). This is consistent with a more detailed analysis of
97 uncertainty of $\pm 8.4\%$ at $\pm 2\sigma$ (Andres et al., 2014) and at the high-end of the range of $\pm 5\text{--}10\%$ at $\pm 2\sigma$ reported by
98 (Ballantyne et al., 2015). This includes an assessment of uncertainties in the amounts of fuel consumed, the carbon and
99 heat contents of fuels, and the combustion efficiency. While we consider a fixed uncertainty of $\pm 5\%$ for all years, the
100 uncertainty as a percentage of emissions is growing with time because of the larger share of global emissions from
101 emerging economies and developing countries (Marland et al., 2009). Generally, emissions from mature economies
102 with good statistical processes have an uncertainty of only a few per cent (Marland, 2008), while emissions from
103 strongly developing economies such as China have uncertainties of around $\pm 10\%$ (for $\pm 1\sigma$; Gregg et al., 2008; Andres
104 et al., 2014). Uncertainties of emissions are likely to be mainly systematic errors related to underlying biases of energy
105 statistics and to the accounting method used by each country.

106 **C.1.4 Growth rate in emissions**

107 We report the annual growth rate in emissions for adjacent years (in percent per year) by calculating the difference
108 between the two years and then normalising to the emissions in the first year: $(E_{FOS}(t+1) - E_{FOS}(t)) / E_{FOS}(t) \times 100\%$. We apply a leap-year adjustment where relevant to ensure valid interpretations of annual
109 growth rates. This affects the growth rate by about 0.3% yr⁻¹ (1/366) and causes calculated growth rates to go up
110 approximately 0.3% if the first year is a leap year and down 0.3% if the second year is a leap year.

112 The relative growth rate of E_{FOS} over time periods of greater than one year can be rewritten using its logarithm
113 equivalent as follows:

$$114 \frac{1}{E_{FOS}} \frac{dE_{FOS}}{dt} = \frac{d(\ln E_{FOS})}{dt} \quad (2)$$

115 Here we calculate relative growth rates in emissions for multi-year periods (e.g. a decade) by fitting a linear trend to
116 $\ln(E_{FOS})$ in Eq. (2), reported in percent per year.

117 **C.1.5 Emissions projection for 2022**

118 To gain insight on emission trends for 2022, we provide an assessment of global fossil CO₂ emissions, E_{FOS} , by
119 combining individual assessments of emissions for China, USA, the EU, and India (the four countries/regions with the
120 largest emissions), and the rest of the world.

121 The methods are specific to each country or region, as described in detail below.

122 **China:** We use a regression between monthly data for each fossil fuel and cement, and annual data for consumption of
123 fossil fuels / production of cement to project full-year growth in fossil fuel consumption and cement production. The
124 monthly data for each product consists of the following:

- 125 • Coal: Proprietary estimate for monthly consumption of main coal types, from SX Coal



- 126 • Oil: Production data from the National Bureau of Statistics (NBS), plus net imports from the China Customs
- 127 Administration (i.e., gross supply of oil, not including inventory changes)
- 128 • Natural gas: Same as for oil
- 129 • Cement: Production data from NBS

130 For oil, we use data for production and net imports of refined oil products rather than crude oil. This choice is made
131 because refined products are one step closer to actual consumption, and because crude oil can be subject to large
132 market-driven and strategic inventory changes that are not captured by available monthly data.

133 For each fuel and cement, we make a Bayesian linear regression between year-on-year cumulative growth in supply
134 (production for cement) and full-year growth in consumption (production for cement) from annual consumption data. In
135 the regression model, the growth rate in annual consumption (production for cement) is modelled as a regression
136 parameter multiplied by the cumulative year-on-year growth rate from the monthly data through July of each year for
137 past years (through 2021). We use broad Gaussian distributions centered around 1 as priors for the ratios between
138 annual and through-July growth rates. We then use the posteriors for the growth rates together with cumulative monthly
139 supply/production data through July of 2022 to produce a posterior predictive distribution for the full-year growth rate
140 for fossil fuel consumption / cement production in 2022.

141 If the growth in supply/production through July were an unbiased estimate of the full-year growth in
142 consumption/production, the posterior distribution for the ratio between the monthly and annual growth rates would be
143 centered around 1. However, in practice the ratios are different from 1 (in most cases below 1). This is a result of
144 various biasing factors such as uneven evolution in the first and second half of each year, inventory changes that are
145 somewhat anti-correlated with production and net imports, differences in statistical coverage, and other factors that are
146 not captured in the monthly data.

147 For fossil fuels, the mean of the posterior distribution is used as the central estimate for the growth rate in 2022, while
148 the edges of a 68% credible interval (analogous to a 1-sigma confidence interval) are used for the upper and lower
149 bounds.

150 For cement, the evolution from January to July has been highly atypical owing to the ongoing turmoil in the
151 construction sector, and the results of the regression analysis are heavily biased by equally atypical but different
152 dynamics in 2021. For this reason, we use an average of the results of the regression analysis and the plain growth in
153 cement production through July 2022, since this results in a growth rate that seems more plausible and in line with
154 where the cumulative cement production appears to be headed at the time of writing.

155

156 **USA:** We use emissions estimated by the U.S. Energy Information Administration (EIA) in their Short-Term Energy
157 Outlook (STEO) for emissions from fossil fuels to get both YTD and a full year projection (EIA, 2022). The STEO also
158 includes a near-term forecast based on an energy forecasting model which is updated monthly (last update with
159 preliminary data through August 2022), and takes into account expected temperatures, household expenditures by fuel
160 type, energy markets, policies, and other effects. We combine this with our estimate of emissions from cement
161 production using the monthly U.S. cement clinker production data from USGS for January-June 2022, assuming
162 changes in cement production over the first part of the year apply throughout the year.



163 **India:** We use monthly emissions estimates for India updated from Andrew (2020b) through July 2022. These
164 estimates are derived from many official monthly energy and other activity data sources to produce direct estimates of
165 national CO₂ emissions, without the use of proxies. Emissions from coal are then extended to August using a regression
166 relationship based on power generated from coal, coal dispatches by Coal India Ltd., the composite PMI, time, and days
167 per month. For the last 3-5 months of the year, each series is extrapolated assuming typical trends.

168 **EU:** We use a refinement to the methods presented by Andrew (2021), deriving emissions from monthly energy data
169 reported by Eurostat. Some data gaps are filled using data from the Joint Organisations Data Initiative (JODI, 2022).
170 Sub-annual cement production data are limited, but data for Germany and Poland, the two largest producers, suggest a
171 small decline. For fossil fuels this provides estimates through July. We extend coal emissions through August using a
172 regression model built from generation of power from hard coal, power from brown coal, total power generation, and
173 the number of working days in Germany and Poland, the two biggest coal consumers in the EU. These are then
174 extended through the end of the year assuming typical trends. We extend oil emissions by building a regression model
175 between our monthly CO₂ estimates and oil consumption reported by the EIA for Europe in its Short-Term Energy
176 Outlook (September edition), and then using this model with EIA's monthly forecasts. For natural gas, the strong
177 seasonal signal allows the use of the bias-adjusted Holt-Winters exponential smoothing method (Chatfield, 1978).

178 **Rest of the world:** We use the close relationship between the growth in GDP and the growth in emissions (Raupach et
179 al., 2007) to project emissions for the current year. This is based on a simplified Kaya Identity, whereby E_{FOS} (GtC yr⁻¹)
180 is decomposed by the product of GDP (USD yr⁻¹) and the fossil fuel carbon intensity of the economy (I_{FOS} ; GtC USD⁻¹)
181 as follows:

$$182 \quad E_{FOS} = GDP \times I_{FOS} \quad (3)$$

183 Taking a time derivative of Equation (3) and rearranging gives:

$$184 \quad \frac{1}{E_{FOS}} \frac{dE_{FOS}}{dt} = \frac{1}{GDP} \frac{dGDP}{dt} + \frac{1}{I_{FOS}} \frac{dI_{FOS}}{dt} \quad (4)$$

185 where the left-hand term is the relative growth rate of E_{FOS} , and the right-hand terms are the relative growth rates of
186 GDP and I_{FOS} , respectively, which can simply be added linearly to give the overall growth rate.

187 The I_{FOS} is based on GDP in constant PPP (Purchasing Power Parity) from the International Energy Agency (IEA) up to
188 2017 (IEA/OECD, 2019) and extended using the International Monetary Fund (IMF) growth rates through 2021 (IMF,
189 2022). Interannual variability in I_{FOS} is the largest source of uncertainty in the GDP-based emissions projections. We
190 thus use the standard deviation of the annual I_{FOS} for the period 2012-2021 as a measure of uncertainty, reflecting a
191 $\pm 1\sigma$ as in the rest of the carbon budget. For rest-of-world oil emissions growth, we use the global oil demand forecast
192 published by the EIA less our projections for the other four regions, and estimate uncertainty as the maximum absolute
193 difference over the period available for such forecasts using the specific monthly edition (e.g. August) compared to the
194 first estimate based on more solid data in the following year (April).

195 **World:** The global total is the sum of each of the countries and regions.

196



197 **C.2 Methodology CO₂ emissions from land-use, land-use change and forestry (E_{LUC})**

198 The net CO₂ flux from land-use, land-use change and forestry (E_{LUC}, called land-use change emissions in the rest of the
199 text) includes CO₂ fluxes from deforestation, afforestation, logging and forest degradation (including harvest activity),
200 shifting cultivation (cycle of cutting forest for agriculture, then abandoning), and regrowth of forests following wood
201 harvest or abandonment of agriculture. Emissions from peat burning and drainage are added from external datasets (see
202 section C.2.1 below). Only some land-management activities are included in our land-use change emissions estimates
203 (Table A1). Some of these activities lead to emissions of CO₂ to the atmosphere, while others lead to CO₂ sinks. E_{LUC} is
204 the net sum of emissions and removals due to all anthropogenic activities considered. Our annual estimate for 1960-
205 2021 is provided as the average of results from three bookkeeping approaches (Section C.2.1 below): an estimate using
206 the Bookkeeping of Land Use Emissions model (Hansis et al., 2015; hereafter BLUE) and one using the compact Earth
207 system model OSCAR (Gasser et al., 2020), both BLUE and OSCAR being updated here to new land-use forcing
208 covering the time period until 2021, and an updated version of the estimate published by Houghton and Nassikas (2017)
209 (hereafter updated H&N2017). All three data sets are then extrapolated to provide a projection for 2022 (Section C.2.5
210 below). In addition, we use results from Dynamic Global Vegetation Models (DGVMs; see Section 2.5 and Table 4) to
211 help quantify the uncertainty in E_{LUC} (Section C.2.4), and thus better characterise our understanding. Note that in this
212 budget, we use the scientific E_{LUC} definition, which counts fluxes due to environmental changes on managed land
213 towards S_{LAND}, as opposed to the national greenhouse gas inventories under the UNFCCC, which include them in E_{LUC}
214 and thus often report smaller land-use emissions (Grassi et al., 2018; Petrescu et al., 2020). However, we provide a
215 methodology of mapping of the two approaches to each other further below (Section C.2.3).

216 **C.2.1 Bookkeeping models**

217 Land-use change CO₂ emissions and uptake fluxes are calculated by three bookkeeping models. These are based on the
218 original bookkeeping approach of Houghton (2003) that keeps track of the carbon stored in vegetation and soils before
219 and after a land-use change (transitions between various natural vegetation types, croplands, and pastures). Literature-
220 based response curves describe decay of vegetation and soil carbon, including transfer to product pools of different
221 lifetimes, as well as carbon uptake due to regrowth. In addition, the bookkeeping models represent long-term
222 degradation of primary forest as lowered standing vegetation and soil carbon stocks in secondary forests, and include
223 forest management practices such as wood harvests.

224 BLUE and the updated H&N2017 exclude land ecosystems' transient response to changes in climate, atmospheric CO₂
225 and other environmental factors, and base the carbon densities on contemporary data from literature and inventory data.
226 Since carbon densities thus remain fixed over time, the additional sink capacity that ecosystems provide in response to
227 CO₂-fertilisation and some other environmental changes is not captured by these models (Pongratz et al., 2014). On the
228 contrary, OSCAR includes this transient response, and it follows a theoretical framework (Gasser and Ciais, 2013) that
229 allows separating bookkeeping land-use emissions and the loss of additional sink capacity. Only the former is included
230 here, while the latter is discussed in Appendix D4. The bookkeeping models differ in (1) computational units (spatially
231 explicit treatment of land-use change for BLUE, country-level for the updated H&N2017 and OSCAR), (2) processes
232 represented (see Table A1), and (3) carbon densities assigned to vegetation and soil of each vegetation type (literature-
233 based for the updated H&N2017 and BLUE, calibrated to DGVMs for OSCAR). A notable difference between models
234 exists with respect to the treatment of shifting cultivation. The update of H&N2017, introduced for the GCB2021
235 (Friedlingstein et al., 2022) changed the approach over the earlier H&N2017 version: H&N2017 had assumed the



236 "excess loss" of tropical forests (i.e., when FRA indicated a forest loss larger than the increase in agricultural areas
237 from FAO) resulted from converting forests to croplands at the same time older croplands were abandoned. Those
238 abandoned croplands began to recover to forests after 15 years. The updated H&N2017 now assumes that forest loss in
239 excess of increases in cropland and pastures represented an increase in shifting cultivation. When the excess loss of
240 forests was negative, it was assumed that shifting cultivation was returned to forest. Historical areas in shifting
241 cultivation were extrapolated taking into account country-based estimates of areas in fallow in 1980 (FAO/UNEP,
242 1981) and expert opinion (from Heinemann et al., 2017). In contrast, the BLUE and OSCAR models include sub-grid-
243 scale transitions between all vegetation types. Furthermore, the updated H&N2017 assume conversion of natural
244 grasslands to pasture, while BLUE and OSCAR allocate pasture proportionally on all natural vegetation that exists in a
245 grid-cell. This is one reason for generally higher emissions in BLUE and OSCAR. Bookkeeping models do not directly
246 capture carbon emissions from peat fires, which can create large emissions and interannual variability due to synergies
247 of land-use and climate variability in Southeast Asia, particularly during El-Niño events, nor emissions from the
248 organic layers of drained peat soils. To correct for this, we add peat fire emissions based on the Global Fire Emission
249 Database (GFED4s; van der Werf et al., 2017) to the bookkeeping models' output. As these satellite-derived estimates
250 start in 1997 only, we follow the approach by Houghton and Nassikas (2017) for earlier years, which ramps up from
251 zero emissions in 1980 to 0.04 Pg C yr⁻¹ in 1996, reflecting the onset of major clearing of peatlands in equatorial
252 Southeast Asia in the 1980s. Similarly, we add estimates of peat drainage emissions. In recent years, more peat
253 drainage estimates that provide spatially explicit data have become available, and we thus extended the number of peat
254 drainage datasets considered: We employ FAO peat drainage emissions 1990–2019 from croplands and grasslands
255 (Conchedda and Tubiello, 2020), peat drainage emissions 1700–2010 from simulations with the DGVM ORCHIDEE-
256 PEAT (Qiu et al., 2021), and peat drainage emissions 1701–2021 from simulations with the DGVM LPX-Bern (Lienert
257 and Joos, 2018; Müller and Joos, 2021) applying the updated LUH2 forcing as also used by BLUE, OSCAR and the
258 DGVMs. We extrapolate the FAO data to 1850–2021 by keeping the post-2019 emissions constant at 2019 levels, by
259 linearly increasing tropical drainage emissions between 1980 and 1990 starting from 0 GtC yr⁻¹ in 1980, consistent
260 with H&N2017's assumption (Houghton and Nassikas, 2017), and by keeping pre-1990 emissions from the often old
261 drained areas of the extra-tropics constant at 1990 emission levels. ORCHIDEE-PEAT data are extrapolated to 2011-
262 2021 by replicating the average emissions in 2000–2010 (pers. comm. C. Qiu). Further, ORCHIDEE-PEAT only
263 provides peat drainage emissions north of 30°N, and thus we fill the regions south of 30°N by the average peat drainage
264 emissions from FAO and LPX-Bern. The average of the carbon emission estimates by the three different peat drainage
265 dataset is added to the bookkeeping models to obtain net ELUC and gross sources.

266 The three bookkeeping estimates used in this study differ with respect to the land-use change data used to drive the
267 models. The updated H&N2017 base their estimates directly on the Forest Resource Assessment of the FAO which
268 provides statistics on forest-area change and management at intervals of five years currently updated until 2020 (FAO,
269 2020). The data is based on country reporting to FAO and may include remote-sensing information in more recent
270 assessments. Changes in land-use other than forests are based on annual, national changes in cropland and pasture areas
271 reported by FAO (FAOSTAT, 2021). On the other hand, BLUE uses the harmonised land-use change data LUH2-
272 GCB2022 covering the entire 850–2021 period (an update to the previously released LUH2 v2h dataset; Hurtt et al.,
273 2017; Hurtt et al., 2020), which was also used as input to the DGVMs (Section C.2.2). It describes land-use change,
274 also based on the FAO data as described in Section C.2.2 as well as the HYDE3.3 dataset (Klein Goldewijk et al.,
275 2017a, 2017b), but provided at a quarter-degree spatial resolution, considering sub-grid-scale transitions between



276 primary forest, secondary forest, primary non-forest, secondary non-forest, cropland, pasture, rangeland, and urban land
277 (Hurtt et al., 2020; Chini et al., 2021). LUH2-GCB2022 provides a distinction between rangelands and pasture, based
278 on inputs from HYDE. To constrain the models' interpretation on whether rangeland implies the original natural
279 vegetation to be transformed to grassland or not (e.g., browsing on shrubland), a forest mask was provided with LUH2-
280 GCB2021; forest is assumed to be transformed to grasslands, while other natural vegetation remains (in case of
281 secondary vegetation) or is degraded from primary to secondary vegetation (Ma et al., 2020). This is implemented in
282 BLUE. OSCAR was run with both LUH2-GCB2022 and FAO/FRA (as used with the updated H&N2017), where the
283 drivers of the latter were linearly extrapolated to 2021 using their 2015–2020 trends. The best-guess OSCAR estimate
284 used in our study is a combination of results for LUH2-GCB2022 and FAO/FRA land-use data and a large number of
285 perturbed parameter simulations weighted against a constraint (the cumulative S_{LAND} over 1960-2020 of last year's
286 GCB). As the record of the updated H&N2017 ends in 2020, we extend it to 2021 by adding the difference of the
287 emissions from tropical deforestation and degradation, peat drainage, and peat fire between 2020 and 2021 to the
288 model's estimate for 2020 (i.e. considering the yearly anomalies of the emissions from tropical deforestation and
289 degradation, peat drainage, and peat fire). The same method is applied to all three bookkeeping estimates to provide a
290 projection for 2022.

291 For E_{LUC} from 1850 onwards we average the estimates from BLUE, the updated H&N2017 and OSCAR. For the
292 cumulative numbers starting 1750 an average of four earlier publications is added (30 ± 20 PgC 1750-1850, rounded to
293 nearest 5; Le Quéré et al., 2016).

294 We provide estimates of the gross land use change fluxes from which the reported net land-use change flux, E_{LUC} , is
295 derived as a sum. Gross fluxes are derived internally by the three bookkeeping models: Gross emissions stem from
296 decaying material left dead on site and from products after clearing of natural vegetation for agricultural purposes or
297 wood harvesting, emissions from peat drainage and peat burning, and, for BLUE, additionally from degradation from
298 primary to secondary land through usage of natural vegetation as rangeland. Gross removals stem from regrowth after
299 agricultural abandonment and wood harvesting. Gross fluxes for the updated H&N2017 for 2020 and for the 2022
300 projection of all three models were calculated by the change in emissions from tropical deforestation and degradation
301 and peat burning and drainage as described for the net E_{LUC} above: As tropical deforestation and degradation and peat
302 burning and drainage all only lead to gross emissions to the atmosphere, only gross (and net) emissions are adjusted this
303 way, while gross sinks are assumed to remain constant over the previous year.

304 This year, we provide an additional split of the net E_{LUC} into component fluxes to better identify reasons for divergence
305 between bookkeeping estimates and to give more insight into the drivers of sources and sinks. This split distinguishes
306 between fluxes from deforestation (including due to shifting cultivation), fluxes from organic soils (i.e., peat drainage
307 and fires), fluxes on forests (slash and product decay following wood harvesting; regrowth associated with wood
308 harvesting or after abandonment, including reforestation and in shifting cultivation cycles; afforestation) and fluxes
309 associated with all other transitions.

310 C.2.2 Dynamic Global Vegetation Models (DGVMs)

311 Land-use change CO_2 emissions have also been estimated using an ensemble of 16 DGVMs simulations. The DGVMs
312 account for deforestation and regrowth, the most important components of E_{LUC} , but they do not represent all processes
313 resulting directly from human activities on land (Table A1). All DGVMs represent processes of vegetation growth and



314 mortality, as well as decomposition of dead organic matter associated with natural cycles, and include the vegetation
315 and soil carbon response to increasing atmospheric CO₂ concentration and to climate variability and change. Most
316 models explicitly simulate the coupling of carbon and nitrogen cycles and account for atmospheric N deposition and N
317 fertilisers (Table A1). The DGVMs are independent from the other budget terms except for their use of atmospheric
318 CO₂ concentration to calculate the fertilisation effect of CO₂ on plant photosynthesis.

319 All DGVMs use the LUH2-GCB2022 dataset as input, which includes the HYDE cropland/grazing land dataset (Klein
320 Goldewijk et al., 2017a, 2017b), and additional information on land-cover transitions and wood harvest. DGVMs use
321 annual, half-degree (regridded from 5 minute resolution), fractional data on cropland and pasture from HYDE3.3.

322 DGVMs that do not simulate subgrid scale transitions (i.e., net land-use emissions; see Table A1) used the HYDE
323 information on agricultural area change. For all countries, with the exception of Brazil and the Democratic Republic of
324 the Congo (DRC), these data are based on the available annual FAO statistics of change in agricultural land area
325 available from 1961 up to and including 2017. The FAO retrospectively revised their reporting for DRC, which was
326 newly available until 2020. In addition to FAO country-level statistics the HYDE3.3 cropland/grazing land dataset is
327 constrained spatially based on multi-year satellite land cover maps from ESA CCI LC (see below). . After the year
328 2017, LUH2 extrapolates, on a gridcell-basis, the cropland, pasture, and urban data linearly based on the trend over the
329 previous 5 years, to generate data until the year 2021. This extrapolation methodology is not appropriate for countries
330 which have experienced recent rapid changes in the rate of land-use change, e.g. Brazil which has experienced a recent
331 upturn in deforestation. Hence, for Brazil we replace FAO state-level data for cropland and grazing land in HYDE by
332 those from in-country land cover dataset MapBiomias (collection 6) for 1985-2020 (Souza et al. 2020). ESA-CCI is
333 used to spatially disaggregate as described below. Similarly, an estimate for the year 2021 is based on the MapBiomias
334 trend 2015-2020. The pre-1985 period is scaled with the per capita numbers from 1985 from MapBiomias, so this
335 transition is smooth.

336 HYDE uses satellite imagery from ESA-CCI from 1992 – 2018 for more detailed yearly allocation of cropland and
337 grazing land, with the ESA area data scaled to match the FAO annual totals at country-level. The original 300 metre
338 spatial resolution data from ESA was aggregated to a 5 arc minute resolution according to the classification scheme as
339 described in Klein Goldewijk et al (2017a).

340 DGVMs that simulate subgrid scale transitions (i.e., gross land-use emissions; see Table A1) use more detailed land use
341 transition and wood harvest information from the LUH2-GCB2022 data set. LUH2-GCB2022 is an update of the more
342 comprehensive harmonised land-use data set (Hurtt et al., 2020), that further includes fractional data on primary and
343 secondary forest vegetation, as well as all underlying transitions between land-use states (850-2020; Hurtt et al., 2011,
344 2017, 2020; Chini et al., 2021; Table A1). This data set is of quarter degree fractional areas of land-use states and all
345 transitions between those states, including a new wood harvest reconstruction, new representation of shifting
346 cultivation, crop rotations, management information including irrigation and fertiliser application. The land-use states
347 include five different crop types in addition to splitting grazing land into managed pasture and rangeland. Wood harvest
348 patterns are constrained with Landsat-based tree cover loss data (Hansen et al. 2013). Updates of LUH2-GCB2022 over
349 last year's version (LUH2-GCB2021) are using the most recent HYDE release (covering the time period up to 2017,
350 revision to Brazil and DRC as described above). We use the same FAO wood harvest data as last year for all dataset
351 years from 1961 to 2019, and extrapolate to the year 2022. The HYDE3.3 population data is also used to extend the
352 wood harvest time series back in time. Other wood harvest inputs (for years prior to 1961) remain the same in LUH2.



353 These updates in the land-use forcing are shown in comparison to the more pronounced version change from the
354 GCB2020 (Friedlingstein et al., 2020) to GCB2021, which was discussed in Friedlingstein et al. (2022a) in Figure B6
355 and their relevance for land-use emissions discussed in Section 3.2.2. DGVMs implement land-use change differently
356 (e.g., an increased cropland fraction in a grid cell can either be at the expense of grassland or shrubs, or forest, the latter
357 resulting in deforestation; land cover fractions of the non-agricultural land differ between models). Similarly, model-
358 specific assumptions are applied to convert deforested biomass or deforested area, and other forest product pools into
359 carbon, and different choices are made regarding the allocation of rangelands as natural vegetation or pastures.

360 The difference between two DGVMs simulations (See Section C4.1 below), one forced with historical changes in land-
361 use and a second with time-invariant pre-industrial land cover and pre-industrial wood harvest rates, allows
362 quantification of the dynamic evolution of vegetation biomass and soil carbon pools in response to land-use change in
363 each model (E_{LUC}). Using the difference between these two DGVMs simulations to diagnose E_{LUC} means the DGVMs
364 account for the loss of additional sink capacity (around 0.4 ± 0.3 GtC yr⁻¹; see Section 2.7.4, Appendix D4), while the
365 bookkeeping models do not.

366 As a criterion for inclusion in this carbon budget, we only retain models that simulate a positive E_{LUC} during the 1990s,
367 as assessed in the IPCC AR4 (Denman et al., 2007) and AR5 (Ciais et al., 2013). All DGVMs met this criterion,
368 although one model was not included in the E_{LUC} estimate from DGVMs as it exhibited a spurious response to the
369 transient land cover change forcing after its initial spin-up.

370 C.2.3 Mapping of national GHG inventory data to E_{LUC}

371 An approach was implemented to reconcile the large gap between E_{LUC} from bookkeeping models and land use, land-
372 use change and forestry (LULUCF) from national GHG Inventories (NGHGI) (see Tab. A8). This gap is due to
373 different approaches to calculating “anthropogenic” CO₂ fluxes related to land-use change and land management
374 (Grassi et al. 2018). In particular, the land sinks due to environmental change on managed lands are treated as non-
375 anthropogenic in the global carbon budget, while they are generally considered as anthropogenic in NGHGIs (“indirect
376 anthropogenic fluxes”; Eggleston et al., 2006). Building on previous studies (Grassi et al. 2021), the approach
377 implemented here adds the DGVMs estimates of CO₂ fluxes due to environmental change from countries’ managed
378 forest area (part of the S_{LAND}) to the original E_{LUC} flux. This sum is expected to be conceptually more comparable to
379 LULUCF than simply E_{LUC} .

380 E_{LUC} data are taken from bookkeeping models, in line with the global carbon budget approach. To determine S_{LAND} on
381 managed forest, the following steps were taken: Spatially gridded data of “natural” forest NBP (S_{LAND} i.e., due to
382 environmental change and excluding land use change fluxes) were obtained with S2 runs from DGVMs up to 2021
383 from the TRENDY v11 dataset. Results were first masked with a forest map that is based on Hansen (Hansen et
384 al.2013) tree cover data. To do this conversion (“tree” cover to “forest” cover), we exclude gridcells with less than 20%
385 tree cover and isolated pixels with maximum connectivity less than 0.5 ha following the FAO definition of forest.
386 Forest NBP are then further masked with the “intact” forest map for the year 2013, i.e. forest areas characterised by no
387 remotely detected signs of human activity (Potapov et al. 2017). This way, we obtained the S_{LAND} in “intact” and
388 “non-intact” forest area, which previous studies (Grassi et al. 2021) indicated to be a good proxy, respectively, for
389 “unmanaged” and “managed” forest area in the NGHGI. Note that only 4 models (CABLE-POP, CLASSIC, JSBACH
390 and YIBs) had forest NBP at grid cell level. For the other DGVMs, when a grid cell had forest, all the NBP was



391 allocated to forest. However, since S2 simulations use pre-industrial forest cover masks that are at least 20% larger than
392 today's forest (Hurt et al. 2020), we corrected this NBP by a ratio between observed (based on Hansen) and prescribed
393 (from DGVMs) forest cover. This ratio is calculated for each individual DGVM that provides information on prescribed
394 forest cover (LPX-Bern, OCN, JULES, VISIT, VISIT-NIES, SDGVM). For the others (IBIS, CLM5.0, ORCHIDEE,
395 ISAM, DLEM, LPJ-GUESS) a common ratio (median ratio of all the 10 models that provide information on prescribed
396 forest cover) is used. The details of the method used are explained here:

397 https://github.com/RamAlkama/LandCarbonBudget_IntactAndNonIntactForest

398 LULUCF data from NGHGs are from Grassi et al. (2022a). While Annex I countries report a complete time series
399 1990-2020, for Non-Annex I countries gap-filling was applied through linear interpolation between two points and/or
400 through extrapolation backward (till 1990) and forward (till 2020) using the single closest available data. For all
401 countries, the year 2021 is assumed to be equal to 2020. This data includes all CO₂ fluxes from land considered
402 managed, which in principle encompasses all land uses (forest land, cropland, grassland, wetlands, settlements, and
403 other land), changes among them, emissions from organic soils and from fires. In practice, although almost all Annex I
404 countries report all land uses, many non-Annex I countries report only on deforestation and forest land, and only few
405 countries report on other land uses. In most cases, NGHGI include most of the natural response to recent environmental
406 change, because they use direct observations (e.g., national forest inventories) that do not allow separating direct and
407 indirect anthropogenic effects (Eggleston et al., 2006).

408 To provide additional, largely independent assessments of fluxes on unmanaged vs managed lands, we include a
409 DGVM that allows diagnosing fluxes from unmanaged vs managed lands by tracking vegetation cohorts of different
410 ages separately. This model, ORCHIDEE-MICT (Yue et al., 2018), was run using the same LUH2 forcing as the
411 DGVMs used in this budget (Section 2.5) and the bookkeeping models BLUE and OSCAR (Section 2.2). Old-aged
412 forest was classified as primary forest after a certain threshold of carbon density was reached again, and the model-
413 internal distinction between primary and secondary forest used as proxies for unmanaged vs managed forests;
414 agricultural lands are added to the latter to arrive at total managed land.

415 Tab. A8 shows the resulting mapping of global carbon cycle models' land flux definitions to that of the NGHGI
416 (discussed in Section 3.2.2). ORCHIDEE-MICT estimates for S_{LAND} on intact forests are expected to be higher than
417 based on DGVMs in combination with the NGHGI managed/unmanaged forest data because the unmanaged forest
418 area, with about 27 mio km², is estimated to be substantially larger by ORCHIDEE-MICT than, with less than 10 mio
419 km², by the NGHGI, while managed forest area is estimated to be smaller (22 compared to 32 mio km²). Related to
420 this, E_{LUC} plus S_{LAND} on non-intact lands is a larger source estimated by ORCHIDEE-MICT compared to NGHGI. We
421 also show as comparison FAOSTAT emissions totals (FAO, 2021), which include emissions from net forest conversion
422 and fluxes on forest land (Tubiello et al., 2021) as well as CO₂ emissions from peat drainage and peat fires. The 2021
423 data was estimated by including actual 2021 estimates for peatlands drainage and fire and a carry forward from 2020 to
424 2021 for the forest land stock change. The FAO data shows a global source of 0.24 GtC yr⁻¹ averaged over 2012-2021,
425 in contrast to the sink of -0.54 GtC yr⁻¹ of the gap-filled NGHGI data. Most of this difference is attributable to different
426 scopes: a focus on carbon fluxes for the NGHGI and a focus on area and biomass for FAO. In particular, the NGHGI
427 data includes a larger forest sink for non-Annex I countries resulting from a more complete coverage of non-biomass
428 carbon pools and non-forest land uses. NGHGI and FAO data also differ in terms of underlying data on forest land
429 (Grassi et al., 2022a).



430 C.2.4 Uncertainty assessment for E_{LUC}

431 Differences between the bookkeeping models and DGVMs models originate from three main sources: the different
432 methodologies, which among others lead to inclusion of the loss of additional sink capacity in DGVMs (see Appendix
433 D1.4), the underlying land-use/land cover data set, and the different processes represented (Table A1). We examine the
434 results from the DGVMs models and of the bookkeeping method and use the resulting variations as a way to
435 characterise the uncertainty in E_{LUC} .

436 Despite these differences, the E_{LUC} estimate from the DGVMs multi-model mean is consistent with the average of the
437 emissions from the bookkeeping models (Table 5). However there are large differences among individual DGVMs
438 (standard deviation at around 0.5 GtC yr^{-1} ; Table 5), between the bookkeeping estimates (average difference 1850-2020
439 BLUE-updated H&N2017 of 0.8 GtC yr^{-1} , BLUE-OSCAR of 0.4 GtC yr^{-1} , OSCAR-updated H&N2017 of 0.3 GtC yr^{-1}),
440 and between the updated estimate of H&N2017 and its previous model version (Houghton et al., 2012). A factorial
441 analysis of differences between BLUE and H&N2017 attributed them particularly to differences in carbon densities
442 between natural and managed vegetation or primary and secondary vegetation (Bastos et al., 2021). Earlier studies
443 additionally showed the relevance of the different land-use forcing as applied (in updated versions) also in the current
444 study (Gasser et al., 2020). Ganzenmüller et al. (2022) recently showed that E_{LUC} estimates with BLUE are
445 substantially smaller when the model is driven by a new high-resolution land-use dataset (HILDA+). They identified
446 shifting cultivation and the way it is implemented in LUH2 as a main reason for this divergence. They further showed
447 that a higher spatial resolution reduces the estimates of both sources and sinks because successive transitions are not
448 adequately represented at coarser resolution, which has the effect that—despite capturing the same extent of transition
449 areas—overall less area remains pristine at the coarser compared to the higher resolution.

450 The uncertainty in E_{LUC} of $\pm 0.7 \text{ GtC yr}^{-1}$ reflects our best value judgement that there is at least 68% chance ($\pm 1\sigma$) that
451 the true land-use change emission lies within the given range, for the range of processes considered here. Prior to the
452 year 1959, the uncertainty in E_{LUC} was taken from the standard deviation of the DGVMs. We assign low confidence to
453 the annual estimates of E_{LUC} because of the inconsistencies among estimates and of the difficulties to quantify some of
454 the processes in DGVMs.

455 C.2.5 Emissions projections for E_{LUC}

456 We project the 2022 land-use emissions for BLUE, the updated H&N2017 and OSCAR, starting from their estimates
457 for 2021 assuming unaltered peat drainage, which has low interannual variability, and the highly variable emissions
458 from peat fires, tropical deforestation and degradation as estimated using active fire data (MCD14ML; Giglio et al.,
459 2016). Those latter scale almost linearly with GFED over large areas (van der Werf et al., 2017), and thus allows for
460 tracking fire emissions in deforestation and tropical peat zones in near-real time.

461

462 C.3 Methodology Ocean CO_2 sink

463 C.3.1 Observation-based estimates

464 We primarily use the observational constraints assessed by IPCC of a mean ocean CO_2 sink of $2.2 \pm 0.7 \text{ GtC yr}^{-1}$ for the
465 1990s (90% confidence interval; Ciais et al., 2013) to verify that the GOBMs provide a realistic assessment of S_{OCEAN} .



466 This is based on indirect observations with seven different methodologies and their uncertainties, and further using
467 three of these methods that are deemed most reliable for the assessment of this quantity (Denman et al., 2007; Ciais et
468 al., 2013). The observation-based estimates use the ocean/land CO₂ sink partitioning from observed atmospheric CO₂
469 and O₂/N₂ concentration trends (Manning and Keeling, 2006; Keeling and Manning, 2014), an oceanic inversion
470 method constrained by ocean biogeochemistry data (Mikaloff Fletcher et al., 2006), and a method based on penetration
471 time scale for chlorofluorocarbons (McNeil et al., 2003). The IPCC estimate of 2.2 GtC yr⁻¹ for the 1990s is consistent
472 with a range of methods (Wanninkhof et al., 2013). We refrain from using the IPCC estimates for the 2000s (2.3 ± 0.7
473 GtC yr⁻¹), and the period 2002-2011 (2.4 ± 0.7 GtC yr⁻¹, Ciais et al., 2013) as these are based on trends derived mainly
474 from models and one data-product (Ciais et al., 2013). Additional constraints summarised in AR6 (Canadell et al.,
475 2021) are the interior ocean anthropogenic carbon change (Gruber et al., 2019) and ocean sink estimate from
476 atmospheric CO₂ and O₂/N₂ (Tohjima et al., 2019) which are used for model evaluation and discussion, respectively.

477 We also use eight estimates of the ocean CO₂ sink and its variability based on surface ocean fCO₂ maps obtained by the
478 interpolation of surface ocean fCO₂ measurements from 1990 onwards due to severe restriction in data availability prior
479 to 1990 (Figure 10). These estimates differ in many respects: they use different maps of surface fCO₂, different
480 atmospheric CO₂ concentrations, wind products and different gas-exchange formulations as specified in Table A3. We
481 refer to them as fCO₂-based flux estimates. The measurements underlying the surface fCO₂ maps are from the Surface
482 Ocean CO₂ Atlas version 2022 (SOCATv2022; Bakker et al., 2022), which is an update of version 3 (Bakker et al.,
483 2016) and contains quality-controlled data through 2021 (see data attribution Table A5). Each of the estimates uses a
484 different method to then map the SOCAT v2022 data to the global ocean. The methods include a data-driven diagnostic
485 method combined with a multi linear regression approach to extend back to 1957 (Rödenbeck et al., 2022; referred to
486 here as Jena-MLS), three neural network models (Landschützer et al., 2014; referred to as MPI-SOMFFN; Chau et al.,
487 2022; Copernicus Marine Environment Monitoring Service, referred to here as CMEMS-LSCE-FFNN; and Zeng et al.,
488 2014; referred to as NIES-NN), one cluster regression approaches (Gregor and Gruber, 2021, referred to as OS-ETHZ-
489 GRaCER), and a multi-linear regression method (Iida et al., 2021; referred to as JMA-MLR), and one method that
490 relates the fCO₂ misfit between GOBMs and SOCAT to environmental predictors using the extreme gradient boosting
491 method (Gloege et al., 2022). The ensemble mean of the fCO₂-based flux estimates is calculated from these seven
492 mapping methods. Further, we show the flux estimate of Watson et al. (2020) who also use the MPI-SOMFFN method
493 to map the adjusted fCO₂ data to the globe, but resulting in a substantially larger ocean sink estimate, owing to a
494 number of adjustments they applied to the surface ocean fCO₂ data. Concretely, these authors adjusted the SOCAT
495 fCO₂ downward to account for differences in temperature between the depth of the ship intake and the relevant depth
496 right near the surface, and included a further adjustment to account for the cool surface skin temperature effect. The
497 Watson et al. flux estimate hence differs from the others by their choice of adjusting the flux to a cool, salty ocean
498 surface skin. Watson et al. (2020) showed that this temperature adjustment leads to an upward correction of the ocean
499 carbon sink, up to 0.9 GtC yr⁻¹, that, if correct, should be applied to all fCO₂-based flux estimates. A reduction of this
500 adjustment to 0.6 GtC yr⁻¹ was proposed by Dong et al. (2022). The impact of the cool skin effect on air-sea CO₂ flux is
501 based on established understanding of temperature gradients (as discussed by Goddijn-Murphy et al 2015), and
502 laboratory observations (Jähne and Haussecker, 1998; Jähne, 2019), but in situ field observational evidence is lacking
503 (Dong et al., 2022). The Watson et al flux estimate presented here is therefore not included in the ensemble mean of the
504 fCO₂-based flux estimates. This choice will be re-evaluated in upcoming budgets based on further lines of evidence.



505 Typically, data products do not cover the entire ocean due to missing coastal oceans and sea ice cover. The CO₂ flux
506 from each fCO₂-based product is already at or above 99% coverage of the ice-free ocean surface area in two products
507 (Jena-MLS, OS-ETHZ-GRaCER), and filled by the data-provider in three products (using Fay et al., 2021a, method for
508 JMA-MLR and LDEO-HPD; and Landschützer et al., 2020, methodology for MPI-SOMFFN). The products that
509 remained below 99% coverage of the ice-free ocean (CMEMS-LSCE-FFNN, MPI-SOMFFN, NIES-NN, UOx-Watson)
510 were scaled by the following procedure.

511 In previous versions of the GCB, the missing areas were accounted for by scaling the globally integrated fluxes by the
512 fraction of the global ocean coverage (361.9e6 km² based on ETOPO1, Amante and Eakins, 2009; Eakins and Sharman,
513 2010) with the area covered by the CO₂ flux predictions. This approach may lead to unnecessary scaling when the
514 majority of the missing data are in the ice-covered region (as is often the case), where flux is already assumed to be
515 zero. To avoid this unnecessary scaling, we now scale fluxes regionally (North, Tropics, South) to match the ice-free
516 area (using NOAA's OISSTv2, Reynolds et al., 2002):

$$517 \quad FCO_2^{reg-scaled} = \frac{A_{(1-ice)}^{region}}{A_{FCO_2}^{region}} \cdot FCO_2^{region}$$

518 In the equation, A represents area, $(1 - ice)$ represents the ice free ocean, $A_{FCO_2}^{region}$ represents the coverage
519 of the data product for a region, and FCO_2^{region} is the integrated flux for a region.

520 We further use results from two diagnostic ocean models, Khatiwala et al. (2013) and DeVries (2014), to estimate the
521 anthropogenic carbon accumulated in the ocean prior to 1959. The two approaches assume constant ocean circulation
522 and biological fluxes, with S_{OCEAN} estimated as a response in the change in atmospheric CO₂ concentration calibrated to
523 observations. The uncertainty in cumulative uptake of ± 20 GtC (converted to $\pm 1\sigma$) is taken directly from the IPCC's
524 review of the literature (Rhein et al., 2013), or about $\pm 30\%$ for the annual values (Khatiwala et al., 2009).

525 C.3.2 Global Ocean Biogeochemistry Models (GOBMs)

526 The ocean CO₂ sink for 1959-20121 is estimated using ten GOBMs (Table A2). The GOBMs represent the physical,
527 chemical, and biological processes that influence the surface ocean concentration of CO₂ and thus the air-sea CO₂ flux.
528 The GOBMs are forced by meteorological reanalysis and atmospheric CO₂ concentration data available for the entire
529 time period. They mostly differ in the source of the atmospheric forcing data (meteorological reanalysis), spin up
530 strategies, and in their horizontal and vertical resolutions (Table A2). All GOBMs except two (CESM-ETHZ, CESM2)
531 do not include the effects of anthropogenic changes in nutrient supply (Duce et al., 2008). They also do not include the
532 perturbation associated with changes in riverine organic carbon (see Section 2.7.3).

533 Four sets of simulations were performed with each of the GOBMs. Simulation A applied historical changes in climate
534 and atmospheric CO₂ concentration. Simulation B is a control simulation with constant atmospheric forcing (normal
535 year or repeated year forcing) and constant pre-industrial atmospheric CO₂ concentration. Simulation C is forced with
536 historical changes in atmospheric CO₂ concentration, but repeated year or normal year atmospheric climate forcing.
537 Simulation D is forced by historical changes in climate and constant pre-industrial atmospheric CO₂ concentration. To
538 derive S_{OCEAN} from the model simulations, we subtracted the slope of a linear fit to the annual time series of the control
539 simulation B from the annual time series of simulation A. Assuming that drift and bias are the same in simulations A
540 and B, we thereby correct for any model drift. Further, this difference also removes the natural steady state flux
541 (assumed to be 0 GtC yr⁻¹ globally without rivers) which is often a major source of biases. This approach works for all
542 model set-ups, including IPSL, where simulation B was forced with constant atmospheric CO₂ but observed historical



543 changes in climate (equivalent to simulation D). This approach assures that the interannual variability is not removed
544 from IPSL simulation A.

545 The absolute correction for bias and drift per model in the 1990s varied between $<0.01 \text{ GtC yr}^{-1}$ and 0.41 GtC yr^{-1} , with
546 seven models having positive biases, two having negative biases and one model having essentially no bias (NorESM).
547 The MPI model uses riverine input and therefore simulates outgassing in simulation B. By subtracting simulation B,
548 also the ocean carbon sink of the MPI model follows the definition of S_{OCEAN} . This correction reduces the model mean
549 ocean carbon sink by 0.04 GtC yr^{-1} in the 1990s. The ocean models cover 99% to 101% of the total ocean area, so that
550 area-scaling is not necessary.

551 C.3.3 GOBM evaluation and uncertainty assessment for S_{OCEAN}

552 The ocean CO_2 sink for all GOBMs and the ensemble mean falls within 90% confidence of the observed range, or 1.5
553 to 2.9 GtC yr^{-1} for the 1990s (Ciais et al., 2013) before and after applying adjustments. An exception is the MPI model,
554 which simulates a low ocean carbon sink of 1.38 GtC yr^{-1} for the 1990s in simulation A owing to the inclusion of
555 riverine carbon flux. After adjusting to the GCB's definition of S_{OCEAN} by subtracting simulation B, the MPI model falls
556 into the observed range with an estimated sink of 1.69 GtC yr^{-1} .

557 The GOBMs and data products have been further evaluated using the fugacity of sea surface CO_2 ($f\text{CO}_2$) from the
558 SOCAT v2022 database (Bakker et al., 2016, 2022). We focused this evaluation on the root mean squared error
559 (RMSE) between observed and modelled $f\text{CO}_2$ and on a measure of the amplitude of the interannual variability of the
560 flux (modified after Rödenbeck et al., 2015). The RMSE is calculated from detrended, annually and regionally
561 averaged time series calculated from GOBMs and data-product $f\text{CO}_2$ subsampled to SOCAT sampling points to
562 measure the misfit between large-scale signals (Hauck et al., 2020). To this end, we apply the following steps: (i)
563 subsample data points for where there are observations (GOBMs/data-products as well as SOCAT), (ii) average
564 spatially, (iii) calculate annual mean, (iv) detrend both time-series (GOBMs/data-products as well as SOCAT), (v)
565 calculate RMSE. This year, we do not apply an open ocean mask of 400 m, but instead a mask based on the minimum
566 area coverage of the data-products. This ensures a fair comparison over equal areas. The amplitude of the S_{OCEAN}
567 interannual variability (A-IAV) is calculated as the temporal standard deviation of the detrended annual CO_2 flux time
568 series after area-scaling (Rödenbeck et al., 2015, Hauck et al., 2020). These metrics are chosen because RMSE is the
569 most direct measure of data-model mismatch and the A-IAV is a direct measure of the variability of S_{OCEAN} on
570 interannual timescales. We apply these metrics globally and by latitude bands. Results are shown in Figure B2 and
571 discussed in Section 3.5.5.

572 We quantify the $1\text{-}\sigma$ uncertainty around the mean ocean sink of anthropogenic CO_2 by assessing random and systematic
573 uncertainties for the GOBMs and data-products. The random uncertainties are taken from the ensemble standard
574 deviation (0.3 GtC yr^{-1} for GOBMs, 0.3 GtC yr^{-1} for data-products). We derive the GOBMs systematic uncertainty by
575 the deviation of the DIC inventory change 1994-2007 from the Gruber et al (2019) estimate (0.4 GtC yr^{-1}) and suggest
576 these are related to physical transport (mixing, advection) into the ocean interior. For the data-products, we consider
577 systematic uncertainties stemming from uncertainty in $f\text{CO}_2$ observations (0.2 GtC yr^{-1} , Takahashi et al., 2009;
578 Wanninkhof et al., 2013), gas-transfer velocity (0.2 GtC yr^{-1} , Ho et al., 2011; Wanninkhof et al., 2013; Roobaert et al.,
579 2018), wind product (0.1 GtC yr^{-1} , Fay et al., 2021a), river flux adjustment (0.3 GtC yr^{-1} , Regnier et al., 2022, formally
580 $2\text{-}\sigma$ uncertainty), and $f\text{CO}_2$ mapping (0.2 GtC yr^{-1} , Landschützer et al., 2014). Combining these uncertainties as their



581 squared sums, we assign an uncertainty of $\pm 0.5 \text{ GtC yr}^{-1}$ to the GOBMs ensemble mean and an uncertainty of ± 0.6
582 GtC yr^{-1} to the data-product ensemble mean. These uncertainties are propagated as $\sigma(S_{\text{OCEAN}}) = (1/2^2 * 0.5^2 + 1/2^2 * 0.6^2)^{1/2}$
583 GtC yr^{-1} and result in an $\pm 0.4 \text{ GtC yr}^{-1}$ uncertainty around the best estimate of S_{OCEAN} .
584 We examine the consistency between the variability of the model-based and the $f\text{CO}_2$ -based data products to assess
585 confidence in S_{OCEAN} . The interannual variability of the ocean fluxes (quantified as A-IAV, the standard deviation after
586 detrending, Figure B2) of the seven $f\text{CO}_2$ -based data products plus the Watson et al. (2020) product for 1990-2021,
587 ranges from 0.12 to 0.32 GtC yr^{-1} with the lower estimates by the two ensemble methods (CMEMS-LSCE-FFNN, OS-
588 ETHZ-GRaCER). The inter-annual variability in the GOBMs ranges between 0.09 and 0.20 GtC yr^{-1} , hence there is
589 overlap with the lower A-IAV estimates of two data-products.
590 Individual estimates (both GOBMs and data products) generally produce a higher ocean CO_2 sink during strong El
591 Niño events. There is emerging agreement between GOBMs and data-products on the patterns of decadal variability of
592 S_{OCEAN} with a global stagnation in the 1990s and an extra-tropical strengthening in the 2000s (McKinley et al., 2020,
593 Hauck et al., 2020). The central estimates of the annual flux from the GOBMs and the $f\text{CO}_2$ -based data products have a
594 correlation r of 0.94 (1990-2021). The agreement between the models and the data products reflects some consistency
595 in their representation of underlying variability since there is little overlap in their methodology or use of observations.
596

597 **C.4 Methodology Land CO_2 sink**

598 **C.4.1 DGVM simulations**

599 The DGVMs model runs were forced by either the merged monthly Climate Research Unit (CRU) and 6 hourly
600 Japanese 55-year Reanalysis (JRA-55) data set or by the monthly CRU data set, both providing observation-based
601 temperature, precipitation, and incoming surface radiation on a $0.5^\circ \times 0.5^\circ$ grid and updated to 2021 (Harris et al., 2014,
602 2020). The combination of CRU monthly data with 6 hourly forcing from JRA-55 (Kobayashi et al., 2015) is performed
603 with methodology used in previous years (Viovy, 2016) adapted to the specifics of the JRA-55 data.

604 Introduced in GCB2021 (Friedlingstein et al., 2022a), incoming short-wave radiation fields to take into account aerosol
605 impacts and the division of total radiation into direct and diffuse components as summarised below.

606 The diffuse fraction dataset offers 6-hourly distributions of the diffuse fraction of surface shortwave fluxes over the
607 period 1901-2021. Radiative transfer calculations are based on monthly-averaged distributions of tropospheric and
608 stratospheric aerosol optical depth, and 6-hourly distributions of cloud fraction. Methods follow those described in the
609 Methods section of Mercado et al. (2009), but with updated input datasets.

610 The time series of speciated tropospheric aerosol optical depth is taken from the historical and RCP8.5 simulations by
611 the HadGEM2-ES climate model (Bellouin et al., 2011). To correct for biases in HadGEM2-ES, tropospheric aerosol
612 optical depths are scaled over the whole period to match the global and monthly averages obtained over the period
613 2003-2020 by the CAMS Reanalysis of atmospheric composition (Inness et al., 2019), which assimilates satellite
614 retrievals of aerosol optical depth.

615 The time series of stratospheric aerosol optical depth is taken from the by Sato et al. (1993) climatology, which has
616 been updated to 2012. Years 2013-2020 are assumed to be background years so replicate the background year 2010.
617 That assumption is supported by the Global Space-based Stratospheric Aerosol Climatology time series (1979-2016;



618 Thomason et al., 2018). The time series of cloud fraction is obtained by scaling the 6-hourly distributions simulated in
619 the Japanese Reanalysis (Kobayashi et al., 2015) to match the monthly-averaged cloud cover in the CRU TS v4.06
620 dataset (Harris et al., 2020). Surface radiative fluxes account for aerosol-radiation interactions from both tropospheric
621 and stratospheric aerosols, and for aerosol-cloud interactions from tropospheric aerosols, except mineral dust.
622 Tropospheric aerosols are also assumed to exert interactions with clouds.

623 The radiative effects of those aerosol-cloud interactions are assumed to scale with the radiative effects of aerosol-
624 radiation interactions of tropospheric aerosols, using regional scaling factors derived from HadGEM2-ES. Diffuse
625 fraction is assumed to be 1 in cloudy sky. Atmospheric constituents other than aerosols and clouds are set to a constant
626 standard mid-latitude summer atmosphere, but their variations do not affect the diffuse fraction of surface shortwave
627 fluxes.

628 In summary, the DGVMs forcing data include time dependent gridded climate forcing, global atmospheric CO₂
629 (Dlugokencky and Tans, 2022), gridded land cover changes (see Appendix C.2.2), and gridded nitrogen deposition and
630 fertilisers (see Table A1 for specific models details).

631 Four simulations were performed with each of the DGVMs. Simulation 0 (S0) is a control simulation which uses fixed
632 pre-industrial (year 1700) atmospheric CO₂ concentrations, cycles early 20th century (1901-1920) climate and applies a
633 time-invariant pre-industrial land cover distribution and pre-industrial wood harvest rates. Simulation 1 (S1) differs
634 from S0 by applying historical changes in atmospheric CO₂ concentration and N inputs. Simulation 2 (S2) applies
635 historical changes in atmospheric CO₂ concentration, N inputs, and climate, while applying time-invariant pre-
636 industrial land cover distribution and pre-industrial wood harvest rates. Simulation 3 (S3) applies historical changes in
637 atmospheric CO₂ concentration, N inputs, climate, and land cover distribution and wood harvest rates.

638 S2 is used to estimate the land sink component of the global carbon budget (S_{LAND}). S3 is used to estimate the total land
639 flux but is not used in the global carbon budget. We further separate S_{LAND} into contributions from CO₂ (=S1-S0) and
640 climate (=S2-S1+S0).

641 C.4.2 DGVM evaluation and uncertainty assessment for S_{LAND}

642 We apply three criteria for minimum DGVMs realism by including only those DGVMs with (1) steady state after
643 spin up, (2) global net land flux ($S_{\text{LAND}} - E_{\text{LUC}}$) that is an atmosphere-to-land carbon flux over the 1990s ranging
644 between -0.3 and 2.3 GtC yr⁻¹, within 90% confidence of constraints by global atmospheric and oceanic observations
645 (Keeling and Manning, 2014; Wanninkhof et al., 2013), and (3) global E_{LUC} that is a carbon source to the atmosphere
646 over the 1990s, as already mentioned in section C.2.2. All DGVMs meet these three criteria.

647 In addition, the DGVMs results are also evaluated using the International Land Model Benchmarking system (ILAMB;
648 Collier et al., 2018). This evaluation is provided here to document, encourage and support model improvements through
649 time. ILAMB variables cover key processes that are relevant for the quantification of S_{LAND} and resulting aggregated
650 outcomes. The selected variables are vegetation biomass, gross primary productivity, leaf area index, net ecosystem
651 exchange, ecosystem respiration, evapotranspiration, soil carbon, and runoff (see Figure B3 for the results and for the
652 list of observed databases). Results are shown in Figure B3 and discussed in Section 3.6.5.

653 For the uncertainty for S_{LAND} , we use the standard deviation of the annual CO₂ sink across the DGVMs, averaging to
654 about ± 0.6 GtC yr⁻¹ for the period 1959 to 2021. We attach a medium confidence level to the annual land CO₂ sink and



655 its uncertainty because the estimates from the residual budget and averaged DGVMs match well within their respective
656 uncertainties (Table 5).

657

658 **C.5 Methodology Atmospheric Inversions**

659 **C.5.1 Inversion System Simulations**

660 Nine atmospheric inversions (details of each in Table A4) were used to infer the spatio-temporal distribution of the CO₂
661 flux exchanged between the atmosphere and the land or oceans. These inversions are based on Bayesian inversion
662 principles with prior information on fluxes and their uncertainties. They use very similar sets of surface measurements
663 of CO₂ time series (or subsets thereof) from various flask and in situ networks. One inversion system also used satellite
664 xCO₂ retrievals from GOSAT and OCO-2.

665 Each inversion system uses different methodologies and input data but is rooted in Bayesian inversion principles. These
666 differences mainly concern the selection of atmospheric CO₂ data and prior fluxes, as well as the spatial resolution,
667 assumed correlation structures, and mathematical approach of the models. Each system uses a different transport model,
668 which was demonstrated to be a driving factor behind differences in atmospheric inversion-based flux estimates, and
669 specifically their distribution across latitudinal bands (Gaubert et al., 2019; Schuh et al., 2019).

670 The inversion systems all prescribe similar global fossil fuel emissions for E_{FOS}; specifically, the GCP's Gridded Fossil
671 Emissions Dataset version 2022 (GCP-GridFEDv2022.2; Jones et al., 2022), which is an update through 2021 of the
672 first version of GCP-GridFED presented by Jones et al. (2021), or another recent version of GCP-GridFED (Table A4).
673 All GCP-GridFED versions scale gridded estimates of CO₂ emissions from EDGARv4.3.2 (Janssens-Maenhout et al.,
674 2019) within national territories to match national emissions estimates provided by the GCP for the years 1959-2021,
675 which are compiled following the methodology described in Appendix C.1. GCP-GridFEDv2022.2 adopts the
676 seasonality of emissions (the monthly distribution of annual emissions) from the Carbon Monitor (Liu et al., 2020a,b;
677 Dou et al., 2022) for Brazil, China, all EU27 countries, the United Kingdom, the USA and shipping and aviation bunker
678 emissions. The seasonality present in Carbon Monitor is used directly for years 2019-2021, while for years 1959-2018
679 the average seasonality of 2019 and 2021 are applied (avoiding the year 2020 during which emissions were most
680 impacted by the COVID-19 pandemic). For all other countries, seasonality of emissions is taken from EDGAR
681 (Janssens-Maenhout et al., 2019; Jones et al., 2022), with small annual correction to the seasonality present in year
682 2010 based on heating or cooling degree days to account for the effects of inter-annual climate variability on the
683 seasonality of emissions (Jones et al., 2021). Earlier versions of GridFED used Carbon Monitor-based seasonality only
684 during the years 2019 onwards. In addition, we note that GCP-GridFEDv2022.1 and v2022.2 include emissions from
685 cement production and the cement carbonation CO₂ sink (Appendix C.1.1), whereas earlier versions of GCP-GridFED
686 did not include the cement carbonation CO₂ sink.

687 The consistent use of recent versions of GCP-GridFED for E_{FOS} ensures a close alignment with the estimate of E_{FOS}
688 used in this budget assessment, enhancing the comparability of the inversion-based estimate with the flux estimates
689 deriving from DGVMs, GOBMs and fCO₂-based methods. To ensure that the estimated uptake of atmospheric CO₂ by
690 the land and oceans was fully consistent with the sum of the fossil emissions flux from GCP-GridFEDv2022.2 and the
691 atmospheric growth rate of CO₂, small corrections to the fossil fuel emissions flux were applied to inversions systems
692 using other versions of GCP-GridFED.



693 The land and ocean CO₂ fluxes from atmospheric inversions contain anthropogenic perturbation and natural pre-
694 industrial CO₂ fluxes. On annual time scales, natural pre-industrial fluxes are primarily land CO₂ sinks and ocean CO₂
695 sources corresponding to carbon taken up on land, transported by rivers from land to ocean, and outgassed by the
696 ocean. These pre-industrial land CO₂ sinks are thus compensated over the globe by ocean CO₂ sources corresponding to
697 the outgassing of riverine carbon inputs to the ocean, using the exact same numbers and distribution as described for the
698 oceans in Section 2.4. To facilitate the comparison, we adjusted the inverse estimates of the land and ocean fluxes per
699 latitude band with these numbers to produce historical perturbation CO₂ fluxes from inversions.

700 C.5.2 Inversion System Evaluation

701 All participating atmospheric inversions are checked for consistency with the annual global growth rate, as both are
702 derived from the global surface network of atmospheric CO₂ observations. In this exercise, we use the conversion
703 factor of 2.086 GtC/ppm to convert the inverted carbon fluxes to mole fractions, as suggested by Prather (2012). This
704 number is specifically suited for the comparison to surface observations that do not respond uniformly, nor
705 immediately, to each year's summed sources and sinks. This factor is therefore slightly smaller than the GCB
706 conversion factor in Table 1 (2.142 GtC/ppm, Ballantyne et al., 2012). Overall, the inversions agree with the growth
707 rate with biases between 0.03-0.08 ppm (0.06-0.17 GtCyr⁻¹) on the decadal average.

708 The atmospheric inversions are also evaluated using vertical profiles of atmospheric CO₂ concentrations (Figure B4).
709 More than 30 aircraft programs over the globe, either regular programs or repeated surveys over at least 9 months, have
710 been used in order to draw a robust picture of the system performance (with space-time data coverage irregular and
711 denser in the 0-45°N latitude band; Table A6). The nine systems are compared to the independent aircraft CO₂
712 measurements between 2 and 7 km above sea level between 2001 and 2021. Results are shown in Figure B4, where the
713 inversions generally match the atmospheric mole fractions to within 0.7 ppm at all latitudes, except for CT Europe in
714 2011-2021 over the more sparsely sampled southern hemisphere.

715

716 Appendix D: Processes not included in the global carbon budget

717 D.1 Contribution of anthropogenic CO and CH₄ to the global carbon budget

718 Equation (1) includes only partly the net input of CO₂ to the atmosphere from the chemical oxidation of reactive
719 carbon-containing gases from sources other than the combustion of fossil fuels, such as: (1) cement process emissions,
720 since these do not come from combustion of fossil fuels, (2) the oxidation of fossil fuels, (3) the assumption of
721 immediate oxidation of vented methane in oil production. However, it omits any other anthropogenic carbon-containing
722 gases that are eventually oxidised in the atmosphere, such as anthropogenic emissions of CO and CH₄. An attempt is
723 made in this section to estimate their magnitude and identify the sources of uncertainty. Anthropogenic CO emissions
724 are from incomplete fossil fuel and biofuel burning and deforestation fires. The main anthropogenic emissions of fossil
725 CH₄ that matter for the global (anthropogenic) carbon budget are the fugitive emissions of coal, oil and gas sectors (see
726 below). These emissions of CO and CH₄ contribute a net addition of fossil carbon to the atmosphere.

727 In our estimate of E_{FOS} we assumed (Section 2.1.1) that all the fuel burned is emitted as CO₂, thus CO anthropogenic
728 emissions associated with incomplete fossil fuel combustion and its atmospheric oxidation into CO₂ within a few



729 months are already counted implicitly in E_{FOS} and should not be counted twice (same for E_{LUC} and anthropogenic CO
730 emissions by deforestation fires). Anthropogenic emissions of fossil CH₄ are however not included in E_{FOS} , because
731 these fugitive emissions are not included in the fuel inventories. Yet they contribute to the annual CO₂ growth rate after
732 CH₄ gets oxidized into CO₂. Emissions of fossil CH₄ represent 30% of total anthropogenic CH₄ emissions (Saunois et
733 al. 2020; their top-down estimate is used because it is consistent with the observed CH₄ growth rate), that is 0.083 GtC
734 yr⁻¹ for the decade 2008-2017. Assuming steady state, an amount equal to this fossil CH₄ emission is all converted to
735 CO₂ by OH oxidation, and thus explain 0.083 GtC yr⁻¹ of the global CO₂ growth rate with an uncertainty range of 0.061
736 to 0.098 GtC yr⁻¹ taken from the min-max of top-down estimates in Saunois et al. (2020). If this min-max range is
737 assumed to be 2 σ because Saunois et al. (2020) did not account for the internal uncertainty of their min and max top-
738 down estimates, it translates into a 1- σ uncertainty of 0.019 GtC yr⁻¹.

739 Other anthropogenic changes in the sources of CO and CH₄ from wildfires, vegetation biomass, wetlands, ruminants, or
740 permafrost changes are similarly assumed to have a small effect on the CO₂ growth rate. The CH₄ and CO emissions
741 and sinks are published and analysed separately in the Global Methane Budget and Global Carbon Monoxide Budget
742 publications, which follow a similar approach to that presented here (Saunois et al., 2020; Zheng et al., 2019).

743 **D.2 Contribution of other carbonates to CO₂ emissions**

744 Although we do account for cement carbonation (a carbon sink), the contribution of emissions of fossil carbonates
745 (carbon sources) other than cement production is not systematically included in estimates of E_{FOS} , except for Annex I
746 countries and lime production in China (Andrew and Peters, 2021). The missing processes include CO₂ emissions
747 associated with the calcination of lime and limestone outside of cement production. Carbonates are also used in various
748 industries, including in iron and steel manufacture and in agriculture. They are found naturally in some coals. CO₂
749 emissions from fossil carbonates other than cement not included in our dataset are estimated to amount to about 0.3%
750 of E_{FOS} (estimated based on Crippa et al., 2019).

751 **D.3 Anthropogenic carbon fluxes in the land-to-ocean aquatic continuum**

752 The approach used to determine the global carbon budget refers to the mean, variations, and trends in the perturbation
753 of CO₂ in the atmosphere, referenced to the pre-industrial era. Carbon is continuously displaced from the land to the
754 ocean through the land-ocean aquatic continuum (LOAC) comprising freshwaters, estuaries, and coastal areas (Bauer et
755 al., 2013; Regnier et al., 2013). A substantial fraction of this lateral carbon flux is entirely ‘natural’ and is thus a steady
756 state component of the pre-industrial carbon cycle. We account for this pre-industrial flux where appropriate in our
757 study (see Appendix C.3). However, changes in environmental conditions and land-use change have caused an increase
758 in the lateral transport of carbon into the LOAC – a perturbation that is relevant for the global carbon budget presented
759 here.

760 The results of the analysis of Regnier et al. (2013) can be summarised in two points of relevance for the anthropogenic
761 CO₂ budget. First, the anthropogenic perturbation of the LOAC has increased the organic carbon export from terrestrial
762 ecosystems to the hydrosphere by as much as 1.0 ± 0.5 GtC yr⁻¹ since pre-industrial times, mainly owing to enhanced
763 carbon export from soils. Second, this exported anthropogenic carbon is partly respired through the LOAC, partly
764 sequestered in sediments along the LOAC and to a lesser extent, transferred to the open ocean where it may accumulate
765 or be outgassed. The increase in storage of land-derived organic carbon in the LOAC carbon reservoirs (burial) and in



766 the open ocean combined is estimated by Regnier et al. (2013) at $0.65 \pm 0.35 \text{GtC yr}^{-1}$. The inclusion of LOAC related
767 anthropogenic CO_2 fluxes should affect estimates of S_{LAND} and S_{OCEAN} in Eq. (1) but does not affect the other terms.
768 Representation of the anthropogenic perturbation of LOAC CO_2 fluxes is however not included in the GOBMs and
769 DGVMs used in our global carbon budget analysis presented here.

770 **D.4 Loss of additional land sink capacity**

771 Historical land-cover change was dominated by transitions from vegetation types that can provide a large carbon sink
772 per area unit (typically, forests) to others less efficient in removing CO_2 from the atmosphere (typically, croplands).
773 The resultant decrease in land sink, called the ‘loss of additional sink capacity’, can be calculated as the difference
774 between the actual land sink under changing land-cover and the counterfactual land sink under pre-industrial land-
775 cover. This term is not accounted for in our global carbon budget estimate. Here, we provide a quantitative estimate of
776 this term to be used in the discussion. Seven of the DGVMs used in Friedlingstein et al. (2019) performed additional
777 simulations with and without land-use change under cycled pre-industrial environmental conditions. The resulting loss
778 of additional sink capacity amounts to $0.9 \pm 0.3 \text{GtC yr}^{-1}$ on average over 2009-2018 and $42 \pm 16 \text{GtC}$ accumulated
779 between 1850 and 2018 (Obermeier et al., 2021). OSCAR, emulating the behaviour of 11 DGVMs finds values of the
780 loss of additional sink capacity of $0.7 \pm 0.6 \text{GtC yr}^{-1}$ and $31 \pm 23 \text{GtC}$ for the same time period (Gasser et al., 2020).
781 Since the DGVM-based ELUC estimates are only used to quantify the uncertainty around the bookkeeping models’
782 ELUC, we do not add the loss of additional sink capacity to the bookkeeping estimate.